ulm university universität ulm

Design, Synthesis, and Characterization of Coordination Compounds and Coordination Polymers Based on 1,2,3-Triazolate Ligands

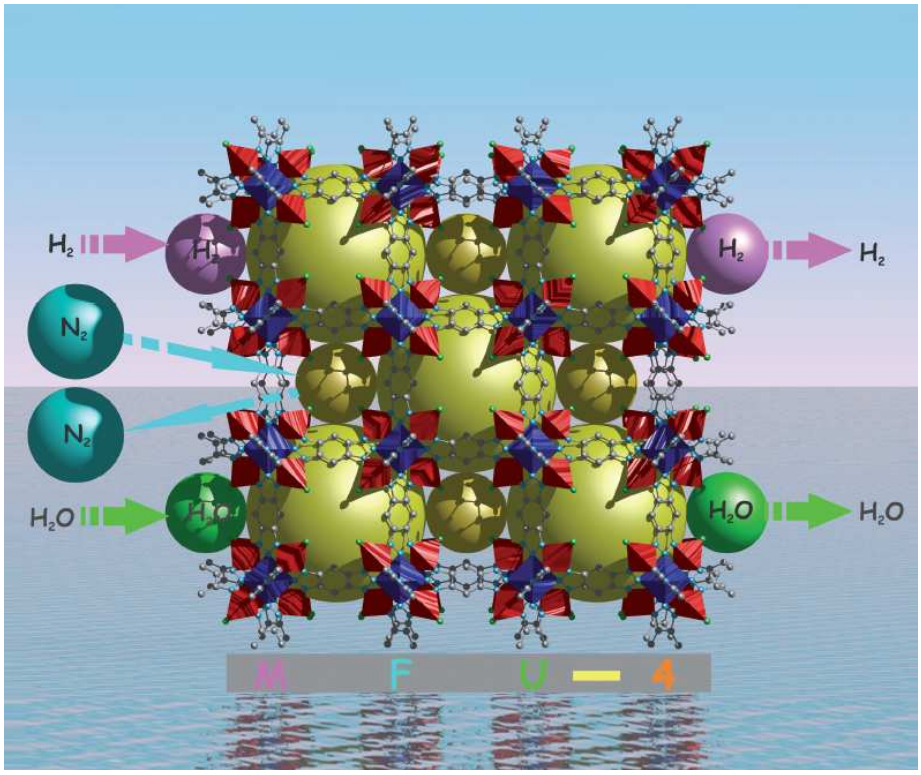

Dissertation

zur Erlangung des Doktorgrades Dr. rer. nat.

der Fakultät für Naturwissenschaften

der Universität Ulm

vorgelegt von

Shyam Biswas

aus North 24 Parganas, Indien

2010

Die vorliegende Arbeit entstand in der Zeit von September 2006 bis Januar 2010 unter der Anleitung von Prof. Dr. Dirk Volkmer am Fachbereich Chemie der Universität Ulm.

1. Gutachter: Prof. Dr. Dirk Volkmer

2. Gutachter: Prof. Dr. Nicola Hüsing

Tag der Promotion: 10.11.2010

Dedicated to my family members, especially to the beloved memory of my grandmother who passed away during the course of this dissertation work

Table of Contents

List of Tables iii

List of Figures and Schemes iv

Chapter 1 Introduction 1

1.1 1,2,3-Triazole 1

1.2 Benzotriazole 1

1.2.1 Synthesis and Applications 1

1.2.2 Role as Corrosion Inhibitors 2

1.2.3 Coordination Modes 2

1.2.4 Penta- and Nonanuclear Compounds 5

1.3 Metal-Organic Frameworks 11

1.3.1 History and Scope 11

1.3.2 Design Principles 12

1.3.3 Synthesis 17

1.3.4 Role as Functional Materials 19

1.4 Summary (Aim of the Dissertation Work) 35

Chapter 2 Homo- and Heteropentanuclear Coordination Compounds $[MZn_4(L)_4(L')_6]$ (M^{II} = Zn, Fe, Co, Ni, or Cu; L = chloride or acac; L' = 1,2,3-benzotriazolate ligand) Represented by the Nonplanar $K_{3,3}$ Graph 36

2.1 Introduction 36

2.2 Results and Discussion 40

2.2.1 Syntheses 40

2.2.2 Characterization 41

2.2.3 Structure Description 60

2.2.4 Magnetic Properties 65

2.2.5 Graph Theoretical Representation 70

2.3 Experimental Section 72

2.3.1 Materials and General Methods 72

2.3.2 Syntheses 73

2.3.3 Structure Determination 77

2.4 Summary 80

Chapter 3 Homo- and Heterononanuclear Coordination Compounds Featuring $\{M_9L_{12}\}^{6+}$ Cores (M^{II} = Co, Ni, Zn, or $Fe_{1/3}Zn_{2/3}$; L = 1,2,3-benzotriazolate) 81

3.1 Introduction 81
3.2 Results and Discussion 84
3.2.1 Syntheses 84
3.2.2 Characterization 86
3.2.3 Structure Description 100
3.2.4 Magnetic Properties 109
3.2.5 Mössbauer Spectroscopy 111
3.3 Experimental Section 113
3.3.1 Materials and General Methods 113
3.3.2 Syntheses 114
3.3.3 Structure Determination 117
3.4 Summary 120

Chapter 4 Two- and Three-Dimensional Coordination Polymers Containing Benzobistriazolate Ligands and Zinc Ions 122
4.1 Introduction 122
4.2 Results and Discussion 124
4.2.1 Syntheses 124
4.2.2 Characterization 124
4.2.3 Rietveld Refinement 133
4.2.4 Structure Description 134
4.2.5 Sorption Properties 139
4.3 Experimental Section 140
4.3.1 Materials and General Methods 140
4.3.2 Syntheses 142
4.3.3 Structure Determination 143
4.4 Summary 145

Chapter 5 Conclusions and Outlook 147
Zusammenfassung und Ausblick 152

References 158
List of Abbreviations 179
Acknowledgements 184
Curriculum Vitae 186

List of Tables

Table 1.1 List of pentanuclear compounds containing bta ligands described in this section. 6
Table 1.2 Selection of catalytically active MOFs and summary of the corresponding catalytic reactions. 20
Table 1.3 Summary of selective gas adsorption in rigid MOFs. 26
Table 1.4 Summary of selective gas adsorption in flexible/dynamic MOFs. 30
Table 1.5 Summary of known MOFs exhibiting kinetic separation of gas mixtures. 33
Table 2.1 List of compounds described in this chapter. 39
Table 2.2 Experimental M (M = Fe, Co, Ni, or Cu):Zn ratios obtained from EDX analyses. 45
Table 2.3 ICP-AES analyses for **3a**, **4a-b**, **5b**, and **6a**. 49
Table 2.4 Selected bond lengths (Å) and angles (°) of **1**. 63
Table 2.5 Selected bond lengths (Å) of **2a**, **3a**, **4a-b**, **5b** and **6a**. 64
Table 2.6 Magnetochemical analysis parameters for **3a**, **4a**, **5b**, and **6a**. 69
Table 2.7 Elemental analyses of all the compounds described in this chapter. 75
Table 2.8 List of infrared frequencies of all the compounds presented in this chapter. 75
Table 2.9 Single crystal X-ray data and refinement summary for **1**, **2a**, **3a**, **4a-b**, **5b**, and **6a**. 78
Table 3.1 List of compounds described in this chapter. 81
Table 3.2 Operating parameters for the ICP-AES spectrometer. 89
Table 3.3 Selected bond lengths (Å) of **3**. 104
Table 3.4 Selected bond lengths (Å) of **4**. 105
Table 3.5 Selected bond lengths (Å) of **5**. 105
Table 3.6 Elemental analyses of all the compounds described in this chapter. 116
Table 3.7 List of infrared frequencies of all the compounds presented in this chapter. 116
Table 3.8 Single crystal X-ray data and refinement summary for **1-5**. 118
Table 4.1 Change of lattice parameters of **1** obtained from VTXRPD data. 134
Table 4.2 Selected bond lengths (Å) of **1** obtained from Rietveld refinement using X-ray diffraction data from powders sampled at 350 °C. 134
Table 4.3 Principal bond lengths (Å) of **1** obtained from single crystal X-ray data. 136
Table 4.4 Principal bond lengths (Å) of **2** obtained from single crystal X-ray data. 138
Table 4.5 Single crystal X-ray data and structure refinement parameters for **1** and **2.** 144
Table 4.6 Crystal data and structure refinement parameters of **1** obtained from Rietveld refinement using powder data at 350 °C. 145

List of Figures and Schemes

Figure 1.1 Structure of 1,2,3-triazole. 1

Figure 1.2 Structure of 1,2,3-benzotriazole. 1

Figure 1.3 Different coordination modes of benzotriazole and its conjugate base. 2

Figure 1.4 Ball-and-stick representation of the molecular structure of (a) $[Ir(CO)(PPh_3)_2(bta)]$ and (b) $[GaCl_3(btaH)_2]$ showing η^1 coordination mode of bta and btaH, respectively. All hydrogen atoms are omitted for clarity. 3

Figure 1.5 Ball-and-stick representation of the molecular structure of $[CH_3Hg(bta)]$ showing μ_2 bridging coordination (via N^1 and N^2) mode of bta ligand. All hydrogen atoms are omitted. 3

Figure 1.6 Ball-and-stick representation of the molecular structure of $[Cu_2(tmbma)_2(bta)][(NO_3)_3]$ showing μ_2 bridging coordination (via N^1 and N^3) mode of bta ligand. For clarity, all hydrogen atoms and nitrate counter anions are omitted. 4

Figure 1.7 Ball-and-stick representation of the molecular structure of $[Cu_5(bta)_6(acac)_4]$ showing the presence of an imaginary $\{Cu_4\}$ tetrahedron. 6

Figure 1.8 Ball-and-stick representation of the molecular structure of compounds **2** (a), **3** (b), **4a** (c), **5** (d), **6** (e), and **7** (f). 8

Figure 1.9 Ball-and-stick representation of the molecular structure of $[Zn_9(Me_2bta)_{12}(acac)_6]$ displaying the presence of two $\{Zn_4\}$ tetrahedra sharing a common apex. All hydrogen atoms are omitted for clarity. 9

Figure 1.10 Plot of $\chi_m T$ versus T in the temperature range 2-300 K for $[Cu_5(bta)_6(trop)_4]$ (**1c**). Open circles: experimental data, graph: a least-squares fit to the employed model. 10

Figure 1.11 Ball-and-stick representation of the **MOF-5** framework with zinc atoms represented as blue tetrahedra. All hydrogen atoms are removed for clarity. The yellow sphere represents a large cavity inside the framework. 11

Figure 1.12 Number of citations containing the key word “coordination polymers” in the past 19 years (source: SciFinder Scholar until September 2009). 12

Figure 1.13 Representative examples of organic ligands used for the construction of metal-organic frameworks (HMTA = hexamethylenetetramine). 13

Figure 1.14 “Node-and-spacer” representations of metal-organic frameworks: *a*) 0D nanoball; *b*) 1D zigzag chain; *c*) 1D helix; *d*) 1D ladder; *e*) 2D bilayers; *f*)

2D square grid; *g*) 2D honeycomb; *h*) 3D (10,3)-a net; *i*) 3D diamondoid net; *j*) 3D primitive cubic net; *k*) 3D NbO net. 14

Figure 1.15 "Vertex-linked Polygons or Polyhedra" (VLPP) representations of metal-organic frameworks: *a*) 0D nanoball; *b*) 3D (10,3)-a net; *c*) 3D diamondoid net; *d*) 3D primitive cubic net; *e*) 3D NbO net. 14

Figure 1.16 Four unitary nets represented in both node-and-spacer and VLPP format: a) (10,3)-a net, b) diamondoid net, c) NbO net, d) primitive cubic net. 15

Figure 1.17 Assembly of metal-organic frameworks (MOFs) by the copolymerization of metal ions with organic linkers to give (a) flexible metal-bipyridine structures with expanded diamond topology, and (b) rigid metal-carboxylate coordination units that can be linked by benzene "struts" to form rigid extended frameworks in which the M-O-C core (SBU) of each coordination unit acts as a large octahedron decorating a 6-connected vertex in a cube. All hydrogen atoms have been omitted for clarity. In (a): M, orange; C, grey; N, blue; in (b): M, pink; O, red; C, grey. 16

Figure 1.18 Wire representation of one the layers of the 2D layered squared grid coordination polymer $[Cd(4,4'\text{-bpy})_2(NO_3)_2]$ synthesized by Fujita *et al*. All hydrogen atoms and coordinated nitrate anions have been omitted for clarity. 20

Figure 1.19 Wire representation along the *c*-direction of the hexagonal framework (with large pores formed with the trinuclear secondary building units) of the enantioselective MOF catalyst, **POST-1** synthesized by Kim *et al*. 23

Figure 1.20 Five types of adsorption isotherm, I to V, in the classification of Brunauer, Deming, Deming, and Teller (BDDT), together with type VI, the stepped isotherm. 25

Figure 2.1 (a) Ball-and-stick representation of $[MZn_4X_4(L)_6]$ coordination units, highlighting the central octahedral coordination site which results from 6 N-donor atoms situated at the centers of the edges of an imaginary tetrahedron which is spanned by the 4 Zn^{II} ions at the corners. (b) Simplified representation of metal centers and ligand donor atoms. (c), (d) Derivation (*cf.* discussion on Graph Theoretical Representation) of a rational graphical scheme representing the connectivity of the coordination units. 38

Figure 2.2 Photographs of all compounds (except **1** which has similar colour as **2a** or **2b**) described in this chapter. Top row: the set of compounds recrystallised

from DMF; bottom row: the set of compounds recrystallised from bromobenzene. 39
Figure 2.3 Structures of the 1,2,3-benzotriazole ligands described in this chapter. 40
Figure 2.4 Theoretical (black) and experimental (grey) XRPD patterns of **1**. 41
Figure 2.5 Theoretical (black) and experimental (grey) XRPD patterns of **2a**. 42
Figure 2.6 Theoretical (black) and experimental (grey) XRPD patterns of **3a**. 42
Figure 2.7 Theoretical (black) and experimental (grey) XRPD patterns of **4a**. 43
Figure 2.8 Theoretical (black) and experimental (grey) XRPD patterns of **4b**. 43
Figure 2.9 Theoretical (black) and experimental (grey) XRPD patterns of **5b**. 43
Figure 2.10 Theoretical (black) and experimental (grey) XRPD patterns of **6a**. 44
Figure 2.11 Experimental XRPD patterns of all the compounds (except **1**) presented in this chapter. Black lines: XRPD patterns of the set of compounds having DMF as occluded solvent molecules; grey lines: XRPD patterns of the set of compounds having bromobenzene as occluded solvent molecules. 44
Figure 2.12 EDX spectrum of **3a**. 45
Figure 2.13 EDX spectrum of **4a**. 46
Figure 2.14 EDX spectrum of **6a**. 46
Figure 2.15 EDX spectrum of **3b**. 47
Figure 2.16 EDX spectrum of **4b**. 47
Figure 2.17 EDX spectrum of **5b**. 48
Figure 2.18 EDX spectrum of **6b**. 48
Figure 2.19 Experimental (a) and theoretical (b) isotopic patterns of **2a**. 50
Figure 2.20 Experimental (a) and theoretical (b) isotopic patterns of **6a**. 51
Figure 2.21 TG analyses of **2**-**4a** under N_2 atmosphere. 52
Figure 2.22 TG analysis of **6a** under N_2 atmosphere. 52
Figure 2.23 TG analysis of **2**-**6b** under N_2 atmosphere. 53
Figure 2.24 FT-IR spectrum of **1**. 54
Figure 2.25 FT-IR spectra of **2a**, **3a**, **4a**, and **6a**. 54
Figure 2.26 FT-IR spectra of **2**-**6b**. 55
Figure 2.27 (a) UV-Vis spectra of **3a**-**b** in ethyl acetate solution. (b) UV-Vis diffuse reflectance spectra of **3a**-**b**. 56
Figure 2.28 (a) UV-Vis spectra of **4a**-**b** in bromobenzene solution measured with the same concentration. (b) UV-Vis diffuse reflectance spectra of **4a**-**b**. 56

Figure 2.29 (a) UV-Vis spectrum of **5b** in ethyl acetate solution. (b) UV-Vis diffuse reflectance spectrum of **5b**. 58

Figure 2.30 (a) UV-Vis spectrum of **5b** in ethyl acetate solution. (b) UV-Vis diffuse reflectance spectrum of **5b**. 59

Figure 2.31 (a) Room temperature photoluminescence spectra of **2a**, **3a**, **4a**, **4b**, **5b**, **6a**, and free Me_2btaH ligand in ethylacetate solution. 60

Figure 2.32 Ball-and-stick representation of the molecular structures of (a) **1**, and (b) **2a**, **3a**, **4a-b**, **5b**, and **6a** (M = Zn, **2a**; Fe, **3a**; Co, **4a-b**; Ni, **5b**; Cu, **6a**). All hydrogen atoms are omitted for clarity. Symmetry operators used to create equivalent atoms are ('): 1/4-x, 1/4-y, z; (''): 1/4-x, y, 5/4-z; ('''): x, 1/4-y, 5/4-z. For **2a**, the labels 'Zn(1)' should be replaced by 'Zn(2)' to compare its bond lengths and angles with other compounds. 61

Figure 2.33 Ball-and-stick representation of the asymmetric units of **2a**, **3a**, **4a-b**, **5b**, and **6a** (M = Zn, **1a**; Fe, **2a**; Co, **3a-b**; Ni, **4b**; Cu, **5a**). Hydrogen atoms and solvent molecules are omitted for clarity. 62

Figure 2.34 Crystal packing diagram of **1** (a) and **2a** (b) wire representation. The black arrow points to a void region in the crystal lattice of **2a** which contains a DMF molecule. All hydrogen atoms and and occluded cyclohexane molecules (**1**) are omitted for clarity. 65

Figure 2.35 Temperature-dependence of the effective magnetic moment μ_{eff} for **3a** at B_0 = 0.1 T. Inset: reciprocal susceptibility at B_0 = 0.1 T. Experimental data: circles, least-squares fit to model Hamiltonian (see text): red line, single-ion effects (without intermolecular coupling): blue line. 67

Figure 2.36 μ_{eff} vs. T for **4a** at B_0 = 0.1 T. Inset: reciprocal susceptibility at B_0 = 0.1 T. Experimental data: circles, least-squares fit to model Hamiltonian (see text): red line, single-ion effects (without intermolecular coupling): blue line. 67

Figure 2.37 μ_{eff} vs. T for **5b** at B_0 = 0.1 T. Insets: M vs. B_0 (left) and χ_m *vs.* B_0 (right) at 2.0 K. Experimental data: circles, least-squares fit to model Hamiltonian (see text): blue line. 68

Figure 2.38 μ_{eff} vs. T for **6a** at B_0 = 0.1 T. Inset: χ_m *vs.* B_0 at 2.0 K. Experimental data: circles, least-squares fit to model Hamiltonian (see text): red line. 69

Figure 2.39 Formal derivation of the $K_{3,3}$ graph which can be used to represent the connectivity scheme in coordination units of type $[MZn_4X_4(L)_6]$.

The schemes follow recommendations as described in ref. 175(l). 70
Figure 2.40 Comparative structural features of the coordination units found in **MFU-1** (left) and **MFU-4** (right) (C: grey, N: blue, Cl: green, Zn: yellow, redox-active metal centres M: pink). 72
Figure 2.41 Optical micrographs of the single crystals of **2a**, **3a**, **4a**-**b**, **5b**, and **6a**. 77
Figure 3.1 Structures of the 1,2,3-benzotriazole ligands described in this chapter. 81
Figure 3.2 (a) Skeletal formula representing the connectivity of $[Fe^{II}_3Zn_6Cl_6(L_{12})]$ units (L: 5,6-dimethoxy-1,2,3-benzotriazolate) present in compound **5**. The structure of this compound is formally obtained from fusing two Kuratowski-type pentanuclear coordination units, a ball-and-stick-model of which is shown in (b). (c-e) Stepwise derivation of a skeletal formula representing the connectivity of $[M^{II}Zn_4X_4(L_6)]$ Kuratowski-type units (X: terminal ligand, L: 1,2,3-triazolate-type ligand) as described in Chapter 2. 84
Figure 3.3 Theoretical (black) and experimental (grey) XRPD patterns of **2**. 86
Figure 3.4 Theoretical (black) and experimental (grey) XRPD patterns of **3**. 87
Figure 3.5 Theoretical XRPD pattern (black) and experimental XRPD patterns of **4** synthesized by solvothermal method (blue) and vapour diffusion method (red). 87
Figure 3.6 Theoretical XRPD pattern (black) and experimental XRPD patterns of **5** synthesized by solvothermal method (blue) and vapour diffusion method (red). 88
Figure 3.7 Experimental XRPD patterns of **4** (black) and **5** (grey) synthesized by (a) solvothermal method and (b) vapour diffusion method. 88
Figure 3.8 EDX spectrum of **5**. Weight % and atom % of the elements (excluding carbon) are shown in the inset. 89
Figure 3.9 FT-IR spectrum of **1**. 90
Figure 3.10 FT-IR spectrum of **1**. 91
Figure 3.11 FT-IR spectrum of **3**. 91
Figure 3.12 FT-IR spectra of as-synthesized (black) and desolvated (grey) **4**. 92
Figure 3.13 FT-IR spectra of as-synthesized (black) and desolvated (grey) **5**. 92
Figure 3.14 TG analysis of **1** under N_2 atmosphere. 93
Figure 3.15 TG analysis of **2** under N_2 atmosphere. 93
Figure 3.16 TG analysis of **3** under N_2 atmosphere. 94
Figure 3.17 TG analysis of desolvated **4** under N_2 atmosphere. 95
Figure 3.18 TG analysis of **5** under N_2 atmosphere. 95
Figure 3.19 FT-IR spectrum of the volatile molecules liberated from **4** at 130 ºC. 96

Figure 3.20 FT-IR spectrum of the volatile molecules liberated from **5** at 130 ºC. 96

Figure 3.21 (a) UV-Vis spectrum of **1** in methanol solution. (b) UV-Vis diffuse reflectance spectrum of **1**. 97

Figure 3.22 (a) UV-Vis spectrum of **2** in methanol solution. (b) UV-Vis diffuse reflectance spectrum of **2**. 98

Figure 3.23 (a) Room temperature UV-Vis spectra of **5** in $CHCl_3$ solution recorded at two different concentrations (2.8×10^{-5} M, black; 1.7×10^{-3} M, grey). (b) Solid state UV-Vis spectrum of **2** calculated from a diffuse reflection spectrum recorded from a powder sample. 99

Figure 3.24 Room temperature cyclic voltammogram of **5** (left) and ferrocene (Fc) (right) in $CHCl_3$ with 1.0 (M) [*n*-Bu_4N][PF_6], at a potential scan rate of 0.01 V/sec at a glassy carbon electrode using Ag/Ag^+ as quasi-reference electrode and Fc/Fc^+ as internal reference. 100

Figure 3.25 Ball-and-stick representation of the molecular structure of **1** (a), **2** (b), **3** (c), **4** (d), and **5** (e). For **1**, the symmetry operators used to create equivalent metal atoms are #1: -x, -y, -z; #2: -x+y, -x, z; #3: -y, x-y, z; #4: y, -x+y, -z and #5: x-y, x, -z. For **2**, they are #1: 2-x, 2-y, -z; #2: y, 1-x+y, -z; #3: 1+x-y, x, -z; #4: 1-x+y, 2-x, z and #5: 2-y, 1+x-y, z. For **4**, it is #1: 3-x, -y, 1-z. For **5**, it is #1: 1-x, -y, -z. 103

Figure 3.26 Crystal packing diagram of **1** (a), **2** (b), **3** (c), **4** (d), and **5** (e) in wire representation. All H atoms and occluded solvent molecules are omitted for clarity. The grey circles represent void regions in the crystal lattices of **4** and **5** which can be occupied by solvent DMF molecules. 108

Figure 3.27 Temperature dependence of μ_{eff} for **1** (red) and **2** (blue) at 0.1 Tesla. Open circles: experimental data, graphs: best fits to the employed phenomenological models (see text). 110

Figure 3.28 Mössbauer spectra of **2a** at (a) 7 K and at (b) 160 K. The purple and red subspectra are fitted with the experimental values (black points with error bars). 112

Figure 3.29 Optical micrographs of the single crystals of **1**-**5**. 117

Figure 4.1 Construction principle of cubic **MFU-4** type frameworks (c) comprising T_d symmetrical $\{Zn_5Cl_4\}^{6+}$ coordination units (a), linked by linear benzobistriazolate linkers (b). (octahedrally coordinated Zn, blue octahedra; tetrahedrally coordinated Zn, red tetrahedra; N, light blue; C,

grey; Cl, green). The light yellow sphere represents a larger cavity inside **MFU-4** framework. 123

Figure 4.2 SEM images of as-synthesized **1** by (a) solvothermal method and (b) microwave irradiation method. 125

Figure 4.3 EDX spectrum of **1**. 125

Figure 4.4 Theoretical XRPD pattern (black) and experimental XRPD patterns of **1** synthesized by solvothermal method (batch 1, blue; batch 2, green) and microwave assisted method (red). 126

Figure 4.5 Theoretical (black) and experimental (grey) XRPD patterns of **2**. 127

Figure 4.6 VTXRPD plots of **1** in the range 30-600 °C. 127

Figure 4.7 VTXRPD plots of **2** in the range 30-500 °C. 128

Figure 4.8 TG analyses under N_2 atmosphere of as-synthesized (solvothermal method, black; microwave irradiation method, blue) and activated (red) **1**. 129

Figure 4.9 TG analysis of **2** under N_2 atmosphere. 129

Figure 4.10 Ion-chromatograms of gases released by heating **1** under Ar atmosphere (m/z = 73 profile, black; m/z = 44 profile, blue; m/z = 30 profile, red). 130

Figure 4.11 FT-IR spectra of as-synthesized (solvothermal method, black; microwave irradiation method, blue) and activated (red) **1**. 131

Figure 4.12 FT-IR spectrum of **2**. 131

Figure 4.13 Soild-state UV-Vis spectra of **1**, **2**, and free H_2-BBTA ligand. 132

Figure 4.14 Soild-state photoluminescence spectra of **1**, **2**, and free H_2-BBTA ligand. 133

Figure 4.15 Rietveld refinement plots for heat-treated **1**. Dotted and solid lines represent observed and calculated patterns, respectively with peak markers and the difference plot shown at the bottom. XRPD data were collected at 350 °C with a total heating period of 8 h. 134

Figure 4.16 Ball-and-stick representation of the **MFU-4** framework along the crystallographic *a*-direction (octahedrally coordinated Zn, blue octahedra; tetrahedrally coordinated Zn, red tetrahedra; N, light blue; C, grey; Cl, green). All hydrogen atoms are removed for clarity. The larger, light yellow spheres represent the cavities of B-cells whereas the smaller, dark yellow spheres represent the cavities of A-cells. 135

Figure 4.17 Crystal packing diagrams of **2**. (a) Ball and stick representation of a single 2D coordination polymer layer. (b) Same representation showing the stacking of adjacent 2D layers of **2** along the crystallographic a-

direction. (Zn, red tetrahedra; N, light blue; C, grey; Cl, green). Zinc atoms located outside of the unit cell boundaries are displayed as broken spheres. Hydrogen atoms are omitted for clarity. 138

Figure 4.18 Hydrogen adsorption (solid symbols) and desorption (empty symbols) isotherms measured for **MFU-4** at -196 ºC up to 1 bar. 139

Figure 4.19 Water adsorption (solid symbols) and desorption (empty symbols) isotherm measured for **1** at 25 ºC. 140

Figure 4.20 Optical micrographs of the single crystals of compound **1** (a) and **2** (b). 143

Figure 4.21 Structural differences between coordination units in (a) **MOF-5**, and (b) **MFU-4** (octahedrally coordinated Zn, blue octahedron; tetrahedrally coordinated Zn, red tetrahedra; N, light blue; C, grey; Cl, green). 146

Scheme 2.1 Chemical equations for the preparation of all the compounds demonstrated in this chapter. B = 2,6-lutidine; M^{II} = Zn, Fe, Co, Ni, Cu; X = (NO_3) for **4a**-**b**, **6a**-**b** and (ClO_4) for **3a**-**b**, **5b**; solvent = DMF for **2a**, **3a**, **4a**, **6a** and methanol for **2**-**6b**. 41

Scheme 3.1 Chemical equations for the syntheses of **4** and **5**. B is the base 2,6-lutidine for room temperature (RT) synthesis, or *in-situ* generated base dimethylamine for the solvothermal (Δ) synthesis. 85

Scheme 4.1 Chemical equations for the preparation of **1** and **2**. 124

Chapter 1

Introduction

1.1 1,2,3-Triazole

1,2,3-Triazole (Figure 1.1) is one of a pair of isomeric chemical compounds with molecular formula $C_2H_3N_3$, called triazoles, which have a five-membered ring of two carbon atoms and three nitrogen atoms. 1,2,3-Triazole is a basic aromatic heterocycle.

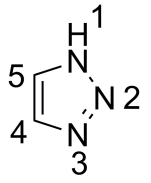

1*H*-[1,2,3]triazole
(taH)

Figure 1.1 Structure of 1,2,3-triazole.

1.2 Benzotriazole

1.2.1 Synthesis and Applications

Benzotriazole (Figure 1.2), often shortened to btaH, is an aromatic azole containing two fused rings. It is produced from the diazotization reaction of *o*-phenylenediamine and sodium nitrite in acetic acid.

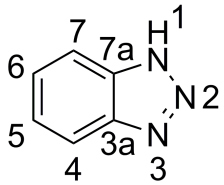

1*H*-benzo[*d*][1,2,3]triazole
(btaH)

Figure 1.2 Structure of 1,2,3-benzotriazole.

Benzotriazole is a complexing agent. It is used as corrosion inhibitor, anti-fog agent in photographic development, aircraft deicing fluid, automotive coolant, antifreeze, cutting fluid, hydraulic brake fluid, coating material, and brightening agents in metal plating industry. Benzotriazole moieties are found in pharmaceuticals such as antifungal, antibacterial, and anthelmintic drugs.[1]

1.2.2 Role as Corrosion Inhibitors

Specific ligands have been found to inhibit the corrosion of particular metals; benzotriazole and its derivatives are technologically important corrosion inhibitors for copper and copper alloys, and a few other metals.[2] By treating copper surfaces with benzotriazole (from aqueous solution, using bentotriazole-impregnated wrapping paper, or from the vapour) the ligand is strongly absorbed and produces a surface film which acts as a barrier to cathodic reactions.[2,3] At low pH values, *i.e.* below pH = 2, the inhibitor action decreases. The nature of the surface layer and its thickness have been the subject of several investigations.[2b-d,4] Both Cu(I)-bta (bta = benzotriazolate) and Cu(II)-bta compounds have been considered to be present in the benzotriazole-treated copper surfaces which have undergone some degree of oxidation.[4c,5] The search for crystalline metal coordination compounds that might act as models of the protective layers formed on the metal surfaces after treatment with benzotriazoles has been carried out over the last few years resulting in many new coordination compounds.

1.2.3 Coordination Modes

Benzotriazole and its conjugate base (bta) are polydentate ligands which can bind to metal centers in four different coordination modes (Figure 1.3): (a) η^1, (b) η^1:η^1:μ_2 (via N^1 and N^2), (c) η^1:η^1:μ_2 (via N^1 and N^3), and (d) η^1:η^1:η^1:μ_3. The following are examples of coordination compounds, documented in literature, and possess the above mentioned binding modes of benzotriazole and its conjugate base.

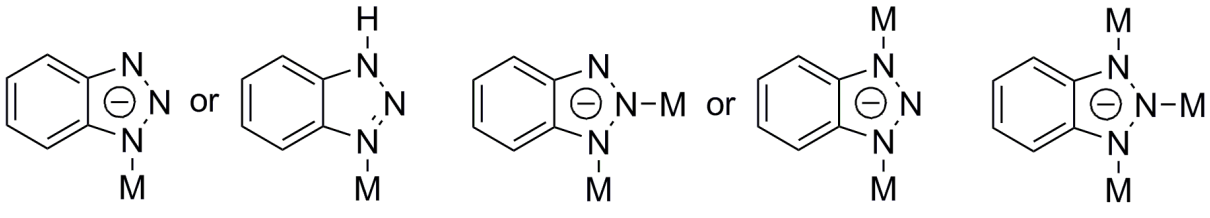

Figure 1.3 Different coordination modes of benzotriazole and its conjugate base.

(a) η^1 mode. Monodentate η^1 coordination via N^1 donor atom of bta ligand to iridium has been observed in the iridium compound $[Ir(CO)(PPh_3)_2(bta)]$[6a] (Figure 1.4a). Moreover, η^1 coordination via N^3 donor atom of btaH ligand to gallium has been found in the gallium compound $[GaCl_3(btaH)_2]$[6b].

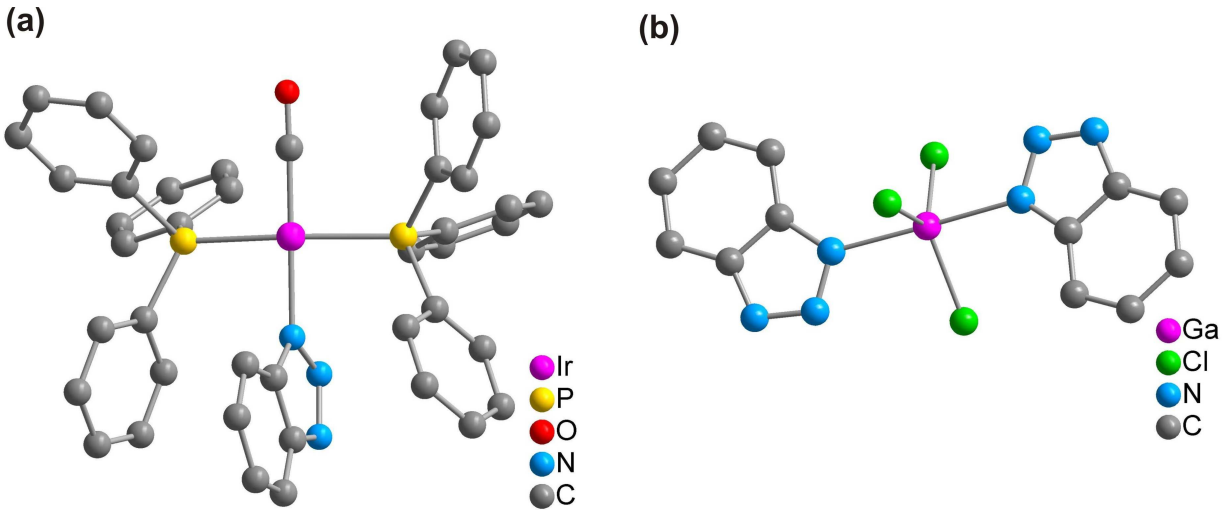

Figure 1.4 Ball-and-stick representation of the molecular structure of (a) $[Ir(CO)(PPh_3)_2(bta)]$ and (b) $[GaCl_3(btaH)_2]$ showing η^1 coordination mode of bta and btaH, respectively. All hydrogen atoms are omitted for clarity.

(b) η^1:η^1:μ_2 (via N^1 and N^2) mode. In the mercury compound $[CH_3Hg(bta)]$[7] (Figure 1.5), bidentate μ_2 bridging coordination using N^1 and N^2 donor atoms of bta ligand has been reported.

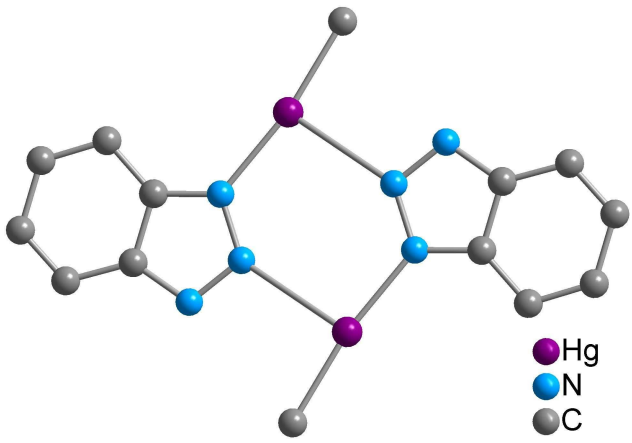

Figure 1.5 Ball-and-stick representation of the molecular structure of $[CH_3Hg(bta)]$ showing μ_2 bridging coordination (via N^1 and N^2) mode of bta ligand. All hydrogen atoms are omitted.

(c) η^1:η^1:μ_2 (via N^1 and N^3) mode. Bidentate μ_2 bridging coordination via N^1 and N^3 donor atoms of bta ligand has been observed in the dinuclear copper compound $[Cu_2(tmbma)_2(bta)][(NO_3)_3]$[8] [tmbma = tris(N-methylbenzimidazole-2-ylmethyl)amine] (Figure 1.6).

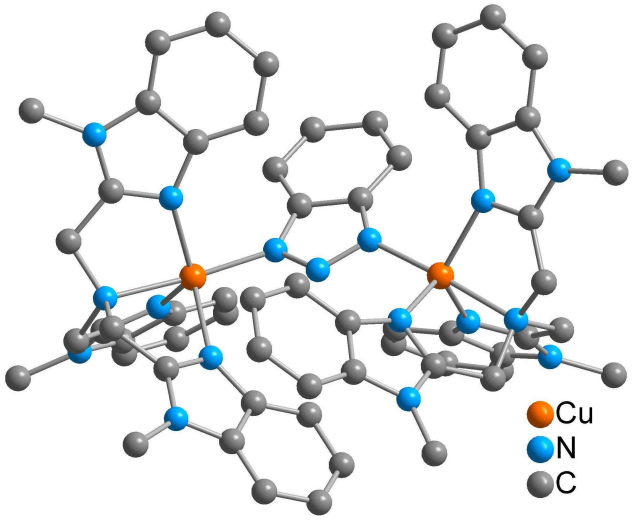

Figure 1.6 Ball-and-stick representation of the molecular structure of $[Cu_2(tmbma)_2(bta)][(NO_3)_3]$ showing μ_2 bridging coordination (via N^1 and N^3) mode of bta ligand. For clarity, all hydrogen atoms and nitrate counter anions are omitted.

(d) η^1:η^1:η^1:μ_3 mode. Tridentate η^1:η^1:η^1:μ_3 bridging coordination through all the three N donor atoms of bta ligand was first proposed for the copper compound $[Cu_5(bta)_6(acac)_4]$[9] (acacH = acetylacetone) (Figure 1.7) by Marshall. Until today, this mode of coordination of bta ligand has been described in literature for a wide variety of coordination compounds and coordination polymers containing Zn(II),[10] Co(II),[10b-c,11] Ni(II),[10b,11a,12] Cu(II),[9,13] Tl(I),[14] M(III)[15] (M = Fe, Cr, V) ions, including two mixed-valent copper[16] compounds. In the next section, the penta- and nonanuclear coordination compounds containing μ_3-bta ligands will be presented in detail.

1.2.4 Penta- and Nonanuclear Compounds

Due to the importance of benzotriazole and its derivatives as corrosion inhibitors, the coordination chemistry of benzotriazole ligands with various metal(II) ions has been throughly investigated, producing many new polynuclear compounds. Focussing on the summary of coordination compounds of benzotriazolate ligands with divalent metal ions, a range of pentanuclear compounds possessing molecular formulae $[M_5(L)_{4-x}(OH)_x(L')_6(H_2O)_{4x}]$ (M^{II} = Zn, Co, Ni, Cu; L' = bta, Mebta, or Me_2bta; L = β-diketonate[9,10c,10f,12a-c,13] or nitrate[10a,11a] ; x = 0, 1) (MebtaH = 5-methyl-1,2,3-benzotriazole; Me_2btaH = 5,6-dimethyl-1,2,3-benzotriazole) have been described in literature. Moreover, two mixed-valent pentanuclear copper compounds $\{[Cu_5(bta)_6(t\text{-}C_4H_9NC)_4]$ (t-C_4H_9NC = *tert*-butylisocyanide) and $[Cu_5Cl(bta)_5(PPh_3)_4]\}$,[16] and two homometallic nonanuclear compounds $\{[Ni_9(Me_2bta)_{12}(bzac)_6(MeOH)_6]$ (bzacH = benzoylacetone) and $[Zn_9(bta)_{12}(acac)_6]\}$[10f,12c] have been reported. The following are the structure descriptions, syntheses, and magnetic properties of the above mentioned penta- and nonanuclear coordination compounds.

Structure descriptions. The pentanuclear copper compounds $[Cu_5(bta)_6(L)_4]$[9,13] (L = β-diketonate) are composed of a tetrahedral arrangement of four pentacoordinate copper(II) ions centered on a fifth hexacoordinate copper(II) ion. Each of the six μ_3-benzotriazolate ligands spans an edge of the tetrahedron and is coordinated to the central octahedral copper(II) ion through their nitrogen donor atom in the 2-position. Six nitrogen atoms from six benzotriazolate ligands therefore complete the coordination sphere of the central copper(II) ion, while each copper(II) ion in the apical positions is coordinated by three nitrogen atoms from three benzotriazolate ligands and one β-diketonate ligand. The molecular structure of the pentanuclear copper compound $[Cu_5(bta)_6(acac)_4]$ along with its imaginary $\{Cu_4\}$ tetrahedron is displayed in Figure 1.7 as an example.

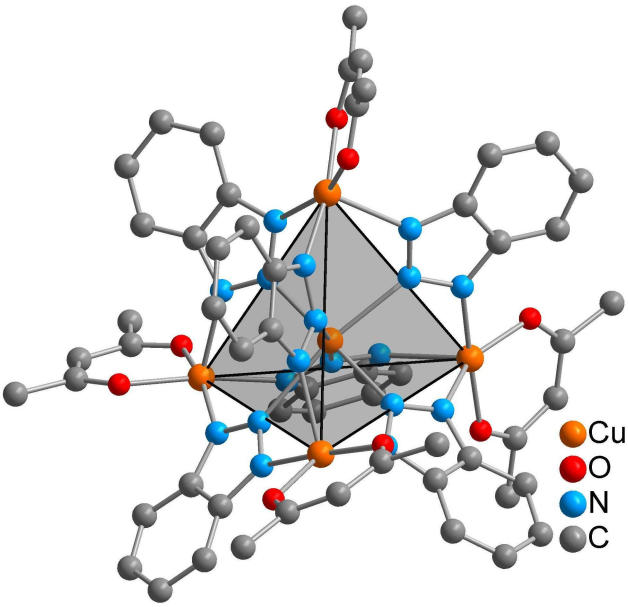

Figure 1.7 Ball-and-stick representation of the molecular structure of $[Cu_5(bta)_6(acac)_4]$ showing the presence of an imaginary $\{Cu_4\}$ tetrahedron.

Table 1.1 List of pentanuclear compounds containing bta ligands described in this section.

Compound	Molecular formula[a]	No. of bta ligands	Coordination no. of peripheral metal ions	Ref.
1a	$[Cu_5(bta)_6(acac)_4]$	6	5	13a-b
1b	$[Cu_5(bta)_6(tfpbd)_4]$	6	5	13a
1c	$[Cu_5(bta)_6(trop)_4]$	6	5	13a
1d	$[Cu_5(bta)_6(Ph/Me\text{-}pd)_4]$	6	5	13a
1e	$[Cu_5(bta)_6(Ph/Ph\text{-}pd)_4]$	6	5	13a
1f	$[Cu_5(bta)_6(C_4H_3S/CF_3\text{-}pd)_4]$	6	5	13a
1g	$[Cu_5(bta)_6(tta)_4]$	6	5	13c
2	$[Cu_5(bta)_6(t\text{-}C_4H_9NC)_4]$	6	4	16a-b
3	$[Cu_5Cl(bta)_5(PPh_3)_4]$	5	4	16c
4a	$[Ni_5(OH)(bta)_5(acac)_4(H_2O)_4]$	5	6	12a-b
4b	$[Ni_5(OH)(Me_2bta)_5(acac)_4(H_2O)_4]$	5	6	12a-b
5	$[Zn_5(bta)_6(NO_3)_4(H_2O)]$	6	6 for one Zn ion, 5 for three other Zn ions	10a
6	$[Co_5(bta)_6(NO_3)_4(H_2O)_4]$	6	6	11a

7	$[Ni_5(bta)_6(NO_3)_4(H_2O)_4]$	6	6	11a
8	$[Zn_5(bta)_6(acac)_4(DMF)]$	6	6 for one Zn ion, 5 for three other Zn ions	10f
9	$[Ni_5(Mebta)_6(dbm)_4(Me_2CO)_4]$	6	6	12c

[a] Abbreviations: acacH = acetylacetone; tfpbdH = 4,4,4-trifluoro-1-phenyl-1,3-butanedione; tropH = tropolone; Ph/Me-pdH = 1-phenyl-1,3-butanedione; Ph/Ph-pdH = 1,3-diphenyl-1,3-propanedione; C_4H_3S/CF_3-pdH = 4,4,4-trifluoro-1-(2-thienyl-1,3-butanedione), ttaH = thenyltrifluoroacetone; DMF = *N,N'*-dimethylformamide; dbmH = dibenzoylmethane; Me_2CO = acetone.

All of the homometallic pentanuclear compounds (Table 1.1 and Figures 1.7-1.8) presented in this section bear structural resemblance with the copper compounds $[Cu_5(bta)_6(L)_4]$. Slight differences occur in the coordination geometries of the peripheral metal centers, and in the number of bta, Mebta, or Me_2bta ligands present in the compounds. In **3**, the bridging μ_3-Cl anion spans the sixth edge of the $\{Cu_4\}$ tetrahedron, while the spanning of the sixth edge of the $\{Ni_4\}$ tetrahedron in **4a-b** is performed by the bridging μ_3-OH anion. In the mixed-valent compounds **2-3**, the central copper ion is in +II oxidation state, whereas each peripheral copper ion is in +I oxidation state. Since the bta ligand has a charge of -1, the overall mixed-valent compounds are electrostatically neutral. Significant amounts of tetragonal distortion with two different Cu-N bond distances (Cu^{II}-N_{axial} and Cu^{II}-$N_{equatorial}$) have been observed in all the pentanuclear copper compounds.[13,16]

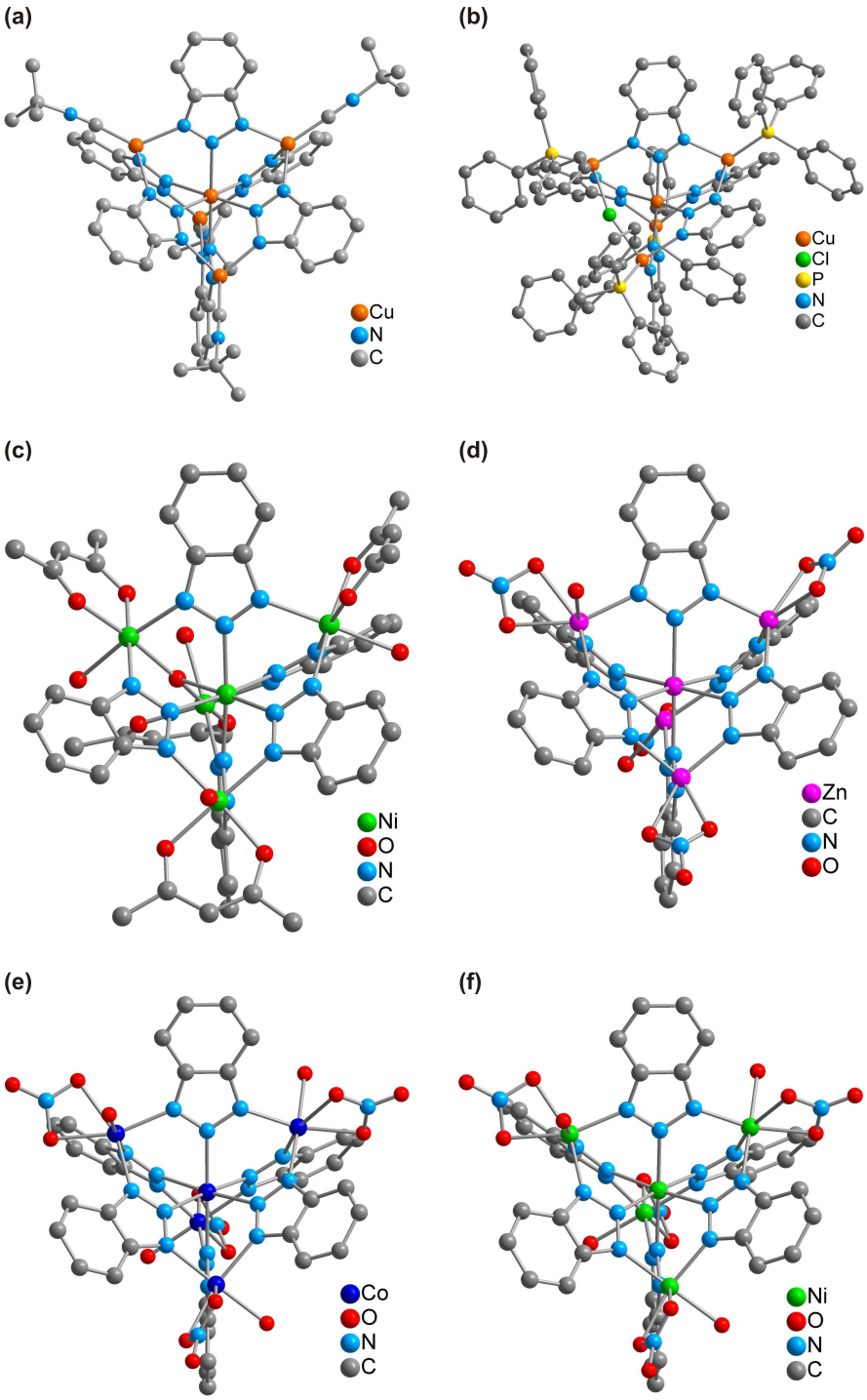

Figure 1.8 Ball-and-stick representation of the molecular structure of compounds **2** (a), **3** (b), **4a** (c), **5** (d), **6** (e), and **7** (f).

The structure of the nonanuclear zinc and nickel compounds $\{[Zn_9(bta)_{12}(acac)_6]$ and $[Ni_9(Me_2bta)_{12}(bzac)_6(MeOH)_6]\}$[10f,12c] (see Figure 1.9) can be formally deduced from two $\{M_4\}$ (M = Zn or Ni) tetrahedra, like that of the pentanuclear compounds described above. Both the two tetrahedra share a common apex. Slight structural differences between the two nonanuclear compounds are observed in the coordination geometries of the peripheral metal

atoms. In the nonanuclear zinc compound, each peripheral Zn atom is pentacoordinated with one bidentate acetylacetonate anion bound as terminal ligand. In contrast, each peripheral Ni atom in the nonanuclear nickel compound is hexacoordinated having one terminal methanol molecule, in addition to one β-diketonate ligand.

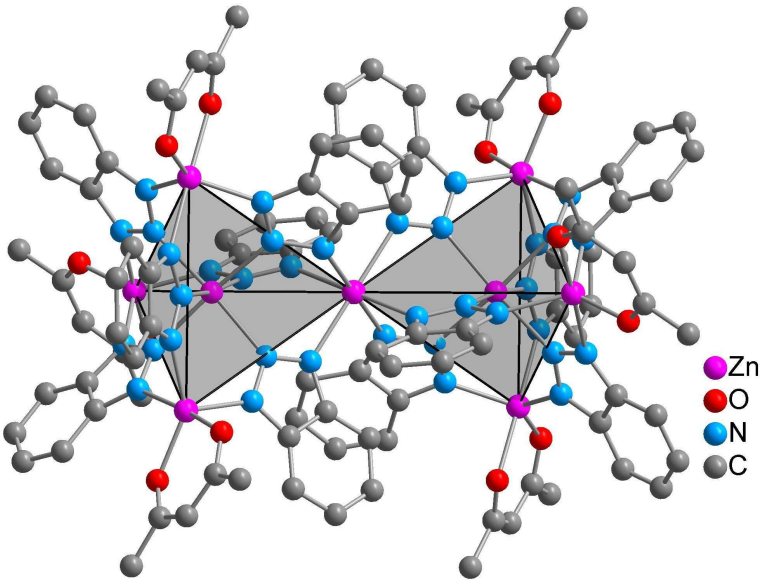

Figure 1.9 Ball-and-stick representation of the molecular structure of $[Zn_9(Me_2bta)_{12}(acac)_6]$[10f] displaying the presence of two $\{Zn_4\}$ tetrahedra sharing a common apex. All hydrogen atoms are omitted for clarity.

Syntheses. All the pentanuclear compounds (**1a-g**, **4a-b**, **8**, and **9**) containing β-diketonate ligands have been prepared in solution employing metal(II) β-diketonates as precursors, thus taking advantage of the proton transfer between metal(II) β-diketonates and benzotriazole ligands, which subsequently leads to partial replacement of β-diketonates by deprotonated benzotriazole ligands. The mixed-valent copper compound $[Cu_5(bta)_6(t\text{-}C_4H_9NC)_4$ (**2**) has been synthesized from the reaction of copper(I) thiophenoxide (CuSPh), btaH, and *tert*-butylisocyanide in dichloromethane solution at room temperature. The thiophenoxide anion present in the reaction mixture acts as an auxiliary base to abstract the acidic –NH protons from the coordinated benzotriazole ligands, and molecular oxygen from air oxidizes some of the Cu(I) ions to Cu(II), which acts as a template for the assembly of the rather complex product. The other mixed-valent copper compound $[Cu_5Cl(bta)_5(PPh_3)_4]$ (**3**) has been prepared from the electrolysis of an aceonitrile solution containing btaH and PPh_3, using Pt as cathode, copper as sacrificial anode, and tetraethylammonium perchlorate (Et_4NClO_4) as supporting electrolyte. During the electrolysis, Cu^I and bta^- ions are generated at the anode and cathode,

respectively, while some of the Cu^{I} ions are oxidised after the electrolysis to Cu^{II}. The pentanuclear zinc compound $[Zn_5(bta)_6(NO_3)_4(H_2O)]$ (**5**) has been obtained from solvothermal reaction of $Zn(NO_3)_2{\cdot}6\ H_2O$ and btaH in methanol/DMA (1:1) (DMA = *N*,*N*′-dimethylacetamide) solvent mixture. The gradual thermal decomposition of the amide solvent (DMA) produces *in-situ* the base (dimethylamine) which is essential for the abstraction of the acidic –NH protons from the coordinated benzotriazole ligands. Compound $[Co_5(bta)_6(NO_3)_4(H_2O)_4]$ (**6**) or $[Ni_5(bta)_6(NO_3)_4(H_2O)_4]$ (**7**) has been prepared from the reaction of $Co(NO_3)_2{\cdot}6\ H_2O$ or $Ni(NO_3)_2{\cdot}6\ H_2O$ and benzotriazole-1-methanol (bta-CH_2OH) in acetone solution. The -CH_2OH group at the 2-position of bta is lost during the reaction liberating bta^- ion in the reaction medium.

The nonanuclear compounds, $[Zn_9(bta)_{12}(acac)_6]$[10f] and $[Ni_9(Me_2bta)_{12}(bzac)_6(MeOH)_6]$[12c] have been prepared by using $[Zn(acac)_2]$ and $[Ni(bzac)_2(EtOH)_2]$ (EtOH = ethanol), respectively as precursors, which play the same synthetic role as the other metal(II) β-diketonates employed for the preparation of the pentanuclear coordination compounds (containing β-diketonate ligands) described above.

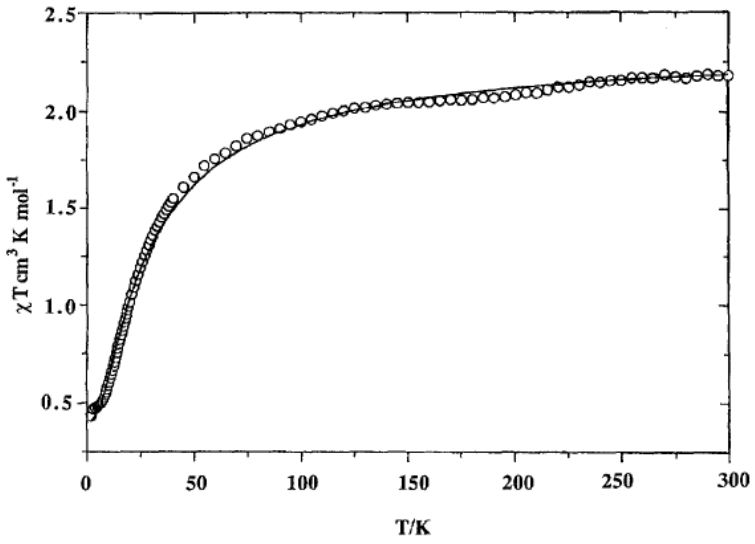

Figure 1.10 Plot of $\chi_m T$ versus T in the temperature range 2-300 K for $[Cu_5(bta)_6(trop)_4]$[13a] (**1c**). Open circles: experimental data, graph: a least-squares fit to the employed model.

Magnetic properties. Magnetic susceptibility studies performed on the pentanuclear copper,[13a] nickel,[12] and the nonanuclear nickel[12c] compounds have shown that weak antiferromagnetic exchange interaction between the metal centers leads to spin ground states equal to that of the *"isolated"* central metal(II) ion. A $\chi_m T$ versus T plot for the copper compound $[Cu_5(bta)_6(trop)_4]$ (**1c**) is shown in Figure 1.10 for an example.

1.3 Metal Organic Frameworks

1.3.1 History and Scope

Metal-organic frameworks (MOFs), also known as metal-organic networks, or coordination polymers, represent a new class of crystalline compounds containing metal ions or discrete meta-organic coordination units linked by rigid organic ligands. The structures resulting from metal-ligand linkages can be discrete zero-dimensional (0D) molecular compounds or infinite one-dimensional (1D), two-dimensional (2D) or three-dimensional (3D) architectures. Whereas the term "coordination polymers" is more commonly referred to the latter, "metal-organic networks" and "metal-organic frameworks" are applicable in a broader context and are interchangeable in most cases. The structure of the prototypic "**MOF-5**"[17] (MOF being the acronym for *M*etal *O*rganic *F*ramework), synthesized by Yaghi *et al*. in the year 1999 is shown in Figure 1.11.

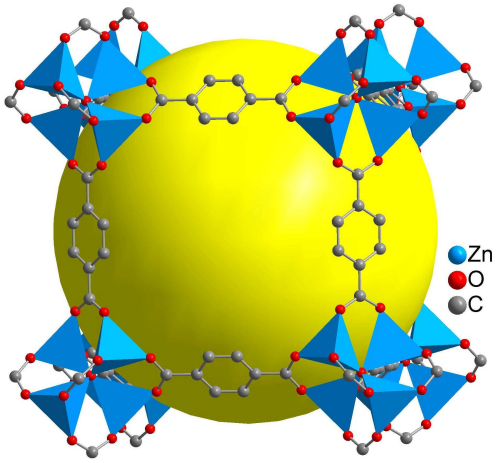

Figure 1.11 Ball-and-stick representation of the **MOF-5** framework with zinc atoms represented as blue tetrahedra. All hydrogen atoms are removed for clarity. The yellow sphere represents a large cavity inside the framework.

One of the very first examples of MOFs that have been structurally characterized appeared in 1943,[18] although similar studies can be traced back to as early as the 1930's. The area of coordination polymers was initially reviewed in 1964 with an emphasis on the preparations.[19] In the early investigations, Prussian blue based on Fe-CN-Fe linkages and its analogues were perhaps among the most systematically studied. Surprisingly, however, the field of metal-

organic frameworks wasn't prospering until the late 1980's when Robson initiated the now famous "node-and-spacer" approach[20] to incorporate both transition metal ions of well-defined coordination geometries and rod-like organic ligands in the design of network materials. Subsequently, the work by Zaworotko,[21] Yaghi,[17,22] and others[23] substantially contributed to the field and it is now so rapidly developing that the number of coordination polymeric compounds has witnessed an exponential growth in the past few years (Figure 1.12).

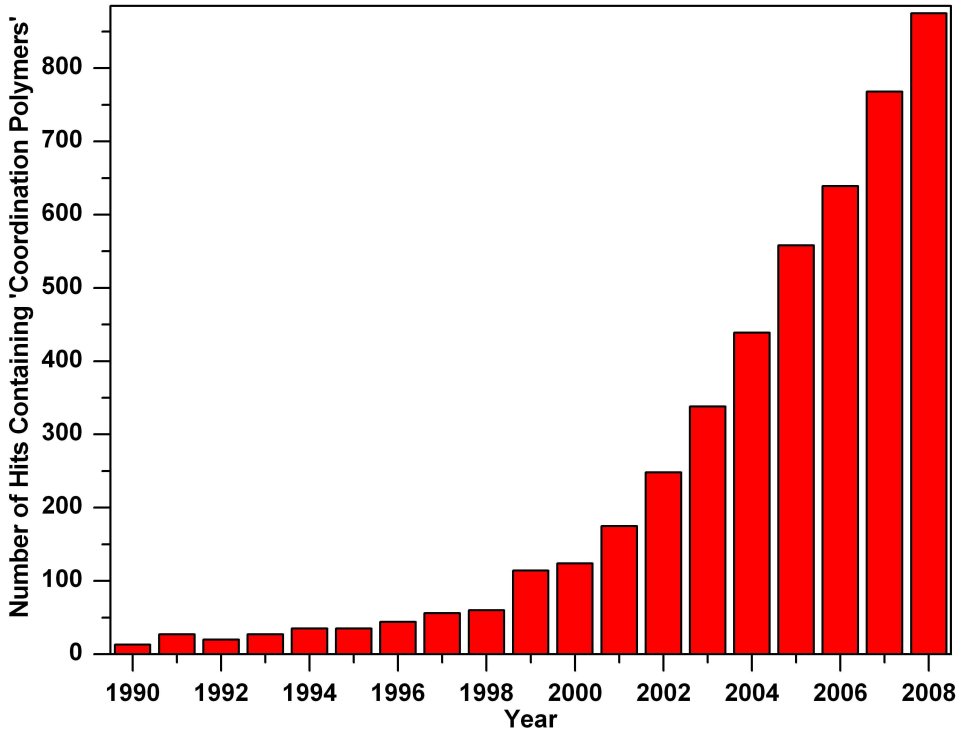

Figure 1.12 Number of citations containing the key word "coordination polymers" in the past 19 years (source: SciFinder Scholar until September 2009).

1.3.2 Design Principles

There exist three different strategies that have been widely used to direct the syntheses of MOFs. The strategies are: (a) node-and-spacer, (b) vertex-linked polygons or polyhedra (VLPP), and (c) secondary building unit (SBU). A brief description of each of these strategies is presented in this section.

(a) Node-and-spacer strategy. In Robson's original node-and-spacer approach, the nets were usually constructed from organic-based linear spacers as well as metal-based nodes that could

be square, tetrahedral, octahedral, etc. This strategy, however, can be conveniently extended to a much broader context where both metal centers and organic ligands can appropriately function as either nodes or spacers.[24] Figure 1.13 illustrates some representative examples of organic ligands with linear, angular, trigonal, and tetrahedral shapes.

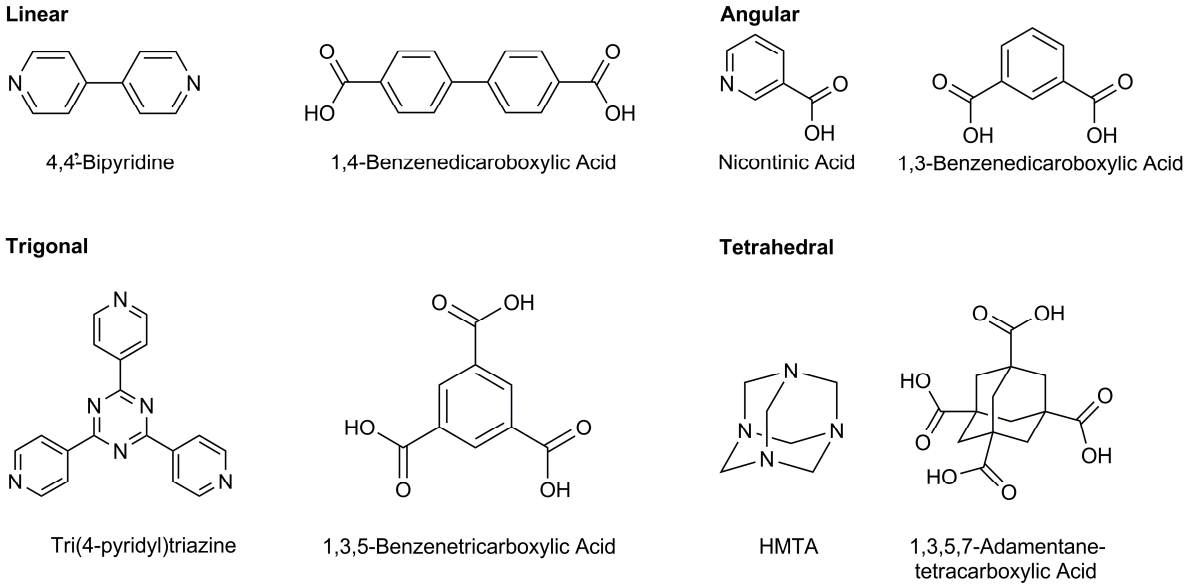

Figure 1.13 Representative examples of organic ligands used for the construction of metal-organic frameworks (HMTA = hexamethylenetetramine).

In the node-and-spacer approach, the building blocks are simplified as topological points and lines, and the nets are represented in their appropriate combinations. Wells was regarded as the pioneer of this approach, thanks to his systematic studies on the geometrical basis of crystal chemistry.[25] Although Wells' initial work was primarily focused upon inorganic crystalline compounds, Robson extrapolated this method into the realm of metal-organic compounds and coordination polymers.[20] As revealed by Figure 1.14, the node-and-spacer approach has afforded a diverse array of metal-organic architectures ranging from 0D discrete nanostructures to 3D infinite networks, some of which have no inorganic analogues.

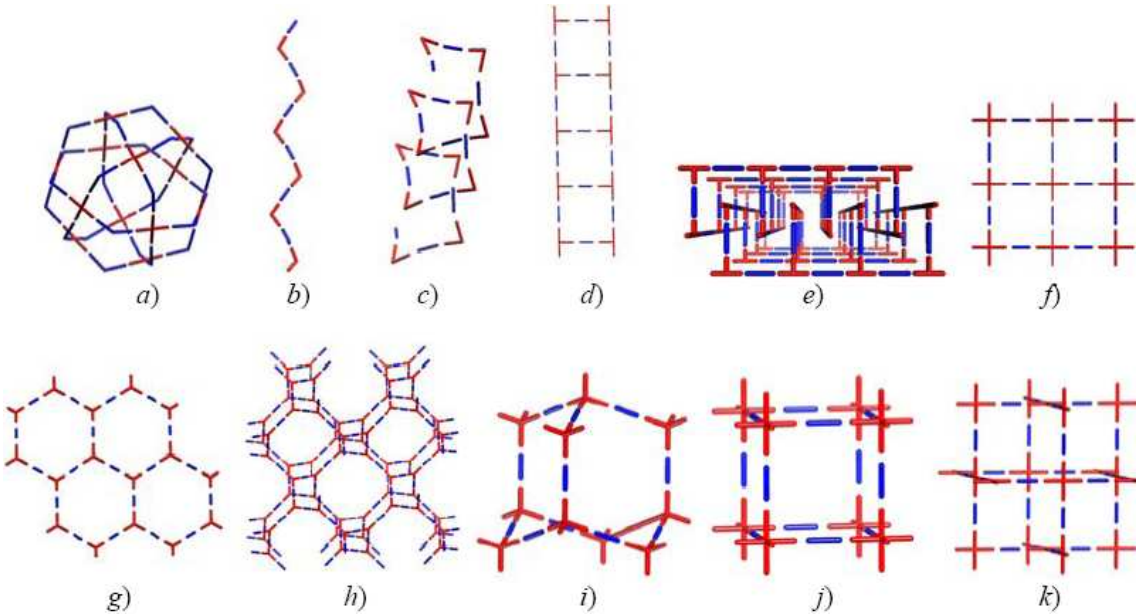

Figure 1.14 "Node-and-spacer" representations of metal-organic frameworks: *a*) 0D nanoball; *b*) 1D zigzag chain; *c*) 1D helix; *d*) 1D ladder; *e*) 2D bilayers; *f*) 2D square grid; *g*) 2D honeycomb; *h*) 3D (10,3)-a net; *i*) 3D diamondoid net; *j*) 3D primitive cubic net; *k*) 3D NbO net. The diagrams have been adopted from ref. 26.

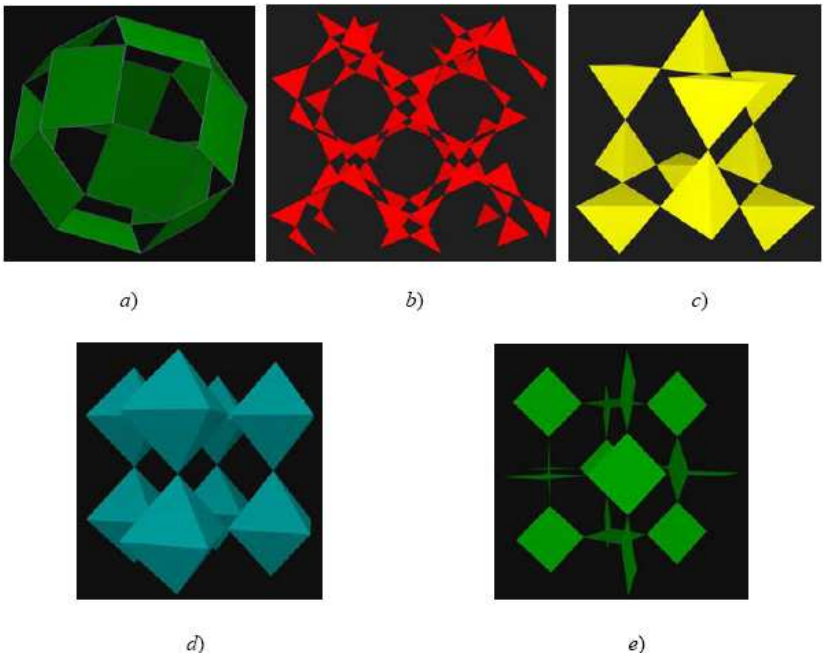

Figure 1.15 "Vertex-linked Polygons or Polyhedra" (VLPP) representations of metal-organic frameworks: *a*) 0D nanoball; *b*) 3D (10,3)-a net; *c*) 3D diamondoid net; *d*) 3D primitive cubic net; *e*) 3D NbO net. The diagrams have been adopted from ref. 26.

(b) VLPP strategy. Another approach that was introduced by Zawrotko based on geometrical principles, takes into account the specific shapes of the building blocks and represents nets as

being sustained by vertex-linked polygons or polyhedra (VLPP)[27] (Figure 1.15). Notably nets shown in Figure 1.14 can be equally well represented in the VLPP fashion (Figure 1.16). Whereas the node-and-spacer approach appears more straightforward in cases involving linear spacers, VLPP perspective reveals the more fundamental geometrical relationship between various building units.

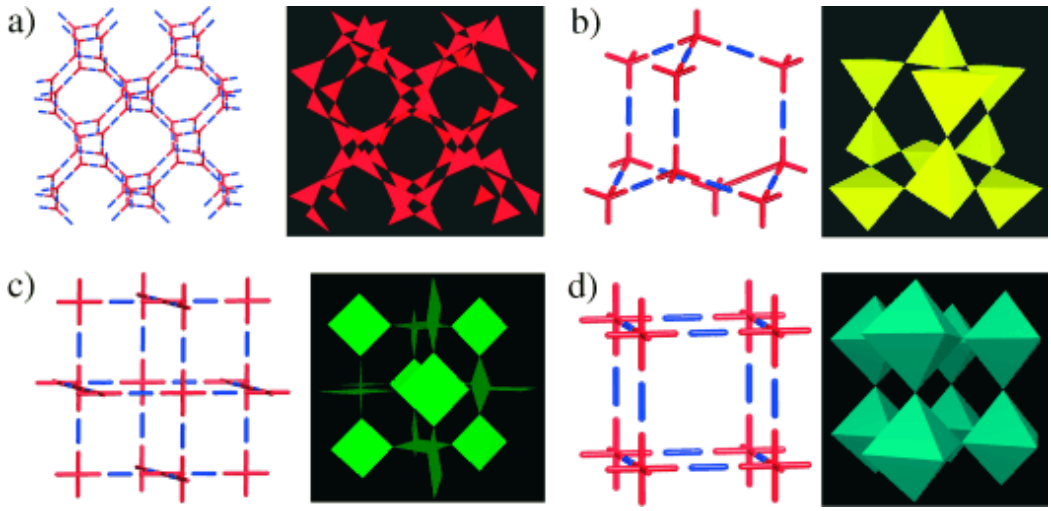

Figure 1.16 Four unitary nets represented in both node-and-spacer and VLPP format: a) (10,3)-a net, b) diamondoid net, c) NbO net, d) primitive cubic net. The diagrams have been adopted from ref. 26.

(c) SBU strategy. Yaghi and co-workers have employed the so-called "secondary building unit (SBU)" strategy for the construction of rigid and porous frameworks.[22c,28] The term 'secondary building unit' was originally used in zeolite chemistry where SBUs are referred to common structural motifs occurring in various tetrahedral frameworks.[29] Yaghi and Eddaoudi extended this idea to metal-organic chemistry and re-defined SBUs as discrete, low-molecular metal-organic coordination units that have well-defined and highly symmetric coordination geometries. The reasons behind the introduction of this widely successful strategy are discussed in the following paragraph.

The self-assembly of 4,4'-bipyridine, a linear spacer, and single metal ions has afforded, depending upon the coordination geometry of metal ions, a wide variety of superstructures.[30] Although this "M-N" (M being referred to single metal ion and N to pyridyl nitrogen) based approach proves to be extremely successful, it is nevertheless inherently associated with a number of issues that could potentially be of weakness, especially in the context of porous materials.

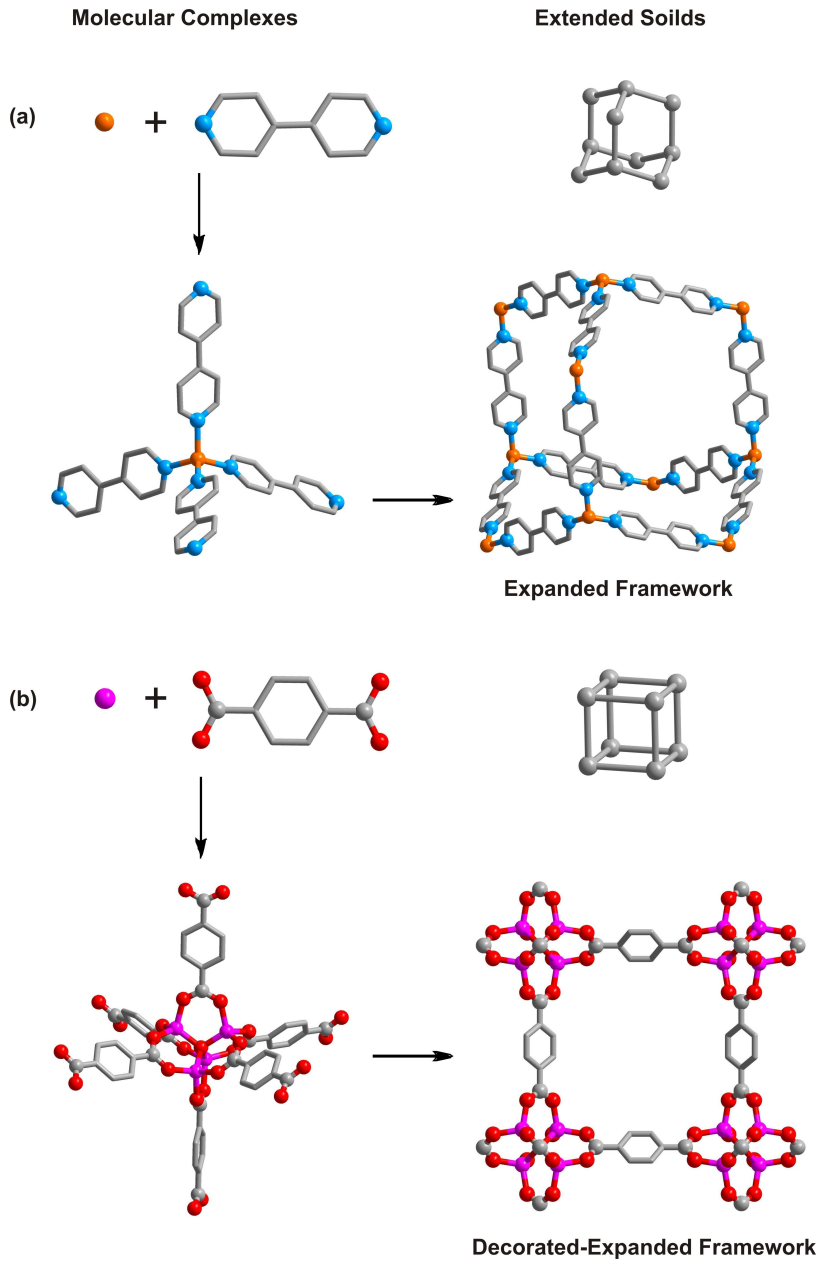

Figure 1.17 Assembly of metal-organic frameworks (MOFs) by the copolymerization of metal ions with organic linkers to give (a) flexible metal-bipyridine structures with expanded diamond topology, and (b) rigid metal-carboxylate coordination units that can be linked by benzene "struts" to form rigid extended frameworks in which the M-O-C core (SBU) of each coordination unit acts as a large octahedron decorating a 6-connected vertex in a cube. All hydrogen atoms have been omitted for clarity. In (a): M, orange; C, grey; N, blue; in (b): M, pink; O, red; C, grey.

For instance, the relative lack of directionality of a single metal ion often results in flexibility of the pyridyl rings surrounding the metal centres, thus limiting the degree of control over the final structures; the presence of anionic species due to the cationic nature of the frameworks

significantly reduces available free space of the structure; attempts to evacuate or exchange guests within the pores almost invariably, with few exceptions,[30d-e] result in collapse of the host framework. To overcome these difficulties, Yaghi *et al*. have focussed on using the carboxylate functionality to chelate metal ions and lock them in rigid and thus directional metal-oxygen-carbon coordination units, with the points of extension (carboxylate carbon atoms) defining geometrical shapes referred to as SBUs[22c,28]. The successful design of rigid porous frameworks based on such SBUs was demonstrated for the first time in **MOF-2**[31] and, later in **MOF-5**[17] (Figure 1.11). Figure 1.17 illustrates the advantages of the "SBU" strategy over the "M-N" based strategy for the design of rigid extended frameworks.

1.3.3 Synthesis[22b,f]

Several factors must be borne in mind when approaching the synthesis of a new metal-organic framework, aside from the geometric principles that are considered during its design. The most important is the maintenance of the structural integrity of the building blocks. The synthetic conditions must be mild enough to maintain the functionality and conformation of the rigid organic linker, yet reactive enough to establish the coordinative bonds. Where a desired SBU is to be generated *in-situ*, the required synthetic conditions must be compatible with the mobilization and preservation of the linking units. In the synthetic procedure, an insoluble product that is obtained by the precipitation from a solution of the precursors, does not require recrystallization. The framework assembly occurs as a single synthetic step, and thus all of the desired attributes of the target material must be carried by the building blocks.

The synthesis of MOFs generally involves the reaction of organic linkers and metal ions in a polar solvent under mild temperatures (up to 200 ºC) and autogenous pressures (up to 100 atm). Since most products can be considered kinetically driven and lie on local thermodynamic minima, factors such as solubility of the organic linker and metal salt, solvent polarity, ionic strength of the medium, pH, temperature, or pressure play critical roles in determining the character of the products. It has been found that subtle changes in any of these parameters lead to poorer quality crystals, reduced yields or the formation of entirely new phases. Fortunately, once these conditions are elucidated, most high yielding syntheses share the attributes of low energy expenditure (temperatures typically range between room temperature and 200 ºC), reasonable time scale (hours to days), possibility of solvent recycling, and facile quality control monitoring by XRPD or microscopy.

Early efforts to produce highly crystalline MOFs involved a variety of techniques previously used to grow crystals of simple inorganic salts. These generally involved the slow introduction of the building blocks to reduce the rate of crystallite nucleation. Methods included slow evaporation of a solution of the precursors, layering of solutions, or slow diffusion of one component solution into another through a membrane or an immobilizing gel. Where a ligand needed to be deprotonated prior to coordination (such as a carboxylic acid), a volatile amine was gradually added via vapour diffusion. Just as for many of the polar solvents used, adroit choice of base was necessary to avoid competitive coordination with the organic links for the available metal sites. While in some cases, blocking of metal coordination sites is necessary for the formation of a particular SBU, this occurrence has generally been regarded as leading to low-dimensional structures that are less likely to define an open framework.[22b,f]

As the need for more robust frameworks was recognized, greater difficulties in crystal growth were encountered. The inverse relationship between metal-organic bond strength and reversible formation is directly responsible for this obstacle. Fortunately, solvothermal techniques were found to be a convenient solution to this dilemma and have largely supplanted the older, often time-consuming methods involving slow coupling of the coordinating species. The precursors are typically combined as dilute solutions in polar solvents such as water, alcohols, acetone or acetonitrile and heated in sealed vessels such as Teflon-lined stainless steel bombs or glass tubes, generating autogenous pressure. Mixed solvent systems are often used to tune the solution polarity and the kinetics of solvent-ligand exchange, effecting enhanced crystal growth. Exposing the growing framework to a variety of space-filling solvent molecules may also be an effective way to stabilize its defect-free construction as they efficiently pack within the defined channels. In cases where deprotonation of the linking molecule is necessary, gradual neutralization of a solution can be effected by thermal decomposition of an amide co-solvent. Fluids such as alkyl formamides and pyrrolidinones have been particularly useful to this end, as they are also excellent solubilizing agents. An alternative method is to generate slowly the desired link *in-situ*, for example, by hydrolyzing nitriles or esters to yield carboxylates. Finally, it should be mentioned that if high yield is desired over crystal quality, reaction times can be greatly reduced by increased concentration and agitation of the solution. Quite often microcrystalline, rather than amorphous, materials are formed under these conditions, as evidenced by electron microscopy and XRPD.[22b,f]

More recently, microwave-assisted synthesis of MOFs has attracted much attention. This technique often leads to a rapid and efficient synthesis of porous materials within a few minutes,[32] instead of days of typical solvothermal routes, and, moreover, it offers phase selectivity[33] and facile control over crystal morphology[34]. This method has been successfully applied for the rapid synthesis of several well-known porous MOFs such as **MOF-5**, **MIL-77** (MIL is the acronym for *M*atérial *I*nstitut *L*avoisier), **MIL-100**, or **MIL-101**.[35]

1.3.4 Role as Functional Materials

Early research in MOFs tended to concentrate on synthesis of a wide variety of new compounds with novel topologies and compositions. Although the design of new structures remains highly topical and a significant amount of research efforts are still devoted to the discovery of unprecedented network topologies,[36] the primary motivation in crystal engineering of MOFs has shifted toward constructing materials that possess interesting physical properties, such as optical,[37] magnetic,[11b,23c-e,38] and electronic properties,[39] as well as their various potential applications such as catalysis,[40,69] ion-exchange,[41] gas storage,[42] separation,[43] sensing,[44] polymerization,[45] and drug delivery.[46] Further details for each of these important properties and applications of MOFs appear in a recent themed issue on "metal-organic frameworks" published by *Chemical Society Reviews*.[47] For the purpose of brevity, in this section we will focus only on MOF based catalysis and gas adsorption (especially, selective adsorption), which are two active areas of MOF research pursued world wide including our laboratory.

Catalytic properties. In 1994, Fujita *et al*. reported a Cd(II)-(4,4'-bipyridine) square grid coordination polymer $[Cd(bpy)_2(NO_3)_2]$ (bpy = 4,4'-bipyridine) (Figure 1.18) that catalyzes cyanosilylation of aldehydes with a moderate shape specificity.[48] The heterogeneous metal-organic catalyst has recently been shown to also promote cyanosilylation of imines under similar conditions.[49] Mechanistic studies suggest that although the active sites are mainly around the surface of the catalyst, binding of substrates by hydrophobic grid cavities also accounts for the acceleration of the reactions.[49] In addition to this pioneering study, examples in which a wide variety of other reactions are catalyzed by MOFs have also been reported recently. The majority of the known catalytic MOFs, together with the descriptions of the specific catalyses are catalogued in Table 1.2.

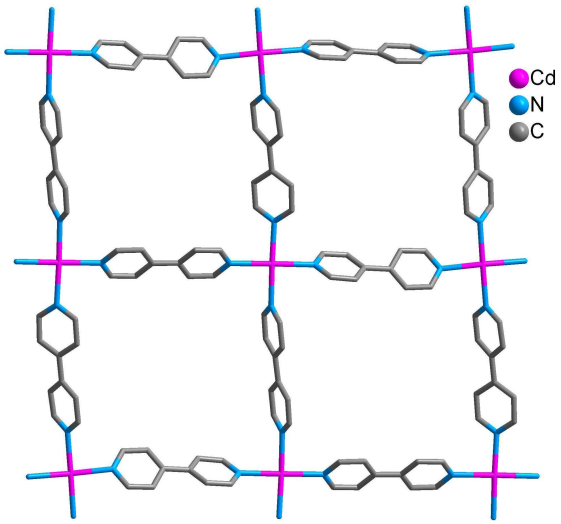

Figure 1.18 Wire representation of one the layers of the 2D layered squared grid coordination polymer [Cd(4,4'-bpy)$_2$(NO$_3$)$_2$] synthesized by Fujita *et al*. All hydrogen atoms and coordinated nitrate anions have been omitted for clarity.

Table 1.2 Selection of catalytically active MOFs and summary of the corresponding catalytic reactions.

MOF material[a]	Substrate(s)	Reaction(s) catalyzed	Ref.
[Cd(btapa)(NO$_3$)$_2$]	benzaldehyde and malonitrile	Knoevenagel condensation	50
[Cd(bpy)$_2$(NO$_3$)$_2$]	benzaldehyde and cyanotrimethylsilane	cyanosilylation of aldehyde	48
[Cd$_3$Cl$_6$(**L1**)$_3$]	aryl aldehyde and diethyl zinc	alkylation of aldehyde	51
[Co(bpb)]	cyclohexene	oxidation of olefin	52
[Co$_4$O(bdpb)$_3$]	cyclohexene	oxidation of olefin	53
[Cr$_3$F(H$_2$O)$_2$O(bdc)$_3$]	benzaldehyde and ethyl cyanoacetate; iodobenzene and acrylic acid	Knoevenagel condensation; Heck coupling	54
[PW$_{11}$TiO$_{40}$]$^{5-}$@ [Cr$_3$F(H$_2$O)$_2$O(bdc)$_3$], and [PW$_{11}$CoO$_{39}$]$^{5-}$@ [Cr$_3$F(H$_2$O)$_2$O(bdc)$_3$]	α-pinene, caryophyllene and cyclohexene	oxidation of olefin	55
[Cu(2-pymo)$_2$] and [Co(Phim)$_2$]	tetralin	aerobic oxidation of olefin	56

Table 1.2 (continued)

MOF material[a]	Substrate(s)	Reaction(s) catalyzed	Ref.
$[Cu(bpy)(H_2O)_2(BF_4)_2(bpy)]$	various epoxides	ring-opening of epoxides	57
$[Cu(D\text{-}asp)(bpe)_{0.5}$ and $[Cu(L\text{-}asp)(bpe)_{0.5}$	*cis*-2,3-epoxybutane and methanol	methanolysis of epoxide	58
$[Cu(\mathbf{L2})_2(H_2O)_2]$, $[Cu(\mathbf{L3})_2(H_2O)(py)_2]$, $[Cu(\mathbf{L3})_3(H_2O)Cl]$ and $[Co(sal)(H_2O)(py)_3]$	linear and cyclic olefins	epoxidation of olefins	59
$[Cu(SO_4)(pbbm)]$ and $[(Cu(Ac)_2(pbbm)]$	2,6-dimethylphenol	oxidative self-coupling	60
$[Cu_3(btc)_2]$	α-pinene oxide; citronellal; ethylene acetal of 2-bromo-propiophenone	isomerisation, cyclization; rearrangement	61
	olive oil and mill waste waters	oxidation of polyphenol	62
	benzaldehyde (or acetone) and cyanotrimethylsilane	cyanosilylation of aldehyde	63
[In(OH)(hfippb)]	benzaldehyde and α-methylbenzene acetaldehyde	acetalization of aldehyde	64
$[In_2(OH)_3(bdc)_{1.5}]$	nitrobenzene and 2-methyl-1-nitronaphthalene; methylphenyl sulfide, (2-ethylbutyl)phenyl sulfide	reduction of nitroaromatic; oxidation of sulfide	65
[Mn(porphyrin)]@ $[In_{48}(imdc)_{96}]$	cyclohexane	oxidation of alkane	66
$[Ln(OH)(nds)(H_2O)]$; Ln = Nd, Pr, La	linalool	epoxidation of olefin	67
$[\{Mn(tcpp)\}Mn_{1.5}(DMF)]$	cyclic alkenes; cyclic or linear alkanes	epoxidation of olefin, oxidation of alkane	68

Table 1.2 (continued)

MOF material[a]	Substrate(s)	Reaction(s) catalyzed	Ref.
$Mn_3[(Mn_4Cl)_3(btt)_8(CH_3OH)_{10})]_2$	aldehydes and cyano-trimethylsilane; benz-aldehyde and methyl-trimethylsilyldimethyl-ketene acetal	cyanosilylation of aldehyde; Mukaiyama-aldol	69
$Na_{20}[Ni_8(\mathbf{L4})_{12}(H_2O)_{28}]$	CO	oxidation to CO_2	70
$[Pd(H\text{-}pymo)_2]$	cinnamyl alcohol; aryl halides and arylboronic acids; 1-octene, cyclododecene	oxidation of alcohol; Suzuki-Miyaura coupling; hydrogenation of olefin	71
$Tb[V_6O_{13}\{(OCH_2)_3C(NH_2CH_2C_6H_4\text{-}4\text{-}CO_2)\}\{(OCH_2)_3C\text{-}(NHCH_2C_6H_4\text{-}4\text{-}CO_2)\}_2]^{4-}$	propanethiol	oxidation of sulfide	72
$[Zn_2(bpdc)_2(\mathbf{L5})]$	2,2-dimethyl-2*H*-chromene	epoxidation of olefins	73
$[Zn_2\{py_2(PhF_5)_2PorZn\}(tcpb)]$	acetyl imidazole and pyridyl carbinols	intermolecular transfer of acyl	74
$[Zn_3(\mu_3\text{-}O)(O_2CR)_6(H_2O)_3]^{n+}$	esters and alcohols	transesterification	75
$[Zn_4O(bdc)_3]$ and $[Zn_4O(ndc)_3]$	*tert*-butyl chloride and toluene	Friedel-Crafts alkylation	76
$[(Zn_4O)(bdc\text{-}NH_2)_3]\text{-}Vsal_{0.4}$	cyclohexene	oxidation of olefin	77

[a] Abbreviations: btapa = 1,3,5-benzenetricarboxylic acid tris[N-(4-pyridyl)amide]; bpy = 4,4'-bipyridine; **L1** = (R)-6,6'-dichloro-2,2'-dihydroxy-1,1'-binaphthyl-4,4'-bipyridine; H_2-bpb = 1,4-bis(4'-pyrazolyl)benzene, H_2-bdpb = 1,4-bis[(3,5-dimethyl)-pyrazol-4-yl]benzene; H_2-bdc = 1,4-benzenedicarboxylic acid; H-pymo = 2-pyrimidinol; H-Phim = phenyl imidazole; D-asp = D-aspartate; ; bpe = *trans*-1,2-bis(4-pyridyl)ethylene); **L2** = (4-formylphenoxy)acetic acid; **L3** = 2-[2-[[(2-aminoethyl)imino]methyl]phenoxy]acetic acid; py = pyridyl; H_2-sal = salen or 2,2'-ethylenebis(nitrilomethylidene)diphenol; pbbm = 1,1'-(1,5-pentanediyl)bis(1*H*-benzimidazole); ac = acetyl; H_3-btc = benzene-1,3,5-tricarboxylic acid; H_2-hfippb = 4,4'-(hexafluoroisopropylidene)bis(benzoic acid); H_3-imdc = 4,5-imidazole dicarboxylic acid; H_2-nds = 1,5-naphthalenedisulfonic acid; H_6-tcpp = tetra-(*p*-carboxyphenyl)porphyrin; DMF =

N,*N*'-dimethylformamide; H_3-btt = 1,3,5-benzenetris(tetrazol-5-yl); **L4** = 4,5-imidazoledicarboxylic acid; H_2-bpdc = 4,4'-biphenyldicarboxylic acid; **L5** = (*R*,*R*)-(–)-1,2-cyclohexanediamino-*N*,*N*-bis(3-*tert*-butyl-5-(4-pyridyl)salicylidene)$Mn^{III}Cl$; $py_2(PhF_5)_2Por$ = 5,15-dipyridyl-10,20-bis(pentafluorophenyl)porphyrin; H_4-tcpb = 1,2,4,5-tetrakis(4-carboxyphenyl)benzene; H_2-ndc = 2,6-naphthalenedicarboxylic acid; bdc-NH_2 = 2-aminobenzene-1,4-dicarboxylate.

Both metal nodes[48,49,52,53,60,61,63,64,69,71,76] and organic struts, either metallated (metalloporphyrins,[68,74] Schiff-base[73] and binaphthyl[51,78] complexes) or metal-free[50,54,58,75], present in the MOF frameworks can act as the active sites for catalytically-active MOF materials. MOF-encapsulated molecular catalyst[66] and clusters/nanoparticles[55] have also proven to be catalytically active. Moreover, MOF materials have been used as supports for catalytic reactions such as epoxidation,[79a] hydrogenation,[79b] methanol[79b] and H_2O_2[79c] syntheses. Nevertheless, the most intriguing opportunity provided by MOF materials in this context is their applications in the asymmetric heterogeneous catalysis.[80] Kim and co-workers constructed a 3D porous homochiral MOF having formula $[Zn_3(\mu_3\text{-}O)(O_2CR)_6(H_2O)_3]^{n+}$ using trimeric $Zn_3(\mu_3\text{-}O)$ units and enantiopure chiral organic building blocks derived from tartaric acid (Figure 1.19). This material, named "**POST-1**" (POST being the acronym for *P*ohang *U*niversity of *S*cience and *T*echnology), revealed enantioselective catalytic activity for the transesterification of 2,4-dinitrophenyl acetate with alcohols.[75]

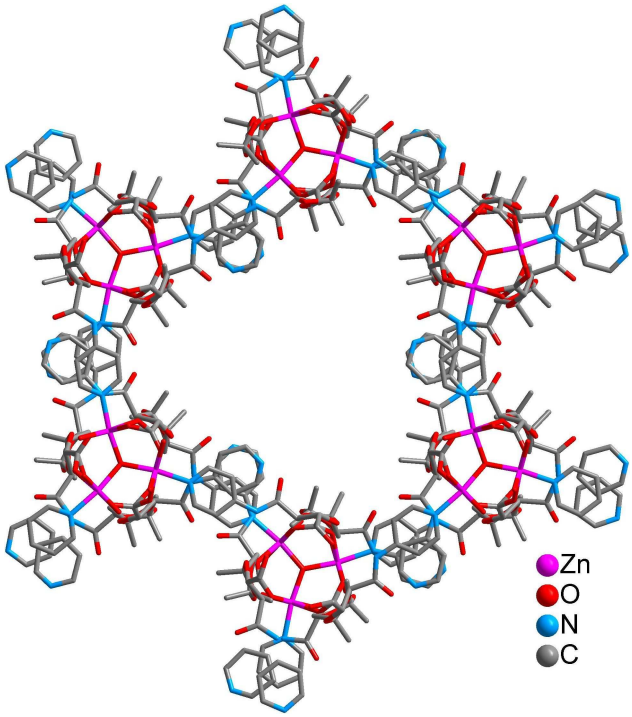

Figure 1.19 Wire representation along the *c*-direction of the hexagonal framework (with large pores formed with the trinuclear secondary building units) of the enantioselective MOF catalyst, **POST-1** synthesized by Kim *et al*.

Lin *et al.* subsequently reported a family of chiral porous solids based on lamellar lanthanide phosphonates, which have been shown to be capable of catalyzing several organic transformations including cyanosilylation of aldehydes and ring opening of *meso*-carboxylic anhydrides.[78a] Earlier attempts focussed on examining the activities of achiral catalytic sites that were incorporated into the homochiral MOFs. Enantioselectivities of such systems arise from the remote influence by chiral environments of the open channels, and to date, disappointingly low levels of enantiomeric excess were obtained with this approach.[75,78a,81] Later efforts were directed toward designing homochiral MOFs with bridging ligands that contain chiral functional groups exploitable for asymmetric catalysis based on two distinct approaches. In the precatalyst approach,[73,78b,82] bridging ligands containing asymmetric catalytic sites are linked with metal-connecting points to generate homochiral MOFs. In an alternative and complementary post-synthetic modification approach,[51,83] homochiral MOFs are constructed with chiral bridging ligands that contain secondary and orthogonal functionalities. The secondary functional groups are then converted into catalytic sites via post-synthetic modification. Although the precatalyst approach provides a versatile method for synthesizing a wide range of catalytically active homochiral MOFs, it is not compatible with some of the less stable Lewis acid and late transition metal catalysts. The post-synthetic modification approach overcomes this limitation and expands the range of heterogeneous asymmetric catalysts based on homochiral MOFs. In both approaches, high enantiomeric excesses have been achieved.[51,73,78b,82,83]

Gas adsorption properties. In addition to facilitating many chemical transformations, the nanoscale space present in MOFs also provides an ideal platform for various physical processes. Whereas traditional porous materials including inorganic solids[84] (e.g., aluminosilicates and aluminophosphates) and carbonaceous compounds[85] have been widely used in commercial applications such as gas separation and storage, MOFs have only recently emerged as a new class of porous materials.[22,23] Similar to their inorganic counterparts, microporous[86] MOF materials typically display type-I[87] adsorption isotherms (Figure 1.20) due to the micro-filling of guest molecules into the crystallographically well-defined pores in MOFs. It is worth noting that although the terms “porous” and “open framework” have been

commonly used in literature to describe MOFs, largely based upon crystallographic evidences only, porosity is actually a property that must be experimentally demonstrated rather than graphically inferred.[88]

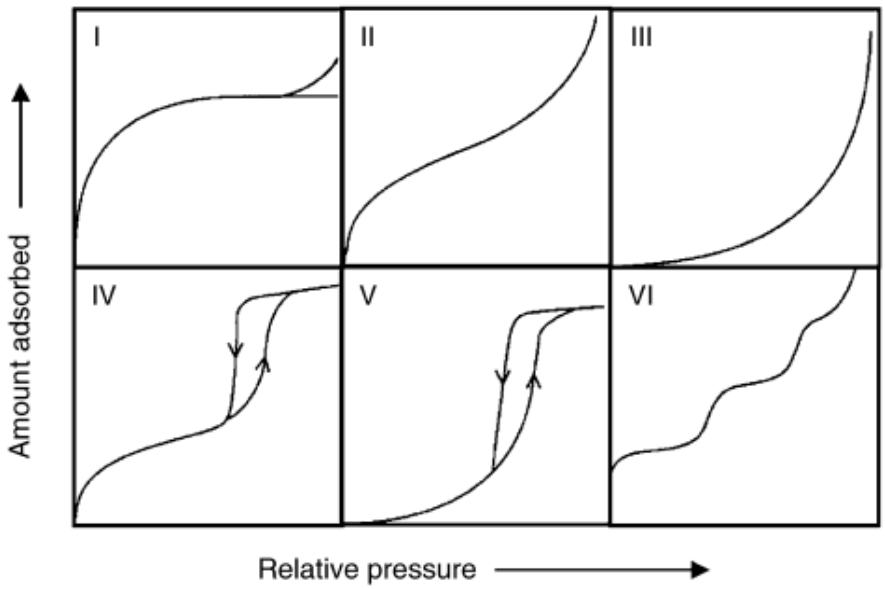

Figure 1.20 Five types of adsorption isotherm, I to V, in the classification of Brunauer, Deming, Deming, and Teller (BDDT),[87a] together with type VI, the stepped isotherm.

One of the first examples of true porous MOFs was reported by Moore and Lee in 1995, in which a (10,3)-b net based MOF exhibits large open channels and remains its structural integrity even upon guest exchange.[89] In two separate reports, Kitagawa[90] and Yaghi[31] further proved that the permanent porosity of MOFs can be experimentally established by gas adsorption isotherms. Following these early studies, a rapidly growing number of other microporous MOFs have appeared thereafter[23e] and the surface areas of this new class of porous materials have been shown to be as high as 4,500m^2/g,[91] which is almost 5 times than that of the best zeolites.[92]

Due to their crystalline, uniform and adjustable micropores, porous MOFs have recently been targeted as potential adsorbents for a wide variety of gases, including CH_4[90,93], CO_2[37f,93d,93o-t,94], acetylene[94o], and H_2[37e,42b-c,42e-f,91b,93n-o,93r-u,94l-m,94p,95,96]. These gaseous molecules are of significance either as important industrial raw materials, alternative fuels, or greenhouse gases; the development of new methods that can efficiently separate, sequester, or store these gases is therefore both scientifically and technologically relevant. Of particular interest in the past several years has been the idea of using microporous MOFs with high surface areas to store molecular hydrogen in light of an optimistic future of the "hydrogen

economy"[97]. Whereas inorganic zeolites have been widely used as "molecular sieves" in various industrial and laboratory separation processes, some of the porous MOFs also reveal similar or, in some cases, unprecedented adsorption selectivity.[98]

Arbitrarily, MOFs can be categorized into rigid and flexible/dynamic classes. Rigid MOFs have comparatively stable and robust porous frameworks with permanent porosity, similar to zeolites and other inorganic porous materials, whereas flexible MOFs possess dynamic, ''soft'' frameworks that respond to external stimuli, such as pressure, temperature, and guest molecules.[22b,99] This extraordinary sensitivity to external stimuli affords MOFs specific properties such as pressure/temperature dependent molecular sieving, which is beyond the scope of traditional adsorbents such as zeolites and activated carbons. In rigid MOFs, much like in zeolites, the adsorption selectivity may be related to the molecular sieving effect and/or preferential adsorption based on the different strengths of the adsorbent-adsorbate and adsorbate-adsorbate interactions. Besides size/shape exclusion and adsorbate-surface interaction, structural rearrangement must also be taken into account while providing probable reasons for selective adsorption of flexible MOFs. Based on the structural features of flexible MOFs and adsorption characteristics, selective gas adsorption in flexible MOFs can be classified into four categories based on: (a) size/shape exclusion accompanied by pore size/shape change, (b) adsorbate-surface interactions accompanied by pore size/shape change, (c) gate-opening or structural rearrangement induced by adsorbate-surface interactions, and (d) adsorbate-specific gate-opening pressures. Table 1.3 and 1.4 summarize the selective gas adsorption properties exhibited by known rigid and flexible MOFs, respectively.

Table 1.3 Summary of selective gas adsorption in rigid MOFs.

MOF material[a]	Pore features	Selectivity[b]	Reason[c]	Ref.
$[Er_2(pda)_3]$	1D circular channel with coordinatively unsaturated Er^{III} sites	$(CO_2)/(N_2, Ar)$	A and B	94i
$[Mn(HCOO)_2]$	1D circular channel with alternating large chambers and small windows interconnected by small apertures	$(H_2)/(N_2, Ar)$	A and/or B	93o
		$(CO_2)/(CH_4, N_2)$		100
		$(CH_2O_2)/(CO_2, CH_4, N_2, O_2, H_2)$		100

Table 1.3 (continued)

MOF material[a]	Pore features	Selectivity[b]	Reason[c]	Ref.
$[Mg_3(ndc)_3]$	1D elliptical channel with coordinatively unsaturated Mg^{II} sites	$(H_2, O_2)/(CO, N_2)$	A	95l
$[Cu(pzdc)_2(pyz)]$	1D rectangular channel with exposed basic O adsorption sites	$(C_2H_2)/CO_2)$	B	94o
$[Cu(hfipbb)\cdot (H_2\text{-}hfipbb)_{0.5}]$	1D near circular channel with hydrophobic internal surface, and alternating oval-shaped large chambers and narrow windows	$(CH_3CH_2CH_3, CH_3(CH_2)_2CH_3)/(CH_3(CH_2)_3CH_3)$	B	101
$[Cr_3O(H_2O)_2F(ntc)_{1.5}]$	1D circular channel with coordinated terminal water molecules and decorated by F^- ions	$(CO_2)/(CH_4, N_2)$	B	102
$Al_{12}O(OH)_{18}(H_2O)_3[Al_2(OH)_4](btc)_6$	Three types of cages connected by small windows	$(CO_2)/(CH_4)$	A	93r
[Zn(tbip)]	1D circular hydrophobic channel	$(MeOH)/(H_2O)$	B	103
[Cu(bdt)]	1D channel with unsaturated coordinated sites	(DME)/(MeOH); $(O_2)/(N_2, H_2)$	B	96h
$[Zn_2(bptc)]$	Two types of intersecting pores with H-bonding based on O atoms and aryl planes suitable for π-π stacking	$(CHCl_3$, MeOH, $(H_2O, C_6H_6, C_6H_5CH_3)/(CH_3(CH_2)_3CH_3, CH_3(CH_2)_4CH_3)$	B	93n
$[Zn_4O(H_2O)_3(adc)_3]$	1D square hydrophobic channel	$(H_2, O_2)/(N_2, CO)$	A	104
$[Cd_3(OH)_2(apt)_4(H_2O)_2]$	1D square channel with high electric field	$(H_2, CO_2)/(N_2)$	B	105

Table 1.3 (continued)

MOF material[a]	Pore features	Selectivity[b]	Reason[c]	Ref.
$[Sm_4Co_3(pyta)_6(H_2O)_x]$ (x < 9)	1D ellipsoid channel with coordinatively unsaturated metal sites	$(H_2, CO_2)/(N_2)$	A	106
$[Zn(bdc)(dabco)_{0.5}]$	Two types of 1D inter-connected hydrophobic channels	(MeOH, EtOH)/(H_2O)	B	107
$[Zn_4O(btb)_2]$	Large cages connected by small windows	$(O_2)/(N_2)$	B	108
$[Co_3(\mu_3\text{-}OH)_2(pdc)_2]$	1D diamondoid-shaped channels with corrugated walls	$(H_2, O_2)/(N_2, Ar)$ $(CO_2)/(CH_4)$	B	109 110
$[Mg(HCOO)_2]$	1D zigzag channels interconnected by small apertures	$(C_2H_2/CO_2, CH_4, N_2, O_2, H_2)$	B	100
[Zn(dtp)]	1D N-rich chiral channels	$(O_2, CO_2)/(N_2)$	A	111
$[Cu(fpymo)_2]$	1D helical channel with O atoms decrorated surface	$(H_2)/(N_2)$	A	112
[Zn(bim)(nim)], [Zn(cbim)(nim)], $[Zn(im)_{1.13}(nim)_{0.87}]$	Large cages connected by relative small apertures	$(CO_2)/(CO)$	B	113
$[Zn(cbim)_2]$	Large cages connected by small apertures	$(CO_2)/(CH_4, CO, N_2)$	A and B	114
$[Zn_{20}(cbim)_{39}(OH)]$	Large cages connected by small apertures	$(CO_2)/(CH_4, CO, N_2)$	A and B	114
$[Cu(gla)(bpy)_{0.5}]$	1D hydrophobic elliptical channel	$(H_2O)/(MeOH)$	A	115
$[Zn_2(cnc)_2(dpt)]\cdot$ guest	Triangular 1D channels	$(O_2)/(N_2)$	A	116
$[Zn_2(cnc)_2(dpt)]$	Triangular 1D channels	$(CO_2)/(CH_4)$	A and B	116
[Mn(ndc)]	Rhombic 1D channels with coordinatively unsaturated Mn^{II} sites	$(CO_2)/(CH_4)$	B	93s

Table 1.3 (continued)

MOF material[a]	Pore features	Selectivity[b]	Reason[c]	Ref.
$[Yb_4(\mu_4\text{-}H_2O)(tatb)_{8/3}(SO_4)_2]$	Large cages connected by small apertures	$(H_2, O_2)/(N_2, CO)$	A	117
$[Zn_3(OH)(cdc)_{2.5}]$	Intersecting rhombic channels with coordinatively unsatureted Zn^{II} sites	$(CO_2)/(CH_4)$	B	118
$[Zn_3(OH)(cdc)_{2.5}(DMF)_2]$	1D square channels	$(CO_2)/(CH_4)$	B	118
$[Co(HCOO)_2]$	1D zigzag channels inter-connected by small apertures	(ethylbenzene)/(*p*-xylene)	B	119
$[Zn_2(ndc)_2(dpni)]$	Intersecting rhombic channels	$(CO_2)/(CH_4)$	B	120

[a] Abbreviations: H_2-pda = 1, 4-phenylendiacetic acid; H_2-ndc = 2,6-naphthalenedicarboxylic acid; H_2-pzdc = pyrazine-2,3-dicarboxylic acid; pyz = pyrazine; H_2-hfipbb = 4,4'-(hexafluoroisopropylidene)bis(benzoic acid); H_4-ntc = naphthalene-1,4,5,8-tetracarboxylic acid; H_3-btc = 1,3,5-benzenetricarboxylic acid; H_2-tbip = 5-tert-butylisophthalic acid; H_2-bdt = 1,4-benzeneditetrazole; H_4-bptc = 4,4'-bipyridine-2,6,2',6'-tetracarboxylic acid; H_2-adc = 9,10-anthracenedicarboxylic acid; H-apt = 4-aminophenyltetrazole; H_3-pyta = 2,4,6-pyridinetricraboxylic acid; H_2-bdc = 1,4-benzenedicarboxylic acid; dabco = 1,4-diazabicyclo[2.2.2]octane; H_3-btb = 1,3,5-benzenetribenzoic acid; H_2-pdc = pyridine-2,4-dicarboxylic acid; H_2-dtp = 2,3-pyrazineditetrazole; H-fpymo = 5-fluoropyrimidin-2-ol; H-im = imidazole; H-nim = 2-nitroimidazole; H-cbim = 5-chlorobenzimidazole; bpy = 4,4'-bipyridine; H_2-gla = glutaric acid; H_2-cnc = 4-carboxycinnamic acid; dpt = 3,6-di-4-pyridyl-1,2,4,5-tetrazine; H_3-tatb = 4,4',4''-S-triazine-2,4,6-triyltribenzoic acid; H_2-cdc = 1,12-dicarba-*closo*-dode-caborane-1,12-dicarboxylic acid; dpni = *N*,*N'*-di-(4-pyridyl)-1,4,5,8-naphthalene tetracarboxydiimide.

[b] The symbol $(A_1, A_2, \ldots)/(B_1, B_2, \ldots)$ means guests $(A_1, A_2, \ldots)$ are favoured over guests $(B_1, B_2, \ldots)$.

[c] Probable reason for selective adsorption: A, size/shape exclusion; B, different adsorbent-adsorbate interactions.

Table 1.4 Summary of selective gas adsorption in flexible/dynamic MOFs.

MOF material[a]	Structural features	Selectivity[b]	Reason[c]	Ref.
$[Cu(dhbc)_2(bpy)]$	Interdigited 2D framework, stacking through π- π interactions to form 1D channels	$(CO_2/CH_4, O_2, N_2)$; $(CO_2, CH_4, O_2)/(N_2)$	C	93d
$[Cu(bdc)(bpy)_{0.5}]$	Interpenetrated 3D pillared-layer framework with inter-secting 1D potential open channels	$(CO_2/CH_4, O_2, N_2)$	C	93d
		$(CO_2, CH_4)/(O_2, N_2)$;		93i
		$(CO_2, CH_4, O_2)/(N_2)$		93i
$[Cu_2(pzdc)_2(dpyg)]$	3D pillared-layer framework with flexible and –OH functional pillars and 1D channels	$(CH_3OH)/(CH_4)$	D	121
[Cd(pzdc)(bpe)]	3D pillared-layer framework with 1D channels decorated by protruded C=O groups	$(H_2O, MeOH)/(EtOH, THF, Me_2CO)$	A	122
[M(OH)(bdc)] (M = Al, Cr)	3D framework with 1D diamond-shaped channels containing H-bonding sites	(CO_2/CH_4)	B	93q
[Cu(pydc)(bpp)]	2D pillared-bilayer framework without pores	$(N_2, O_2)/(CO_2,$ MeOH, EtOH)	C	123
$[Cr(OH)(bdc)]\cdot H_2O$	3D framework with 1D diamond-shaped channels containing H-bonding sites	(CO_2/CH_4)	B	124
$[Zn(adc)(bpe)_{0.5}]$	Interpenetrated 3D pillared-layer framework with inter-secting 1D potential open channels	$(H_2)/(N_2, CO)$; (CO_2/CH_4)	A	125

Table 1.4 (continued)

MOF material[a]	Structural features	Selectivity[b]	Reason[c]	Ref.
$H_2[Ni_3O(H_2O)_3(tatb)_2]\cdot 2H_2O$	Interpenetrated 3D framework stabilized by H-bonding with three types of intersecting 1D channels in three directions	(CO_2/CH_4)	A	126
$[Zn(pur)_2]$	3D framework with large cages connected by small distensible apertures	(CO_2/CH_4)	D	127
$[Cd(btapa)(NO_3)_2]$	Interpenetrated 3D framework with channels functionalized by amide groups	$(MeOH)/(N_2)$	D	50
$[Ni(bpe)_2(N(CN)_2)](N(CN)_2)$	Interpenetrated 3D framework with bimodal functionality	$(CO_2)/(N_2, O_2, Xe)$; $(H_2O, MeOH)/(EtOH, Me_2CO)$	B	128
[Ce(tci)]	3D nonporous framework	$(H_2O)/(MeOH, CO_2, N_2)$	B	129
$[Co(ndc)(bpy)_{0.5}]$	Interpenetrated 3D pillared-layer framework with intersecting 1D potential open channels	$(H_2)/(N_2)$	A	130
$[Cu(fma)(bpe)_{0.5}]$	Interpenetrated 3D pillared-layer framework with intersecting 1D potential open channels	$(H_2)/(CO, Ar, N_2)$; $(CO_2/CH_4, N_2)$	A	131
[Cu(bpndc)(bpy)]	Interdigited 2D framework, stacking with H-bonding to from 0D cavities	$(O_2)/(N_2, Ar)$; $(O_2, Ar)/(N_2)$	C	132
$[Ni_2(cyclam)_2(mtb)]$	Interpenetrated 3D framework with wide inside pockets connected by narrow entrances	$(H_2, CO_2, O_2)/(N_2, CH_4)$	A	133

Table 1.4 (continued)

MOF material[a]	Structural features	Selectivity[b]	Reason[c]	Ref.
[Cu(etz)]	3D framework with large cages connected by small hydrophobic changeable apertures	(MeOH, EtOH, MeCN)/(H_2O)	B	134
[Ln(tci)((H_2O)]	3D framework with 1D channels with ligand having highly flexible arms and secondary functional groups	(H_2O, MeOH)/ (EtOH, THF, Me_2CO)	A	135
[Zn_2(tcom)(bpy)]	Interpenetrated 3D PtS-type framework with intersecting channels	(CO_2)/(H_2, N_2)	B	136
Ag_2[Cr_3O($OOCC_2H_5$)$_6$(H_2O)$_3$]$_2$ [α-$SiW_{12}O_{40}$]	Nonporous layered ionic framework with exposed Ag^+ sites	(small unsaturated hydrocarbons)/ (paraffins and larger unsaturated hydrocarbons	D	137

[a] Abbreviations: H_3-dhbc = 2,5-dihydroxybenzoic acid; bpy = 4,4'-bipyridine; H_2-bdc = 1,4-benzenedicarboxylic acid; H_2-pzdc = pyrazine-2,3-dicarboxylic acid; H_2-dpyg = 1,2-di(4-pyridyl)glycol; bpe = *trans*-1,2-bis(4-pyridyl)ethylene; H_2-pydc = pyridine-2,3-dicarboxylic acid; bpp = 1,3-bis(4-pyridyl)propane; H_2-adc = 9,10-anthracenedicarboxylic acid; H_3-tatb = 4,4',4''-S-triazine-2,4,6-triyltribenzoic acid; H-pur = purine; btapa = 1,3,5-benzenetricarboxylic acid tris[N-(4-pyridyl)amide]; H_3-tci = tris(2-carboxyethyl)isocyanuric acid; H_2-ndc = 2,6-naphthalenedicarboxylic acid; H_2-fma = fumaric acid; H_2-bpndc = benzophenone-4,4'-dicarboxylic acid; H_4-cyclam = 1,4,8,11-tetraazacyclotetradecane; H_4-mtb = methanetetrabenzoic acid; H-etz = 3,5-diethyl-1,2,4-triazole; H_4-tcom = tetrakis[4-(carboxyphenyl)oxamethyl]methane.

[b] The symbol (A_1, A_2, …)/(B_1, B_2, …) means guests (A_1, A_2, …) are favoured over guests (B_1, B_2, …).

[c] Probable reason for selective adsorption: A, size/shape exclusion; B, different guest-adsorbate interactions; C, different guest-dependent gate-opening pressures; D, host-guest interaction induced gate-opening.

Apart from the selective adsorption characteristics presented in Table 1.3 and Table 1.4, the first MOF-based mesh-adjustable molecular sieve (**MAMS-1**), constructed from the amphiphilic ligand 5-*tert*-butyl-1,3-benzenedicarboxylate (bbdc) and Ni^{II} coordination unit, has been reported recently.[138] This material changes its gate size on variation of temperature, and hence exhibits a temperature-dependent selective gas adsorption effect.

Selective adsorption properties have demonstrated that MOFs have great potential in the separation and purification of gas mixtures. However, investigations in actual separations of gas mixtures with MOFs are scarce, although recent studies in kinetic separation, isotope separation, and membrane-based separation have illustrated encouraging potential for real applications. Different from the molecular-sieving effect, kinetic separation, accomplished by virtue of the differences in the diffusion rates of different components, is of great importance in industrial applications such as gas-chromatographic separation and fixed-bed adsorption. The majority of the known MOFs, which have been investigated for the kinetic separation of gas mixtures, are catalogued in Table 1.5.

Table 1.5 Summary of known MOFs exhibiting kinetic separation of gas mixtures.

MOF material[a]	Types of gas mixtures separated	Ref.
$[Cu_3(btc)_2]$	CO_2 and CO; CO_2 and MeOH; C_2H_4 and C_2H_6	43f
	CF_4 and Ar	139
	isobutane and isobutene	140
	xylenes and ethylbenzene	141
	Ar, Kr and Xe	96n
[Al(OH)(bdc)]	xylenes and ethylbenzene	141
	xylenes and ethylbenzene; ethyltoluenes; cymenes	142
[V(OH)(bdc)]	xylenes and ethylbenzene	141, 143
$[Zn_2(bdc)_2(dabco)]$	hexanes	144
$[Zn(bdc)(bpy)_{0.5}]$	pentanes; hexanes	145
	CO_2 and N_2; CO_2 and CH_4; CO_2, CH_4, and N_2	146
[Zn(bim)(nim)], [Zn(cbim)((nim)], $[Zn(im)_{1.13}(nim)]$	CO_2 and CO	113
$[Zn(cbim)_2]$, $[Zn_{20}(cbim)_{39}(OH)]$	CO_2 and CH_4; CO_2 and CO; CO_2 and N_2	114

[a] Abbreviations: benzene-1,3,5-tricarboxylic acid; H_2-bpdc = 4,4'-biphenyldicarboxylic acid; bpy = 4,4'-bipyridine; H_2-bdc = 1,4-benzenedicarboxylic acid; dabco = 1,4-diazabicyclo[2.2.2]octane; H-bim = benzimidazole; H-nim = 2-nitroimidazole; H-cbim = 5-chlorobenzimidazole; H-im = imidazole.

The classical molecular sieving principle can't be applied to isotope separation as isotopes have identical adsorption-based properties. Therefore, a quantum sieving process for isotope separation has been proposed by Beenakker *et al.*[147] Quantum sieving is based on the preferential adsorption of heavier isotopes due to the difference in the quantum energy levels of atoms or molecules confined in a very narrow space that is comparable to the de Broglie wave length. This effect has been demonstrated for H_2 and D_2 separation in two MOFs having molecular formulae of $Zn_3(bdc)_3[Cu(pyen)]$[148] (H_2-bdc = 1,4-benzenedicarboxylic acid; H_2-pyen = 5-methyl-4-oxo-1,4-dihydropyridine-3-carbaldehyde) and $[Cu(bpy)_2(CF_3SO_3)_2]$[149] (bpy = 4,4'-bipyridine).

Gas separations using MOFs as membrane materials have been accomplished employing two strategies: (A) preparation of thin films of MOF crystals on a metal support, and (B) incorporation of MOFs within a polymer matrix, resulting in a hybrid membrane material. Strategy (A) has allowed the preparation of a copper net supported $Cu_3(btc)_2$ MOF film[150] which, when attempted to separate gas mixtures such as H_2/N_2, H_2/CO_2, and H_2/CH_4, exhibited high permeability and selectivity for H_2. Three reports of membrane-based separation applying strategy (B) have been appeared so far. Using molecular dispersions of a MOF having composition of $[Cu_2(PF_6)(NO_3)(bpy)]$ confined in polysulfone, Won *et. al.*[151] have prepared a composite membrane which exhibited high selectivity for H_2 and He over CH_4, when separation of a mixture of gases like He, H_2, O_2, N_2, and CH_4 was examined. Car *et al.*[152] investigated the separation of H_2, O_2, N_2, CO_2, and CH_4, by two MOFs, $Cu_3(btc)_2$ and $Mn(HCOO)_2$ in polydimethylsiloxane and polysulfone matrices, and found improved permeability for H_2, CO_2, and CH_4, as well as selectivity for H_2 over N_2 and CO_2 over N_2, when compared to pure polymeric membranes. In addition, mixed-matrix membranes of Matrimid® containing **MOF-5** for separations of gas mixtures such as H_2/CO_2, CH_4/CO_2, and CH_4/N_2 have been investigated by Perez *et al.*[153] who have observed increased permeability but unaltered selectivity for any pair of gases.

1.4 Summary (Aim of the Dissertation Work)

A well-established class of pentanuclear coordination compounds with the chemical formulae $[M_5(L)_4(OH)_x(L')_{6-x}]$ (M^{II} = first-row transition metal ion; L = β-diketonate or nitrate; L' = 1,2,3-triazolate; x = 0, 1) have been known in literature before the start of this dissertation work. At the same time, research activity on metal-organic framework (MOF) materials has been found to grow enormously due to their various potential applications. While many MOFs so far have been synthesized using 3d transition metal ions and multidentate arylcarboxylate[22] ligands, the area of MOF type of compounds using the N-donor ligand benzobistriazole (H_2-BBTA) has remained largely unexplored. Molecular mechanic simulations showed that the assembly of pentanuclear $\{Zn_5Cl_4\}^{6+}$ coordination units and $\{BBTA\}^{2-}$ dianions results in a 3D cubic coordination framework. Once this design principle was successful to get a cubic porous material $[Zn_5Cl_4(BBTA)_3]$ or "**MFU-4**" (*M*etal-organic *F*ramework *U*lm University-4, *cf.* Chapter 4) having coordinatively unsaturated tetrahedral Zn sites, efforts were undertaken to search for its discrete low-molecular counterparts (secondary building units or SBUs) in order to get mechanistic insights into the proposed catalytic properties of **MFU-4** type of heterogenous catalysts. The peripheral M^{II} ions in the previously reported pentanuclear compounds $[M_5(L)_4(OH)_x(L')_{6-x}]$ are either penta- or hexacoordinated with bidentate β-diketonate, nitrate and/or monodentate solvent molecules, and thus they are structurally related though not strictly isotypic with **MFU-4** type SBUs. The necessity to achieve a better structural congruence with **MFU-4** was fulfilled through the successful design and synthesis of a novel family of coordination compounds, represented by the chemical formula $[M^{II}Zn_4Cl_4(L)_6]$ (M^{II} = Zn, Fe, Co, Ni, or Cu; L = 5,6-dimethyl-1,2,3-benzotriazolate), in which the peripheral zinc ions are tetrahedrally coordinated. The coordinatively unsaturated Zn sites and the redox-active open-shell metal ions are supposed to catalyze homogenous Lewis-acid and redox catalyzed reactions, respectively.

Chapter 2

Homo- and Heteropentanuclear Coordination Compounds $[MZn_4(L)_4(L')_6]$ (M^{II} = Zn, Fe, Co, Ni, or Cu; L = chloride or acac; L' = 1,2,3-benzotriazolate ligand) Represented by the Nonplanar $K_{3,3}$ Graph

2.1 Introduction

A rational approach towards catalytically active metal-organic frameworks (MOFs) rests on the systematic design of discrete secondary building units (SBUs)[22c,22e,28a] that can be linked into 3D porous solids. However, while for most MOFs there is lack of experimental evidence in favor to framework build-up from SBUs during synthesis, it seems undisputable that the availability of discrete coordination compounds comprising structures and functions similar or identical to SBUs - into which a MOF can be formally subdivided - would represent an enormous speed-up for an efficient and rapid prototyping of functional MOFs. Discrete coordination compounds frequently are much more easy to prepare in pure form, and their good solubility in common solvents allows for investigating their functional properties by a range of different spectroscopic techniques which are commonly available.

Thermally and solvolytically stable model coordination compounds were required in order to get mechanistic insights into the proposed catalytic properties of recently synthesized **MFU-4** (*cf.* Chapter 4)[10d] type of porous framework. An intensive literature survey for coordination compounds (Table 1.1, Figure 1.7 and 1.8), which are structurally related to the SBUs from which **MFU-4** could be formally erected, revealed the existence of a class of coordination compounds with the chemical formulae $[M_5(L)_4(OH)_x(L')_{6-x}]$ (M^{II} = first-row transition metal ion; L = β-diketonate or nitrate; L' = 1,2,3-triazolate; x = 0, 1).[9,10a,10f,11a,12,13] However, the peripheral M^{II} ions in these compounds are either penta- or hexacoordinated with bidentate β-diketonate, nitrate and/or monodentate solvent molecules, and thus they are structurally related though not strictly isotypic with **MFU-4** type SBUs. The demand to achieve a better structural congruence with **MFU-4** was fulfilled through the development of a novel family of coordination compounds, represented by the chemical formula $[M^{II}Zn_4Cl_4(L)_6]$, in which the peripheral zinc ions are tetrahedrally coordinated (Figure 2.1). These compounds should best

serve the purpose of **MFU-4** model compounds which could be screened for catalytic activities in homogeneous test reactions. This approach is intended to gain further insights into catalytic and functional properties, which then might be transferable on the design of future **MFU-4** type heterogeneous catalysts.

Tri- or tetranuclear oxo-bridged basic metal carboxylates are known for decades, and serve as the discrete low-molecular counterparts for most of the MOFs containing polydentate arylcarboxylates as linkers. A huge variety of homo- and heterotrinuclear carboxylates[154] $[M_3O(L)_6]^{n+}$ (M^{III} = transition metal ion, L = bridging carboxylate) show moderate stability against hydro-/solvolysis, and provide examples of low-molecular analogues of many isoreticular frameworks within the **MIL** series[155] and **POST-1**[75]. Several basic Zn[156] or Be[157] carboxylates $[M_4O(L)_6]$ are structurally related to the coordination units of prototypic **MOF-5**[17] and its topologically related[22b-g] porous frameworks. However, these compounds are hydro-/solvolytically unstable,[156c-d] and hence will pose difficulties when investigating their activity in homogenous test reactions. Relating to the recent work, all attempts to prepare model compounds of the SBU found in **MFU-1**[53] (which is topologically related with **MOF-5**) have failed, although single crystal X-ray data of the compound $[Co_4^{II}O(dmpz)_6]$ (dmpz = 3,5-dimethylpyrazolate) have been reported previously.[158]

In contrast to the former compound, the synthesis of suitable model compounds relating to **MFU-4** proved to be straight-forward. In the following, syntheses and comparative magnetostructural and spectroscopic investigations on homo- and heteropentanuclear coordination compounds $[M^{II}Zn_4Cl_4(L)_6]$ (M^{II} = Zn, Fe, Co, Ni, or Cu; L = 5,6-dimethyl-1,2,3-benzotriazolate) are presented, for which the term “Kuratowski-type” coordination units is proposed.

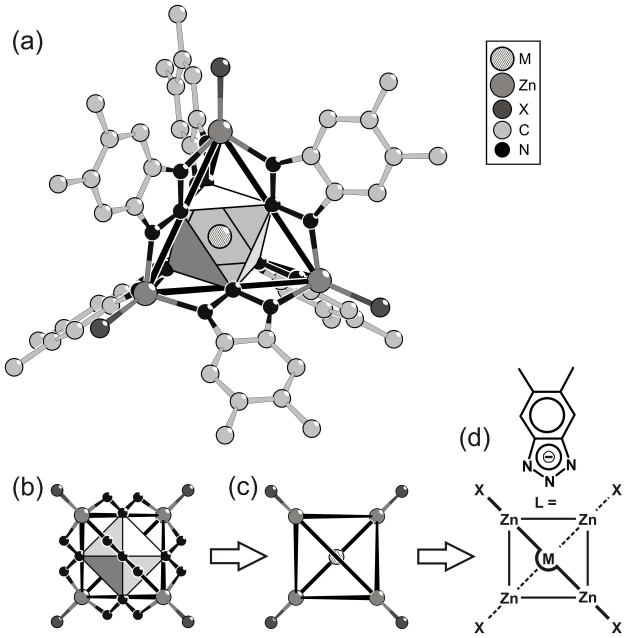

Figure 2.1 (a) Ball-and-stick representation of $[MZn_4X_4(L)_6]$ coordination units, high-lighting the central octahedral coordination site which results from 6 N-donor atoms situated at the centers of the edges of an imaginary tetrahedron which is spanned by the 4 Zn^{II} ions at the corners. (b) Simplified representation of metal centers and ligand donor atoms. (c), (d) Derivation (*cf.* discussion on Graph Theoretical Representation) of a rational graphical scheme representing the connectivity of the coordination units.

From a topological point of view, the coordination units $[MZn_4Cl_4(L)_6]$ represent the rare class of minimum nonplanar building units having T_d point group symmetry and $K_{3,3}$ as molecular graph (Figure 2.1, see also Figure 2.39), constituting versatile models of a future library of structurally related cubic **MFU-4** type porous frameworks. As shown in Figure 2.1, the homopentanuclear $[Zn_5Cl_4(L)_6]$ coordination unit has two different coordination sites: one central octahedral site and four tetrahedral sites at peripheral positions. Substituting the central octahedrally coordinated Zn^{II} ion by an open-shell d-transition metal ion M^{II} causes a huge gain in crystal-field stabilization energy (CFSE). Therefore, the use of stoichiometric mixtures of different metal salts (M^{II} / Zn^{II}) enabled to synthesize a series of heteropentanuclear compounds in which the open-shell M^{II} ions occupy the octahedral coordination sites. To the best of knowledge, these are the first examples of heterometallic compounds containing 1,2,3-triazolates. The open-shell M^{II} ions might act as redox catalysts in homogenous reactions. Moreover, the coordinatively unsaturated Zn^{II} ions may fill up (either permanently or transiently) the number of coordinated ligands,[9,10a,10f,11a,12] and may thus be employed as Lewis acid catalysts for a wide variety of homogenous reactions (*e.g.*,

Diels-Alder, Aldol, Mannich, Friedel-Crafts, 1,2- and 1,4-addition, oxidation and reduction, esterification, and Claisen rearrangement).[159]

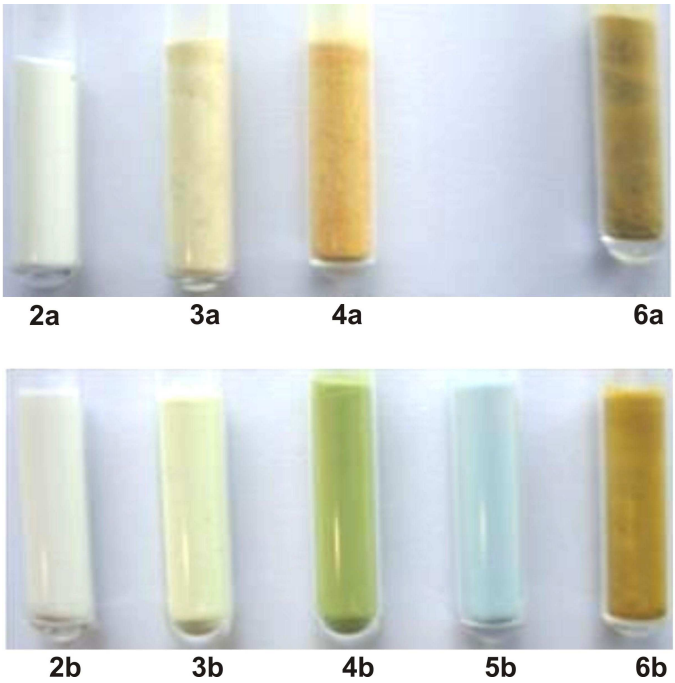

Figure 2.2 Photographs of all compounds (except **1** which has similar colour as **2a** or **2b**) described in this chapter. Top row: the set of compounds recrystallised from DMF; bottom row: the set of compounds recrystallised from bromobenzene.

In this chapter, the syntheses, crystal structures as well as thermal, electronic and magnetic properties of the above mentioned homo- and heteropentanuclear coordination compounds (Figure 2.2, Table 2.1) are presented.

Table 2.1 List of compounds described in this chapter.

Compound	Molecular formula	Compound	Molecular formula
1	$[Zn_5(acac)_4(bta)_6]\cdot 4C_6H_{12}$[a]	**4a**	$[CoZn_4Cl_4(Me_2bta)_6]\cdot 2DMF$
2a	$[Zn_5Cl_4(Me_2bta)_6]\cdot 2DMF$[b]	**4b**	$[CoZn_4Cl_4(Me_2bta)_6]\cdot 2C_6H_5Br$
2b	$[Zn_5Cl_4(Me_2bta)_6]\cdot 2C_6H_5Br$[c]	**5b**	$[NiZn_4Cl_4(Me_2bta)_6]\cdot 2C_6H_5Br$
3a	$[FeZn_4Cl_4(Me_2bta)_6]\cdot 2DMF$	**6a**	$[CuZn_4Cl_4(Me_2bta)_6]\cdot 2DMF$
3b	$[FeZn_4Cl_4(Me_2bta)_6]\cdot 2C_6H_5Br$	**6b**	$[CuZn_4Cl_4(Me_2bta)_6]\cdot 2C_6H_5Br$

[a] C_6H_{12} = cyclohexane, [b] DMF = *N*,*N*'-dimethylformamide, [c] C_6H_5Br = bromobenzene.

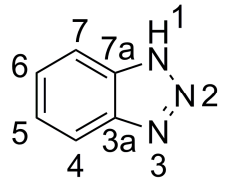

1*H*-benzo[*d*][1,2,3]triazole
(btaH)

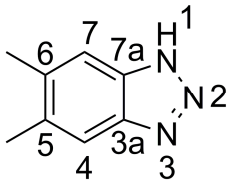

5,6-dimethyl-1*H*-benzo[*d*][1,2,3]triazole
(Me_2btaH)

Figure 2.3 Structures of the 1,2,3-benzotriazole ligands described in this chapter.

2.2 Results and Discussion

2.2.1 Syntheses

All metal compounds described in this chapter are crystalline and stable in air at ambient conditions. Compound **1** is soluble in chloroform, dichloromethane, DMF, dimethyl sulfoxide (DMSO) and even in non-polar solvents such as diethyl ether or benzene. All the other compounds are sparingly soluble in solvents such as chlorobenzene, 1,2-dichlorobenzene, 1,3-dichlorobenzene, 1,2,4-trichlorobenzene, bromobenzene, xylene, mesitylene, 1-methyl-2-pyrrolidone (NMP) or ethylacetate.

A previously developed synthetic method[10c,12,13] was employed to synthesize **1** while a completely different strategy was adopted to prepare all the other compounds. Compounds **2a**, **3a**, **4a**, and **6a** were crystallized from DMF solution containing suitable metal precursors and ligand with the calculated stoichiometric ratio employing slow vapour diffusion of lutidine into the crystallization vial. The weakly coordinating base (lutidine) is employed to deprotonate the -NH group of the 1,2,3-benzotriazole ligand. However, this strategy was unsuccessful for the preparation of heteropentanuclear compound $[NiZn_4Cl_4(Me_2bta)_6]\cdot 2DMF$ (**5a**). Therefore, an alternate synthetic strategy, namely the dropwise addition of lutidine was applied for the synthesis of this compound. In fact, direct addition of lutidine to a methanol solution containing stoichiometric required amounts of the metal salts and the ligand, followed by recrystallisation of the resulting solid from bromobenzene, produced light blue octahedral crystals of **5b**. During the course of the investigations, it was also found that a series of homo- and heteropentanuclear coordination compounds of general formula $[MZn_4Cl_4(Me_2bta)_6]\cdot 2C_6H_5Br$ (M^{II} = Zn, **2a**-**b**; Fe, **3a**-**b**; Co, **4a**-**b**; Ni, **5b**; Cu, **6a**-**b**) can likewise be synthesized in large quantities from methanol solution employing the "direct addition of lutidine" approach which is much faster than the "vapour diffusion of lutidine" route. Compound **2a** can also be prepared by the solvothermal approach in which thermal

decomposition of DMF liberates the base (dimethylamine) in the reaction medium. The *in-situ* generated base (dimethylamine) abstracts the acidic protons from 1,2,3-benzotriazole ligands. However, the solvothermal approach was unsuccessful for the synthesis of all the other compounds. The preparations of all the compounds are summarized in Scheme 2.1.

Compound **1:**

$$5\ Zn(acac)_2 + 6\ btaH \xrightarrow[RT]{DCM} [Zn_5(acac)_4(bta)_6] + 6\ acacH$$

Homopentanuclear compounds $[Zn_5Cl_4(Me_2bta)_6]$:

$$5\ ZnCl_2 + 6\ Me_2btaH + 6\ B \xrightarrow[RT]{solvent} [Zn_5Cl_4(Me_2bta)_6] + 6\ BH^{\oplus} + 6\ Cl^{\ominus}$$

Heteropentanuclear compounds $[MZn_4Cl_4(Me_2bta)_6]$:

$$MX_2(H_2O)_6 + 4\ ZnCl_2 + 6\ Me_2btaH + 6\ B \xrightarrow[RT]{solvent} [MZn_4Cl_4(Me_2bta)_6] + 6\ BH^{\oplus} + 4\ Cl^{\ominus} + 2\ X^{\ominus} + 6\ H_2O$$

Scheme 2.1 Chemical equations for the preparation of all the compounds demonstrated in this chapter. B = 2,6-lutidine; M^{II} = Zn, Fe, Co, Ni, Cu; X = (NO_3) for **4a**-**b**, **6a**-**b** and (ClO_4) for **3a**-**b**, **5b**; solvent = DMF for **2a**, **3a**, **4a**, **6a** and methanol for **2**-**6b**.

2.2.2 Characterization

X-ray powder diffraction. Phase purity of all the metal compounds was confirmed by X-ray powder diffraction (XRPD). The experimental XRPD patterns are consistent with the simulated ones as determined from the single-crystal X-ray diffraction data (Figures 2.4-2.10).

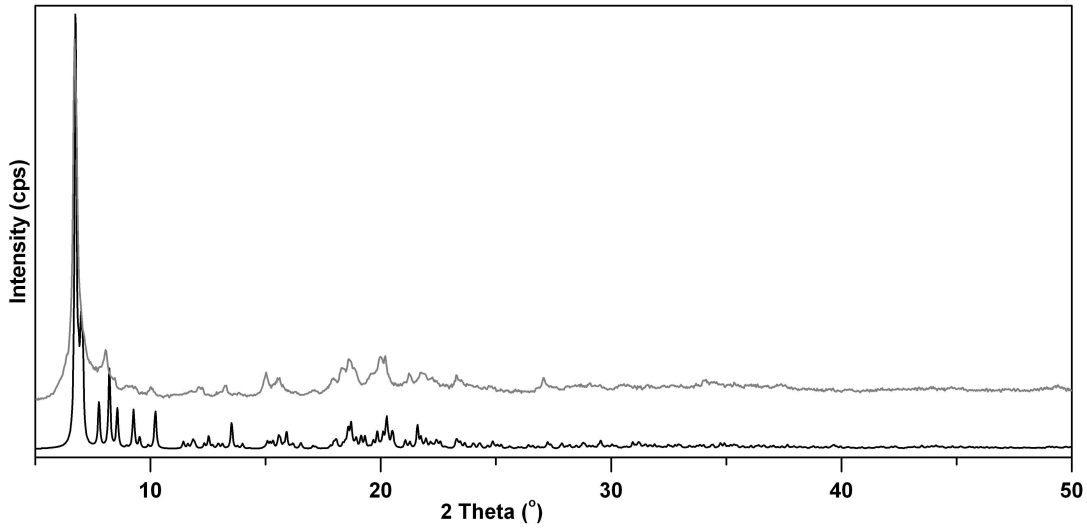

Figure 2.4 Theoretical (black) and experimental (grey) XRPD patterns of **1**.

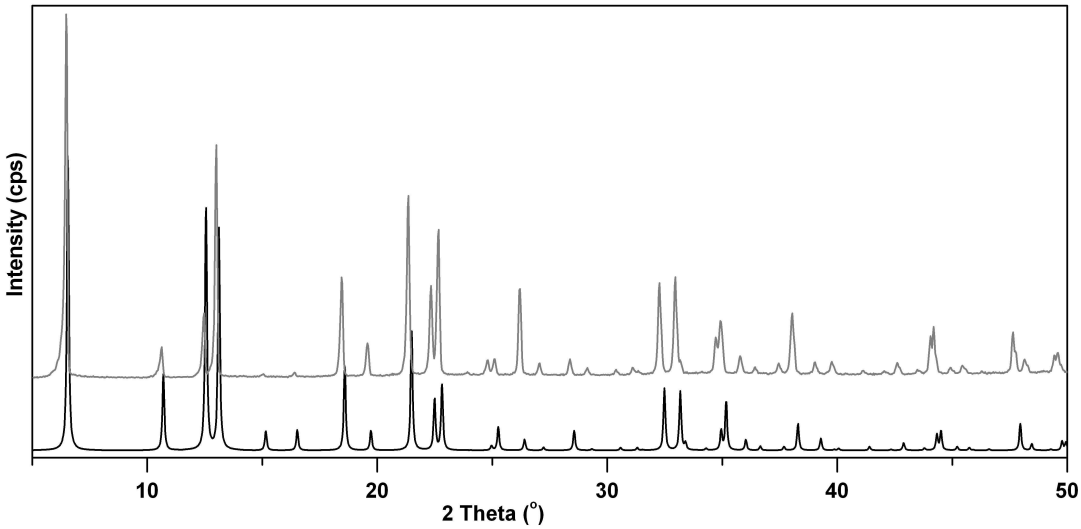

Figure 2.5 Theoretical (black) and experimental (grey) XRPD patterns of **2a**.

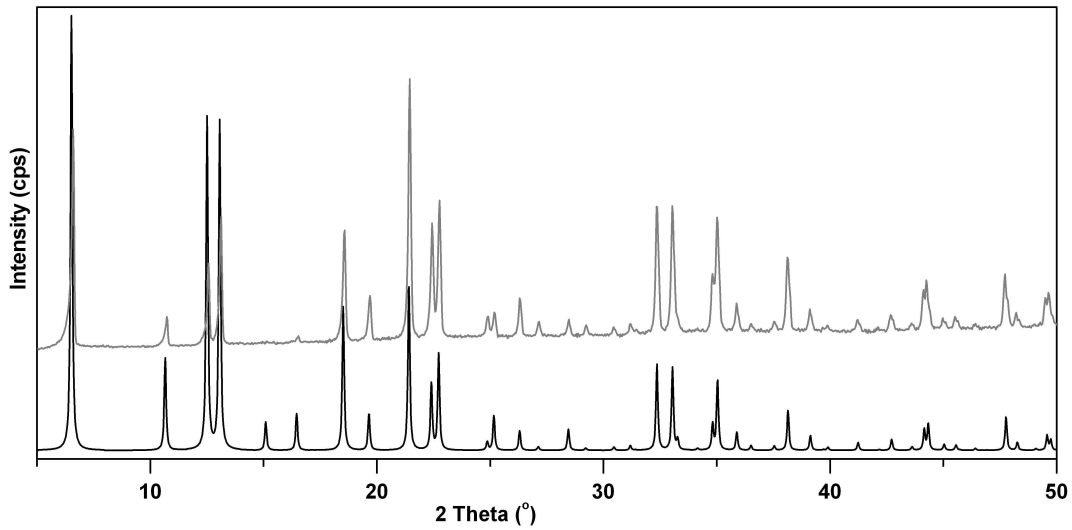

Figure 2.6 Theoretical (black) and experimental (grey) XRPD patterns of **3a**.

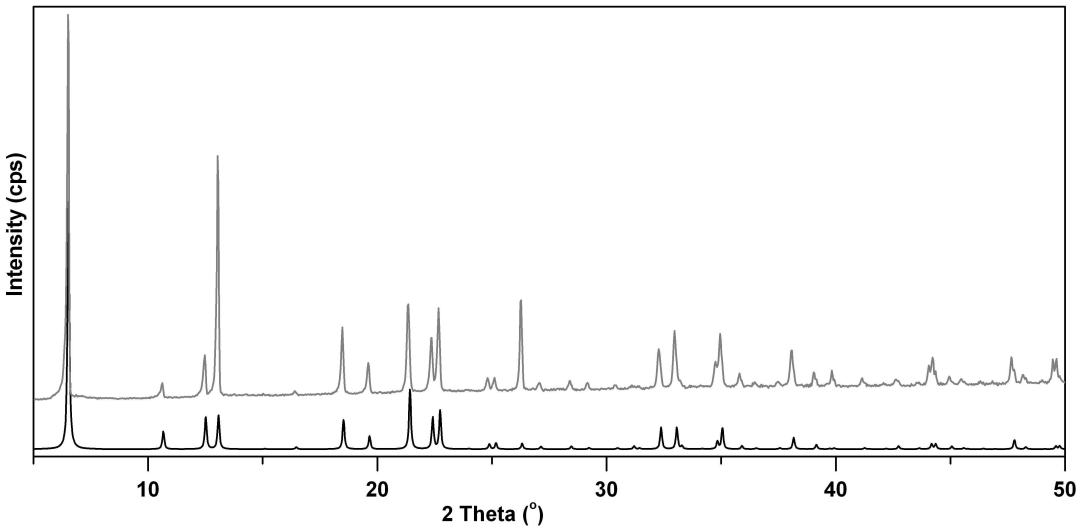

Figure 2.7 Theoretical (black) and experimental (grey) XRPD patterns of **4a**.

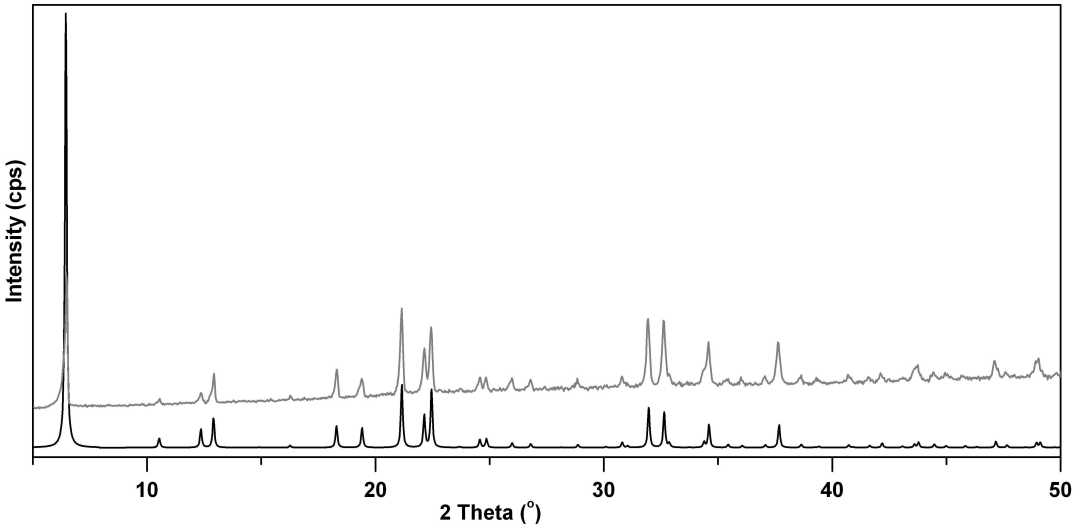

Figure 2.8 Theoretical (black) and experimental (grey) XRPD patterns of **4b**.

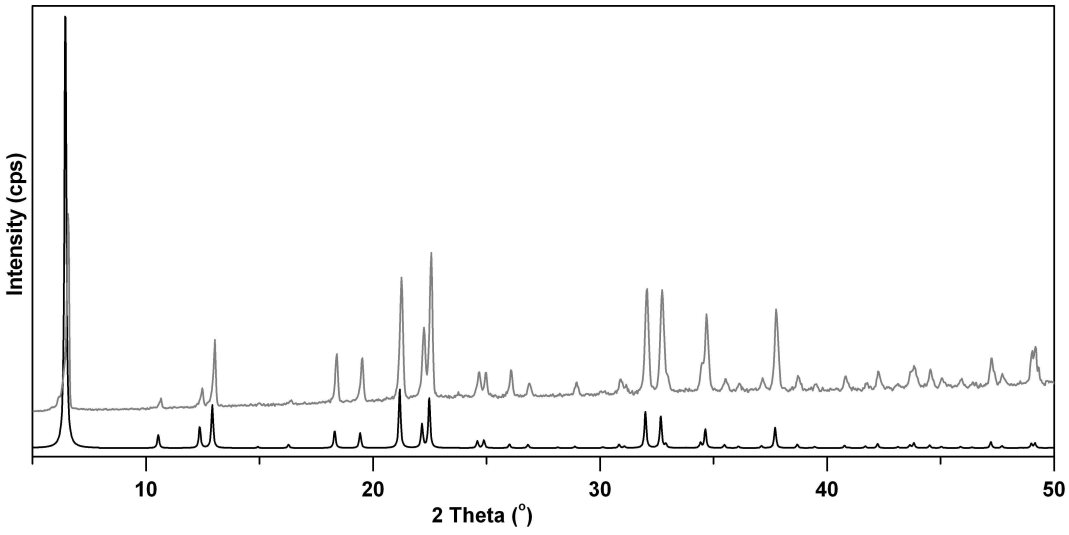

Figure 2.9 Theoretical (black) and experimental (grey) XRPD patterns of **5b**.

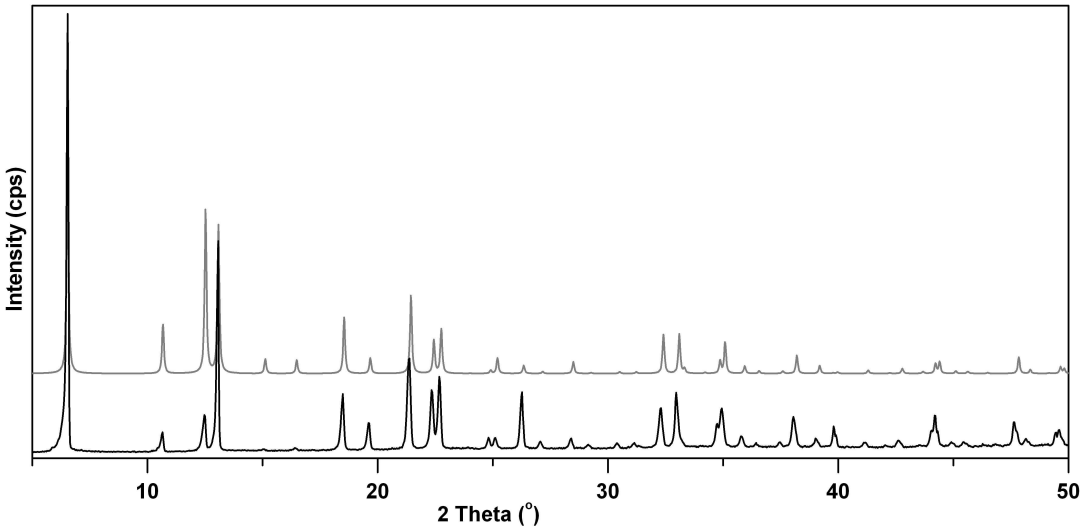

Figure 2.10 Theoretical (black) and experimental (grey) XRPD patterns of **6a**.

All the compounds in each set of compounds (each set having either DMF or brombenzene as occluded solvent molecules) possess similar XRPD patterns (Figure 2.11). Slight differences in intensities and peak positions between the XRPD patterns of the two sets of compounds occur due to the different non-coordinating solvent molecules.

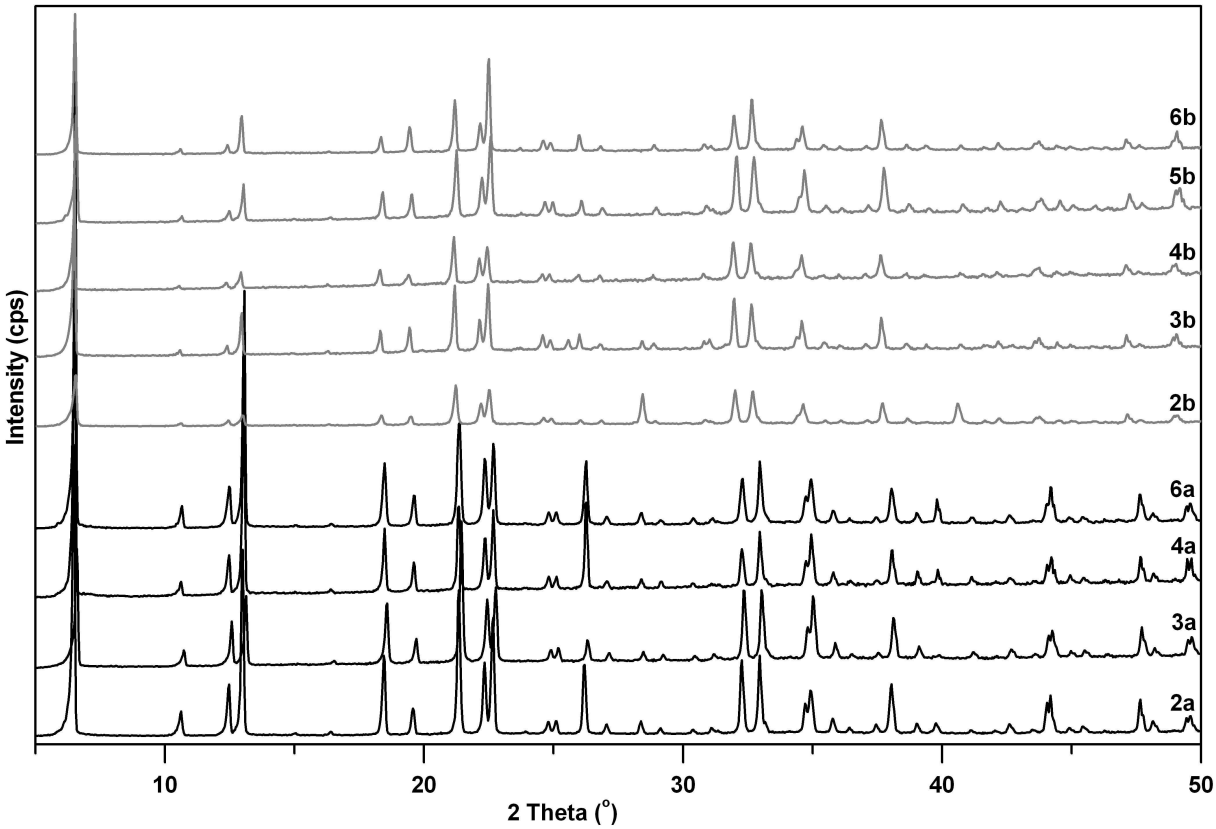

Figure 2.11 Experimental XRPD patterns of all the compounds (except **1**) presented in this chapter. Black lines: XRPD patterns of the set of compounds having DMF as occluded

solvent molecules; grey lines: XRPD patterns of the set of compounds having bromobenzene as occluded solvent molecules.

EDX analysis. EDX measurements (Figure 2.12-2.18) were performed on all the heteropentanuclear compounds to determine the M (M = Fe, Co, Ni, or Cu):Zn ratios. The experimental M:Zn ratios (Table 2.2) match quite closely with the theoretical M:Zn ratio of 1:4.0.

Table 2.2 Experimental M (M = Fe, Co, Ni, or Cu):Zn ratios obtained from EDX analyses.

Compound	M:Zn ratio	Compound	M:Zn ratio
3a	3.80	**5b**	4.0
3b	3.87	**6a**	3.79
4a	4.12	**6b**	3.99
4b	3.76		

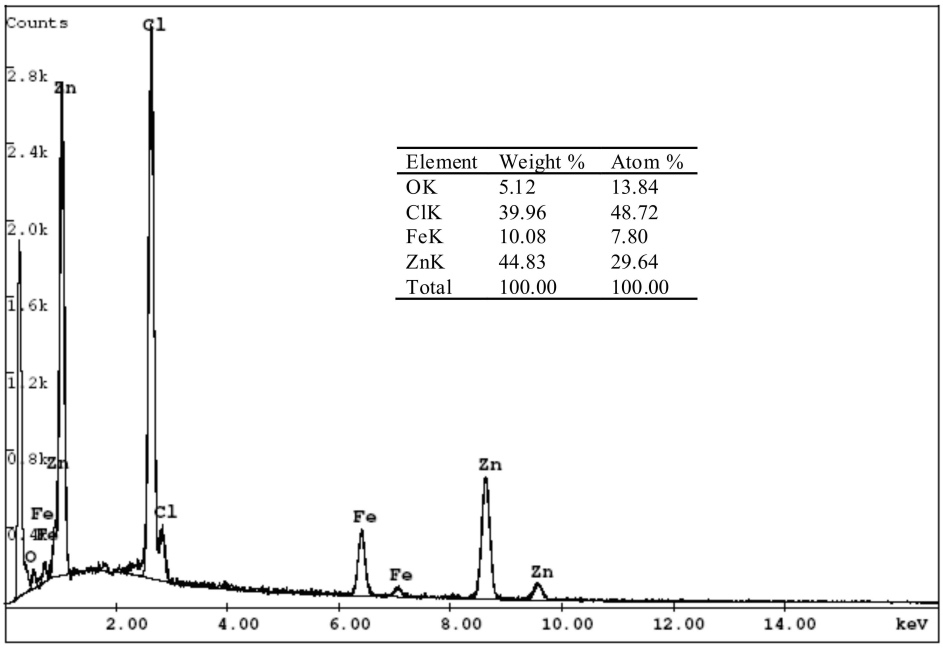

Figure 2.12 EDX spectrum of **3a**.

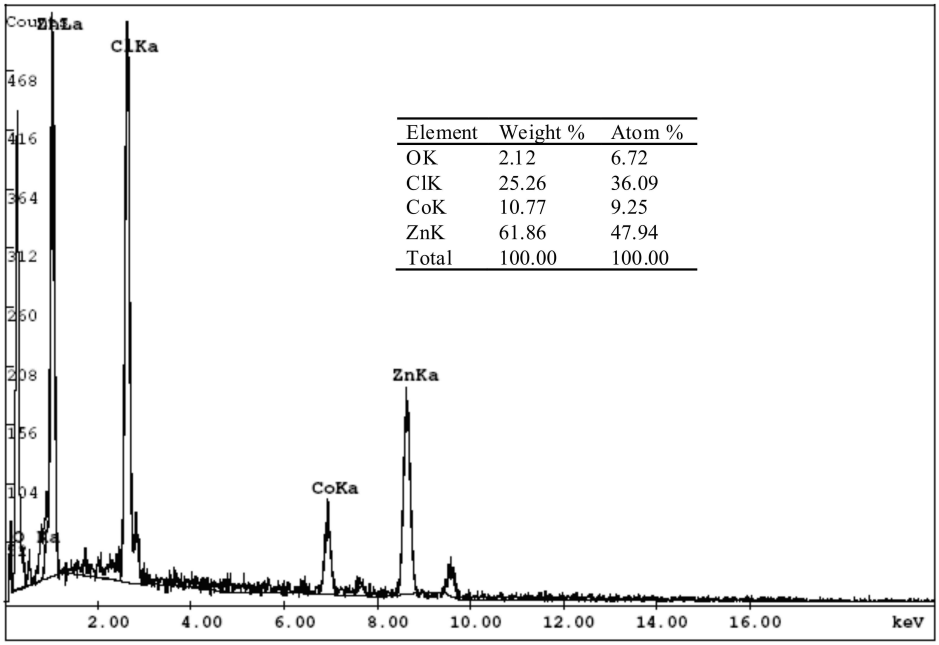

Element	Weight %	Atom %
OK	2.12	6.72
ClK	25.26	36.09
CoK	10.77	9.25
ZnK	61.86	47.94
Total	100.00	100.00

Figure 2.13 EDX spectrum of **4a**.

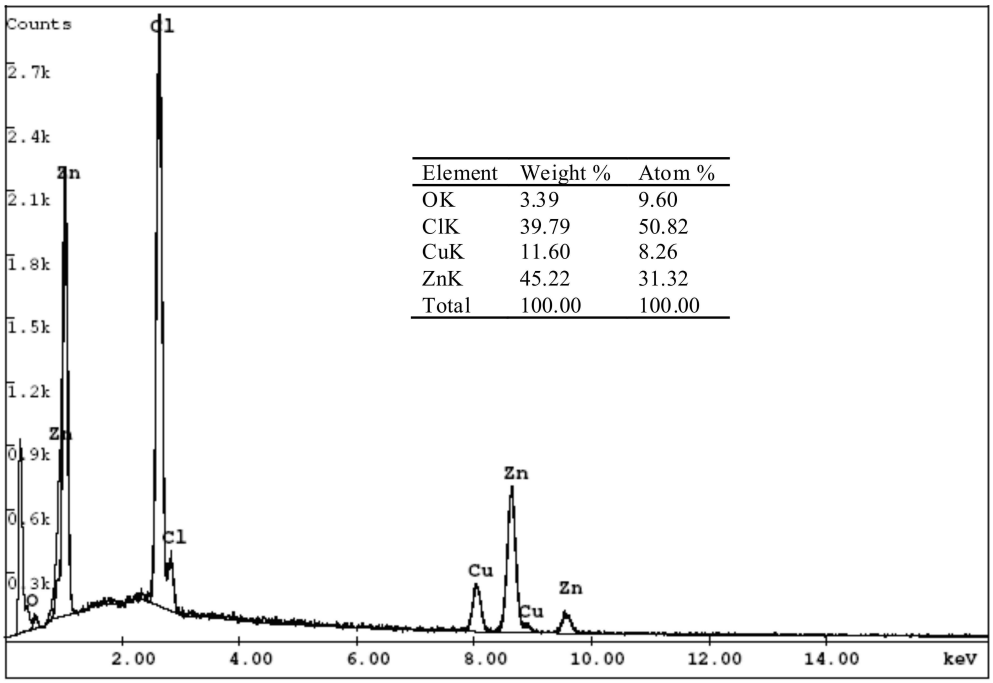

Element	Weight %	Atom %
OK	3.39	9.60
ClK	39.79	50.82
CuK	11.60	8.26
ZnK	45.22	31.32
Total	100.00	100.00

Figure 2.14 EDX spectrum of **6a**.

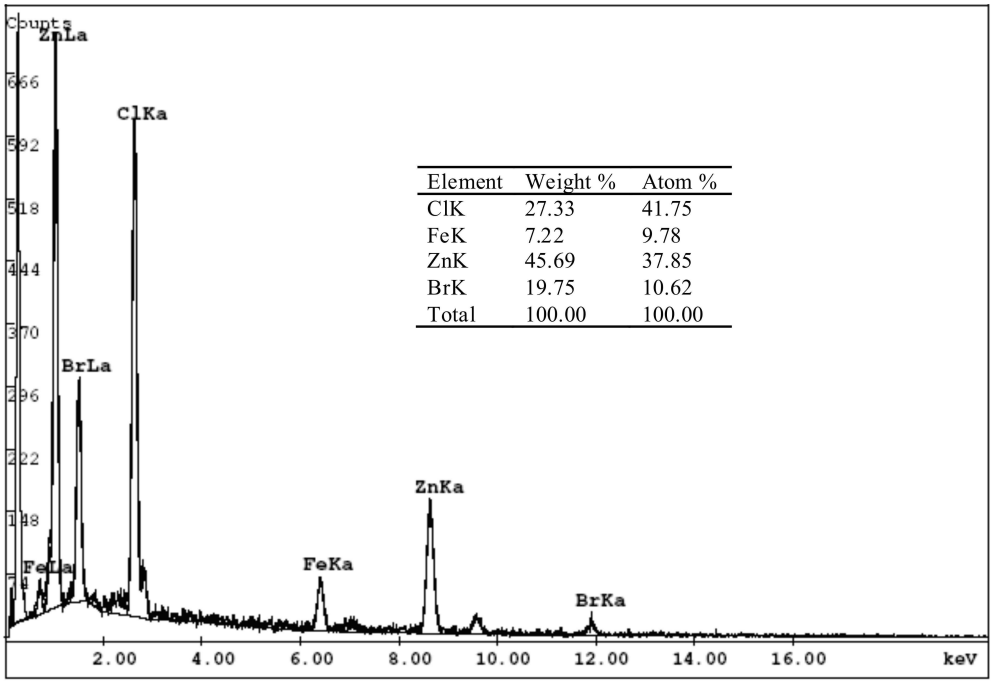

Element	Weight %	Atom %
ClK	27.33	41.75
FeK	7.22	9.78
ZnK	45.69	37.85
BrK	19.75	10.62
Total	100.00	100.00

Figure 2.15 EDX spectrum of **3b**.

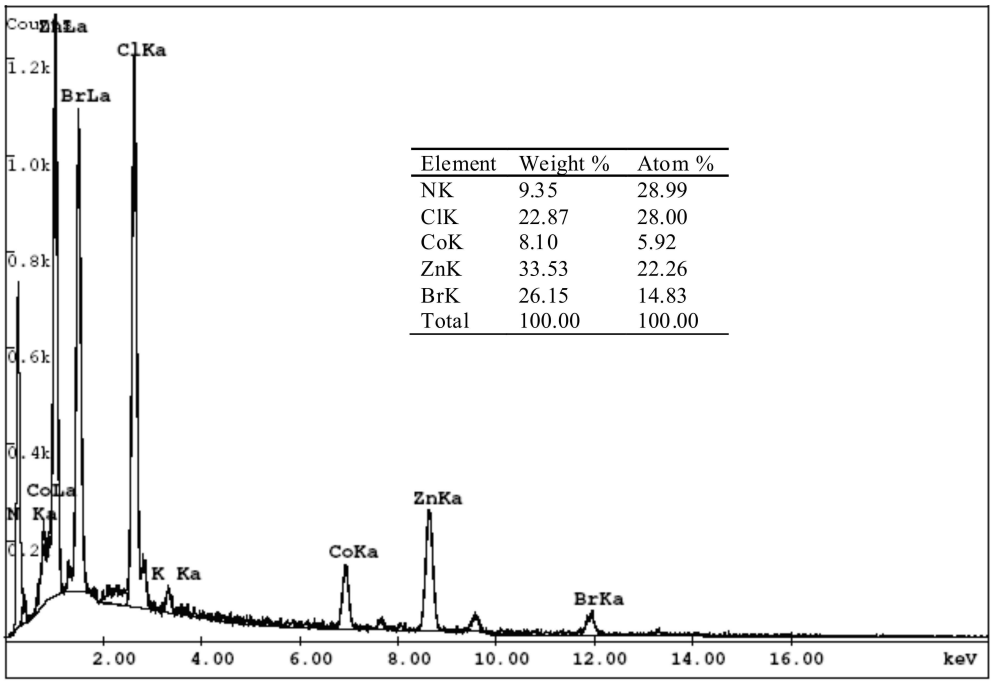

Element	Weight %	Atom %
NK	9.35	28.99
ClK	22.87	28.00
CoK	8.10	5.92
ZnK	33.53	22.26
BrK	26.15	14.83
Total	100.00	100.00

Figure 2.16 EDX spectrum of **4b**.

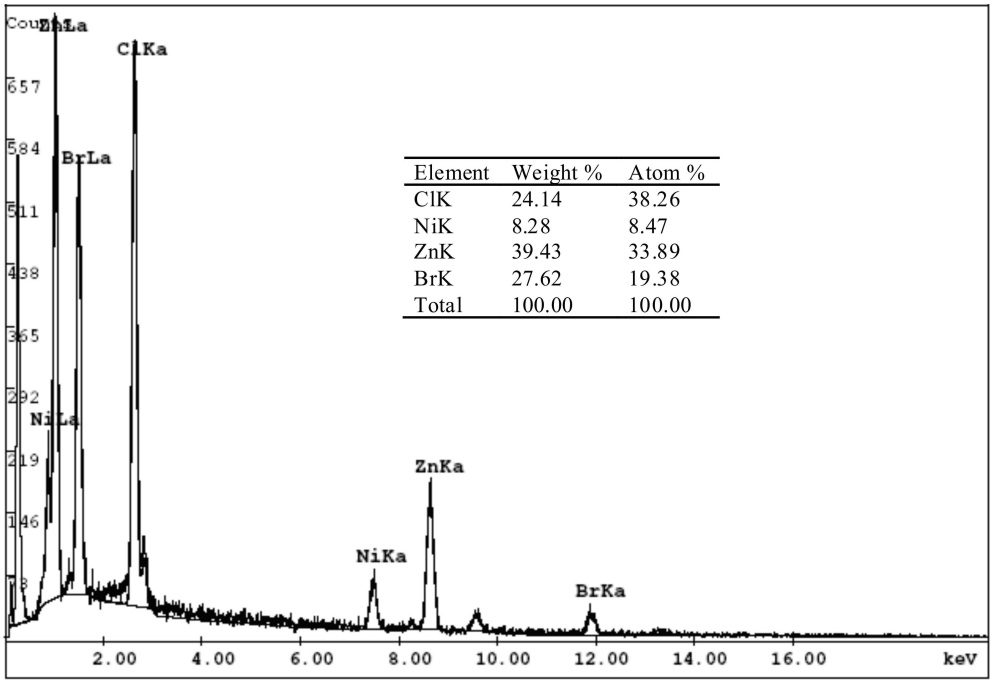

Element	Weight %	Atom %
ClK	24.14	38.26
NiK	8.28	8.47
ZnK	39.43	33.89
BrK	27.62	19.38
Total	100.00	100.00

Figure 2.17 EDX spectrum of **5b**.

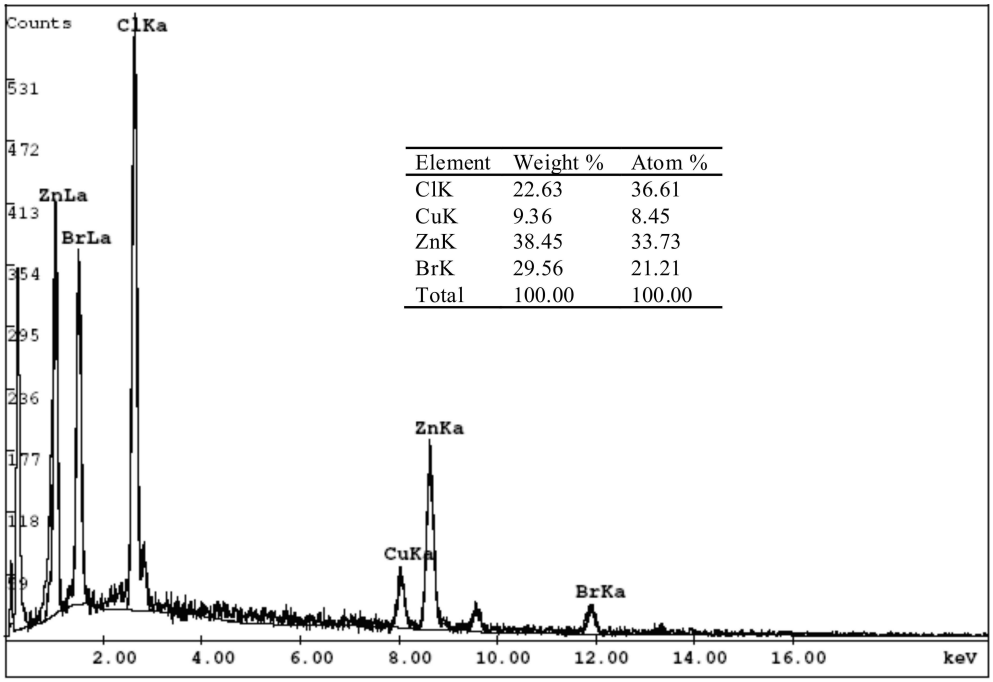

Element	Weight %	Atom %
ClK	22.63	36.61
CuK	9.36	8.45
ZnK	38.45	33.73
BrK	29.56	21.21
Total	100.00	100.00

Figure 2.18 EDX spectrum of **6b**.

ICP-AES analysis. ICP-AES analyses were carried out on **3a**, **4a**-**b**, **5b**, and **6a** in order to derive more precise M/Zn ratios. The experimental weight percentages of the metal ions (Table 2.3) are in agreement with the estimated ones, which unequivocally prove the coexistence of open-shell metal and Zn ions in the expected ratios.

Table 2.3 ICP-AES analyses for **3a**, **4a-b**, **5b**, and **6a**.

Compound	Element	Experimental wt. %	Calculated wt. %
3a	Fe	3.76	3.47
	Zn	17.64	17.60
4a	Co	3.96	3.85
	Zn	17.60	17.60
4b	Co	3.36	3.34
	Zn	15.82	15.40
5b	Ni	3.55	3.46
	Zn	15.82	15.60
6a	Cu	4.26	4.26
	Zn	17.55	17.10

TOF-MS analysis. In order to ensure the structural integrity of the pentanuclear compounds in solution, TOF-MS analyses were performed with ethylacetate solutions of **2a** and **6a** (Figures 2.19 and 2.20, respectively). The MS analyses were carried out with a Liquid Injection Field Desorption Ionization (LIFDI)[160] source which ionizes neutral transition metal compounds without any protonation or fragmentation. The m/z ratios (1345.7, **2a**; 1343.9, **6a**) calculated for the desolvated compounds are in agreement with the observed m/z ratios (1345.9, **2a**; 1344.2, **6a**). Moreover, the simulated and the experimental isotopic patterns of the two compounds are quite similar. These results confirm that the compounds maintain their structural integrity in solution. Noteworthily, the stability of a structurally related homopentanuclear Zn^{II} compound in DMA solution at 358 K has been previously verified by ESI-MS studies.[10a]

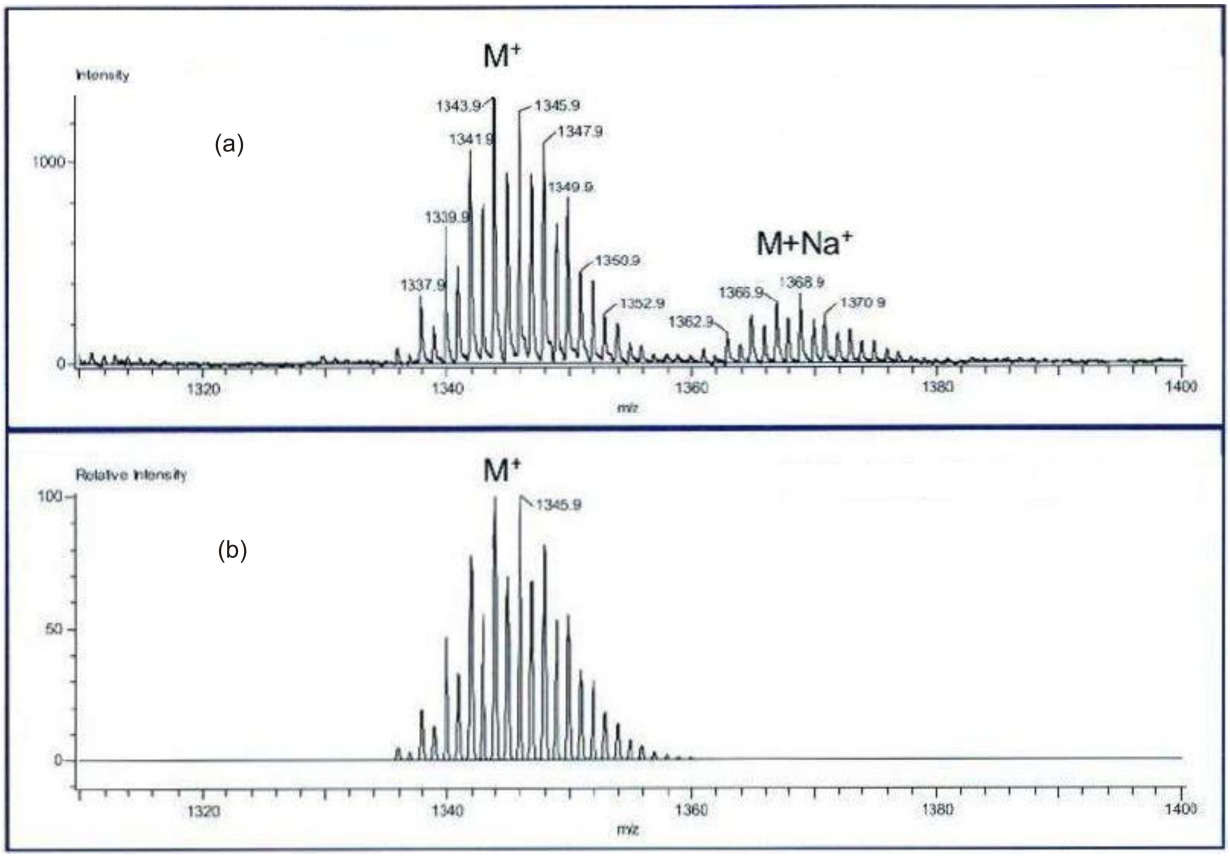

Figure 2.19 Experimental (a) and theoretical (b) isotopic patterns of **2a**.

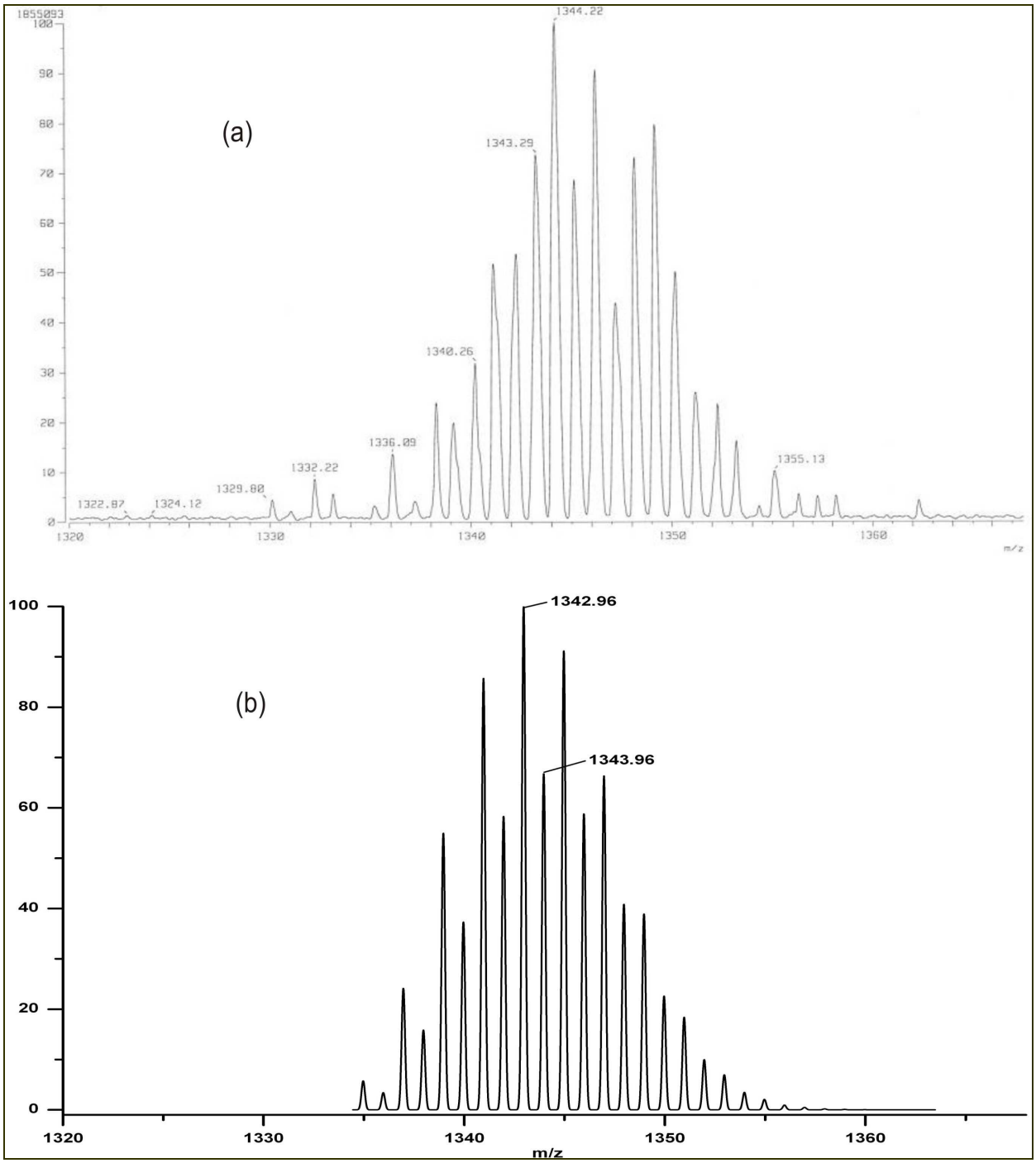

Figure 2.20 Experimental (a) and theoretical (b) isotopic patterns of **6a**.

Thermogravimetric analysis. In order to examine the thermal stability of the compounds, thermogravimetric analyses (TGA) were performed on polycrystalline samples of all the compounds in a nitrogen atmosphere.

In the TGA curves of **2**-**4a** (Figure 2.21), the first weight loss steps (12.15 % for **2a**, 11.48 % for **3a**, 10.14 % for **4a**) in the temperature range 150-400 °C are attributed to the removal of two occluded DMF molecules per formula unit (calcd.: 9.79 % for **2a**, 9.86 % for **3a**, 9.84 % for **4a**). All the other weight loss steps which occur at a temperature above 400 °C can be

attributed to the decomposition of these compounds. The DMF molecules from the void regions of compound **2a** can be removed by heating at 200 °C under vacuum for 24 h. The fully desolvated sample of **2a** (Figure 2.21) displays no weight loss until 400 °C, thus confirming the complete removal of DMF molecules.

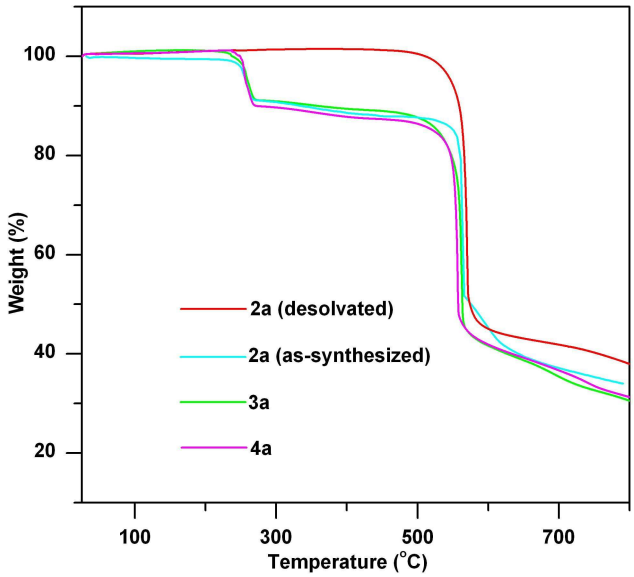

Figure 2.21 TG analyses of **2**-**4a** under N_2 atmosphere.

The TGA curve of **6a** (Figure 2.22) shows a five-step weight loss process. The first weight loss is 8.47 % from 145 to 300 °C, and the second step is 2.81 % from 300 to 370 °C, both assigned to the loss of two non-coordinated DMF molecules per formula unit (calcd. 9.79 %). The third (9.69 %), fourth (35.48 %), and fifth (21.06 %) weight loss steps may be due to decomposition of the compound.

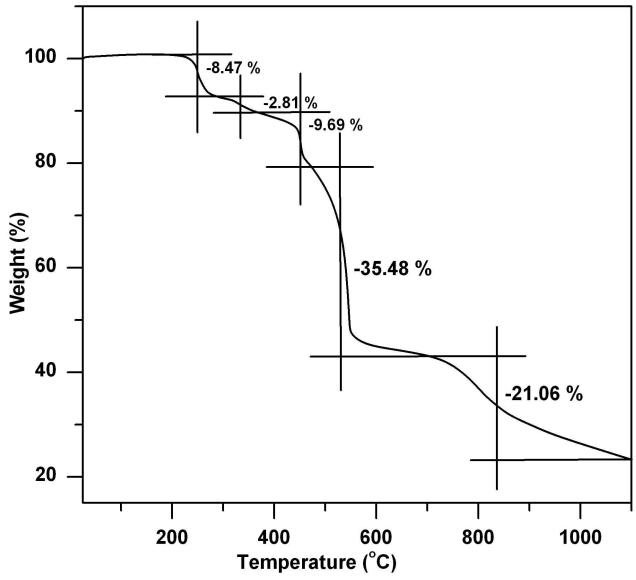

Figure 2.22 TG analysis of **6a** under N_2 atmosphere.

In the TGA curves of **2**-**6b** (Figure 2.23), the first weight loss steps (17.59 % for **2b**, 17.04 % for **3b**, 17.94 % for **4b**, 20.11 % for **5b**, and 17.82 % for **6b**) in the temperature range 150-400 °C are attributed to the removal of two occluded bromobenzene molecules per formula unit (calcd.: 18.92 % for **2b**, 19.02 % for **3b**, 18.99 % for **4b**, 18.99 % for **5b**, and 18.93 % for **6b**). All other weight loss steps which occur at a temperature above 400 °C can be assigned to the decomposition of these compounds.

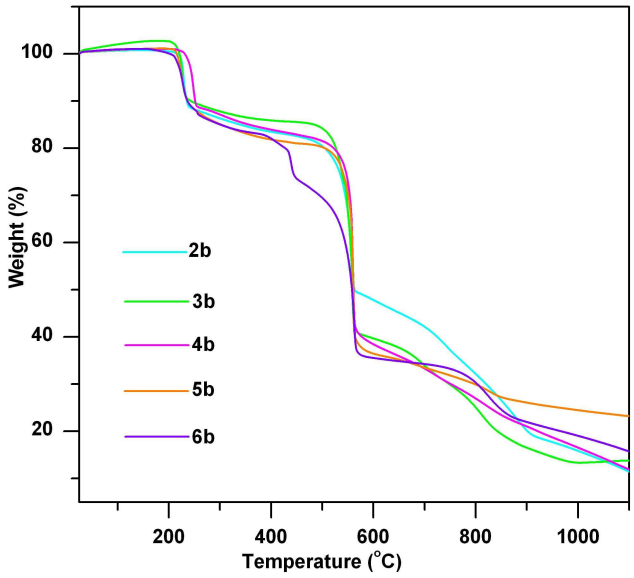

Figure 2.23 TG analyses of **2**-**6b** under N_2 atmosphere.

Infrared spectroscopy. The FT-IR spectra of all the compounds (Figures 2.24-2.26) described in this chapter show characteristic strong bands of the coordinated btaH and Me_2btaH ligand at *ca*. 1000 and 1200 cm^{-1} which are assigned to C-H out-of-plane bending vibrations, and vibrations involving both triazole ring breathing and C-H in-plane bending, respectively.[161] The FT-IR spectrum of **1** (Figure 2.24) is dominated by strong absorption attributable to the bidentate oxygen chelate, and contains strong absorption bands between *ca*. 1500 to 1600 cm^{-1} attributable to C=C and C=O stretching modes.[162] The IR spectra of all isostructural homo- and heteropentanuclear metal compounds having molecular formula $[MZn_4Cl_4(Me_2bta)_6]$ (M^{II} = Zn, Fe, Co, Ni, or Cu) are very similar, as expected. The occluded solvent molecules cause slight differences between the IR spectra of both set of compounds.

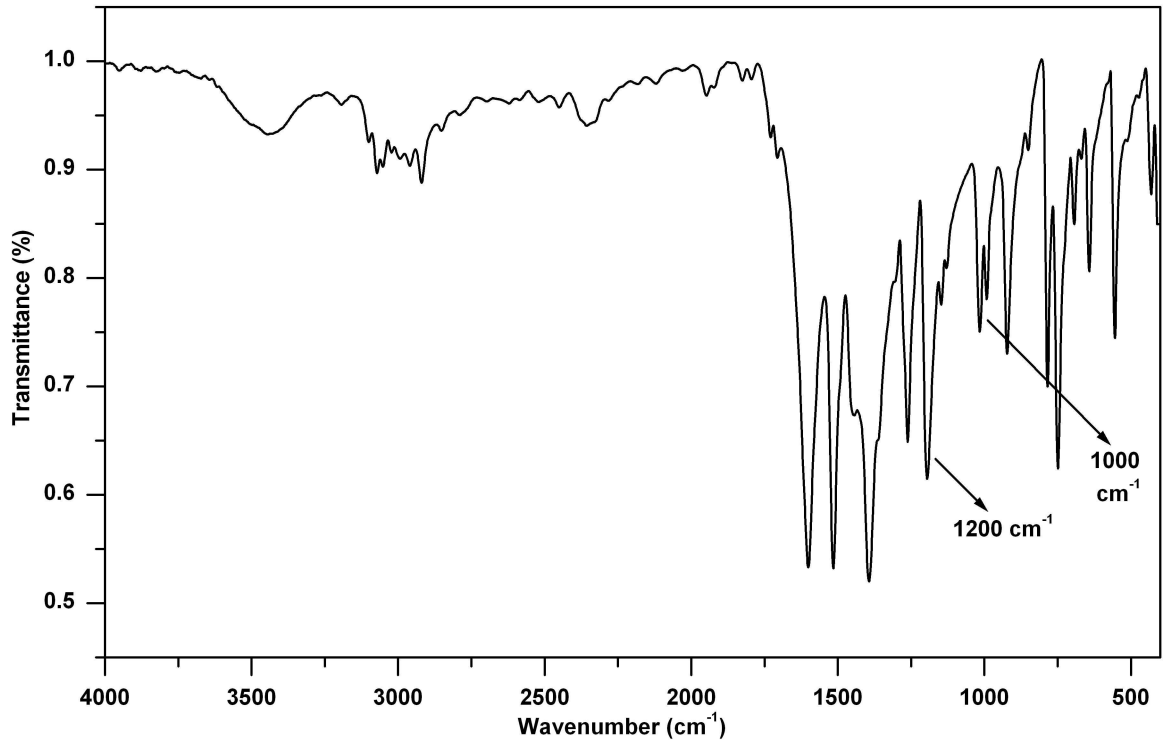

Figure 2.24 FT-IR spectrum of **1**.

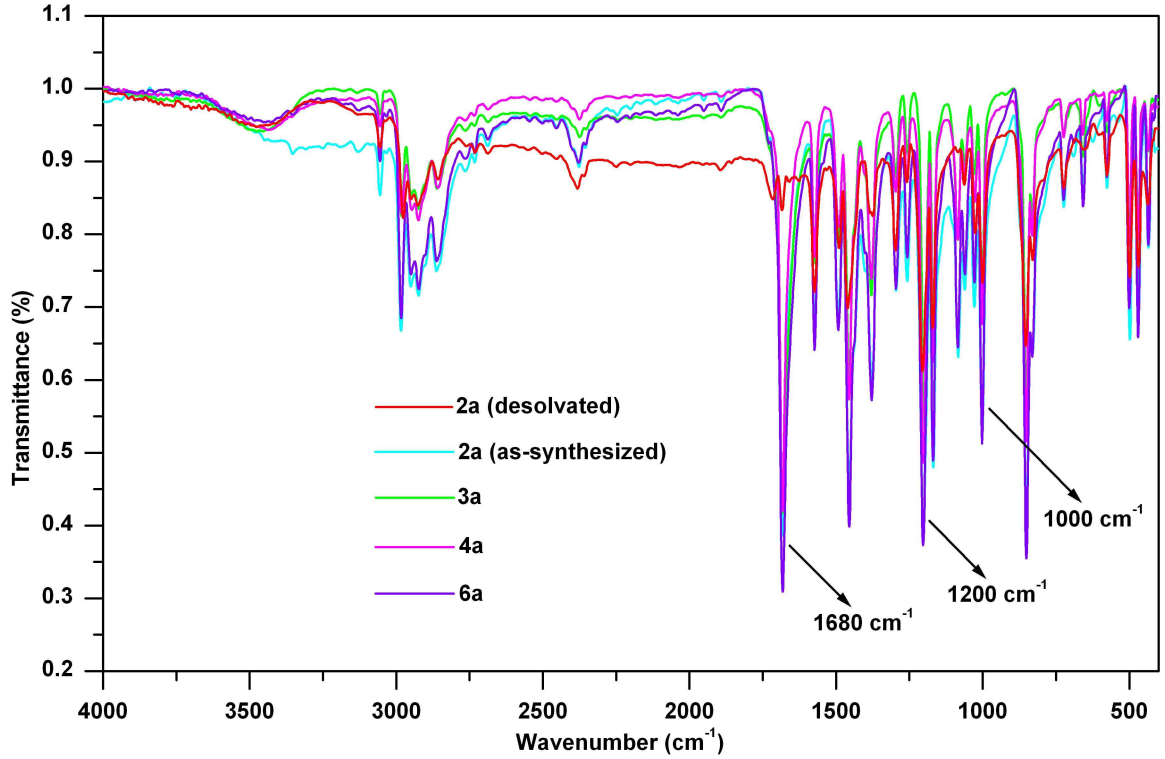

Figure 2.25 FT-IR spectra of **2a**, **3a**, **4a**, and **6a**.

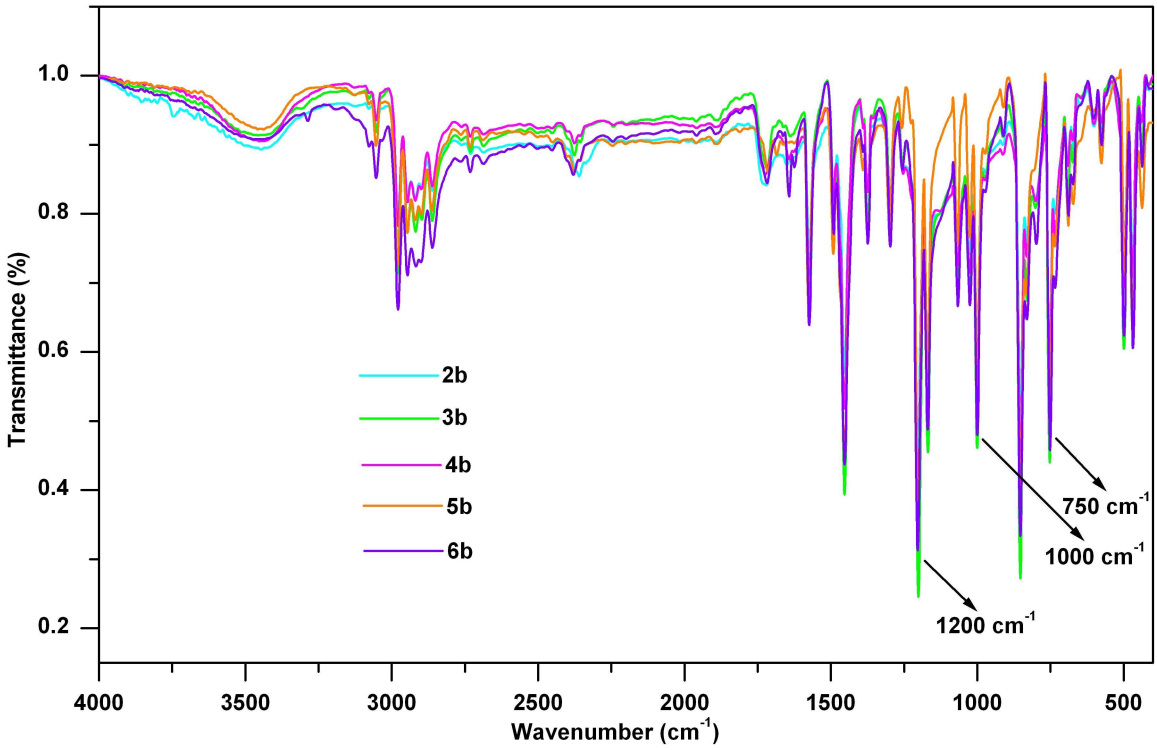

Figure 2.26 FT-IR spectra of **2-6b**.

The strong absorption band at *ca*. 1680 cm^{-1} in the IR spectra of the as-synthesized **2a**, **3a**, **4a**, and **6a** (Figure 2.25) is due to the C=O stretching frequency of non-coordinated DMF molecules. The intense infrared absorbance at *ca*. 750 cm^{-1} for **2-6b** (Figure 2.26) is attributed to the occluded bromobenzene molecules.[163] The occluded DMF molecules can be removed from the void regions of **2a** by heating at 200 °C under vacuum for 24 h. The absence of the strong absorption band at *ca*. 1680 cm^{-1} in the FT-IR spectrum of the fully desolvated sample of **2a** (Figure 2.26) confirms the complete removal of DMF molecules.

UV-Vis spectroscopy. The UV-Vis spectra of **3a-b**, **4a-b**, **5b**, and **6a-b** in ethylacetate solution display a common absorption band in the UV region at around 380 nm, which corresponds to the intraligand $n \rightarrow \pi^*$ transition.[164] In addition, all of these compounds exhibit well-developed bands in the range of 400–1100 nm (Figures 2.27a, 2.28a, 2.29a, and 2.30a) owing to the d–d transitions of Fe^{II}, Co^{II}, Ni^{II} and Cu^{II} ions.[165]

Compounds **3a-b**, which contain octahedrally coordinated Fe^{II} ions, display one broad absorption band in the region 700-1050 nm due to the spin-allowed transition from $^5T_{2g}$ to ^5E_g. The simple nature of the UV-Vis spectra of these two compounds indicates that Fe^{II} ions are in high-spin state inducing no tetragonal distortion in the compounds.

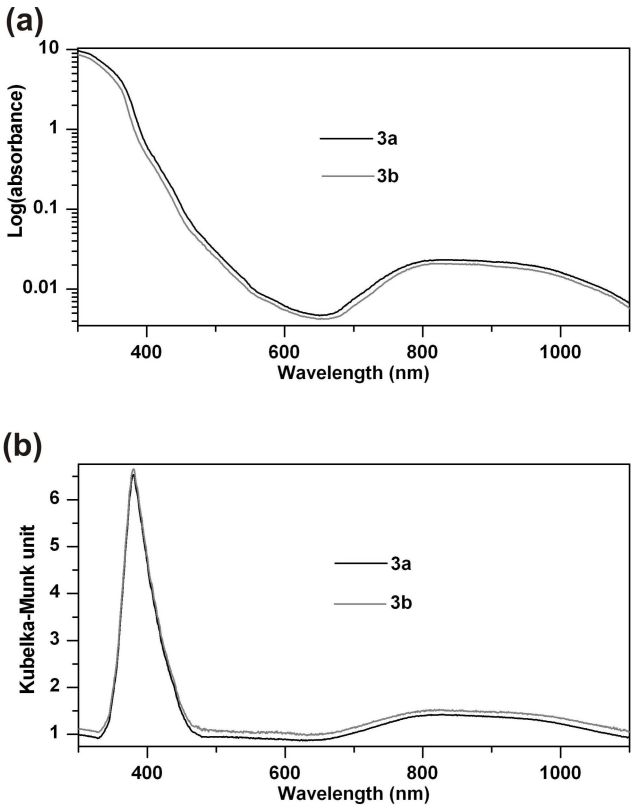

Figure 2.27 (a) UV-Vis spectra of **3a**-**b** in ethyl acetate solution. (b) UV-Vis diffuse reflectance spectra of **3a**-**b**.

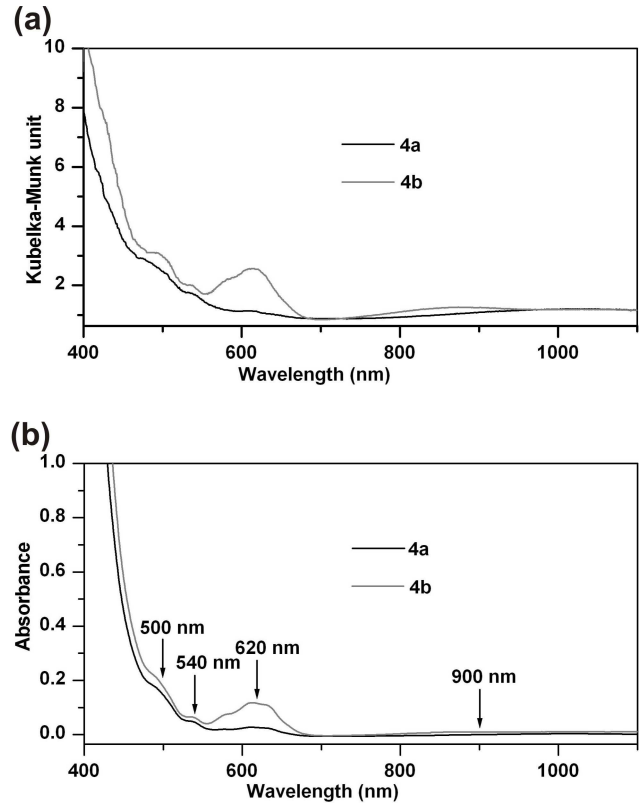

Figure 2.28 (a) UV-Vis spectra of **4a**-**b** in bromobenzene solution measured with the same concentration. (b) UV-Vis diffuse reflectance spectra of **4a**-**b**.

The octahedrally coordinated Co^{II} ions in **4a**-**b** show three absorption bands at 900, 540 and 500 nm, which can be attributed to the spin-allowed transitions from $^4T_{1g}(F)$ to $^4T_{2g}(F)$ (ν_1), $^4T_{1g}(P)$ (ν_2) and $^4A_{2g}$ (ν_3), respectively. The calculated values of *Dq* (1200 cm^{-1}) and *B* (665 cm^{-1}) from these transitions are comparable to those of other compounds with octahedrally coordinated Co^{II}.[165] In addition, **4b** shows a relatively stronger absorption band at 620 nm (with a shoulder at 575 nm), which is a typical position where tetrahedrally coordinated Co^{II} ions display strong absorption band due to the spin-allowed transition from $^4A_{2g}$ to $^4T_{1g}(P)$ (ν_3). This fact indicates that the fast precipitation method employed for the preparation of **4b** results in the formation of a (variable amount) of a coordination isomer of **4a**, in which some of the peripheral tetrahedrally coordinated sites are occupied by Co^{II} instead of Zn^{II} ions, along with the desired compound. The light greenish **4b** (Figure 2.2) is therefore a mixture of the 'pure' compound with orange color as **4a**, and and an isomeric compound showing the typical deep blue or purple color of compounds with tetrahedrally coordinated Co^{II}.

Compound **5b**, which contains an octahedrally coordinated Ni^{II} ion, exhibits three absorption bands at 980, 600 and 380 nm, which can be attributed to the spin-allowed transitions from $^3A_{2g}$ to $^3T_{2g}(F)$ (ν_1), $^3T_{1g}(F)$ (ν_2) and $^3T_{1g}(P)$ (ν_3), respectively. The ν_3 transition of **5b** is probably overlapped with the intraligand $n\rightarrow\pi^*$ transition. The values of *Dq* (1085 cm^{-1}) and *B* (775 cm^{-1}) which have been estimated from these transitions are typical for compounds with octahedrally coordinated Ni^{II}.[165]

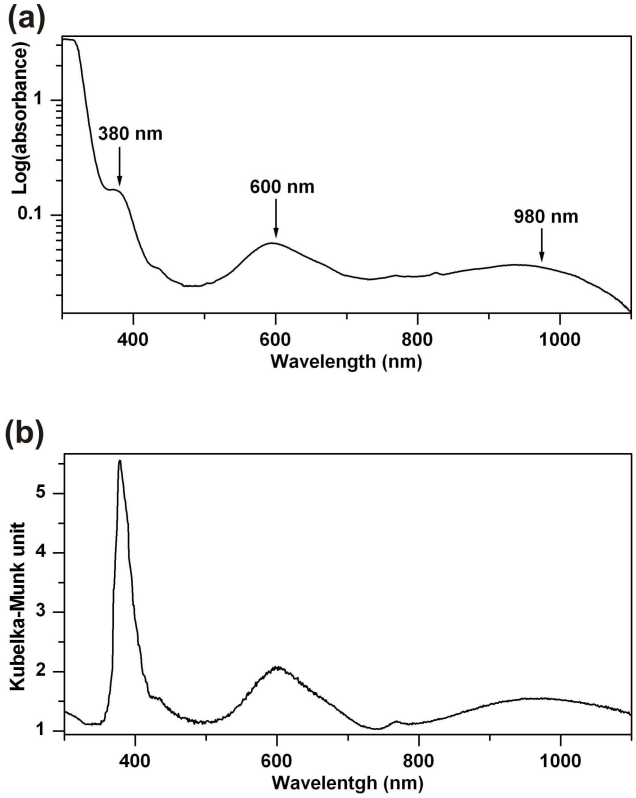

Figure 2.29 (a) UV-Vis spectrum of **5b** in ethyl acetate solution. (b) UV-Vis diffuse reflectance spectrum of **5b**.

The octahedrally coordinated Cu^{II} ions in **6a-b** show only one absorption band in the visible region at 700 nm, which is assigned to the spin allowed transition from ^2E_g to $^2T_{2g}$. The simple spectra of these type are typical for Cu^{II} compounds which exhibit $[CuN_6]$ octahedra without a significant Jahn-Teller distortion towards a tetragonally elongated octahedron.

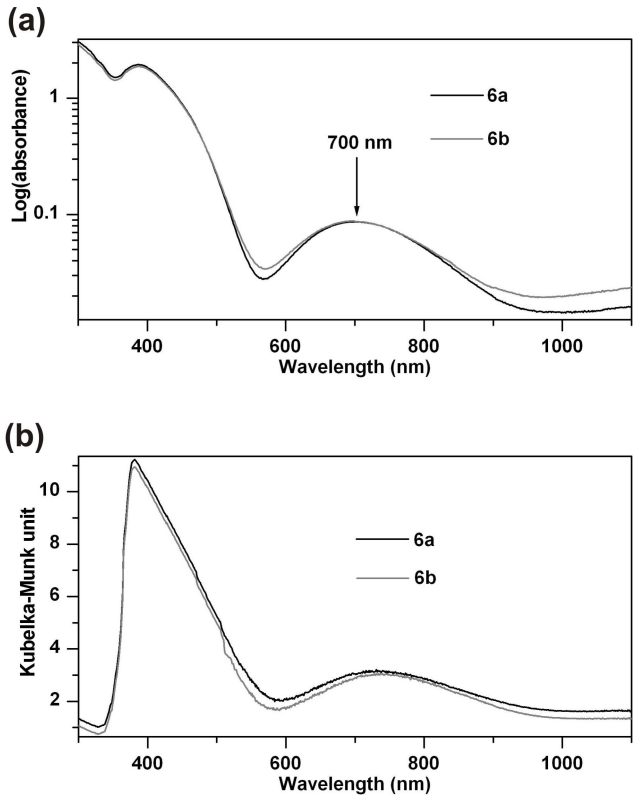

Figure 2.30 (a) UV-Vis spectra of **6a**-**b** in ethyl acetate solution. (b) UV-Vis diffuse reflectance spectra of **6a**-**b**.

The UV-Vis diffuse reflectance spectra (DRS) of **3a**-**b**, **4a**-**b**, **5b**, and **6a**-**b** (Figures 2.27b, 2.28b, 2.29b, and 2.30b) show similar absorption bands when compared to the solution UV-Vis spectra, which indicates that the compounds maintain their structural integrity in solution. These electronic spectral features of the compounds are consistent with their structural and magnetic characteristics.

Luminescence spectroscopy. Inspired by the strong fluorescence emissions of previously reported coordination polymers[166] and metal-organic frameworks[10d-e] containing zinc ions and benzotriazolate ligands, the luminescent properties of **2a**, **3a**, **4a**, **4b**, **5b**, and **6a** were investigated. As shown in Figure 2.31, free Me_2btaH ligand exhibits a broad fluorescence emission band centered at ~320 nm upon excitation at a wavelength of 280 nm. Because the emission bands of **2a**, **3a**, **4a**, **4b**, **5b**, and **6a** are similar to that of the free Me_2btaH ligand, it should be assigned to the intraligand $\pi \rightarrow \pi^*$ transition of the Me_2bta ligand.

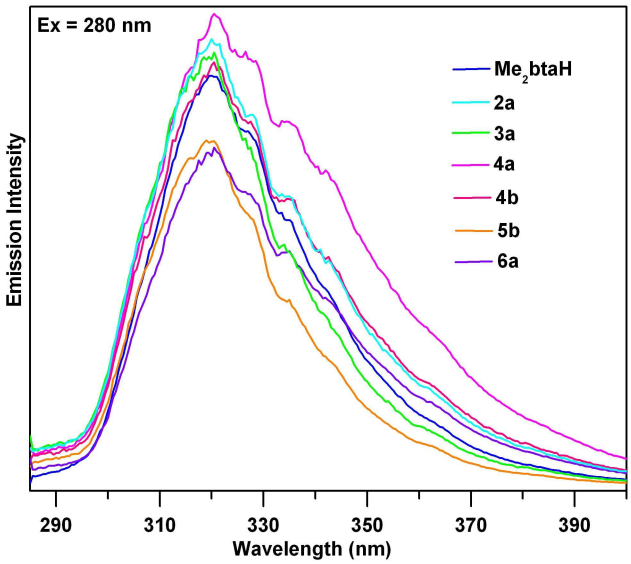

Figure 2.31 Room temperature photoluminescence spectra of **2a**, **3a**, **4a**, **4b**, **5b**, **6a**, and free Me_2btaH ligand in ethylacetate solution.

2.2.3 Structure Description

X-ray crystallographic analyses reveal that **1** crystallizes in the monoclinic space group $P2_1/c$, whereas **3a**, **4a-b**, **5b**, and **6a** crystallize in highly symmetrical space group $Fd\bar{3}m$. The molecular structures of all the pentanuclear compounds described in this chapter are displayed in Figure 2.32.

Each pentanuclear coordination compound is composed of a tetrahedral arrangement of four Zn^{II} ions surrounding a fifth hexacoordinate M^{II} ion (M = Zn, Fe, Co, Ni, or Cu) in the center. Each benzotriazolate ligand bonds to the central octahedrally coordinated metal ion through its nitrogen donor atom in the 2-position (N^2). Six nitrogen atoms from six benzotriazolate ligands therefore complete the coordination sphere of the central metal ion, while each Zn^{II} ion in the apical positions is coordinated by three nitrogen atoms from three benzotriazolate ligands and one acetylacetonate ligand (for **1**) or chlorine atom (for **3a**, **4a-b**, **5b**, and **6a**).

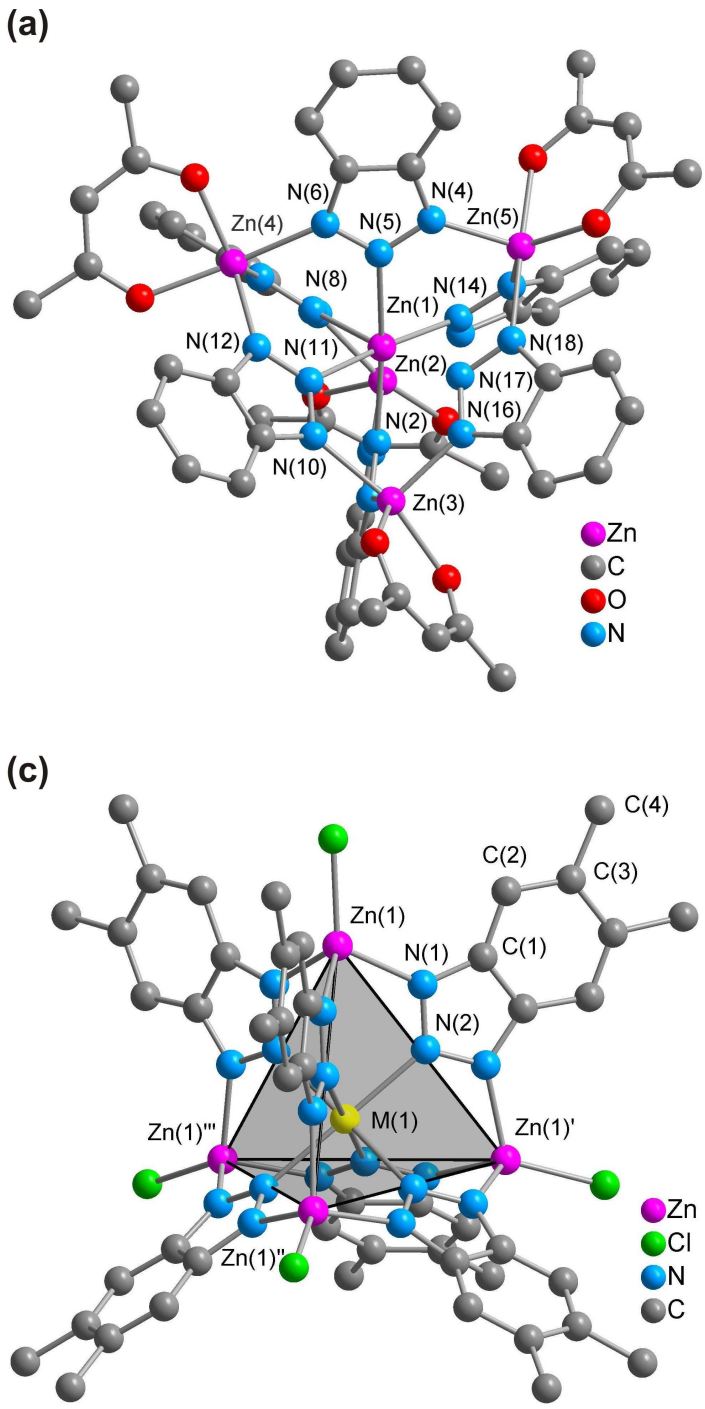

Figure 2.32 Ball-and-stick representation of the molecular structures of (a) **1**, and (b) **2a**, **3a**, **4a-b**, **5b**, and **6a** (M = Zn, **2a**; Fe, **3a**; Co, **4a-b**; Ni, **5b**; Cu, **6a**). All hydrogen atoms are omitted for clarity. Symmetry operators used to create equivalent atoms are ('): 1/4-x, 1/4-y, z; (''): 1/4-x, y, 5/4-z; ('''): x, 1/4-y, 5/4-z. For **2a**, the labels 'Zn(1)' should be replaced by 'Zn(2)' to compare its bond lengths and angles with other compounds.

Therefore, the peripheral zinc atoms in **1** are pentacoordinated due to the bidentate acetylacetonate ligand, whereas those are tetracoordinated in **2a**, **3a**, **4a-b**, **5b**, and **6a** due to the monodentate chloride ligand, leading to a distorted tetrahedral coordination environment.

In **1**, the coordination of acetylacetonate ligand to the peripheral zinc ions leads to a reduction of molecular symmetry (C_1 instead of T_d) since the local five-fold coordination motif of the peripheral zinc ions is incompatible with the high local symmetry of the $[Zn_5(bta)_6]^{4+}$ coordination unit. Using monodentate chloride ligands, the pentanuclear coordination units in **3a**, **4a-b**, **5b**, and **6a** assume T_d point group symmetry. Noteworthingly, the atoms of **3a**, **4a-b**, **5b**, and **6a** occupy special positions within the crystal lattice, such that the asymmetric unit (Figure 2.33) in the cubic space group $Fd\bar{3}m$ contains only the minimum subset (= 9) of atoms required for a complete representation of a pentanuclear metal compound containing six Me_2bta ligands (75 atoms for each compound, excluding hydrogen atoms). On the other hand, the asymmetric unit in **1** possesses one whole molecule with 111 atoms, excluding hydrogen atoms. It should be noted that the η^1:η^1:η^1:μ_3 coordination mode of benzotriazolate ligands observed in the present compounds was previously documented for a wide variety of coordination compounds and coordination polymers containing Zn(II),[10] Co(II),[10b-c,11] Ni(II),[10b,11a,12] Cu(II),[9,13] Tl(I),[14] M(III)[15] (M = Fe, Cr, V) ions, including two mixed-valent copper[16] compounds.

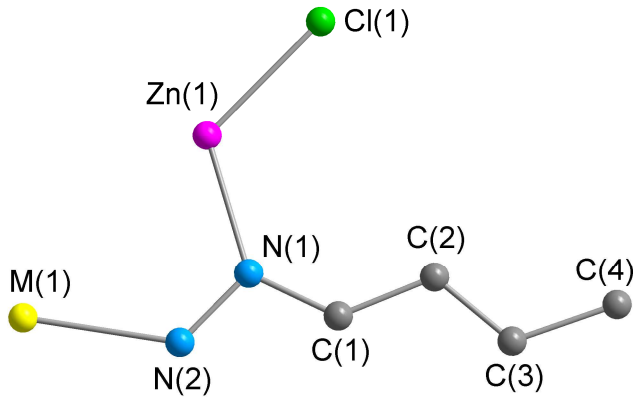

Figure 2.33 Ball-and-stick representation of the asymmetric units of **2a**, **3a**, **4a-b**, **5b**, and **6a** (M = Zn, **1a**; Fe, **2a**; Co, **3a-b**; Ni, **4b**; Cu, **5a**). Hydrogen atoms and solvent molecules are omitted for clarity.

For all the homo- and heteropentanuclear compounds, selected bond lengths and bond angles obtained from single crystal X-ray diffraction data are summarized in Tables 2.4 and 2.5. In **2a**, **3a**, **4a-b**, **5b**, and **6a**, the Zn(1)-N(1) distances for the tetrahedrally coordinated, peripheral zinc atoms are in a narrow range range of 2.00-2.02 Å. Compared to **2a**, **3a**, **4a-b**, **5b**, and **6a**, the average Zn-N distance (2.07 Å) for the four tetrahedral zinc atoms in **1** is slightly larger due to the binding of the bidentate acetylacetonate ligand. In **2a**, **3a**, **4a-b**, **5b**, and **6a**, the M(1)-N(2) (M = Zn, **1a**; Fe, **2a**; Co, **3b**; Ni, **4b**; Cu, **5a**) distances for the octahedrally

coordinated, central metal (M) atoms lie in a relatively larger range of 2.14-2.20 Å. The Zn-N distances for the octahedral Zn atoms in **1** fall in a significantly larger range (2.02-2.22) compared to that of **2a**, **3a**, **4a**-**b**, **5b**, and **6a**. All these values are in agreement with literature data (1.98-2.16 Å for tetrahedrally coordinated[10a,10f] Zn and 1.98-2.47 Å for octahedrally coordinated[10a,10f,11a,12,13] Zn, Co, Ni or Cu) reported for structurally related metal(II) triazolate compounds. The M(1)-N(2) distances in **2a**, **3a**, **4a**-**b**, **5b**, and **6a** decrease with increasing atomic number (from M = Fe (**2a**) to Cu (**5a**)), a trend that is expected for high-spin transition metal ions.

In **2a**, **3a**, **4a**-**b**, **5b**, and **6a**, the N(2)-M(1)-N(2) angles for the central metal atoms do not deviate from right (90°) and straight (180.0°) angles due to the special crystallographic positions of these atoms, leading to a perfect octahedral environment around these metal atoms. Effected by the highly symmetric space group, the M(1)-N(2) distances for the central metal atoms are same, also indicating the presence of no tetragonal distortion in any of these compounds, as supported by the UV-Vis spectroscopic and magnetic studies. It is worth noting that considerable deviations from the ideal octahedral coordination have been observed in **1** and few structurally related[13,16] copper compounds owing to the Jahn-Teller effect. In **1**, the tetragonal distortion is reflected in the difference among the various Zn-N distances for the octahedral Zn atoms. This distortion in **1** also causes the N-Zn-N angles for the octahedral Zn atoms to deviate from right (90°) and straight angles (180°).

Table 2.4 Selected bond lengths (Å) and angles (°) of **1**.

Zn(1)-N(14)	2.159(3)	Zn(3)-N(16)	2.017(3)
Zn(1)-N(8)	2.177(3)	Zn(3)-N(3)	2.034(3)
Zn(1)-N(11)	2.187(3)	Zn(3)-N(10)	2.131(3)
Zn(1)-N(17)	2.203(3)	Zn(4)-N(12)	2.025(3)
Zn(1)-N(5)	2.210(3)	Zn(4)-N(7)	2.081(3)
Zn(1)-N(2)	2.221(3)	Zn(4)-N(6)	2.131(4)
Zn(2)-N(1)	2.074(4)	Zn(5)-N(13)	2.015(3)
Zn(2)-N(9)	2.022(3)	Zn(5)-N(4)	2.042(4)
Zn(2)-N(15)	2.100(3)	Zn(5)-N(18)	2.158(3)
N(14)-Zn(1)-N(11)	173.33(12)	N(8)-Zn(1)-N(5)	87.12(12)
N(8)-Zn(1)-N(17)	174.53(12)	N(11)-Zn(1)-N(5)	90.79(12)
N(5)-Zn(1)-N(2)	176.34(13)	N(17)-Zn(1)-N(5)	87.51(12)
N(14)-Zn(1)-N(8)	90.63(13)	N(14)-Zn(1)-N(2)	87.57(12)

N(8)-Zn(1)-N(11)	92.48(12)	N(8)-Zn(1)-N(2)	90.54(13)
N(14)-Zn(1)-N(17)	88.85(13)	N(11)-Zn(1)-N(2)	86.50(12)
N(11)-Zn(1)-N(17)	88.62(13)	N(17)-Zn(1)-N(2)	94.88(12)
N(14)-Zn(1)-N(5)	95.26(13)		

Table 2.5[a] Selected bond lengths (Å) of **2a**, **3a**, **4a**-**b**, **5b** and **6a**.

Compound	**2a**	**3a**	**4a**	**4b**	**5b**	**6a**
	M = Zn	M = Fe	M = Co	M = Co	M = Ni	M = Cu
Zn(1)-N(1)	2.024(5)	2.022(5)	2.022(5)	2.016(3)	2.009(2)	2.014(7)
M(1)-N(2)	2.183(7)	2.198(8)	2.177(8)	2.178(4)	2.156(3)	2.140(10)
Zn(1)-Cl(1)	2.174(3)	2.168(3)	2.169(3)	2.181(2)	2.1803(15)	2.161(4)
N(1)-N(2)	1.346(7)	1.345(7)	1.348(7)	1.335(3)	1.333(3)	1.352(9)
N(1)-C(1)	1.345(8)	1.341(9)	1.331(8)	1.353(4)	1.357(4)	1.323(11)
C(1)-C(2)	1.414(9)	1.417(10)	1.422(9)	1.412(5)	1.414(4)	1.421(14)
C(2)-C(3)	1.394(9)	1.389(10)	1.393(10)	1.369(5)	1.370(5)	1.411(14)
C(3)-C(4)	1.496(8)	1.491(10)	1.489(10)	1.514(5)	1.509(5)	1.472(14)

[a] Except for **5b** (296 K), single crystal X-ray diffraction data were recorded at T = 293 K. For **2a**, 'Zn(1)' should be replaced with 'Zn(2)'.

Compound **1** (Figure 2.34a) pack in a completely different way in the crystal lattice than **2a**, **3a**, **4a**-**b**, **5b**, and **6a** (Figure 2.34b). The different occluded solvent molecules and terminally coordinated anions are responsible for this difference in packing. However, each set of compounds having either DMF or bromobenzene as occluded solvent molecules show identical packing arrangements in the crystal lattices. The positions of the occluded cyclohexane molecules in **1** and the non-coordinated bromobenzene molecules in **4b** and **5b** can be unequivocally determined from single crystal X-ray data. However, the occluded DMF molecules in **2a**, **3a**, **4a**, and **5a** are highly disordered, thus it was impossible to refine their positions from the electron density distribution obtained from X-ray diffraction data, even with reduction of crystallographic symmetry. Void estimation for **2a**, **3a**, **4a**, and **6a** with PLATON/SQUEEZE[167] reveals that the average potentially accessible void volume per unit cell volume is 22 % and every unit cell contains 16 voids (in which the remaining, unmodeled electron density is located). Each of these voids possesses an average volume of 152.5 $Å^3$ and might contain a DMF molecule having a volume of 129 $Å^3$ (calculated from the mass and density of DMF at room temperature). This value is equivalent to two DMF molecules per

formula unit, in accordance with the TGA and elemental analysis. Figure 2.34b illustrates the possible void regions in **2a** which are occupied by non-coordinated DMF molecules.

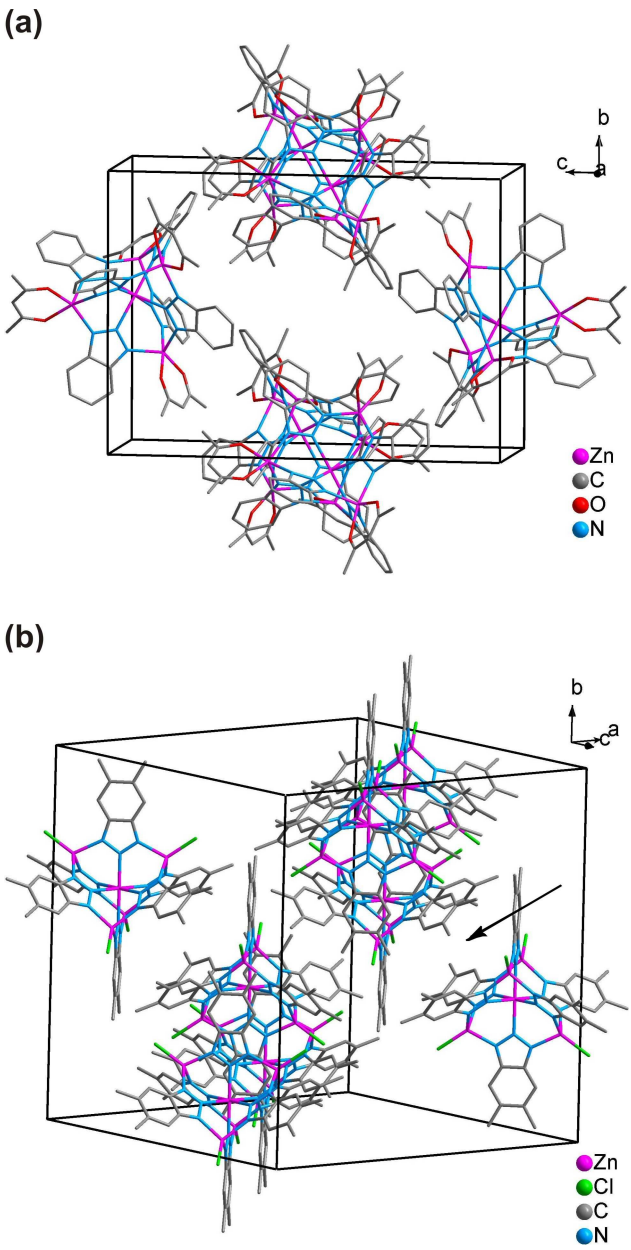

Figure 2.34 Crystal packing diagram of **1** (a) and **2a** (b) wire representation. The black arrow points to a void region in the crystal lattice of **2a** that contains a DMF molecule. All hydrogen atoms and and occluded cyclohexane molecules (**1**) are omitted for clarity.

2.2.4 Magnetic Properties

The magnetism of **3a**, **4a**, **5b**, and **6a** is dominated by the single-ion effects of the central open-shell 3d ions residing in a crystallographically O_h-symmetric [MN_6] environment, as intermolecular exchange or dipole-dipole coupling is expected to be low. Both low-field and

field-dependent susceptibilities were modeled using the computational framework CONDON, adopting a spin Hamiltonian that incorporates all relevant single-ion effects: interelectronic repulsion (H_{ee}), spin-orbit coupling (H_{so}), ligand-field effect (H_{lf}), and Zeeman effect of the applied external field (H_{mag}) (eq. 1).[168] The exchange interactions between neighboring molecules in the solid-state lattices are described using a molecular field approximation, eq. 2, where χ'_m represents the single-ion susceptibility contribution and λ_{MF} the molecular field parameter (positive and negative values of λ_{MF} correlate with ferromagnetic and antiferromagnetic interactions, respectively).

$$\hat{H} = H_{ee} + H_{lf} + H_{so} + H_{mag} \qquad (1)$$

$$\chi_m^{-1} = \chi'^{-1}_m \left(B, C, \varsigma, B_q^k, J_{ex}\right) - \lambda_{MF} \qquad (2)$$

The parameterization of the octahedral ligand-field requires the ligand-field parameter B^4_0. The corresponding ligand-field operator with reference to the fourfold rotation axis for the angular part of the wave function then becomes

$$H_{lf}^{cub} = +B_0^4 \sum_{i=1}^{N} C_0^4(i) + B_4^4 \sum_{i=1}^{N} \left(C_4^4(i) + C_{-4}^4(i)\right)$$

Since in a cubic system a fixed relation $B_4^4 = \sqrt{5/14}\, B_0^4$ exists, only the coefficient B^4_0 is essential.[169]

The high-spin Fe(II) (d^6) compound **3a** and the Co(II) (d^7) compound **4a** display a continuous decrease in the effective magnetic moment (**3a**: from 5.77 at 290.0 K; **4a**: from 5.03 at 290.0 K) towards low temperatures (Figures 2.35 and 2.36). The effective magnetic moment of the cobalt(II) compound **4a** at room temperature is slightly smaller than the value resulting for both spin and orbital momentum ($\mu_{LS} = \sqrt{L(L+1) + 4S(S+1)} = 5.20$). For octahedral high-spin Co(II) complexes (S = 3/2) in magnetically dilute systems, μ_{eff} values in the range 4 – 5 are expected as a result of spin and first-order orbital contributions.

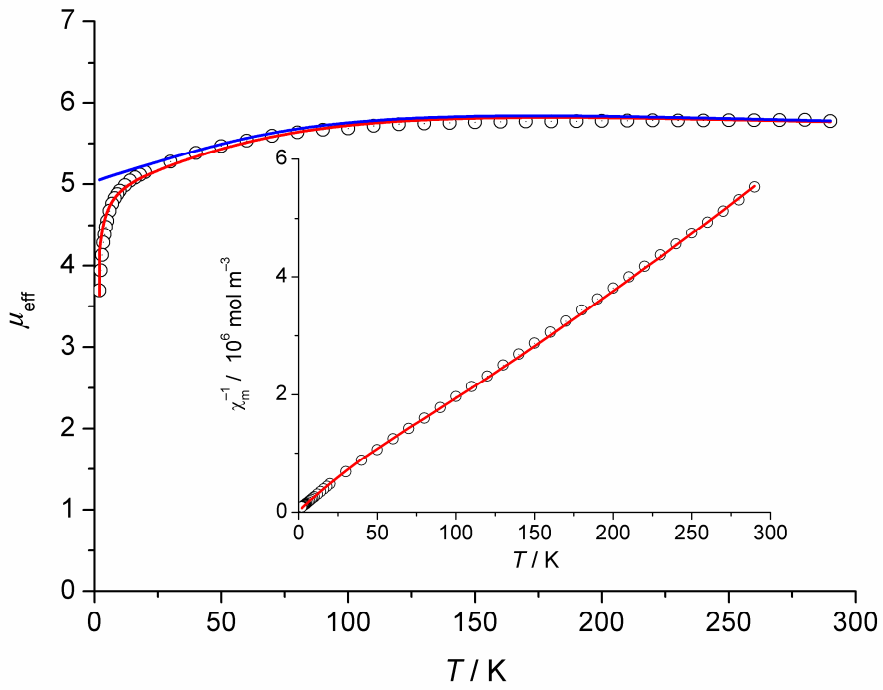

Figure 2.35 Temperature-dependence of the effective magnetic moment μ_{eff} for **3a** at B_0 = 0.1 T. Inset: reciprocal susceptibility at B_0 = 0.1 T. Experimental data: circles, least-squares fit to model Hamiltonian (see text): red line, single-ion effects (without intermolecular coupling): blue line.

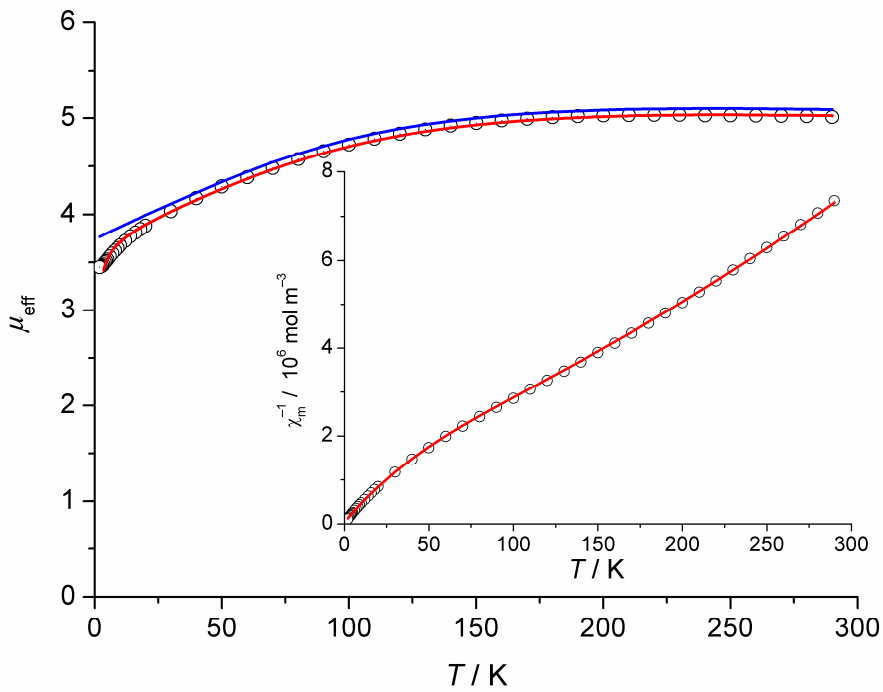

Figure 2.36 μ_{eff} vs. T for **4a** at B_0 = 0.1 T. Inset: reciprocal susceptibility at B_0 = 0.1 T. Experimental data: circles, least-squares fit to model Hamiltonian (see text): red line, single-ion effects (without intermolecular coupling): blue line.

The Ni(II) (d^8) compound **5b** exhibits nearly temperature-independent μ_{eff} *vs.* *T* behavior (Figure 2.37) due to a ligand-field ground state derived from the cubic term $^3A_2$.[170] The effective magnetic moment of **5b** at 290.0 K of 3.16 is larger than the spin-only value 2.87 μ_B, as a result of mixing excited terms into the ground state $^3A_2$ via spin-orbit coupling, which also explains the expected range for octahedral high-spin Ni(II) complexes (S = 1) of 2.8 – 3.5 μ_B.[171] The susceptibility data display Curie law behavior in the temperature range 20 to 300 K with a Curie constant $C = 1.569 \times 10^{-5}$ m^3 K mol^{-1} (μ_{eff} = 3.16) in very good agreement with the expected value for an isolated paramagnetic Ni^{2+} ion in an octahedral coordination environment. The Brillouin fit to the field-dependent magnetization M(H) at 2.0 K with S = 1 (Figure 2.37, left inset) yields g = 2.20, which corresponds to the μ_{eff} value at room temperature.

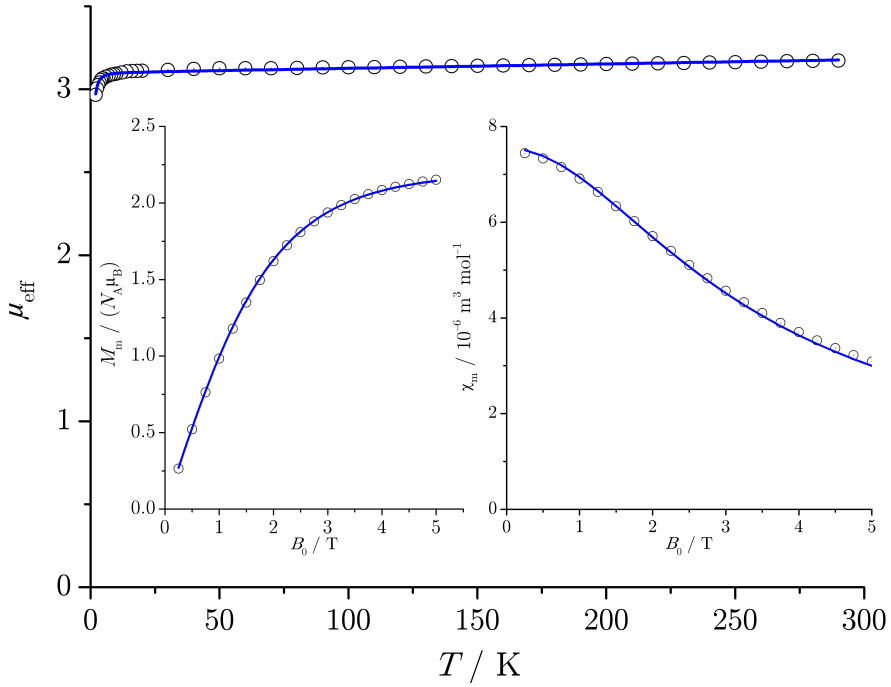

Figure 2.37 μ_{eff} vs. *T* for **5b** at B_0 = 0.1 T. Insets: *M* vs. B_0 (left) and χ_m *vs.* B_0 (right) at 2.0 K. Experimental data: circles, least-squares fit to model Hamiltonian (see text): blue line.

The Cu(II) (d^9) compound **6a** exhibits a virtually temperature-independent effective magnetic moment μ_{eff} = 1.98, and only marginally decreases towards 2 K. However, the appearance of a spin-only system (Figure 2.38) is caused by the counteracting effects of the ligand-field effect and the spin-orbit coupling in this particular system.

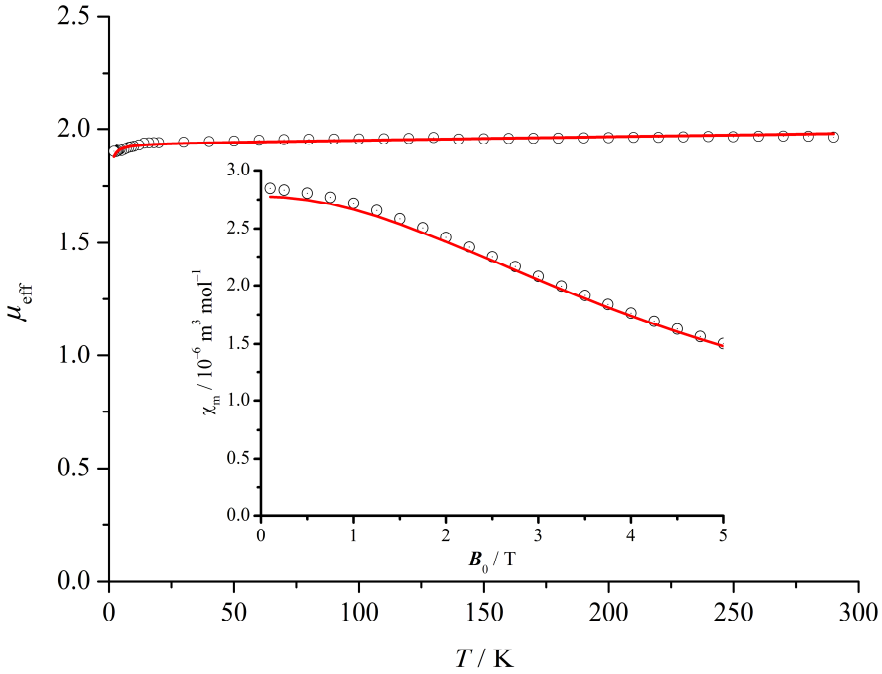

Figure 2.38 μ_{eff} vs. T for **6a** at B_0 = 0.1 T. Inset: χ_m *vs.* B_0 at 2.0 K. Experimental data: circles, least-squares fit to model Hamiltonian (see text): red line.

It is worth noting that the ligand-field parameters (Table 2.6) resulting from the least-squares fits for **3a**, **4a**, **5b**, and **6a** are in overall good agreement with the ligand-field splitting parameters obtained from UV-Vis spectroscopy.

Table 2.6 Magnetochemical analysis parameters for **3a**, **4a**, **5b**, and **6a**.

Compound	**3a** M = Fe(II)	**4a** M = Co(II)	**5b** M = Ni(II)	**6a** M = Cu(II)
B / cm^{-1} (C = 4B)	806	765	715	—
ζ / cm^{-1}	420	475	649	820
Dq / cm^{-1} [a]	1140	1200	1085	1430
B_0^4 / cm^{-1}	27300	28700	20800	30100
λ_{MF} / 10^5 m^{-3} mol	–0.233	–0.350	— [b]	–0.2137
θ / K [c]	–2	—	—	–2
SQ / % [d]	1.2	1.5	0.6	0.6

[a] Experimental ligand-field splitting parameter (Dq) from UV-Vis spectroscopy; $B_0^4 = 21 \times Dq$.

[b] Addition of the molecular field parameter as a free variable to a least-squares fit did not yield a better fit.

[c] Value of Weiss temperature in a spin-only Curie-Weiss description corresponding to λ_{MF}.

[d] $SQ = \sqrt{\sum_{i=1}^{n}([\chi_{obs}(i) - \chi_{cal}(i)]/\chi_{obs}(i))^2}$.

2.2.5 Graph Theoretical Representation

The justification to represent the molecular constitution of $[MZn_4X_4(L)_6]$ coordination units by means of a nonplanar graph arises from graph theoretical considerations[172] that prove that these coordination units contain the $K_{3,3}$ graph. In mathematical graph theory, any graph can be classified as planar (those which can be drawn on a plan so that no two edges intersect except at a vertex) or nonplanar (when this can not be done). The mathematician Casimir Kuratowski was the first to note that all nonplanar graphs contain one of only two basic non-planar graphs as a subgraph: K_5 (the complete graph on five vertices) and $K_{3,3}$ (the complete, bipartite graph on six vertices, three of which connect to each of the other three).[173] As shown in Figure 2.39, the molecular graph of $[MZn_4X_4(L)_6]$ coordination units in fact contain a subgraph of $K_{3,3}$. Accordingly, there is no way to represent $[MZn_4X_4(L)_6]$ coordination units as a planar graph and thus the pseudo-perspective representation shown in Figure 2.1d seems to be most appropriate for this and related[9,10a,10f,11a,12,13,16] type of coordination compounds.

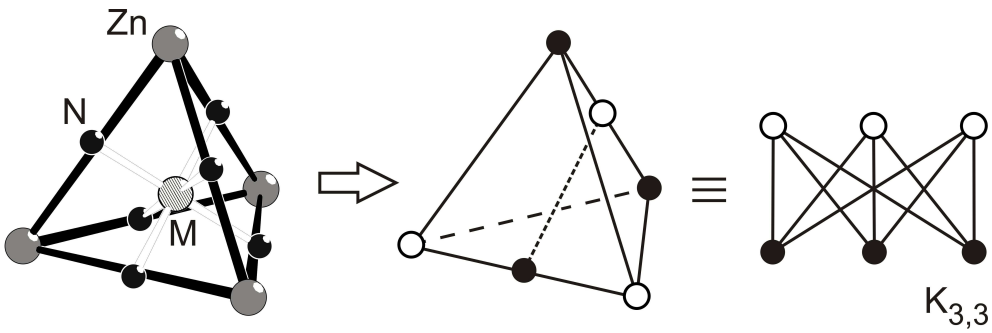

Figure 2.39 Formal derivation of the $K_{3,3}$ graph which can be used to represent the connectivity scheme in coordination units of type $[MZn_4X_4(L)_6]$. The schemes follow recommendations as described in ref. 175(l).

The graph theoretical representation of the present coordination compounds is interesting in view of the fact that topologically nonplanar molecules are extremely rare in both organic and inorganic chemistry. The molecular graphs of several centrohexacyclic organic (*e.g.*, a centrohexaquinane known as the "Simmons-Paquette molecule",[174] Kuck's centrohexaindanes,[175] and few ferrocenophanes[176]), metal-organic (*e.g.*, centrohexasexanes such as basic zinc[156] or beryllium[157] carboxylates and related[177] compounds) and inorganic

(*e.g.*, centrohexaquadranes such as mixed metal-sulfur cluster anions[178]) species can be reduced to the first Kuratowski graph, K_5. Molecules corresponding to the second Kuratowski graph, $K_{3,3}$ have remained even more scarce than those represented by K_5 graphs. The "Kuratowski cyclophane",[179] Walba's three-rung molecular Möbius ladder[180] Otsubo's triple-layered naphthalenophane,[181] a Co^{III} sepulchrate compound[182] and the recently synthesized cyclohexamantane[183] are among the few molecules with nonplanar $K_{3,3}$ topology. The molecular graphs of polynuclear metal carbonyl carbide clusters[184] and several other[185] molecules are reducible to either K_5 and $K_{3,3}$ graphs by suitable deletions or contractions and hence, may be considered as topologically nonplanar.

From topological point of view, all the above mentioned organic, metal-organic or inorganic centrohexacyclic compounds are isostructural to the coordination units of **MOF-5** and **MFU-1** type of frameworks. Focusing only on the metal-organic compounds, the coordination units $[MZn_4X_4(L)_6]$ and the basic Zn or Be carboxylates represent the only two classes of minimum nonplanar coordination units having T_d point group symmetry, from which highly regular 3D porous frameworks can be constructed in a predictable and systematic fashion (see Figure 2.40). Therefore, it can be safely predicted that the chemistry of such coordination units and their integration into MOF networks will develop rapidly in the near future. Moreover, and in sharp contrast with the molecular coordination units featured by **MOF-5**, **MFU-1** and related networks, the present coordination units are likewise stable and can be easily prepared at a multi-gram scale, which opens up possibilities for rational systematic design of the corresponding frameworks as well as for optimization of their functional properties. Notably, the Kuratowski-type of $K_{3,3}$ nodes in **MFU-4** type of frameworks are interconnected with the planar organic linkers in a streochemically-defined manner. In contrast, the K_5 nodes are cross-linked via single-bonded type of linkages, leading to extensive formation of supramolecular isomers of the same basic framework topology.

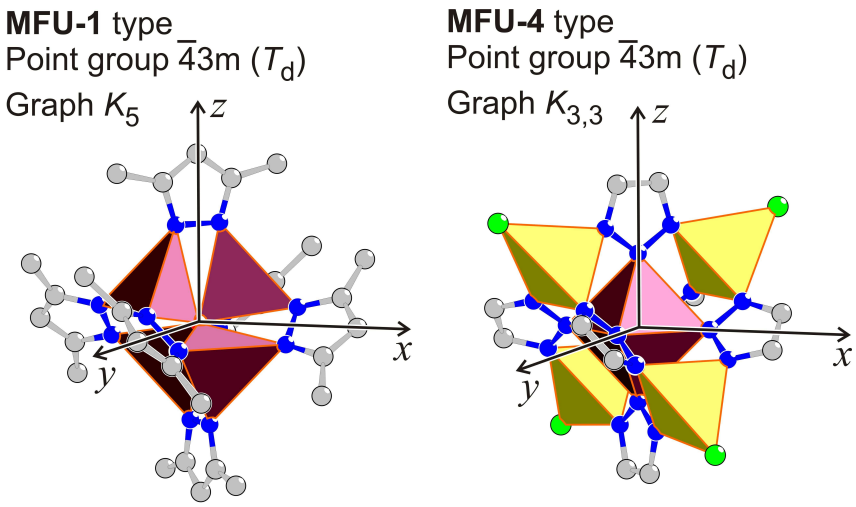

Figure 2.40 Comparative structural features of the coordination units found in **MFU-1** (left) and **MFU-4** (right) (C: grey, N: blue, Cl: green, Zn: yellow, redox-active metal centres M: pink).

2.3 Experimental Section

2.3.1 Materials and General Methods

All starting materials were of reagent grade and used as received from the commercial supplier. Fourier transform infrared (FT-IR) spectra were recorded from KBr pellets in the range 4000–400 cm^{-1} on a Bruker IFS FT-IR spectrometer. The following indications are used to characterize absorption bands: very strong (vs), strong (s), medium (m), weak (w), shoulder (sh), and broad (br). UV-Vis diffuse reflectance spectra (DRS) were recorded on an Analytik Jena Specord 50 UV-Vis spectrometer in the range of 300-1100 nm and converted into normal absorption spectra with the Kubelka–Munk function.[186] The lamps change at 320 nm and the mirrors change at 370, 400, 700 and 900 nm. UV-Vis spectra in solution were measured using the same UV-Vis spectrometer. Elemental analyses (C, H, N) were carried out on a Perkin-Elmer 2400 Elemental Analyzer. Thermogravimetric analyses (TGA) were performed with a TGA/SDTA851 Mettler Toledo analyzer in a temperature range of 25–1100 °C in flowing nitrogen at a heating rate of 10 °C min^{-1}. Ambient temperature X-ray powder diffraction (XRPD) patterns were measured using a Philips X′Pert PRO powder diffractometer operated at 40 kV, 40 mA for Cu target (λ = 1.5406 Å) with a scan speed of 30 s $step^{-1}$ and a step size of 0.008°. The simulated powder patterns were calculated using single crystal X-ray diffraction data. Energy dispersive X-ray analyses (EDX) were performed on an EDAX (Phönix) X-ray detection system with 30 mm^2 SUTW window. ICP-AES analyses

were carried out with a Thermo Scientific iCap 6500 emission spectrometer. TOF-MS analyses were performed with a JMS-T100GCV time-of-flight mass spectrometer (TOF-MS) and a liquid injection field desorption ionization (LIFDI) source. Fluorescence emission spectra in ethylacetate solution were collected on a Perkin-Elmer LS 55 luminescence spectrometer in the 285-555 nm region at room temperature using an excitation wavelength of 280 nm. Magnetic susceptibility data of compounds **3a**, **4a**, **5b**, and **6a** were determined using a SQUID magnetometer (Quantum Design MPMS-XL5) in the temperature range T = 2.0 to 290 K and at an applied field of B_0 = 0.1 to 5.0 T. Susceptibility data were corrected for sample holder (PTFE capsules) and diamagnetic contributions. The latter was determined from measurement of the diamagnetic compound **2a**, and used as the uniform value χ_{dia} = 0.981×10^{-8} m^3 mol^{-1} for **3a**, **4a**, **5b**, and **6a**.

Safety Note! Perchlorate salts and benzotriazolate compounds are potentially explosive, and caution should be exercised when dealing with such materials. However, the small quantities used in this study were not found to present a hazard.

2.3.2 Syntheses

Synthesis of $[Zn_5(acac)_4(bta)_6]\cdot 4C_6H_{12}$ (1). To a suspension of $Zn(acac)_2$ (0.26 g, 1.00 mmol) in 70 mL dichloromethane was added a solution of btaH (0.143 g, 1.20 mmol) in 10 mL dichloromethane. The mixture becomes clear within 5 minutes of stirring at room temperature. Stirring was continued for 1 h and the solution was kept at room temperature in an open vial. After evaporation of the solvent, the residue (0.28 g) was dissolved in cyclohexane (25 mL) and the solution was left to evaporate slowly at room temperature. Having reduced the volume of the solution by 50 %, colourless brick-like crystals of **1** were obtained within a week. They were filtered off and dried in vacuum. Yield: 0.10 g (0.06 mmol, 29 %). No melting point. ^{1}H NMR (400 MHz, $CDCl_3$, 25 °C, ppm): δ 8.08 (dd, 12H, PhH, $^3J_{H,H}$ = 6.6, $^3J_{H,H}$ = 3.03 Hz), 7.29 (dd, 12H, PhH, $^3J_{H,H}$ = 6.6, $^3J_{H,H}$ = 3.03 Hz), 5.82 (s, 4H, C=O-CH), 2.11 (s, 24H, CH_3-C=O), 1.45 (s, 41H, CH_2).

Synthesis of $[Zn_5Cl_4(Me_2bta)_6]\cdot 2DMF$ (2a): solvothermal method. A mixture of anhydrous $ZnCl_2$ (0.028 g, 0.20 mmol) and Me_2btaH (0.123 g, 0.83 mmol) was dissolved in 4 mL of DMF and the solution was placed in a heating tube (10 mL). The tube was sealed and heated at 120 ºC for 20 h, then cooled to room temperature. The supernatant was removed and the remaining colourless octahedral crystals of **2a** were washed with DMF (3 × 1 mL) and dried

in air. Yield: 0.025 g (0.018 mmol, 46 %). No melting point, decomposition at 490 °C. ^{1}H NMR (400 MHz, bromobenzene-d_5, 25 °C, ppm): δ 8.73 (s, 12H, PhH), 8.08 (s, 2H, CHO), 2.84 (s, 12H, CH_3), 2.64 (s, 12H, CH_3), 2.43 (s, 36H, CH_3).

Vapour diffusion Method. A mixture of anhydrous $ZnCl_2$ (0.10 g, 0.73 mmol) and Me_2btaH (0.15 g, 0.91 mmol) was placed in a small vial (5 mL) and dissolved in 3 mL of DMF. The vial was then placed in a larger vial (30 mL) containing 6 mL of DMF and 210 µL of 2,6-lutidine. The larger vial was sealed and left undisturbed for 3 days. The resulting colorless octahedral crystals of **2a** were collected by filtration, washed with DMF (3 × 1 mL), and dried in air. Yield: 0.08 g (0.05 mmol, 37 %). This material exhibited the same analytical results as the one obtained by the solvothermal method.

Synthesis of $[Zn_5Cl_4(Me_2bta)_6]\cdot 2C_6H_5Br$ (2b). A solution of lutidine (1.05 mL, 9.04 mmol) in methanol (5 mL) was added to a solution of Me_2btaH (1.50 g, 9.08 mmol) in the same solvent (20 mL). To this mixture was added a methanolic solution (10 mL) of $ZnCl_2$ (1.03 g, 7.55 mmol).

The mixture was stirred at room temperature for 30 min and the resulting white solid (1.84 g) was collected by filtration, washed with 10 mL of MeOH, and dried in air. This solid was dissolved in hot bromobenzene (35 mL) and the resulting clear solution was allowed to cool to room temperature spontaneously to grow white octahedral crystals of **2b**. Yield: 1.68 g (1.01 mmol, 67 %).

Synthesis of $[FeZn_4Cl_4(Me_2bta)_6]\cdot 2DMF$ (3a). This compound was obtained after 5 days as yellow octahedral crystals by the procedure described for **2a** (vapour diffusion method) except the addition of a mixture of $ZnCl_2$ (0.08 g, 0.59 mmol) and $Fe(ClO_4)_2\cdot 6H_2O$ (0.04 g, 0.15 mmol) instead of $ZnCl_2$. Yield: 0.08 g (0.05 mmol, 36 %).

Synthesis of $[FeZn_4Cl_4(Me_2bta)_6]\cdot 2C_6H_5Br$ (3b). Yellow octahedral crystals of **3b** were obtained by the procedure described for **2b** except the addition of a mixture of $ZnCl_2$ (0.82 g, 6.01 mmol) and $Fe(ClO_4)_2\cdot 6H_2O$ (0.38 g, 1.50 mmol) instead of $ZnCl_2$. Yield: 1.71 g (1.03 mmol, 69 %).

Synthesis of $[CoZn_4Cl_4(Me_2bta)_6]\cdot 2DMF$ (4a). This compound was obtained after 4 days as orange octahedral crystals by the procedure described for **3a** except the addition of $Co(NO_3)_2\cdot 6H_2O$ (0.04 g, 0.15 mmol) instead of $Fe(ClO_4)_2\cdot 6H_2O$. Yield: 0.07 g (0.05 mmol, 32 %).

Synthesis of $[CoZn_4Cl_4(Me_2bta)_6]\cdot 2C_6H_5Br$ (4b). Light green octahedral crystals of **4b** were obtained by the procedure described for **3b** except the addition of $Co(NO_3)_2\cdot 6\ H_2O$ (0.44 g, 1.50 mmol) instead of $Fe(ClO_4)_2\cdot 6H_2O$. Yield: 1.22 g (0.74 mmol, 49 %).

Synthesis of $[NiZn_4Cl_4(Me_2bta)_6]\cdot 2C_6H_5Br$ (5b). Light blue octahedral crystals of **5b** were obtained by the procedure described for **3b** except the addition of $Ni(ClO_4)_2\cdot 6\ H_2O$ (0.55 g, 1.50 mmol) instead of $Fe(ClO_4)_2\cdot 6H_2O$. Yield: 1.06 g (0.64 mmol, 43 %).

Synthesis of $[CuZn_4Cl_4(Me_2bta)_6]\cdot 2DMF$ (6a). This compound was obtained after two weeks as brown octahedral crystals by the procedure described for **3a** except the addition of $Cu(NO_3)_2\cdot 3H_2O$ (0.04 g, 0.14 mmol) instead of $Fe(ClO_4)_2\cdot 6H_2O$. Yield: 0.08 g (0.05 mmol, 37 %).

Synthesis of $[CuZn_4Cl_4(Me_2bta)_6]\cdot 2C_6H_5Br$ (6b). Brown octahedral crystals of **6b** were obtained by the procedure described for **3b** except the addition of $Cu(NO_3)_2\cdot 3H_2O$ (0.37 g, 1.50 mmol) instead of $Fe(ClO_4)_2\cdot 6H_2O$. Yield: 1.75 g (1.05 mmol, 70 %).

Table 2.7 Elemental analyses[a] of all the compounds described in this chapter.

Compound	C (%)	H (%)	N (%)
1	54.09 (54.53)	5.60(5.72)	14.35(14.31)
2a	43.35 (43.72)	4.22 (4.21)	18.74 (18.89)
2b	43.50 (43.41)	3.61 (3.52)	14.90 (15.18)
3a	43.65 (43.75)	4.61 (4.21)	18.56 (18.89)
3b	43.56 (43.66)	3.63 (3.54)	14.96 (15.27)
4a	43.94 (43.87)	4.37 (4.23)	18.97 (18.96)
4b	43.45 (43.58)	3.50 (3.53)	15.07 (15.24)
5b	43.62 (43.59)	3.56 (3.53)	15.19 (15.25)
6a	43.62 (43.52)	4.34 (4.19)	19.02 (18.79)
6b	43.37 (43.46)	3.60 (3.52)	14.82 (15.20)

[a] Calculated values are given within parentheses.

Table 2.8 List of infrared frequencies of all the compounds presented in this chapter.

Compound	Infrared frequencies (KBr, cm^{-1})
1	3446 (br), 3071 (m), 3053 (sh), 2959 (w), 2919 (s), 2357 (br), 1947 (w), 1825

	(w), 1600 (vs), 1515 (vs), 1393 (vs), 1261 (s), 1195 (vs), 1147 (w), 1015 (m), 991 (w), 922 (s), 850 (w), 784 (s), 748 (vs), 693 (w), 642 (m), 554 (s), 430 (w)
2a	3055 (w), 2984 (s), 2958 (sh), 2923 (m), 2862 (m), 2376 (w), 1683 (vs), 1573 (m), 1492 (w), 1455 (vs), 1378 (m), 1295 (w), 1257 (w), 1202 (vs), 1168 (s), 1083 (m), 1061 (w), 1028 (w), 1001 (s), 850 (vs), 830 (sh), 723 (w), 656 (w), 576 (w), 498 (s), 468 (s), 434 (m), 412 (w)
2b	3444 (br), 3052 (w), 2978 (w), 2919 (w), 2861 (w), 2359 (br), 1720 (br), 1649 (w), 1573 (m), 1490 (w), 1453 (vs), 1373 (w), 1297 (w), 1202 (w), 1169 (s), 1067 (w), 1026 (w), 1000 (s), 852 (vs), 829 (sh), 800 (w), 752 (s), 733 (sh), 690 (w), 498 (m), 468 (m), 439 (w)
3a	3418 (br), 3054 (w), 2983 (m), 2948 (sh), 2922 (w), 2860 (w), 2371 (w), 1679 (vs), 1570 (m), 1490 (m), 1454 (vs), 1376 (s), 1296 (m), 1257 (m), 1199 (vs), 1166 (s), 1085 (m), 1058 (w), 1028 (w), 1001 (s), 851 (vs), 829 (sh), 719 (w), 657 (w), 574 (w), 498 (m), 468 (m), 433 (w)
3b	3455 (br), 3052 (w), 2978 (w), 2918 (w), 2861 (w), 2376 (br), 1718 (br), 1637 (w), 1573 (m), 1490 (w), 1454 (vs), 1376 (w), 1292 (w), 1201 (w), 1168 (s), 1067 (w), 1026 (w), 1000 (s), 852 (vs), 829 (sh), 801 (w), 752 (s), 734 (sh), 690 (w), 499 (m), 468 (m), 437 (w)
4a	3437 (br), 3055 (w), 2982 (s), 2947 (sh), 2924 (m), 2857 (m), 2375 (w), 1683 (vs), 1573 (m), 1491 (w), 1456 (vs), 1379 (m), 1296 (w), 1258 (w), 1202 (vs), 1169 (s), 1085 (m), 1062 (w), 1027 (w), 1001 (s), 852 (vs), 831 (sh), 723 (w), 658 (w), 577 (w), 499 (s), 470 (s), 437 (w)
4b	3451 (br), 3052 (w), 2978 (w), 2919 (w), 2861 (w), 2375 (br), 1723 (br), 1642 (w), 1574 (m), 1491 (w), 1454 (vs), 1374 (w), 1298 (w), 1202 (w), 1169 (s), 1067 (w), 1025 (w), 1000 (s), 853 (vs), 831 (sh), 800 (w), 752 (s), 734 (sh), 690 (w), 499 (m), 469 (m), 439 (w)
5b	3436 (br), 3053 (w), 2980 (w), 2919 (w), 2863 (w), 2376 (br), 1715 (br), 1575 (m), 1491 (w), 1453 (vs), 1374 (w), 1300 (w), 1201 (w), 1168 (s), 1068 (w), 1025 (w), 999 (s), 853 (vs), 832 (sh), 752 (s), 735 (sh), 689 (w), 496 (m), 469 (m), 437 (w)
6a	3418 (br), 3054 (w), 2983 (m), 2948 (sh), 2922 (w), 2860 (w), 2375 (w), 1680 (vs), 1574 (m), 1490 (m), 1454 (vs), 1376 (s), 1296 (m), 1257 (m), 1199 (vs), 1169 (s), 1085 (m), 1058 (w), 1028 (w), 1001 (s), 851 (vs), 829 (sh), 723 (w), 657 (w), 574 (w), 498 (m), 468 (m), 433 (w)

6b	3441 (br), 3053 (w), 2978 (w), 2915 (w), 2861 (w), 2379 (br), 1717 (br), 1642 (w), 1574 (m), 1490 (w), 1453 (vs), 1373 (w), 1297 (w), 1203 (w), 1169 (s), 1066 (w), 1025 (w), 999 (s), 852 (vs), 830 (sh), 798 (w), 751 (s), 734 (sh), 688 (w), 498 (m), 468 (m), 436 (w)

2.3.3 Structure Determination

Single crystals suitable for X-ray crystallographic analysis were selected following examination under a microscope (Figure 2.41).

The intensity data of **5b** were collected with a Bruker APEXII CCD diffractometer employing monochromated Mo-Kα radiation (λ = 0.71073 Å) at T = 296 K. For all other compounds, the data were recorded on a STOE IPDS diffractometer using Mo-Kα radiation with graphite monochromatization (λ = 0.71073 Å) at T = 293 K. Initial structures of all the compounds were solved by direct methods and refined by full-matrix least-squares techniques based on F^2 using the SHELXL-97 program.[187] Hydrogen atoms were placed at calculated positions and refined using a riding model. All non-hydrogen atoms were refined anisotropically. Details of data collection and refinement of the compounds are summarized in Table 2.9.

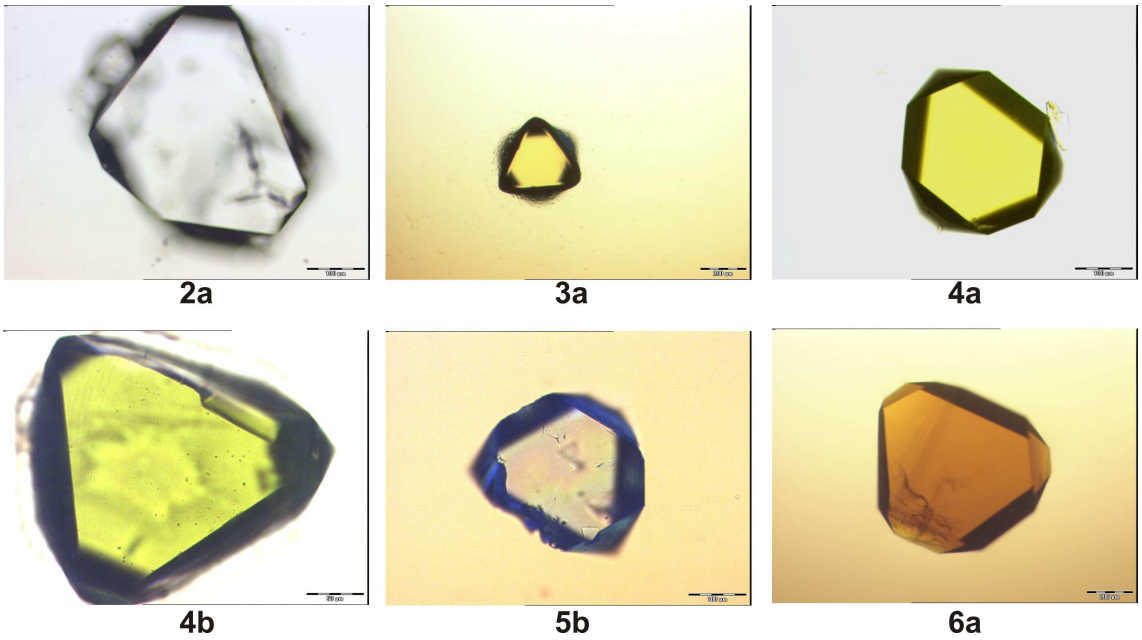

Figure 2.41 Optical micrographs of the single crystals of **2a**, **3a**, **4a**-**b**, **5b**, and **6a**.

Table 2.9 Single crystal X-ray data and refinement summary for **1**, **2a**, **3a**, **4a-b**, **5b**, and **6a**.

Compound	**1**	**2a**	**3a**	**4a**
Formula	$C_{80}H_{100}N_{18}O_8Zn_5$	$C_{48}H_{48}Cl_4N_{18}Zn_5$	$C_{48}H_{48}Cl_4FeN_{18}Zn_4$	$C_{48}H_{48}Cl_4CoN_{18}Zn_4$
Formula mass	1768.63	1345.77	1336.18	1339.32
T/K	190(2)	193(2)	293(2)	293(2)
λ/Å	0.71073	0.71073	0.71073	0.71073
Crystal dimensions/ mm	0.23×0.27×0.31	0.23×0.23×0.31	0.31×0.31×0.39	0.23×0.31×0.38
Crystal system	Monoclinic	Cubic	Cubic	Cubic
Space group	$P2_1/c$	$Fd\bar{3}m$	$Fd\bar{3}m$	$Fd\bar{3}m$
a/Å	23.781(5)	23.367(3)	23.456(3)	23.443(3)
b/Å	16.000(3)			
c/Å	25.170(5)			
β/°	115.29(3)			
V/Å^3	8659(3)	12759(3)	12905(3)	12884(3)
Z	4	8	8	8
D_c/g cm^{-3}	1.357	1.553	1.375	1.532
M/mm^{-1}	1.427	2.077	1.895	1.942
F(000)	3680	6080	5408	6056
θ Range/°	2.01–25.99	2.47–25.93	2.46-25.96	2.46–25.93
Measured reflections	67610	22859	24622	24619
Independent reflections	16887	645	648	647
Data/restraints/ parameters	16887 / 42 / 985	645 / 0 / 43	648/0/43	647 / 0 / 43
R_1 (I >2σ(I))[a]	0.0462	0.0567	0.0653	0.0659
wR_2 (all data)[b]	0.1111	0.2090	0.2239	0.2274
Goodness-of-fit on F^2	0.828	1.181	1.278	1.274
$\Delta\rho_{max,\ min}$/e Å^{-3}	0.486,–0.340	2.639,–0.714	2.919, -0.430	2.852,–0.427

Table 2.9 (continued)

Compound	**4b**	**5b**	**6a**
Formula	$C_{60}H_{58}Br_2Cl_4CoN_{18}Zn_4$	$C_{60}H_{58}Br_2Cl_4N_{18}NiZn_4$	$C_{48}H_{48}Cl_4CuN_{18}Zn_4$
Formula mass	1653.33	1653.09	1343.86
T/K	293(2)	296(2)	293(2)
λ/Å	0.71073	0.71073	0.71073
Crystal dimensions/ mm	0.24×0.24×0.32	0.36×0.36×0.24	0.27×0.31×0.33
Crystal system	Cubic	Cubic	Cubic
Space group	$Fd\bar{3}m$	$Fd\bar{3}m$	$Fd\bar{3}m$
a/Å	23.737(3)	23.7160(4)	23.421(3)
b/Å			
c/Å			
β/°			
V/Å^3	13375(3)	13339.0(4)	12848(3)
Z	8	8	8
D_c/g cm^{-3}	1.642	1.646	1.389
M/mm^{-1}	3.065	3.107	2.009
F(000)	6632	6640	5432
θ Range/°	2.43-25.91	2.43-32.35	2.46-25.87
Measured reflections	24077	54846	24421
Independent reflections	673	1182	646
Data/restraints/ parameters	673/0/55	1182/0/55	646/0/44
R_1 (I >2σ(I))[a]	0.0316	0.0362	0.0779
wR_2 (all data)[b]	0.0849	0.0994	0.2193
Goodness-of-fit on F^2	1.085	1.172	1.049
$\Delta\rho_{max, min}$/e Å^{-3}	1.004/-0.268	0.595, -0.453	2.625, -0.419

[a] $R_1 = \sum||F_o| - |F_c||/ \sum|F_o|$. [b] $wR_2 = \{\sum [w(F_o^2 - F_c^2)^2]/ \sum[w(F_o^2)^2]\}^{1/2}$.

2.4 Summary

The successful design, syntheses and in-depth characterization of a novel series of readily available, thermally and solvolytically stable homo- and heteropentanuclear compounds, which represent discrete molecular analogues of the secondary building unit of the metal-organic framework **MFU-4**, have been demonstrated. The Kuratowski-type coordination compounds $[M^{II}Zn_4Cl_4(Me_2bta)_6]$ (M^{II} = Zn, Fe, Co, Ni, or Cu) can be readily synthesized at multigram scale. Single crystal X-ray data reveal that the open-shell metal ions in all heteropentanuclear complexes are in high-spin state without undergoing any Jahn-Teller distortion, which has been further verified by electronic spectroscopy and magnetic measurements. TGA and TOF-MS analyses exhibit exceptionally high thermal and solvolytic stability of the compounds, respectively. These properties in combination with the presence of coordinatively unsaturated Zn sites and the redox-active open-shell metal ions would make them model catalysts in homogenous Lewis-acid and redox catalyzed reactions for structurally related **MFU-4** type of heterogeneous catalysts. Moreover, such compounds might display interesting combinations of useful properties such as luminescence or reversible electron transfer. Finally, the present compounds represent the rare class of topologically nonplanar building units having T_d point group symmetry and $K_{3,3}$ as molecular graph, in analogy of which a large number of cubic porous frameworks can be constructed in a predictable and systematic fashion.

Chapter 3

Homo- and Heterononanuclear Coordination Compounds Featuring $\{M_9L_{12}\}^{6+}$ Cores (M^{II} = Co, Ni, Zn, or $Fe_{1/3}Zn_{2/3}$; L = 1,2,3-benzotriazolate)

3.1 Introduction

Realizing and understanding magnetic phenomena in quasi-zero dimensional molecular systems are key to the development of molecule-based magnetic materials that promise tailored physical properties[188] that will allow the use of this class of compounds as "smart" switches, molecular sensors and as components in molecular spintronics. Of particular interest in this context are strategies that allow to systematically vary and thus tune the magnetic properties of such molecular systems.[189] Given the intricate structure-property relationships that govern the intramolecular interactions between the spin centers in a magnetic molecule, synthesis of isostructural compounds comprising different spin centers is of particular importance for the development of rational approaches to pre-defined magnetic properties. The similarity of the coordination chemistry of Ni(II) and Co(II) suit these spin centers for the production of common structural motifs.[190] In this chapter, five polynuclear M(II) (M = Ni, Co, Zn) coordination compounds (Table 3.1), featuring both bridging benzotriazolate (Figure 3.1) and different terminal ligands, are demonstrated.

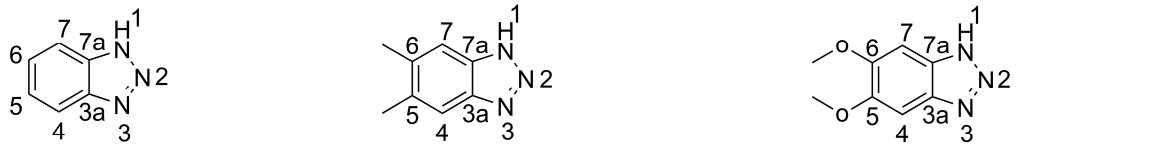

Figure 3.1 Structures of the 1,2,3-benzotriazole ligands described in this chapter.

Table 3.1 List of compounds described in this chapter.

Compound	Molecular formula	Compound	Molecular formula
1	$[Co_9(bta)_{12}(MeOH)_{18}][(NO_3)_6]\cdot$	**4**	$[Zn_9(OMe_2bta)_{12}Cl_6]\cdot$

	$9C_6H_6$		DMF
2	$[Ni_9(bta)_{12}(NO_3)_6(MeOH)_6]\cdot$ 4THF	**5**	$[Fe_3Zn_6(OMe_2bta)_{12}Cl_6]\cdot$ DMF
3	$[Zn_9(Me_2bta)_{12}(CH_3COO)_6]\cdot$ 3DMF		

The design and synthesis of polynuclear metal complexes with versatile physical and chemical properties are of great current interest in the areas of molecular based electronic, photochemistry and magnetism. The goal is to develop novel materials the properties of which can be controlled by the input of external information. In this context, particular interest has been focused on Fe^{II} spin-crossover (SCO) compounds because they can be considered among the best examples of switchable molecules. In response to external perturbation, distinctive reversible changes occur in the magnetic, structural, dielectric, and optical properties associated with the respective spin state of the SCO materials.[191] Potential applications of SCO materials as molecular switches in information storage and display devices employing these properties have been described and patented, while several other potential uses of SCO materials have also been proposed and, in some cases, demonstrated.[192] As a result, interest in the synthesis, structural chemistry and physics of SCO materials has continued to grow.

Six-coordinate Fe^{II} compounds may occur in a paramagnetic high-spin (HS, S = 2) or diamagnetic low-spin (LS, S = 0) state depending on whether the ligand field strength is weak or strong, respectively. For intermediate ligand fields, the energy gap between the excited HS state and the ground LS state may fall in the range of thermal energy. Consequently, a reversible transition between the two states can be induced by variation of temperature, pressure, or light irradiation.[191] Although this energy gap can be tuned in a relatively predictable fashion by variation of the ligand field force, this is not the only factor upon which the existence and character of a spin transition depends. This phenomenon is very sensitive to packing effects in the crystal lattice of the compounds, and entities such as lattice solvent molecules or counterions may have a drastic influence on the SCO properties of the material.[191a,191c-d,191g,191i,191p,195m]

The synthesis of new Fe^{II} SCO compounds is of outmost importance for this research area, particularly when the syntheses have to be performed in a controlled manner with the aim of obtaining compounds exhibiting anticipatable SCO behaviours. Unfortunately, an unambiguous predictive method for the rational design of a new Fe^{II} SCO compound is still

not available, as pointed out by Gütlich *et al.*[191l] "Fine tuning" of the $[Fe^{II}N_6]$ ligand field strength is often required, if the SCO condition is not obtained at first attempt. Experience has led to "rules of thumb" in choosing the susscessful combination of ligands which will yield the ligand field strength required to induce SCO of the coordinated Fe^{II} ion, and these are generally aromatic heterocyclic N-donors (pyridyls, 1,2,4-triazoles, tetrazoles, pyrazoles, imidazoles, thiazoles, thiazolines, isoxazoles, pyrazines, pyridazines), being present either as monodentate ligands or as polydentate chelate ligands, often in combination with monodentate N-bonded NCX^- (X = S, Se) ligands.[191] To the best of knowledge, no report on Fe^{II} SCO compound containing μ_3-bridging 1,2,3-triazolate ligands has been appeared up to now. In this chapter, the syntheses and characterization of $[Fe_3Zn_6Cl_6(OMe_2bta)_{12}]\cdot DMF$ (**5**) and its desolvated form (**5a**), the latter representing the first example of a Fe^{II} SCO compound containing the OMe_2bta ligand, are presented.

The particular development of compounds **4** and **5** of this chapter was stimulated by the previous work (*cf.* Chapter 2) on Kwiatkowski-type homo- and heteropentanuclear coordination compounds (Figure 3.2) represented by structural formulae $[MZn_4Cl_4(Me_2bta)_6]\cdot$(solvent) (M = Zn, Fe^{II}, Co^{II}, Ni^{II}, or Cu^{II}; Me_2bta = 5,6-dimethyl-1,2,3-benzotriazolate; solvent = DMF or bromobenzene),[10c] and the fact that these coordination units can be fused into oligonuclear compounds,[10b] or even into metal-organic frameworks.[10d] Magnetic, structural and UV-Vis spectroscopic investigations on the heteropentanuclear compound $[FeZn_4Cl_4(Me_2bta)_6]$ from the series referred to above, however, indicated the presence of a weak ligand, thus leading to a HS state of the central hexacoordianted Fe^{II} ion in this particular compound. In order to tailor a stronger ligand field, we envisaged the ligand OMe_2bta instead of Me_2bta in the syntheses of the compounds presented in this chapter, expecting the former ligand to provide more field strength around Fe^{II} ions due to the electron-donating ability of the methoxy substituents of the 1,2,3-benzotriazolate moieties. Though numerous attempts were undertaken to obtain pentanuclear compounds of the formula $[FeZn_4Cl_4(OMe_2bta)_6]$, all synthetic efforts led to compound **5**, which could be formally derived from two lacunary Kuratowski-type coordination units $[FeZn_3Cl_3L_6]^-$ being fused via a shared hexacoordinate Fe ion in the centre of the nonanuclear coordination unit. Spectroscopic properties of compounds **5** and **5a** were studied in detail in order to investigate the possibility of HS↔LS transitions. Mössbauer measurements show that the central Fe^{II} ion, which bridges the lacunary Kuratowski-type $[FeZn_3Cl_3L_6]^-$ units in **5a** indeed changes its HS state upon cooling. Noteworthingly, the central Fe^{II} ion in a formerly reported linear trinuclear

Fe^{II} compound, $[Fe_3(Ettrz)_6(H_2O)_6][(CF_3SO_3)_6]$ (Ettrz = 4-ethyl-1,2,4-triazole) showed analogous SCO behaviour.[195d-e]

Compound $[Zn_9Cl_6(OMe_2bta)_{12}]\cdot DMF$ (**4**) represents an isostructural homononanuclear analogue of **5**, which serves as reference sample in the following studies. It was after obtained from directed synthesis, starting from a stoichiometric ratio of suitable metal salts and benzotriazole ligands.

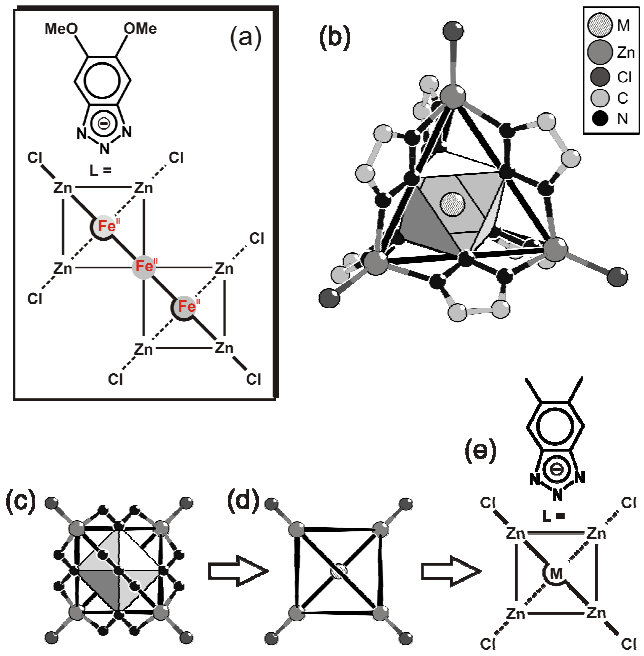

Figure 3.2 (a) Skeletal formula representing the connectivity of $[Fe^{II}_3Zn_6Cl_6(L_{12})]$ units (L: 5,6-dimethoxy-1,2,3-benzotriazolate) present in compound **5**. The structure of this compound is formally obtained from fusing two Kuratowski-type pentanuclear coordination units, a ball-and-stick-model of which is shown in (b). (c-e) Stepwise derivation of a skeletal formula representing the connectivity of $[M^{II}Zn_4X_4(L_6)]$ Kuratowski-type units (X: terminal ligand, L: 1,2,3-triazolate-type ligand) as described in Chapter 2.

In this chapter, the syntheses, structural characterizations as well as thermal, electronic, magnetic, and spin-crossover properties of the above mentioned homo- and heterononanuclear coordination compounds are presented.

3.2 Results and Discussion

3.2.1 Syntheses

Many polynuclear metal compounds containing benzotriazolate ligands have been prepared using metal(II) β-diketonates as precursors, thus taking advantage of the fact that the reaction between metal(II) β-diketonates and benzotriazole ligands leads to a partial replacement of β-diketonato ligands by deprotonated benzotriazoles, and, finally, to formation of large heteroleptic metal coordination compounds.[10c,10f,12,13] However, the synthesis of the nonanuclear compounds **1-3** is based on a completely different strategy.

Compound **2** was synthesized using an M:L ratio of 1:4, whereas in the preparation of **1** and **3**, an M:L ratio of 1:8 was employed. In both synthetic procedures, a huge excess of ligand with regard to the calculated stoichiometric ratio (M:L = 1:1.33) was employed, the excess benzotriazole molecules acting as auxiliary base in the reaction mixture, leading to deprotonation of the acidic –NH protons from coordinated benzotriazole ligands. Deprotonation is a necessary requirement for the ligand coordinating to three adjacent metal centers via its three N-donor atoms (μ_3-bridging mode).

Compounds **4** and **5** were synthesized applying the previously established strategy which was used to prepare the homo- and heteropentanuclear compounds of the type $[MZn_4Cl_4L_6]$ (M^{II} = Zn, Fe, Co, Ni, or Cu; L = 1,2,3-benzotriazolate ligand) as described in Chapter 2. In these synthetic procedures, vapor of a weakly coordinating base such as 2,6-lutidine is introduced into a DMF solution via vapor diffusion. The solution contains the metal salt(s) and benzotriazole ligands at the stoichiometric ratio. The auxiliary base (2,6-lutidine) presumably abstracts the acidic –NH protons of benzotriazole ligands that become coordinated to the metal ions. Both **4** and **5** have also been prepared by a solvothemal method using stoichiometric quantities of appropriate metal salts and benzotriazole ligands dissolved in DMF. The gradual decomposition of DMF under solvothermal condition liberates the base (dimethylamine) in the reaction medium. The base generated *in-situ* is essential for the abstraction of the acidic –NH protons from the coordinated benzotriazole ligands. The synthetic procedures leading to **4** and **5** are summarized in Scheme 3.1.

Compound **4**:

$$9\ ZnCl_2 + 12\ OMe_2btaH + 12\ B \xrightarrow[RT/\Delta]{DMF} [Zn_9Cl_6(OMe_2bta)_{12}] + 12\ BH^{\oplus} + 12\ Cl^{\ominus}$$

Compound **5:**

$$3\ Fe(ClO_4)_2(H_2O)_6 + 6\ ZnCl_2 + 12\ OMe_2btaH + 12\ B \xrightarrow[RT/\Delta]{DMF}$$

$$[Fe_3Zn_6Cl_6(OMe_2bta)_{12}] + 12\ BH^{\oplus} + 6\ Cl^{\ominus} + 6\ (ClO_4)^{\ominus} + 6\ H_2O$$

Scheme 3.1 Chemical equations for the syntheses of **4** and **5**. B is the base 2,6-lutidine for room temperature (RT) synthesis, or *in-situ* generated base dimethylamine for the solvothermal (Δ) synthesis.

All compounds are stable in air under ambient conditions. Compounds **1** and **2** are soluble in water, methanol and DMF. Compound **3** is insoluble in common organic solvents including chloroform, methanol, acetonitrile, DMF, and DMSO (DMSO = dimethyl sulfoxide). Compounds **4** and **5** are soluble in chloroform, NMP (NMP = 1-methyl-2-pyrrolidone), DMA (DMA = *N*,*N*'-dimethylacetamide), and DMSO.

3.2.2 Characterization

X-ray powder diffraction. Phase purity of all the five homo- and heterononanuclear compounds was confirmed by X-ray powder diffraction (XRPD).

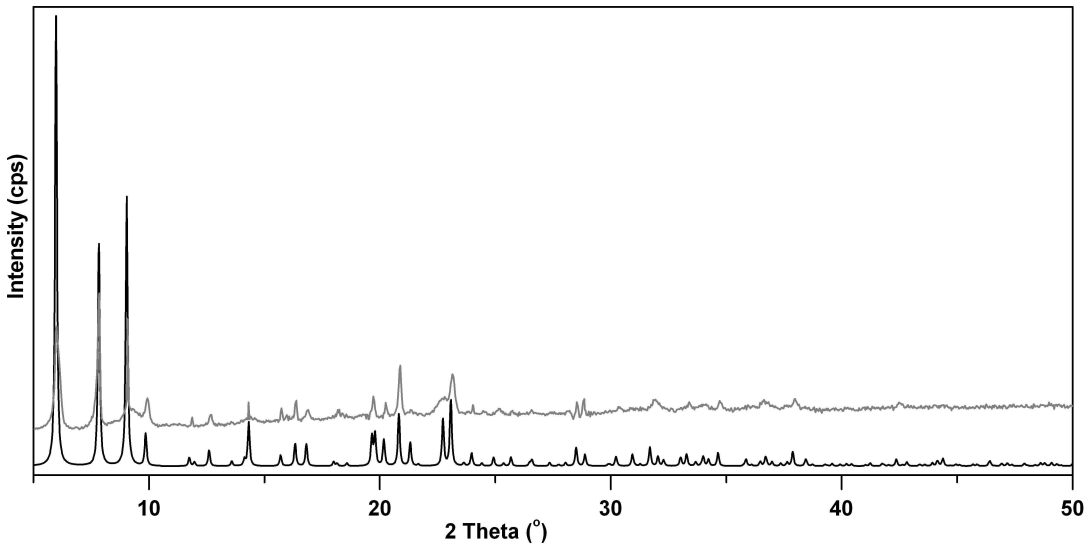

Figure 3.3 Theoretical (black) and experimental (grey) XRPD patterns of **2**.

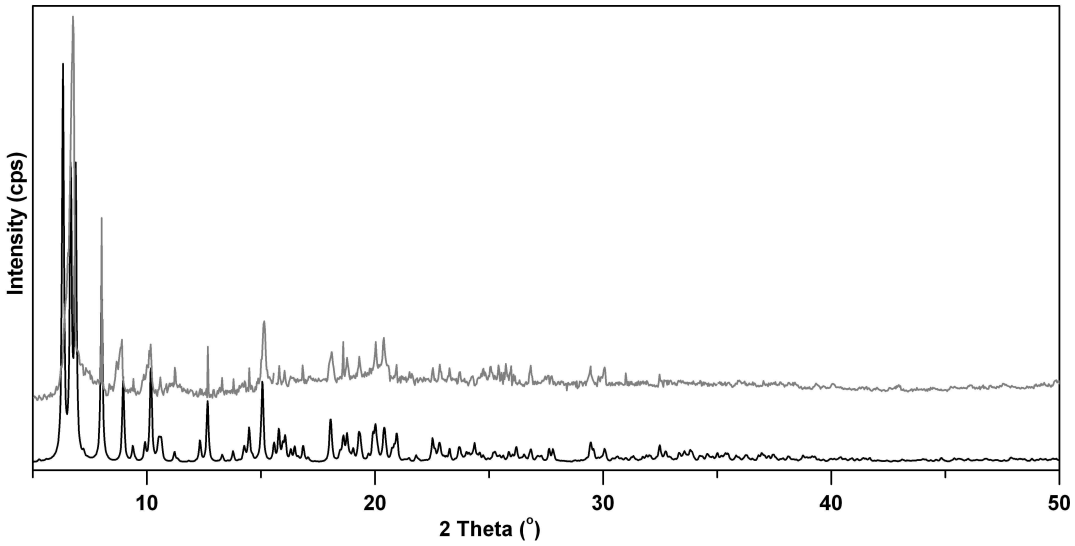

Figure 3.4 Theoretical (black) and experimental (grey) XRPD patterns of **3**.

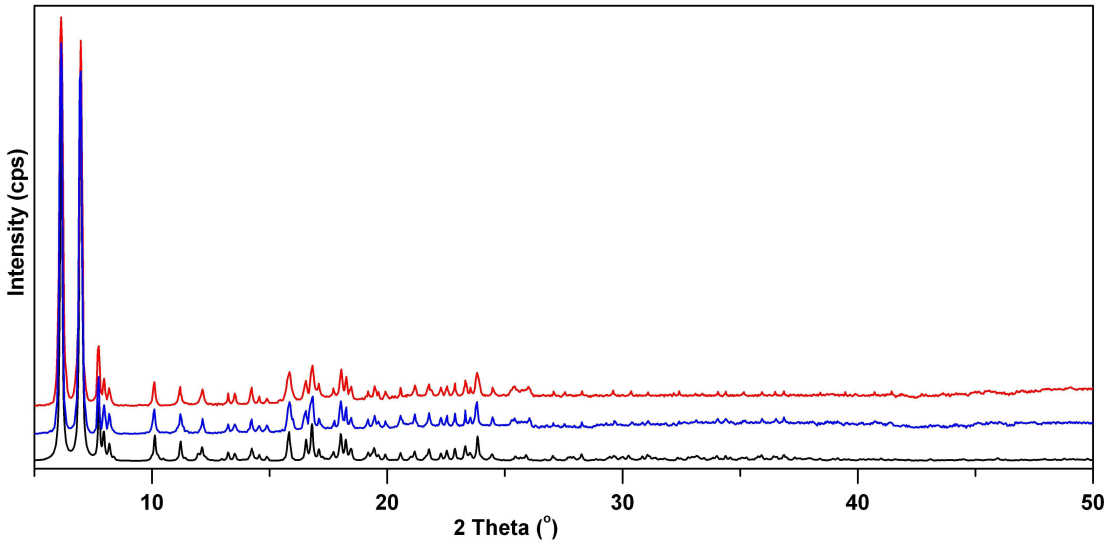

Figure 3.5 Theoretical XRPD pattern (black) and experimental XRPD patterns of **4** synthesized by solvothermal method (blue) and vapour diffusion method (red).

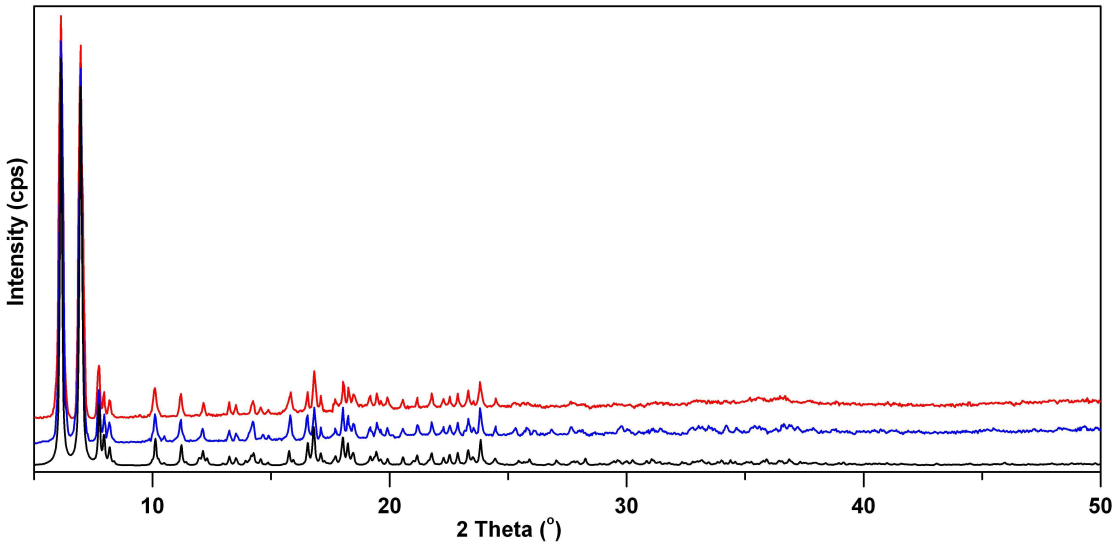

Figure 3.6 Theoretical XRPD pattern (black) and experimental XRPD patterns of **5** synthesized by solvothermal method (blue) and vapour diffusion method (red).

The experimental XRPD patterns are consistent with the simulated ones as determined from the single-crystal X-ray diffraction data (Figure 3.3-3.6). The experimental XRPD patterns of the isostructural nonanuclear compounds **4** and **5**, synthesized both by solvothermal and vapor diffusion method, are expectedly similar (Figure 3.7).

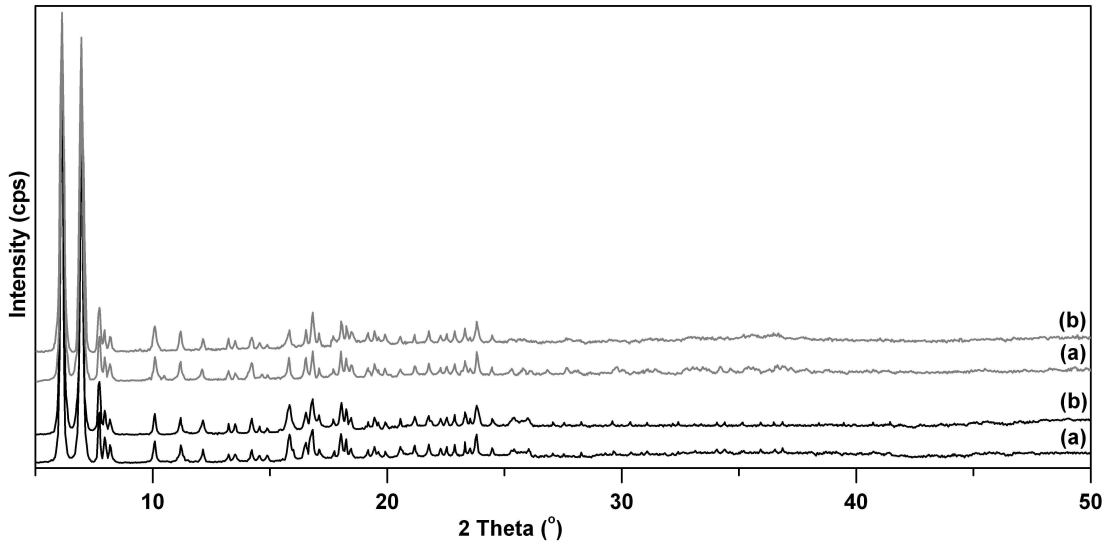

Figure 3.7 Experimental XRPD patterns of **4** (black) and **5** (grey) synthesized by (a) solvothermal method and (b) vapour diffusion method.

EDX analysis. An EDX measurement (Figure 3.8) performed on the single crystals of the heterononanuclear compound **5** shows that the relative ratio of Fe:Zn is 1:2.13, which closely matches with the theoretical ratio (1:2.0).

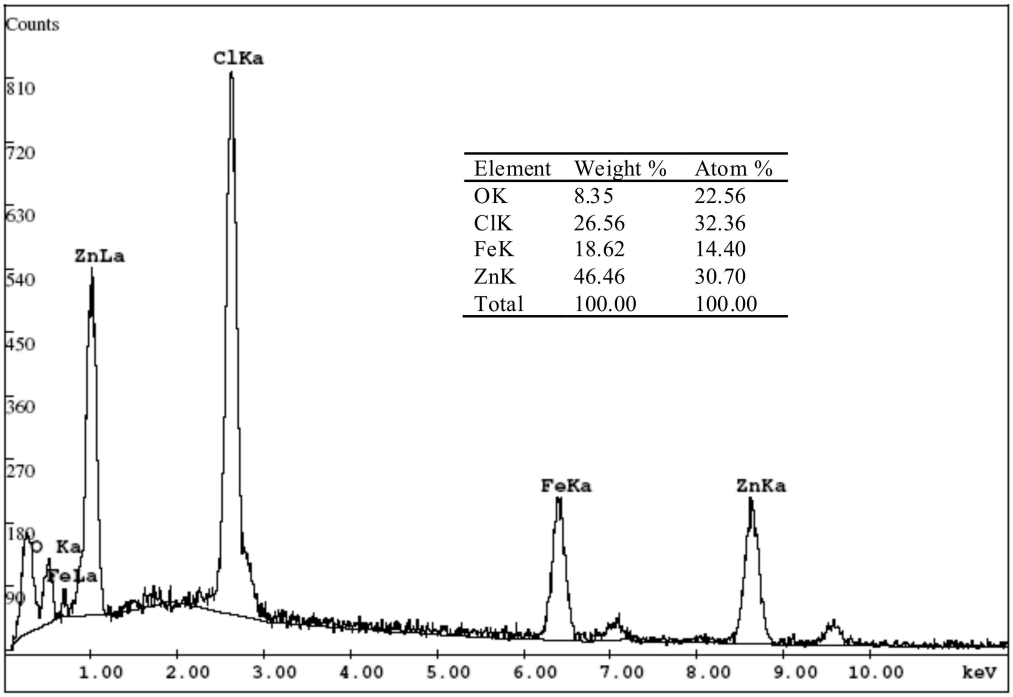

Figure 3.8 EDX spectrum of **5**. Weight % and atom % of the elements (excluding carbon) are shown in the inset.

ICP-AES analysis. In order to determine the exact amounts of Fe(II) and Zn(II) ions present in **5**, ICP-AES analysis was performed on the fully desolvated sample (**5a**) of this compound. The experimental weight percentages of Fe(II) and Zn(II) ions are 5.79 and 13.60, respectively. These values match quite closely with the theoretical weight percentages (calcd. for $C_{96}H_{96}Cl_6Fe_3N_{36}O_{24}Zn_6$: Fe = 5.75 %, Zn = 13.47%). The emission intensity measurements were made under the conditions summarized in Table 3.2.

Table 3.2 Operating parameters for the ICP-AES spectrometer.

Incident output power	1150 W
Nebulizer	PTFE, Mira Mist
Plasma gas flow rate	12 L min^{-1}
Auxiliary gas flow rate	0.5 L min^{-1}
Aerosol carrier gas flow	0.6 L min^{-1}
Solution uptake rate	1 mL min^{-1}
Signal integration time	10 s
Integration for determination	3
Wavelength	Fe = 259.93 nm, Zn = 213.85 nm

Infrared spectroscopy. The FT-IR spectra of **1**-**3** (Figures 3.9-3.11) show characteristic strong bands of the coordinated benzotriazolate ligand at *ca.* 1000 and 1200 cm^{-1} assigned for C-H out-of-plane bending vibrations, and vibrations involving both triazole ring breathing and C-H in-plane bending, respectively.[161] Compound **2** shows an absorption shoulder at 1480 cm^{-1} which is a typical value for a nitrate anion coordinating to an octahedral Ni^{II} center.[193] The absorption band for coordinated methanol molecules overlaps with the broad absorption bands of the bta ligand in the region around 2600–3700 cm^{-1} for both **1** and **2**. The coordinated acetate anions in **3** show strong bands at 1570 and 1460 cm^{-1} for the asymmetric and symmetric stretching vibrations, respectively.[194] The FT-IR spectra of **4** and **5** (Figure 3.12 and 3.13) exhibit characteristic strong bands of the coordinated benzotriazolate ligand at *ca.* 1000 cm^{-1} assigned for C-H out-of-plane bending vibrations.[161] Since **4** and **5** are isostructural, their IR spectra are anticipatedly similar. The absorption band at *ca*. 1680 cm^{-1} in the IR spectra of the as-synthesized **4** and **5** is due to the C=O stretching frequency of non-coordinated DMF molecules. The occluded DMF molecules can be removed from the void regions of the crystal lattices of **4** and **5** if samples are kept for 10 h in vacuum at room temperature. The absence of the strong absorption band at *ca*. 1680 cm^{-1} in the FT-IR spectra of the fully desolvated samples (**4a** and **5a**) confirms the complete removal of DMF molecules.

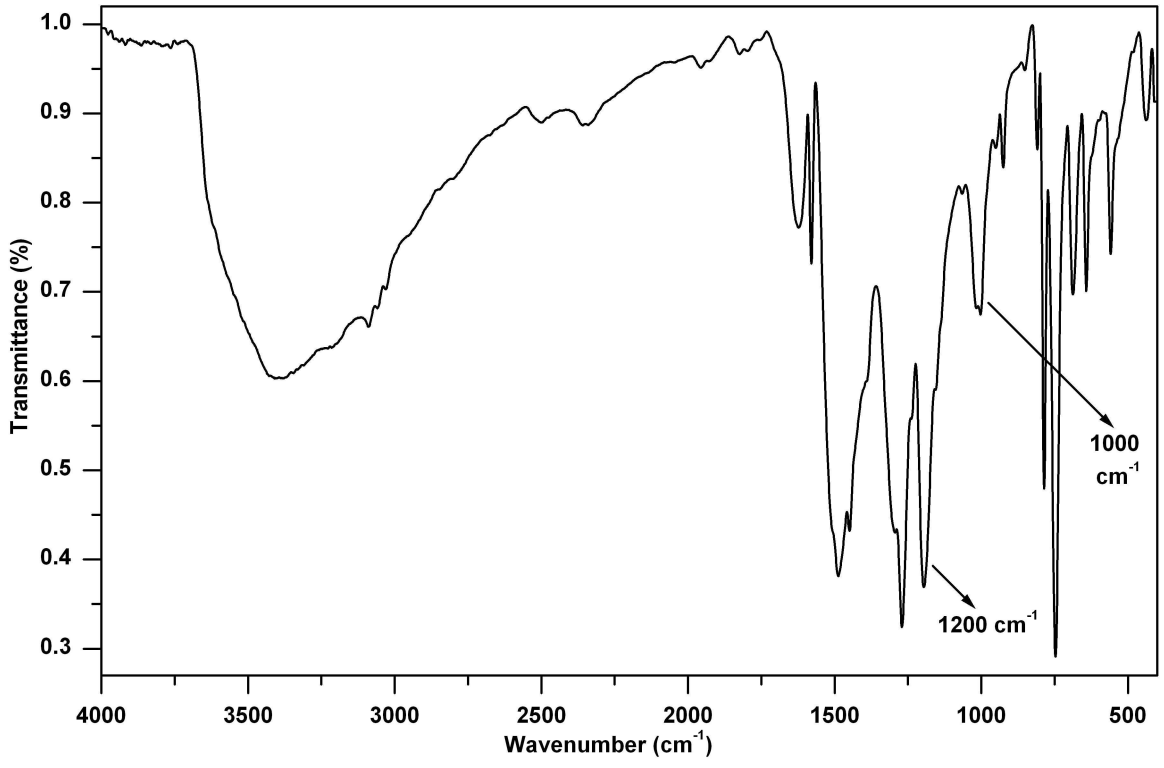

Figure 3.9 FT-IR spectrum of **1**.

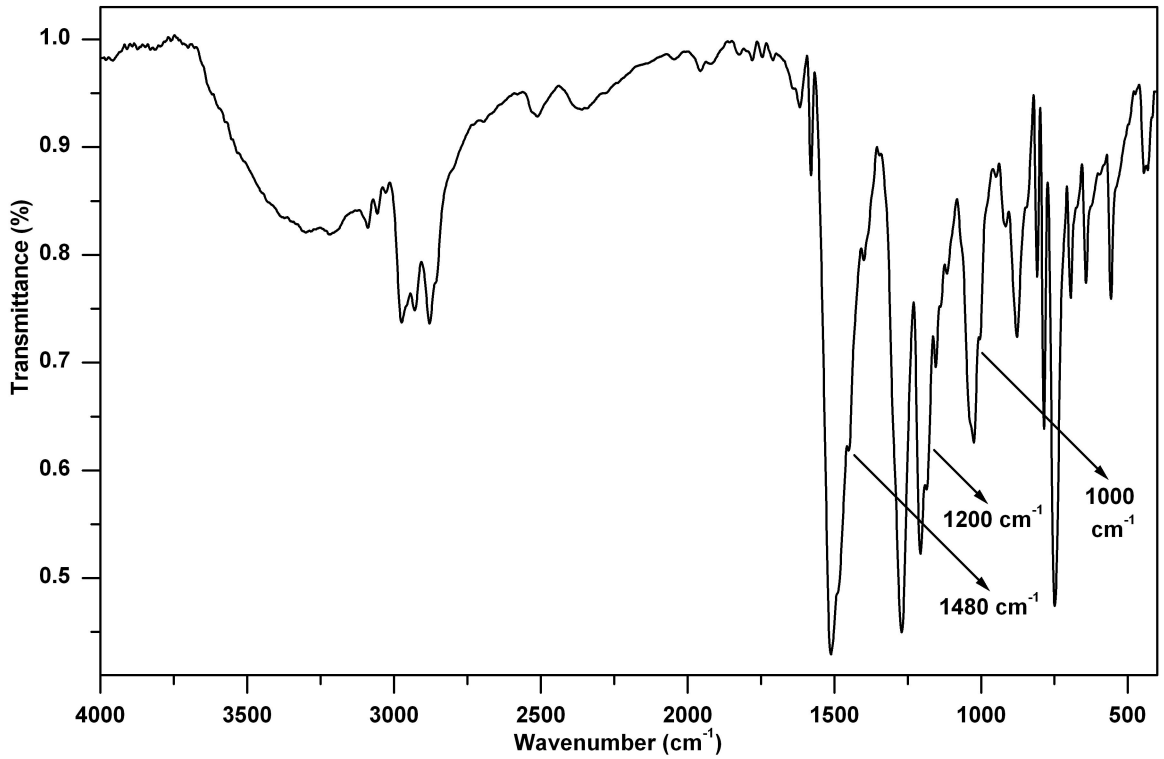

Figure 3.10 FT-IR spectrum of **2**.

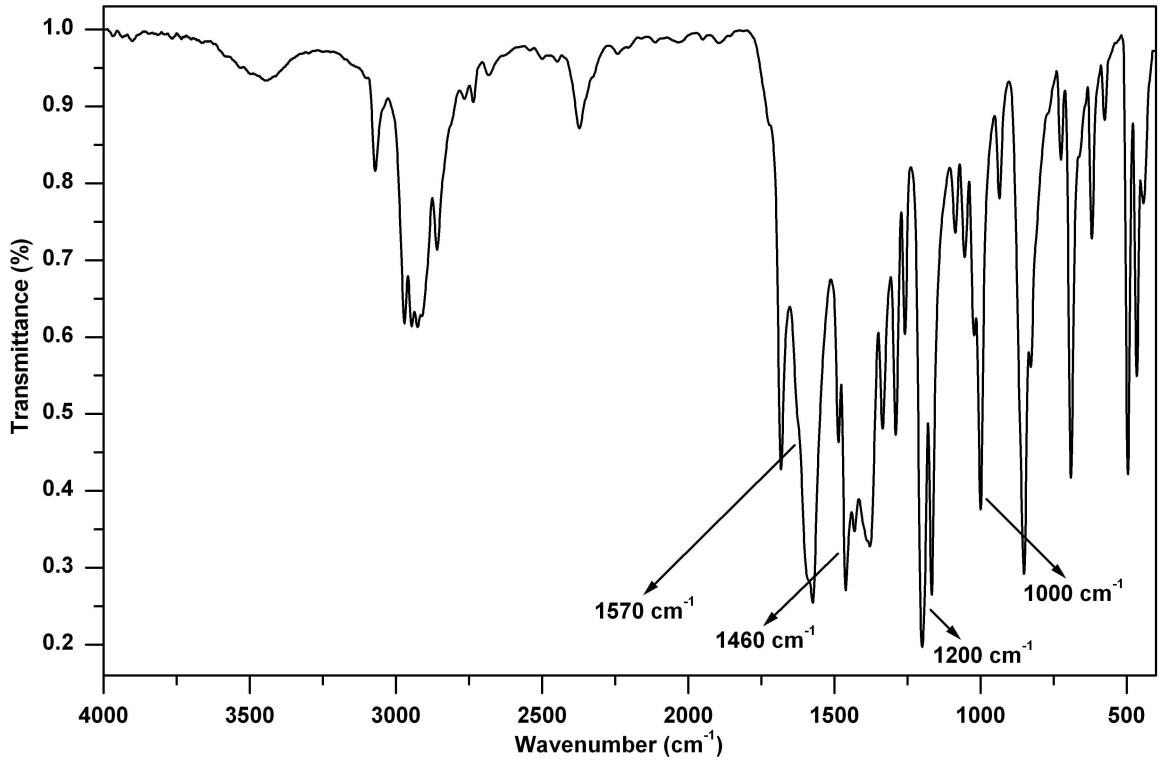

Figure 3.11 FT-IR spectrum of **3**.

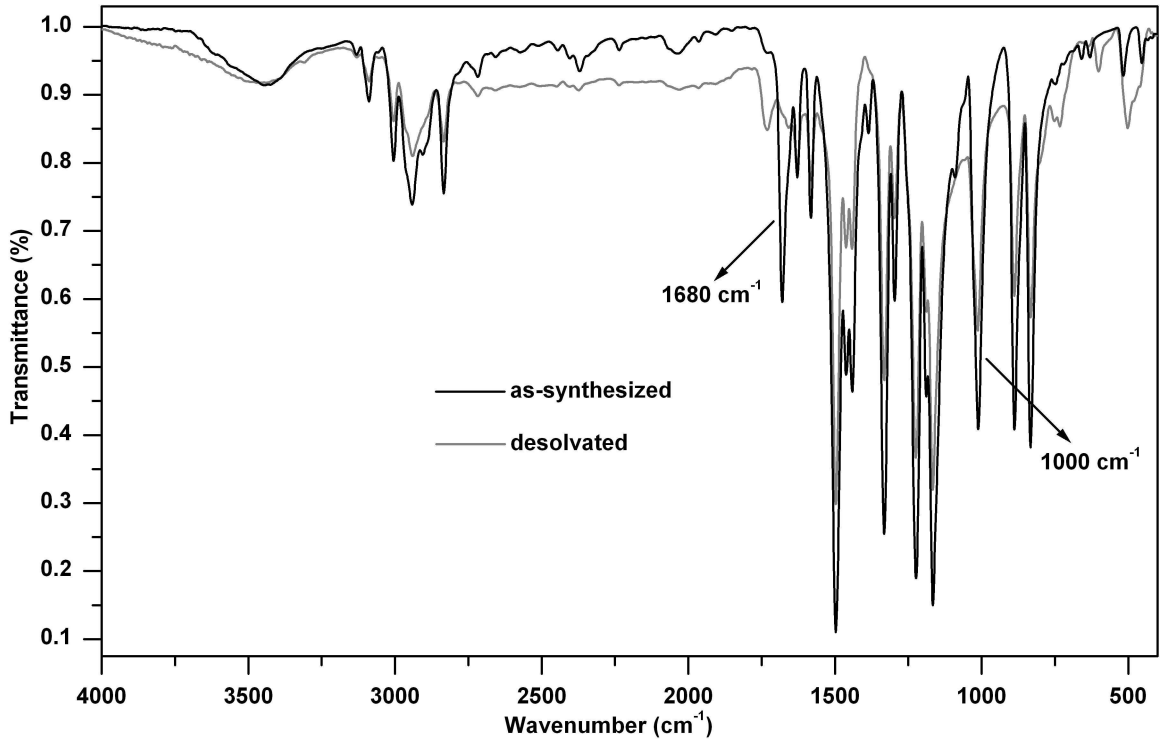

Figure 3.12 FT-IR spectra of as-synthesized (black) and desolvated (grey) **4**.

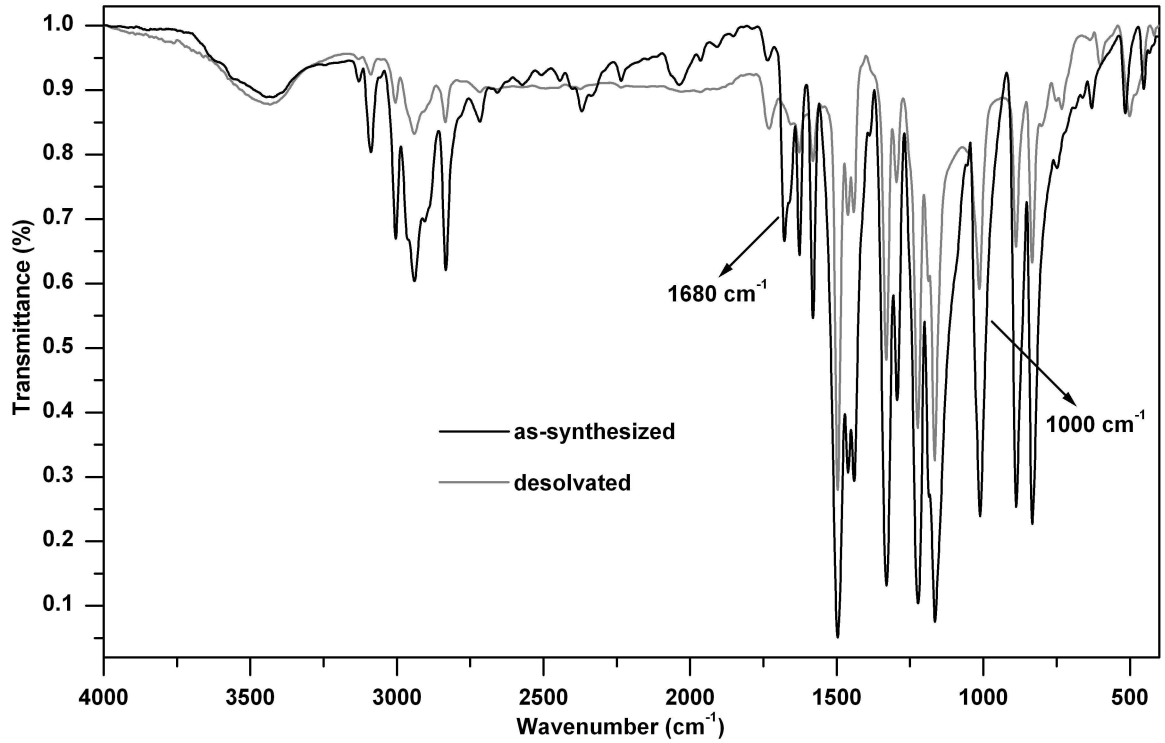

Figure 3.13 FT-IR spectra of as-synthesized (black) and desolvated (grey) **5**.

Thermogravimetric analysis. In order to examine the thermal stability of the compounds, thermogravimetric analyses (TGA) were performed on polycrystalline samples of **1-5** in nitrogen atmosphere.

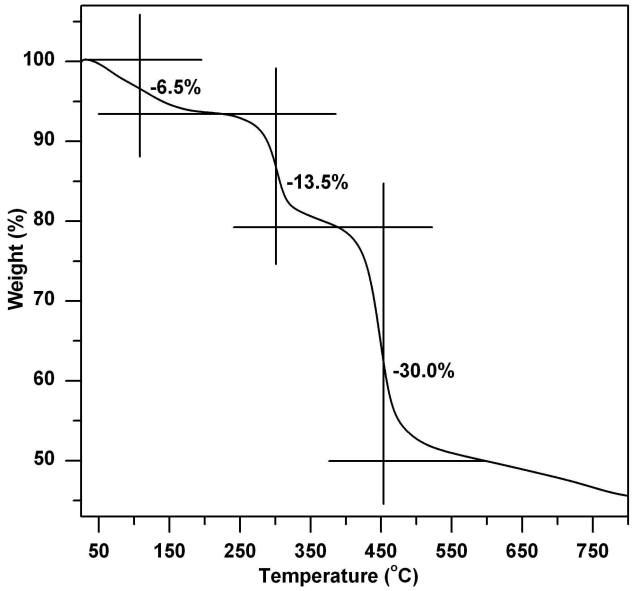

Figure 3.14 TG analysis of **1** under N_2 atmosphere.

The TGA curve of **1** (Figure 3.14) shows a three-step weight loss process. The first weight loss is 6.5 % from 45 to 205 °C, and the second step is 13.5 % from 205 to 370 °C, both assigned to the loss of 18 coordinated methanol molecules per formula unit (calcd. 19.9 %). The third weight loss of 30.0 % is assigned to the decomposition of **1**.

Three weight loss steps can be observed in the TGA curve of **2** (Figure 3.15). The first weight loss of 18.5 % in the temperature range 30–300 °C is attributed to the loss of four isolated THF and six coordinated methanol molecules per formula unit (calcd. 17.2 %). The second (9.3 %) and third (26.4 %) weight loss steps are due to decomposition of the compound.

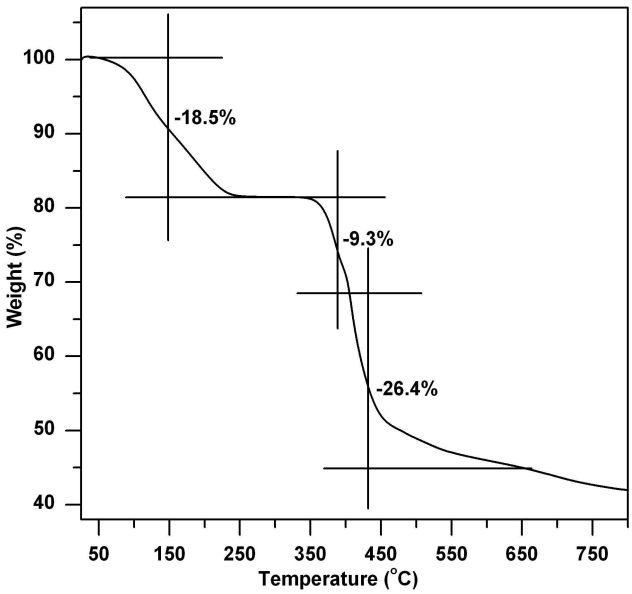

Figure 3.15 TG analysis of **2** under N_2 atmosphere.

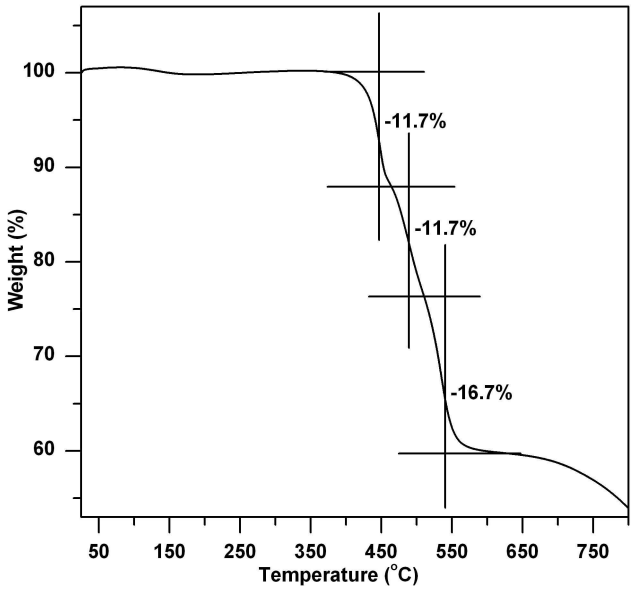

Figure 3.16 TG analysis of **3** under N_2 atmosphere.

In the TGA curve of the desolvated sample of compound **3** (Figure 3.16), no considerable weight loss is observed until 400 °C, which indicates that the compound is stable up to this temperature. After that three consecutive weight loss steps (11.7, 11.7 and 16.7 %) occur in the range 400–600°C, which are attributed to the decomposition of the compound.

In the TGA traces of the as-synthesized samples of **4** and **5** (Figure 3.17 and 3.18), the first weight loss steps (2.15 %, **4**; 1.76 %, **5**) in the temperature range 80–150 °C is attributed to the loss of one DMF molecule per formula unit (calcd.: 2.42 %, **4**; 2.44 %, **5**). No further weight loss steps are observed until 400 ºC, when the compounds start to decompose. The fully desolvated samples (**4a** and **5a**) show no weight loss until 400 ºC (Figure 3.17 and 3.18), suggesting complete removal of occluded DMF molecules.

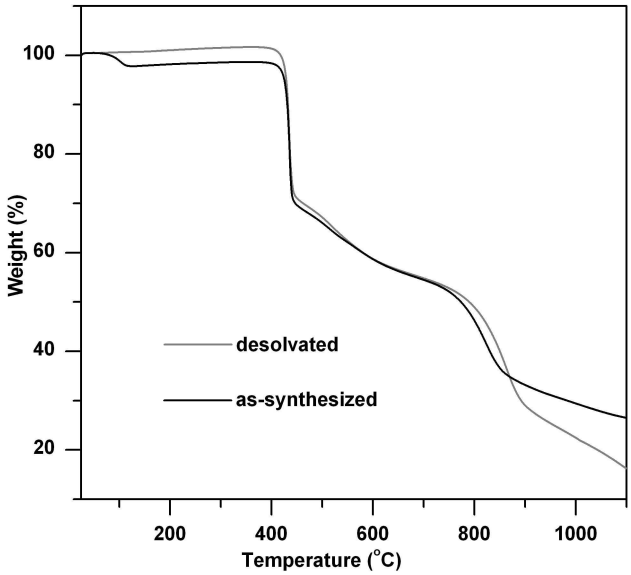

Figure 3.17 TG analysis of desolvated **4** under N_2 atmosphere.

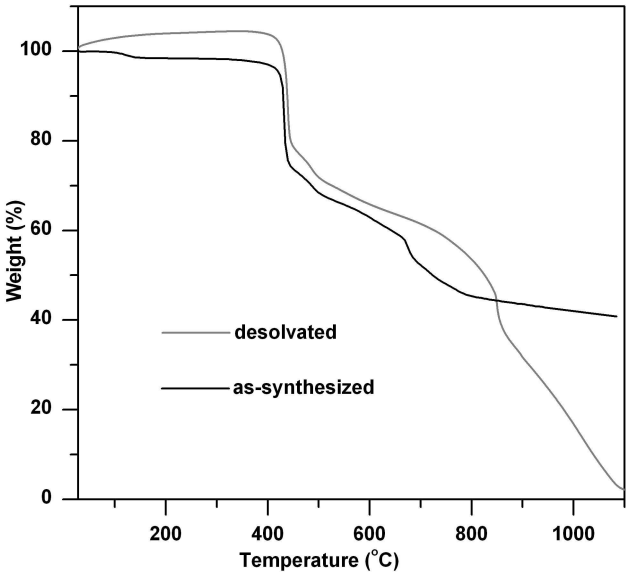

Figure 3.18 TG analysis of **5** under N_2 atmosphere.

TG-IR analysis. TG-IR analyses were carried out in order to identify the occluded solvent molecules present inside the void regions of **4** and **5**.

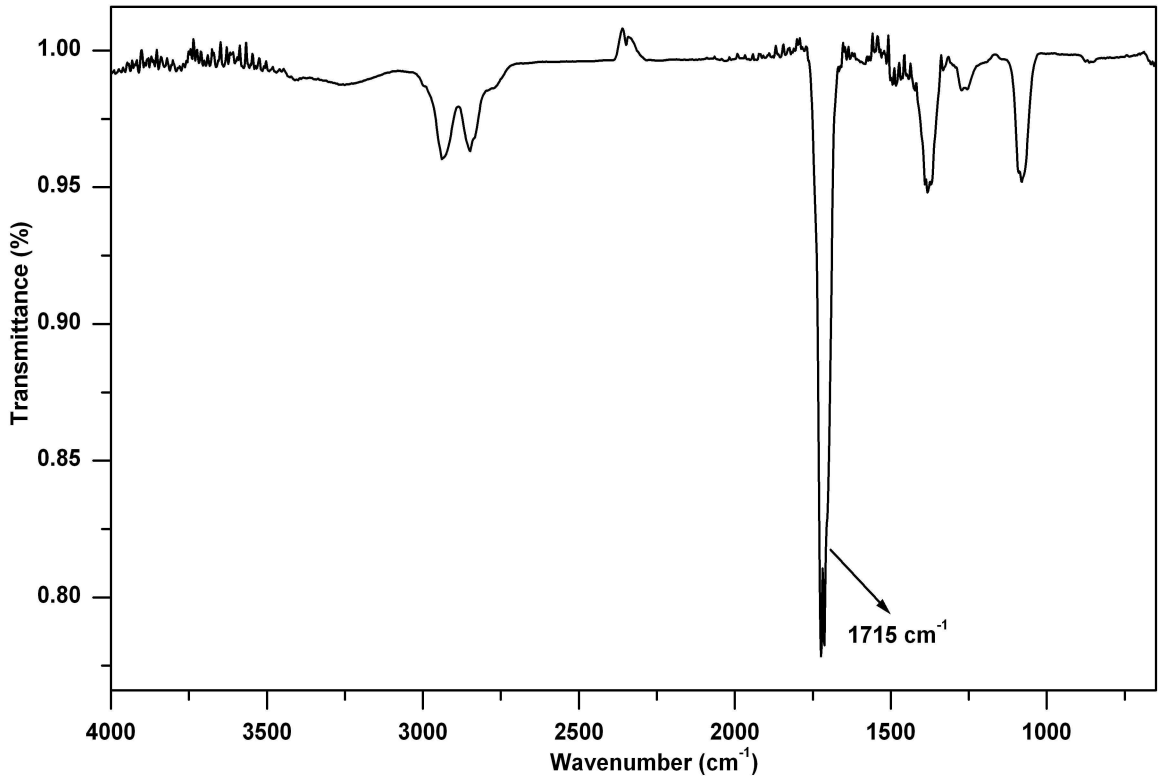

Figure 3.19 FT-IR spectrum of the volatile molecules liberated from **4** at 130 ºC.

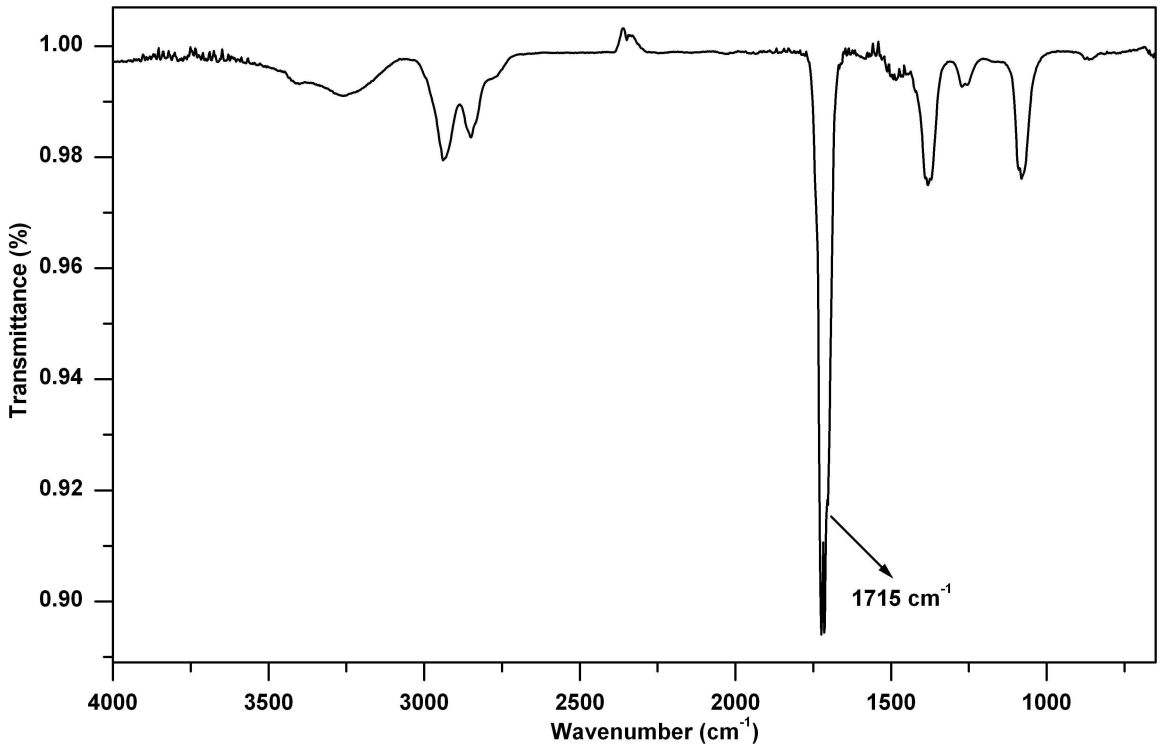

Figure 3.20 FT-IR spectrum of the volatile molecules liberated from **5** at 130 ºC.

The existence of volatile DMF molecules, liberated by heating the as-synthesized samples of **4** and **5**, was confirmed by TG-IR analysis (Figure 3.19 and 3.20). In the FT-IR spectra of the

volatile molecules removed from **4** and **5** at 130 ºC, the strong absorption band at *ca.* 1715 cm^{-1} is due to the C=O stretching frequency of gaseous DMF molecules.

UV-Vis spectroscopy. The UV-Vis spectra of **1** and **2** in methanol solution display a common absorption band in the UV region at around 380 nm, which corresponds to the intraligand $n \rightarrow \pi^*$ transition.[164] In addition, both **1** and **2** also exhibit well-developed bands in the range of 370–1100 nm (Figures 3.21a and 3.22a) owing to the d–d transitions of Co^{II} and Ni^{II} ions.[165]

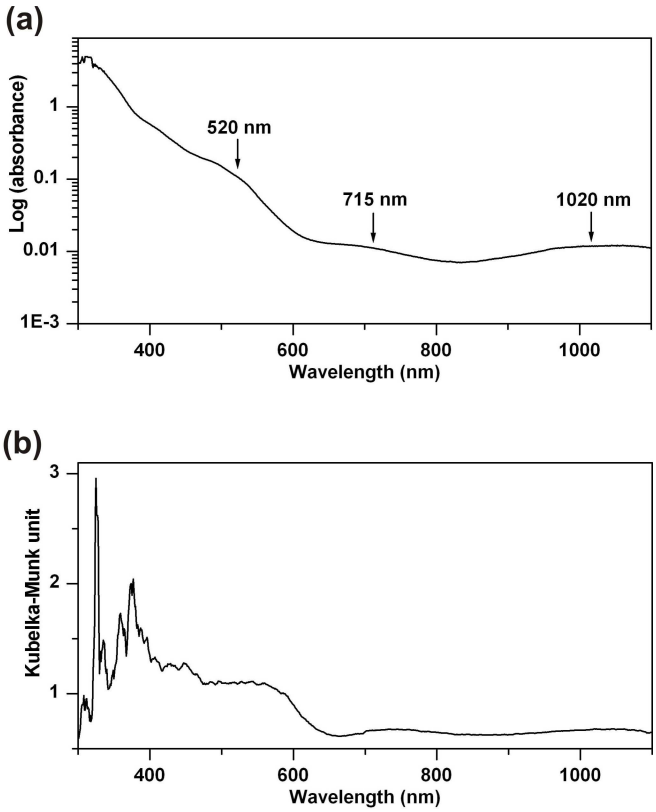

Figure 3.21 (a) UV-Vis spectrum of **1** in methanol solution. (b) UV-Vis diffuse reflectance spectrum of **1**.

Compound **1**, which contains all octahedrally coordinated Co^{II} ions displays three absorption bands at 1020, 715 and 520 nm, which can be attributed to the spin-allowed transitions from $^4T_{1g}(F)$ to $^4T_{2g}(F)$ (ν_1), $^4T_{1g}(P)$ (ν_2) and $^4A_{2g}$ (ν_3), respectively. The calculated values of *Dq* (1070 cm^{-1}) and *B* (715 cm^{-1}) from these transitions is comparable to those of other six-coordinate octahedral Co^{II} compounds.

Compound **2**, which possesses all octahedrally coordinated Ni^{II} ions, shows three absorption bands at 980, 615 and 380 nm due to the spin-allowed transitions from $^3A_{2g}$ to $^3T_{2g}(F)$ (ν_1),

$^3T_{1g}(F)$ (ν_2) and $^3T_{1g}(P)$ (ν_3), respectively. The ν_3 transition of **2** is probably overlapped with the intraligand $n \rightarrow \pi^*$ transition. The values of Dq (1085 cm^{-1}) and B (775 cm^{-1}) which have been estimated from these transitions are typical for six-coordinate octahedral Ni^{II} compounds.

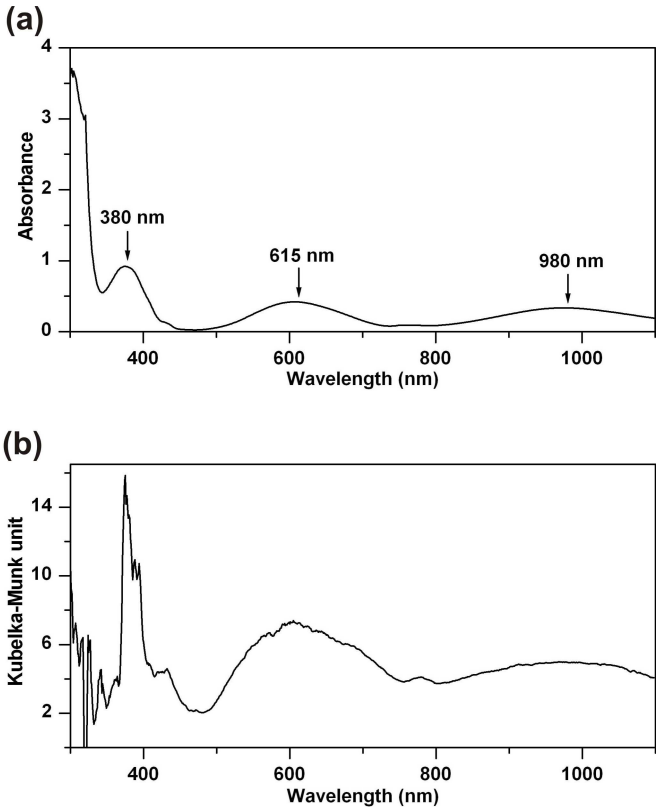

Figure 3.22 (a) UV-Vis spectrum of **2** in methanol solution. (b) UV-Vis diffuse reflectance spectrum of **2**.

The UV-Vis diffuse reflectance spectra (DRS) of **1** and **2** (Figure 3.21b and 3.22b) show similar absorption bands if compared to the solution UV-Vis spectra, which indicates that the compounds maintain their structural integrity in solution.

The UV-Vis spectra (Figure 3.23a) of **5** recorded at room temperature in chloroform solution, displays one strong absorption band at 390 nm (ε = 45,700 L mol^{-1} cm^{-1}), which can be assigned to a metal-to-ligand charge transfer (MLCT) from the occupied d orbitals of the Fe^{II} ions to the empty π^* orbitals of the OMe_2bta ligands.[165] MLCT bands at analogous positions have been reported for a series of octahedral Fe^{II} compounds with N-donor ligands.[191g] In addition, **5** exhibits two weak absrption bands at 850 and 540 nm (respective ε values are 41 and 1150 L mol^{-1} cm^{-1}) owing to the d–d transition of the octahedrally

coordinated HS and LS Fe^{II} ions, respectively.[165] The absorption peak at 540 nm is due to transition from $^1A_{1g}$ to $^1T_{2g}$, whereas the weak, broad absorption peak at 850 nm is attributed to transition from $^5T_{2g}$ to ^5E_g. Absorption bands at similar positions for both HS and LS Fe^{II} ions have been previously observed in the Fe^{II} compound, $[Fe_3(Ettrz)_6(H_2O)_6][(CF_3SO_3)_6]$ at 77 K in solid-state.[195d-e]

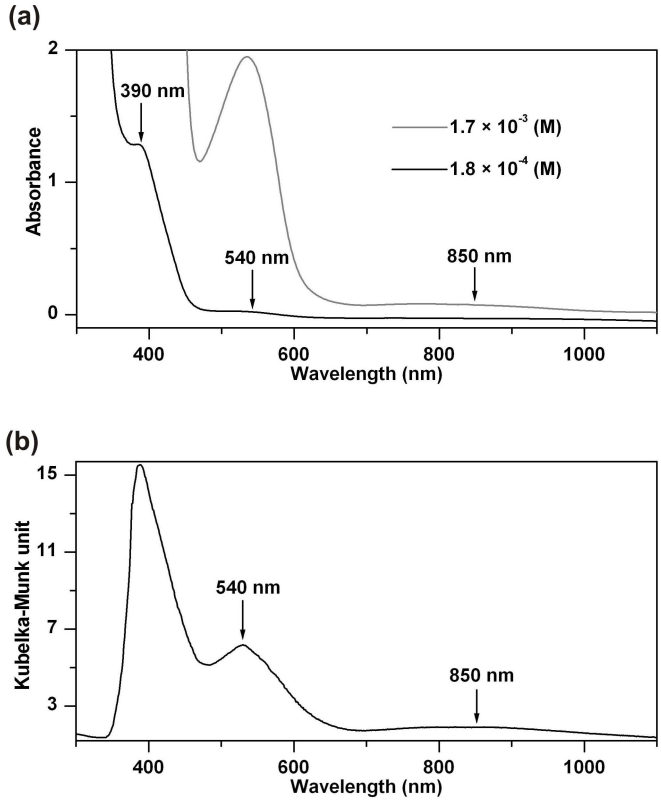

Figure 3.23 (a) Room temperature UV-Vis spectra of **5** in $CHCl_3$ solution recorded at two different concentrations (2.8×10^{-5} M, black; 1.7×10^{-3} M, grey). (b) Solid state UV-Vis spectrum of **2** calculated from a diffuse reflection spectrum recorded from a powder sample.

The solid state UV-Vis spectrum (Figure 3.23b) of **5** recorded at room temperature exhibits bands similar to those found in the solution UV-Vis spectrum. The similar position of absorption bands in both the solid-state and solution UV-Vis spectra recorded at room temperature provide substantial evidence for the fact that all three Fe^{II} ions retain their octahedral coordination environment in solution.

Electrochemistry. The cyclic voltammogram (CV) of **5** in chloroform solution recorded at room temperature is shown in Figure 3.24.

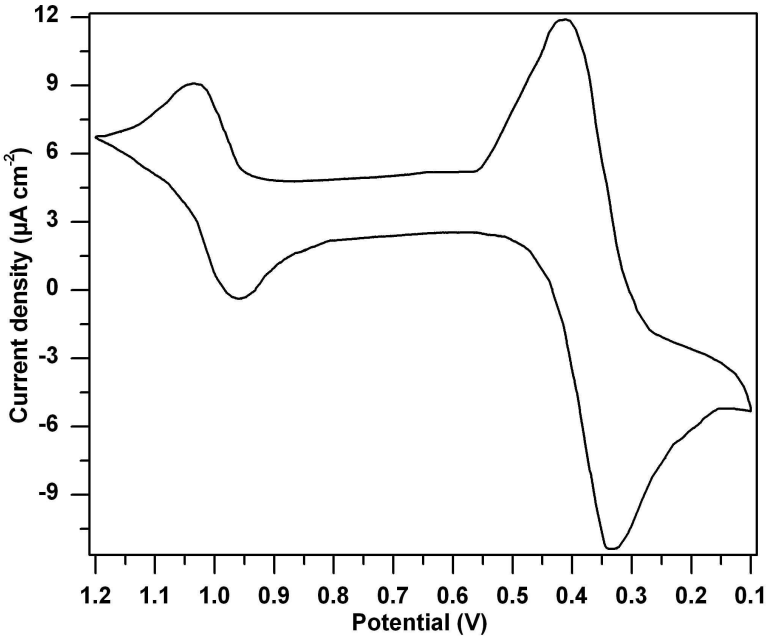

Figure 3.24 Room temperature cyclic voltammogram of **5** (left) and ferrocene (Fc) (right) in $CHCl_3$ with 1.0 (M) [*n*-Bu_4N][PF_6], at a potential scan rate of 0.01 V/sec at a glassy carbon electrode using Ag/Ag^+ as quasi-reference electrode and Fc/Fc^+ as internal reference.

The CV of **5** shows a one-electron transfer attributed to the oxidation of Fe^{II} to Fe^{III} ion. The values of cathodic and anodic peak potentials (E_{pc} and E_{pa}) evaluated from the CV at a potential scan rate of 0.01 V/sec are 1.04 and 0.98 V vs. Ag/Ag^+ quasi-reference electrode, respectively. The oxidation process is reversible, since the difference between the cathodic and anodic peak potentials ($\Delta E_p = E_{pc}-E_{pa}$ = 0.06 V) remains unchanged on variation of potential sweep rate. Due to poor electron conjugation of the metal ions, the three Fe^{II} centres present in **5** show no electronic interactions, and thus all of them are oxidized to Fe^{III} at roughly the same potential. The estimated value of half-wave potential ($E_{1/2}$) for the Fe^{2+}/Fe^{3+} redox couple of **5** vs. Ag/Ag^+ quasi-reference electrode is 1.01 V. Employing Fc/Fc^+ ($E_{1/2}$ = 0.36 V) as internal reference, the corresponding $E_{1/2}$ value vs. Fc/Fc^+ becomes 0.65 V. Thus, the oxidation of **5** occurs at a significantly higher potential compared to ferrocene.

3.2.3 Structure Description

The structures of the nonanuclear compounds can be deduced from the pentanuclear Kuratowski-type coordination units having $\{MZn_4L_6\}^{4+}$ (M = Zn, Fe^{II}, Co^{II}, Ni^{II}, or Cu^{II}; L = 1,2,3-benzotriazolate) cores, which have been described in Chapter 2. In the pentanuclear compounds,[10c,10f,12,13] six tridentate Me_2bta ligands are coordinated to the central ion (M) (Figure 3.2). The six Me_2bta ligands span a Cartesian coordinate system with the Cartesian

axes running through the octahedral metal ion at the origin and the N^2 donor atoms of the coordinated ligands. The Me_2bta ligands are twisted around their coordinative bond to the central metal ion such that the nitrogen atoms are placed on the edges of an imaginary tetrahedron. At the corners of this tetrahedron are placed four additional Zn^{II} ions which are coordinated to three benzotriazolate ligands (via their N^1 and N^3 donor atoms) and one chloride anion. Following this, the structures of the nonanuclear compounds described herein can be formally derived from fusing two tetrahedral lacunary $\{MZn_4L_6\}^{4+}$ cores via a shared metal ion that is placed in the centre (Figure 3.25a). In the asymmetric unit of the crystallographic unit cell, the common metal(II) ion resides on an inversion center.

X-ray crystallographic analyses reveal that **1** and **2** crystallize in the highly symmetric hexagonal space groups $R\bar{3}c$ and $R\bar{3}$, respectively, whereas **3**-**5** crystallize in the relatively lower symmetric space groups (**3**: triclinic $P\bar{1}$, **4**-**5**: monoclinic $P2_1/n$). The molecular structures of **1**-**5** are shown in Figure 3.25. All of them contain six tetrahedral (peripheral) and three octahedral metal ions. Each of the peripheral metal ions is coordinated to three different benzotriazolate ligands (via their N^1 and N^3 donor atoms), and variable number (4-6) of terminal ligands, leading to different coordination geometries (**1**-**2**: hexacoordination, **3**: pentacoordination, **4**-**5**: tetracoordination). Three methanol molecules are coordinated to the peripheral Co(II) ions in compound **1**, and nitrate counteranions are placed at suitable positions in the crystal lattice. In contrast, the nitrate anion in compound **2** is coordinated directly to the peripheral Ni(II) centers together with an additional methanol molecule. In compound **3**, each peripheral Zn atom is coordinated by one bidentate acetate anion, which binds in η^2-mode. The peripheral Zn atoms in **4** and **5** are coordinated with one monodentate chloride anion. Thus, the charges of the $\{M_9L_{12}\}^{6+}$ cores are balanced by either coordinated (**2**: nitrate, **3**: acetate, **4**-**5**: chloride) or non-coordinated (**1**: nitrate) anions. The two octahedral metal ions which reside in the centre of the imaginary tetrahedrons are coordinated to six different benzotriazolate ligands via their N^2 donor atoms. On the other hand, the octahedral metal atom through which the two imaginary tetrahedrons are connected is bound to six different benzotriazolate ligands via their N^1 and N^3 donor atoms. Hence, the three six-coordinated metal ions in all the compounds reside in an octahedral $[M^{II}N_6]$ ligand field.

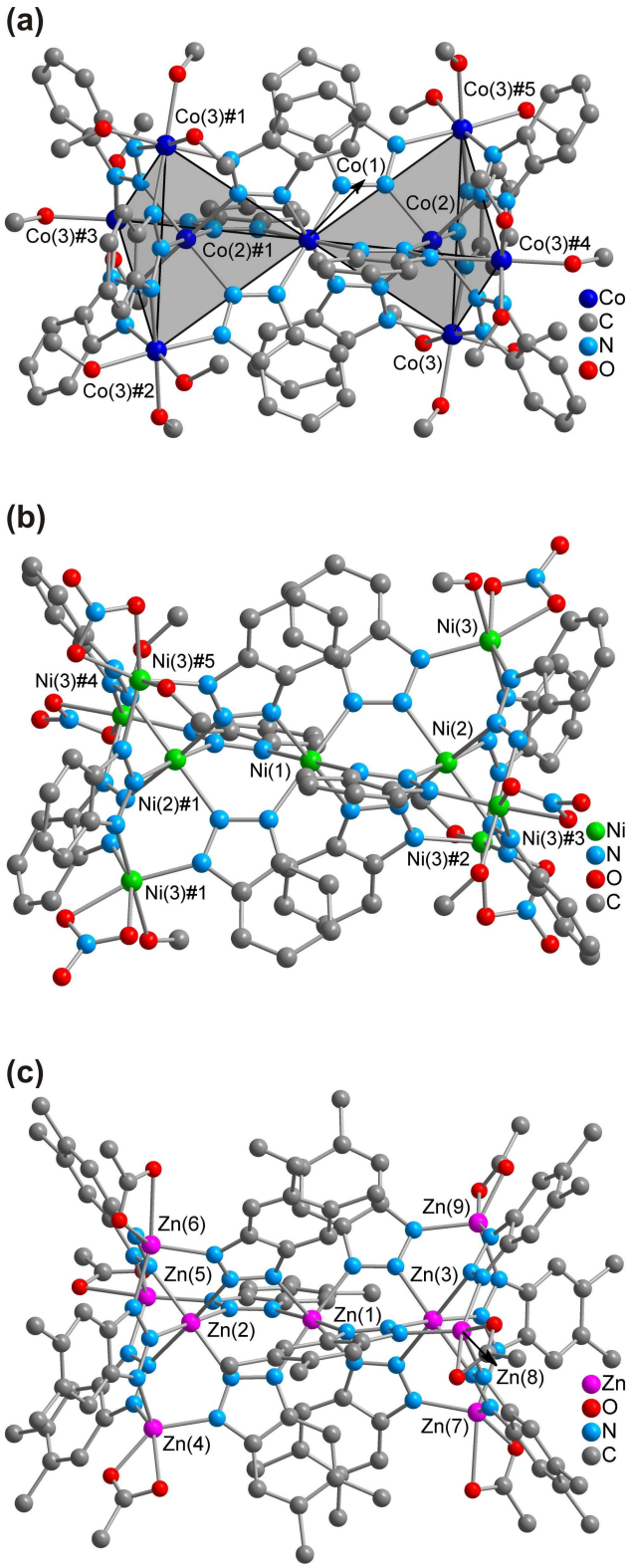
(a)
Co(3)#1
Co(3)#5
Co(1)
Co(2)
Co(3)#3
Co(2)#1
Co(3)#4
Co
C
N
O
Co(3)
Co(3)#2
(b)
Ni(3)
Ni(3)#5
Ni(3)#4
Ni(2)
Ni(1)
Ni(2)#1
Ni(3)#3
Ni
N
O
C
Ni(3)#2
Ni(3)#1
(c)
Zn(9)
Zn(6)
Zn(5)
Zn(3)
Zn(1)
Zn(2)
Zn(8)
Zn
O
N
C
Zn(7)
Zn(4)

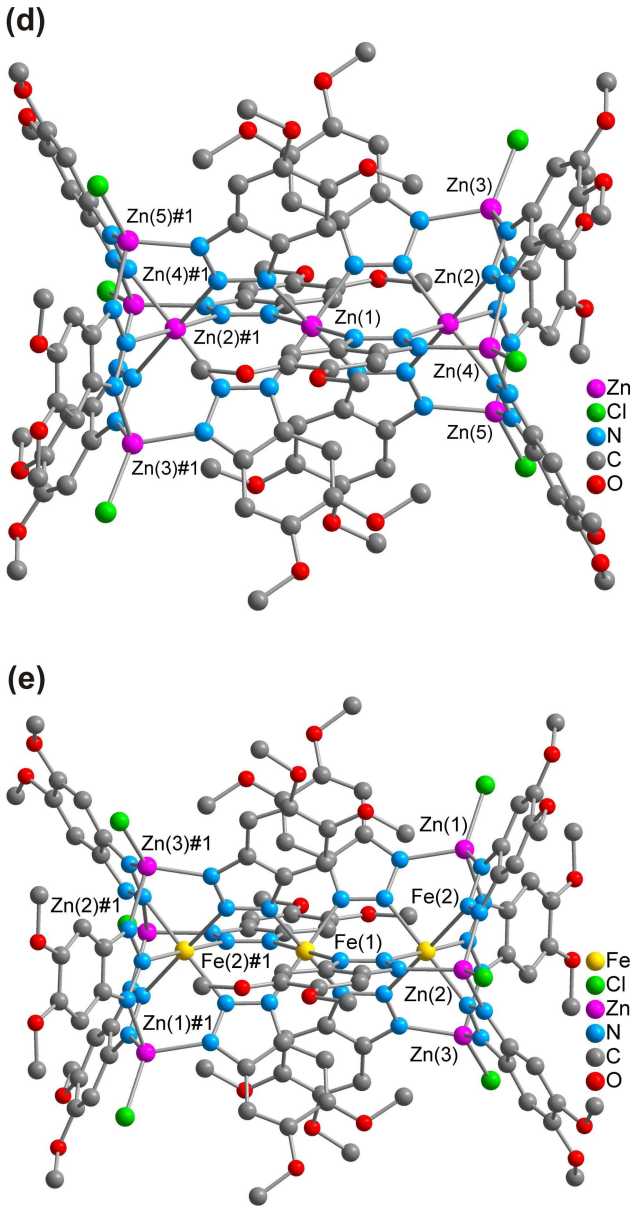

Figure 3.25 Ball-and-stick representation of the molecular structure of **1** (a), **2** (b), **3** (c), **4** (d), and **5** (e). For **1**, the symmetry operators used to create equivalent metal atoms are #1: -x, -y, -z; #2: -x+y, -x, z; #3: -y, x-y, z; #4: y, -x+y, -z and #5: x-y, x, -z. For **2**, they are #1: 2-x, 2-y, -z; #2: y, 1-x+y, -z; #3: 1+x-y, x, -z; #4: 1-x+y, 2-x, z and #5: 2-y, 1+x-y, z. For **4**, it is #1: 3-x, -y, 1-z. For **5**, it is #1: 1-x, -y, -z.

The selected bond lengths obtained from single crystal X-ray diffraction data of **4** and **5** are summarized in Table 3.4 and 3.5, respectively. The Zn-N distances for the six tetrahedral Zn^{II} ions in **4** fall into the narrow range of 2.00-2.01 Å. However, the six tetrahedrally coordinated Zn^{II} ions in **5** exhibit Zn-N distances with slightly larger deviations (1.99-2.06 Å) compared to that of **4**. For the three octahedral metal(II) (M^{II}) ions in both **4** and **5**, the M-N distances fall in a wide range of 2.00-2.23 Å. The Zn-N distances for the central and the two

adjacent octahederally coordinated Zn^{II} ions in **4** range from 2.14-2.15 Å and from 2.16-2.23 Å, respectively. For **5**, the Fe-N distances for the central and the adjacent octahedrally coordinated Fe^{II} ions show bond length variations from 2.00-2.03 Å and 2.13-2.22 Å, respectively. Noteworthingly, the central, octahedral M^{II} ions in each compound have smaller M-N distances than the two adjacent octahedrally coordinated M^{II} ions. For **5**, the difference between the average Fe-N distances for the central (Fe(1)) and the adjacent (Fe(2)) ions is 0.16 Å. This significant difference between the Fe-N distances of two crystallographically unique Fe^{II} ions indicates that the Fe^{II} ions are in different spin states, of which the LS state can be tentatively assigned to the central Fe^{II} ion, which rests in a more compressed coordination cage if compared to the other Fe ions (all data refering to the single crystalline state at a temp. of 223 K). Similar values of Fe-N distances with large difference between them ($\Delta r = r_{HS} - r_{LS} \approx 2.20\text{-}2.00 \approx 0.20$ Å) have been documented in literature for LS and HS Fe^{II} ions, respectively, in compounds bearing octahedral $[Fe^{II}N_6]$ units.[191a,191d-g,195] Crystallographic studies on the heteropentanuclear Fe^{II} compound, $[FeZn_4Cl_4(Me_2bta)_6]\cdot 2DMF$ (**3a** of Chapter 2) reveal an average Fe-N distance of 2.198(8) Å, indicating the compound to be present in HS state at 298 K. Noteworthingly, the existence of one LS (central) and two HS Fe^{II} ions has been previously reported by Reedijk *et al.* in the crystal structure of the linear trinuclear Fe^{II} compound, $[Fe_3(Ettrz)_6(H_2O)_6][(CF_3SO_3)_6]$ at 105 K.[195d-e] The different M-N distances for all the three octahedral M^{II} ions in both **4** and **5** suggest that they are in distorted octahedral $[M^{II}N_6]$ environments. The values of Zn-N distances observed in the present compounds fall in the typical range of distances from 1.98-2.22 Å for tetrahedral Zn^{II} and 2.14-2.25 Å for octahedral Zn^{II} of **3** (Table 3.3) and a previously reported[10f] structurally similar homononanuclear Zn^{II} triazolate compound.

Table 3.3 Selected bond lengths (Å) of **3**.

Zn(6)-N(16)	2.137(5)	Zn(4)-N(26)	2.168(6)	Zn(5)-N(24)	1.991(5)
Zn(6)-N(10)	2.142(6)	Zn(4)-N(23)	2.168(6)	Zn(5)-N(30)	2.004(6)
Zn(6)-N(22)	2.144(6)	Zn(4)-N(20)	2.186(6)	Zn(5)-N(34)	2.061(6)
Zn(6)-N(21)	2.165(6)	Zn(4)-N(29)	2.193(5)	Zn(7)-N(25)	1.981(5)
Zn(6)-N(13)	2.167(6)	Zn(4)-N(35)	2.215(6)	Zn(7)-N(33)	2.005(6)
Zn(6)-N(27)	2.170(6)	Zn(4)-N(32)	2.255(6)	Zn(7)-N(36)	2.042(6)
Zn(1)-N(17)	2.151(5)	Zn(2)-N(12)	1.992(5)	Zn(8)-N(3)	2.023(6)
Zn(1)-N(14)	2.154(6)	Zn(2)-N(9)	2.009(6)	Zn(8)-N(7)	2.028(6)
Zn(1)-N(11)	2.177(5)	Zn(2)-N(6)	2.028(6)	Zn(8)-N(18)	2.045(5)

Zn(1)-N(5)	2.220(6)	Zn(3)-N(31)	1.997(6)	Zn(9)-N(4)	2.003(6)
Zn(1)-N(8)	2.222(5)	Zn(3)-N(19)	2.006(5)	Zn(9)-N(15)	2.004(5)
Zn(1)-N(2)	2.223(6)	Zn(3)-N(28)	2.047(6)	Zn(9)-N(1)	2.034(6)

Table 3.4 Selected bond lengths (Å) of **4**.

Zn(1)-N(18)	2.139(6)	Zn(2)-N(17)	2.177(5)	Zn(4)-N(16)	2.002(5)
Zn(1)-N(12)	2.139(5)	Zn(2)-N(5)	2.197(6)	Zn(4)-N(1)	2.006(6)
Zn(1)-N(15)	2.150(6)	Zn(2)-N(8)	2.232(6)	Zn(4)-N(4)	2.014(6)
Zn(2)-N(14)	2.157(6)	Zn(3)-N(10)	2.004(5)	Zn(5)-N(7)	1.997(6)
Zn(2)-N(11)	2.160(5)	Zn(3)-N(9)	2.005(6)	Zn(5)-N(13)	2.004(6)
Zn(2)-N(2)	2.172(6)	Zn(3)-N(3)	2.011(6)	Zn(5)-N(6)	2.012(6)

Table 3.5 Selected bond lengths (Å) of **5**.

Fe(1)-N(18)	2.005(8)	Fe(2)-N(8)	2.182(9)	Zn(2)-N(13)	1.992(9)
Fe(1)-N(15)	2.020(8)	Fe(2)-N(5)	2.201(9)	Zn(2)-N(4)	2.014(10)
Fe(1)-N(12)	2.026(9)	Fe(2)-N(2)	2.219(8)	Zn(2)-N(7)	2.061(10)
Fe(2)-N(11)	2.125(9)	Zn(1)-N(1)	2.019(10)	Zn(3)-N(3)	1.990(9)
Fe(2)-N(17)	2.143(9)	Zn(1)-N(6)	2.032(9)	Zn(3)-N(16)	2.010(9)
Fe(2)-N(14)	2.165(9)	Zn(1)-N(10)	2.040(9)	Zn(3)-N(9)	2.018(9)

In the crystal lattices of **1** and **2**, the coordination compounds are arranged along imaginary lines parallel to the crystallographic *c*-axis, as shown in Figures 3.26a-b. They are more densely packed in **1** than in **2**. In **1**, neighboring molecules maintain a distance of 0.35 nm with each other. In **2**, on the other hand, adjacent molecules are 0.8 nm apart from each other, leading to large voids in the structure. Due to the increased steric hindrance caused by the additional two methyl (**3**) and methoxy groups (**4**-**5**) attached with the benzotriazolate ligands in compounds **3**-**5**, the neighboring molecules do not arrange along one line (Figures 3.26c-e), thus reducing the space group symmetry of the corresponding crystal lattices. Though **4** and **5** are isostructural, they pack in slightly different ways within the crystal lattices.

For **1**-**3**, some residual electron density was found in the unit cell, which we ascribe to vastly disordered solvent molecules, the atom positions of which could not be refined. For **3**, several restraints on intramolecular bond distances of occluded DMF molecules had to be applied. The occluded DMF molecules in **4** and **5** are highly disordered, thus it was impossible to refine their positions from electron density distribution obtained from X-ray diffraction data,

even with reduction of crystallographic symmetry. An estimation with the program PLATON/SQUEEZE[167] using the single crystal X-ray data of **5** reveals that the total potentially accessible void volume per unit cell volume is 3428 $Å^3$ which is 41 % of the unit cell volume. Slightly smaller values (2360 $Å^3$ and 31 %) are obtained for **4**, if calculated using crystallographic atom positions with the same program. These void volumes (Figures 3.26d-e) are occupied by the occluded DMF molecules at ambient conditions, as suggested by TG-IR analysis. Noteworthily, the $\eta^1:\eta^1:\eta^1:\mu_3$ coordination mode of deprotonated benzotriazole observed in all the compounds was previously documented for a wide variety of coordination compounds and coordination polymers containing Zn(II),[10] Co(II),[10b-c,11] Ni(II),[10b,11a,12] Cu(II),[9,13] Tl(I),[14] M(III)[15] (M = Fe, Cr, V) ions, including two mixed-valent copper[16] compounds.

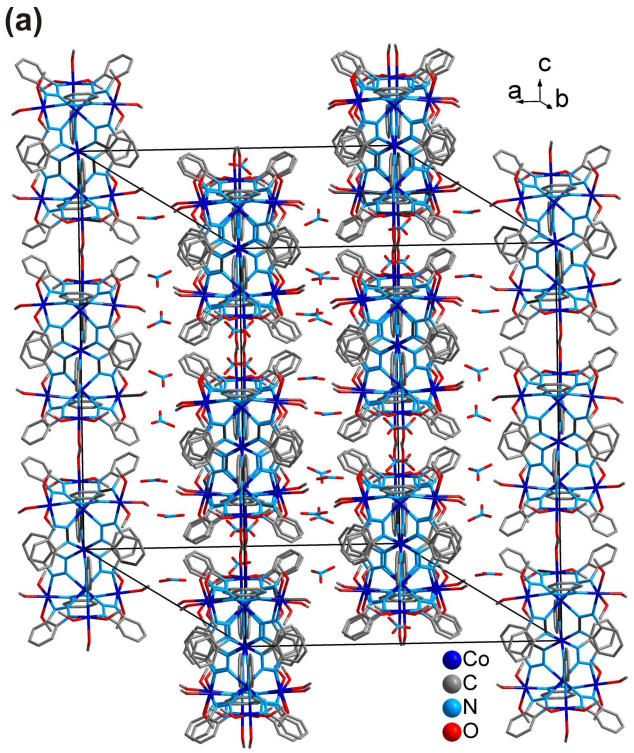
(a)
c
a
b
Co
C
N
O

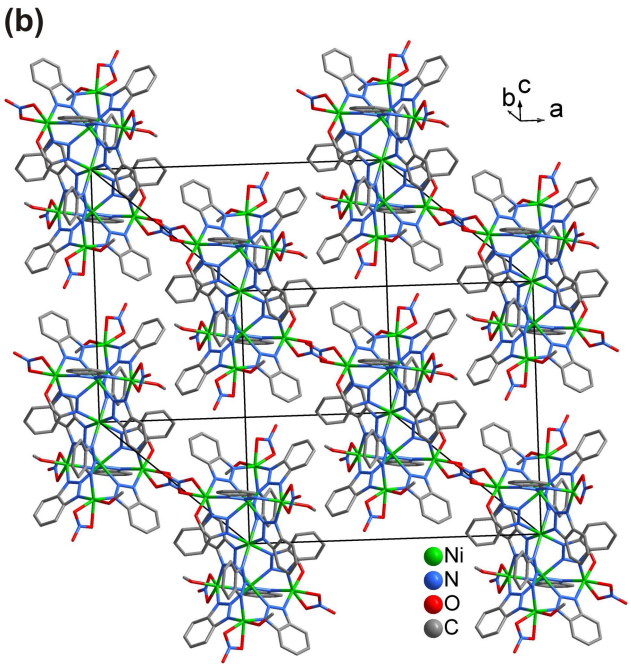
(b)
b
c
a
Ni
N
O
C

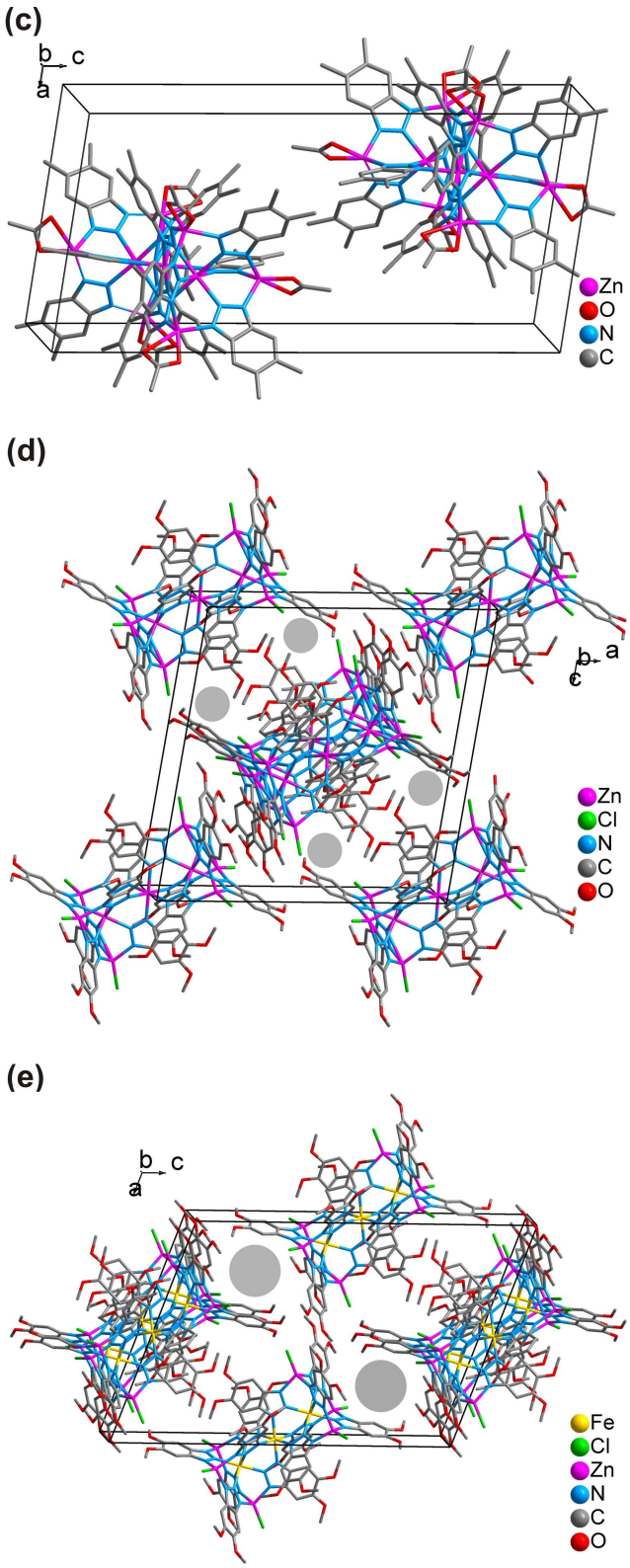

Figure 3.26 Crystal packing diagram of **1** (a), **2** (b), **3** (c), **4** (d), and **5** (e) in wire representation. All H atoms and occluded solvent molecules are omitted for clarity. The grey circles represent void regions in the crystal lattices of **4** and **5** which can be occupied by solvent DMF molecules.

3.2.4 Magnetic Properties

The magnetochemical description of the Co(II)- and Ni(II)-based compounds on the sole basis of low-field susceptibility data is inherently limited to a phenomenological description due to the presence of a multitude of distinct exchange pathways as well as the different local coordination environments. The interpretation of the magnetism of the Co(II)-based **1** is complicated by the fact that the free-ion ^{4}F ground term of Co(II) is separated by the first excited ^{4}P state by more than 104 cm^{-1}.[196] In a weak ligand field with octahedral symmetry, the ^{4}F term splits into $^4T_1$(F), $^4T_2$, and $^4A_2$ terms, while the ^{4}P term transforms into a $^4T_1$(P) term (*cf.* discussion of UV-Vis spectra). The $^4T_1$(F) ground term for a high-spin Co(II) center implies a significant contribution of the orbital momentum. The situation for the Ni(II)-based **2** is less complicated since the d^8 configuration results in an orbital singlet ground state (A_2).[197]

The magnetic data for **1** and **2** were analyzed using a complete basis set (full d manifolds, *i.e.* 120 functions for Co(II) and 45 functions for Ni(II)) as a function of the applied field.[168] Both aspects are necessary to yield reliable information on the magnetic dipole orientation with respect to the local symmetry elements. The simulations take into account the following single-ion effects: interelectronic repulsion (H_{ee}), spin-orbit coupling (H_{SB}), ligand-field effects (H_{lf}), and the applied field (H_{mag}). Generally, for a magnetically isolated 3 d^N metal ion in a ligand field (lf) environment in an external magnetic field *B*, the Hamiltonian of the metal ion is represented by[169,198]

$$\begin{aligned}\hat{H} \;=\; & \underbrace{\sum_{i=1}^{N}\left[-\frac{\hbar^2}{2m_e}\nabla_i^2 + V(r_i)\right]}_{\hat{H}^{(0)}} + \underbrace{\sum_{i>j}^{N}\frac{e^2}{r_{ij}}}_{\hat{H}_{ee}} + \underbrace{\sum_{i=1}^{N}\zeta(r_i)\,\kappa\;\hat{\boldsymbol{l}}_i\cdot\;\hat{\boldsymbol{s}}_i}_{\hat{H}_{so}} + \\ & \underbrace{\sum_{i=1}^{N}\sum_{k=0}^{\infty}\left\{B_0^k C_0^k(i) + \sum_{q=2}^{k}\left[B_q^k\left(C_{-q}^k(i) + (-1)^q C_q^k(i)\right)\right]\right\}}_{\hat{H}_{LF}} + \\ & \underbrace{\sum_{i=1}^{N}\mu_B(\kappa\;\hat{\boldsymbol{l}}_i + 2\;\hat{\boldsymbol{s}}_i)\cdot\;\boldsymbol{B}}_{\hat{H}_{mag}}\end{aligned}$$

Figure 3.27 displays the results of the magnetic susceptibility measurement in the temperature range 2–290 K using μ_{eff} *vs. T* plots (SI units: $\mu_{eff} = 797.74(\chi T)^{1/2}$).

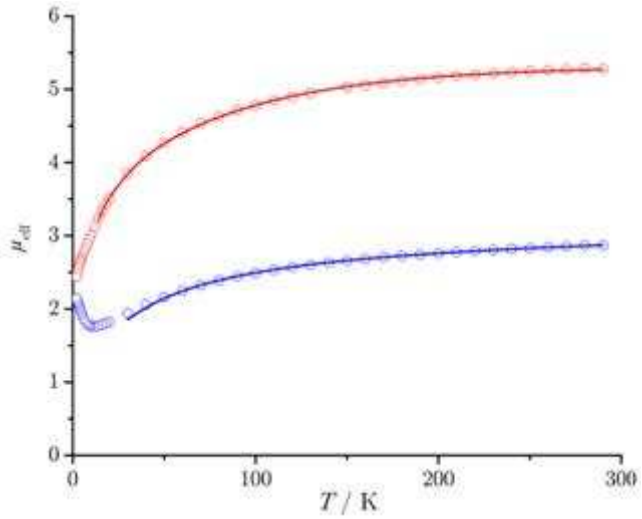

Figure 3.27 Temperature dependence of μ_{eff} for **1** (red) and **2** (blue) at 0.1 Tesla. Open circles: experimental data, graphs: best fits to the employed phenomenological models (see text).

The effective magnetic moment of **1** at 290 K is 5.27 μ_B per Co(II) ion, which is larger than the spin-only value of 3.87 μ_B as a result of spin and first-order orbital contributions. The monotonous decrease of μ_{eff} towards lower temperatures can thus be attributed to both single-ion effects and antiferromagnetic intramolecular exchange coupling. To quantify these effects, the magnetic data considering ligand-field effect, spin-orbit coupling and external magnetic field were analyzed. Note that as stated above the presence of at least four different exchange pathways, all mediated by the benzotriazolate ligands, in both **1** and **2** precludes the unambiguous determination of their associated exchange energies ($J_{1–4}$) based solely on $\chi(B, T)$ data. In such cases, over-parameterization leads to isospectrality issues, i.e. several sets of $J_{1–4}$ reproduce the same thermodynamical susceptibility data. Additional low-temperature, high-field magnetization and neutron scattering measurements are currently planned in order to develop a Heisenberg-type exchange model that identifies all relevant exchange energies. Here, however, the interpretation of the exchange interactions is limited to the phenomenological molecular field approximation:

$$\chi_{\text{m}}^{-1} = \chi_{\text{m}}^{-1}\left(\varsigma, B_q^k\right) - \lambda_{MF}$$

where χ_m is the single-center susceptibility and λ is the molecular field parameter. Positive and negative λ indicates dominant ferromagnetic and antiferromagnetic interactions,

respectively. Note that this effectively reduces the number of exchange parameters from four to one. The parameters λ_{MF} and B_q^k were determined by a least-squares fit. For **1** the best fit for calculated and experimental χ_m values was found for $\lambda_{MF} = -0.463 \times 10^6$ mol m^{-3}, $B_0^2 = 3096$ cm^{-1}, $B_0^4 = 10405$ cm^{-1}, $B_4^4 = 5462$ cm^{-1} ($SQ = 0.5$ %). Note that the negative molecular field parameter λ_{MF} is essential for a good fit. The ligand field splitting based on the magnetochemical analysis of **1**, yielding $Dq = 1167$ cm^{-1}, corresponds well to the parameter established from UV-Vis spectra.

The effective magnetic moment of **2** decreases from 2.83 μ_B per Ni(II) ion (290 K) to a minimum of 1.76 μ_B at 12 K, indicating net antiferromagnetic interactions in this temperature interval. However, ferromagnetic coupling becomes dominant below 12 K and μ_{eff} increases with decreasing temperature, which possibly stems from coupling between the tetranuclear Ni_4 fragments in **2**. Similar differences in coupling have also been observed in other isostructural Ni(II) and Co(II) compounds.[199] For the interval 30 – 290 K, the best fit for calculated and experimental χ_m values was found for $\lambda_{MF} = -0.463 \times 10^6$ mol m^{-3}, $B_0^2 = 8286$ cm^{-1}, $B_0^4 = 25185$ cm^{-1}, $B_4^4 = 15552$ cm^{-1} ($SQ = 0.4$ %).

3.2.5 Mössbauer Spectroscopy

Due to the easy loss of solvent molecules from the crystalline material **5**, Mössbauer experiments were carried out with the fully desolvated **5a** at 7 K and at 160 K. The resulting spectra are shown in Figure 3.28. The spectrum at 7 K (Figure 3.28a) consists of two doublets with relative intensities of 1:2 (34:66), which is consistent with the results from the single-crystal structure determination where the peripheral two of the three Fe^{II} ions are related by symmetry due to a crystallographical inversion center and are quite distinct from the third Fe^{II} ion. Based on the isomer shift (δ_{IS}) of 0.43 mm s^{-1} and the quadrupole splitting (ΔE_Q) of 0.48 mm s^{-1}, the less intense signal of the two is attributed to a LS Fe^{II} ion. The second component displays an isomer shift (δ_{IS}) of 1.21 mm s^{-1} and a quadrupole splitting (ΔE_Q) of 1.68 mm s^{-1}. The larger values for the isomer shift and the quadrupole splitting of the second component are clear evidence that the origin of this signal comes from the peripheral HS Fe^{II} ions. A comparison of the results of the Mössbauer spectrum at 7 K with that of the structure determination at 223 K supports the previous assignment of the central iron site to a LS Fe^{II} ion and the peripheral ones to HS Fe^{II} ions.

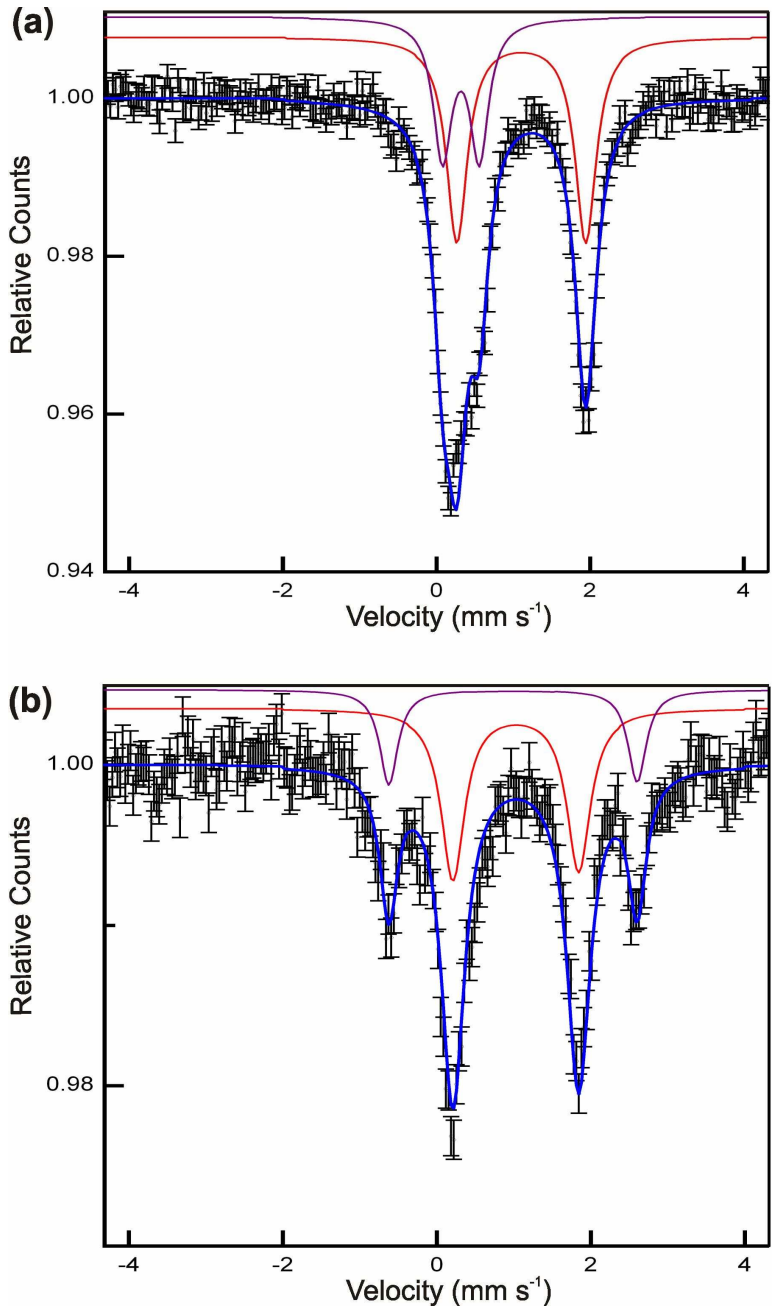

Figure 3.28 Mössbauer spectra of **2a** at (a) 7 K and at (b) 160 K. The purple and red subspectra are fitted with the experimental values (black points with error bars).

Upon raising the temperature to 160 K, the Mössbauer spectrum (Figure 3.28b) shows severe changes. The spectrum is still a superposition of signals arising from two components. The ratio of intensities is, however, now 1:3 (25:75), which is lower than expected. This might be a consequence of lowering the signal to noise ratio in the Mössbauer spectrum with increasing temperature and/or of different temperature dependencies of the Debye-Waller factors associated with the two contributing iron sites. The larger signal occurs at an isomer shift (δ_{IS}) of 1.13 mm s^{-1} with a quadrupole splitting (ΔE_Q) of 1.63 mm s^{-1}. These parameters are similar to the previous parameters of the larger signal at 7 K and display the typically observed decrease of δ_{IS} and ΔE_Q values with temperature. The weaker signal, on the other

hand, experiences a drastic change. Thus, the new values for δ_{IS} of 1.10 mm s^{-1} and for ΔE_Q of 3.22 mm s^{-1} arising from the central Fe^{II} ion can only be rationalized as the result of a spin crossover during which the central Fe^{II} adopts a HS state at 160 K. The conclusion of a spin crossover process below 160 K is also corroborated by the observation that the powder **5a** changes its color from brownish-yellow to red upon cooling to liquid nitrogen temperatures. The spin state of the central Fe^{II} ion in this powder contrasts with that of the crystalline material. Due to the presence of additional solvent molecules in the crystal lattice, the LS state of the central Fe^{II} ion is stabilized and is still observable at 223 K. The decisive dependence of spin crossover properties on crystal solvent molecules or type of counteranions has already been noted in many other examples.[191a,191c-d,191g,191i,191p,195m]

3.3 Experimental Section

3.3.1 Materials and General Methods

The OMe_2btaH ligand was synthesized as described previously.[200] All other starting materials were of reagent grade and used as received from the commercial supplier. Fourier transform infrared (FT-IR) spectra were recorded from KBr pellets in the range 4000–400 cm^{-1} on a Bruker IFS FT-IR spectrometer. The following indications are used to characterize absorption bands: very strong (vs), strong (s), medium (m), weak (w), shoulder (sh), and broad (br). UV-Vis diffuse reflectance spectra (DRS) were recorded on an Analytik Jena Specord 50 UV-Vis spectrometer in the range of 300–1100 nm and converted into normal absorption spectra with the Kubelka–Munk function.[186] The lamps change at 320 nm and the mirrors change at 370, 400, 700 and 900 nm. For **2**, the sample was diluted with $BaSO_4$ (sample:$BaSO_4$ = 1:3) prior to measurement. UV-Vis spectra in solution were measured using the same UV-Vis spectrometer. Elemental analyses (C, H, N) were carried out on a Perkin-Elmer 2400 Elemental Analyzer. Thermogravimetric analyses (TGA) were performed with a TGA/SDTA851 Mettler Toledo analyzer in a temperature range of 25–800 °C in flowing nitrogen at a heating rate of 10 °C min^{-1}. TG-IR analyses were carried out using a Netzsch STA 409 simultaneous thermal analyzer coupled with a Bruker IFS 55 Equinox FT-IR spectrometer in a temperature range of 30–1100 °C under N_2 atmosphere with a heating rate 10 °C min^{-1}. X-ray powder diffraction (XRPD) patterns were measured using a Philips X′Pert PRO powder diffractometer operated at 40 kV, 40 mA for Cu target (λ = 1.5406 Å) with a scan speed of 30 s $step^{-1}$ and a step size of 0.008°. The simulated powder patterns were

calculated using single-crystal X-ray diffraction data. Energy dispersive X-ray analysis (EDX) was performed on an EDAX (Phönix) X-ray detection system with 30 mm^2 SUTW window. ICP-AES analysis was carried out with a Thermo Scientific iCap 6500 emission spectrometer. Magnetic susceptibility data were determined by SQUID magnetometer (MPMS-XL5, Quantum Design) in the temperature range T = 2.0 to 290 K and at an applied field of B_0 = 0.1 T. The data were corrected for the sample holder (PTFE tubes) and calculated diamagnetic contributions (χ_{dia}(**1**) = -2.75×10^{-8} m^3 mol^{-1}., χ_{dia}(**2**) = -1.75×10^{-8} m^3 mol^{-1}). Cyclic voltammetry experiments were performed with a computer-controlled VoltaLab 40 PGZ301 potentiostat (Radiometer Analytical, France) potentiostat in a three-electrode single-compartment cell with a glassy carbon working electrode, a platinum wire counter electrode, and an Ag/AgCl reference electrode. All potentials were internally referenced to the ferrocene/ferrocenium (Fc/Fc^+) couple. Mössbauer spectra were recorded with a conventional spectrometer (Wissel GmbH, Germany) in a constant acceleration mode. The temperature can be maintained between 6 K and 400 K by a closed-cycle cryostat unit (Advanced Research Systems Inc., USA). The sample holder is mounted on the tip of the second stage heat station of the expander unit DE204SF inside a radiation shield and a vacuum shroud. The expander unit is decoupled from the vibrations of the compressor ARS-4HW by a DMX20-41 interface. The temperature is controlled by a Lakeshore 331S unit. The sample was diluted in lactose and placed between aluminium foils in the sample holder. Thus, below 30 K the accuracy of the temperature is within 1 K. The windows of the vacuum shroud are made of mylar foils. The spectra were analyzed by least-square fits using a Lorentzian line shape with the program WinNormus-for-Igor Version 2.0. The isomer shifts are given relative to α-iron at room temperature.

Safety Note! Benzotriazoles and benzotriazolate compounds are potentially explosive, and caution should be exercised when dealing with such derivatives. However, the small quantities used in this study were not found to present a hazard.

3.3.2 Syntheses

Synthesis of $[Co_9(bta)_{12}(MeOH)_{18}][(NO_3)_6]\cdot 9C_6H_6$ (1). A solution of btaH (3.33 g, 27.96 mmol) in ethanol (100 mL) was combined with a solution of $Co(NO_3)_2\cdot 6H_2O$ (1.02 g, 3.49 mmol) in the same solvent (100 mL). The mixture was refluxed for 1 h and cooled to room temperature. The resulting precipitate (0.73 g) was collected by filtration and dried in vacuum. Reddish orange rhombohedral crystals of **1** suitable for single crystal X-ray

diffraction were grown within 3 days by layering a methanol solution (1 mL) of this precipitate (0.06 g) over benzene (1 mL) in a NMR tube. Samples for analytical studies were dried under vacuum, thus removing all non-coordinated benzene molecules.

Synthesis of $[Ni_9(bta)_{12}(NO_3)_6(MeOH)_6]\cdot 4THF$ (2). To a solution of btaH (1.69 g, 14.25 mmol) in acetonitrile (150 mL), $Ni(NO_3)_2\cdot 6H_2O$ (1.04 g, 3.56 mmol) was added as solid. The mixture was stirred at room temperature for 30 min and left undisturbed at room temperature for 2 days. The resulting purple precipitate (0.56 g) was collected by filtration and dried in vacuum. Blue rhombohedral crystals of **2** were obtained within a week by layering a methanol solution (1 mL) of this precipitate (0.05 mg) over THF (1 mL) in a NMR tube.

Synthesis of $[Zn_9(Me_2bta)_{12}(CH_3COO)_6]\cdot 3DMF$ (3). A solution of $Zn(CH_3COO)_2\cdot 2H_2O$ (0.10 g, 0.46 mmol) in DMF (10 mL) was combined with a solution of Me_2btaH (0.61 g, 3.72 mmol) in the same solvent (10 mL). The mixture was stirred at room temperature for 30 min and left undisturbed at room temperature. Slow evaporation of the solvent within 3 days resulted colorless, block-shaped crystals of **3**. They were filtered off and dried in vacuum, thus removing all occluded DMF molecules. Yield: 0.07 g (0.03 mmol, 49 %).

Synthesis of $[Zn_9(OMe_2bta)_{12}Cl_6]\cdot DMF$ (4): solvothermal method. A mixture of anhydrous $ZnCl_2$ (0.05 g, 0.36 mmol) and OMe_2btaH (0.09 g, 0.50 mmol) was dissolved in 4 mL of DMF and the solution was placed in a heating tube (10 mL). The tube was sealed and heated at 120 ºC for 20 h, then cooled to room temperature. The supernatant was removed and the remaining colorless block-shaped crystals of **4** were washed with DMF (3 × 1 mL) and dried in air. Yield: 0.06 g (0.02 mmol, 49 %).

Vapor diffusion method. A mixture of anhydrous $ZnCl_2$ (0.05 g, 0.36 mmol) and OMe_2btaH (0.09 g, 0.50 mmol) was placed in a small vial (5 mL) and dissolved in 3 mL of DMF. The vial was then placed in a larger vial (30 mL) containing 6 mL of DMF and 113 µL of 2,6-lutidine. The larger vial was sealed and left undisturbed for 5 days. The resulting colorless block-shaped crystals of **4** were collected by filtration, washed with DMF (3 × 1 mL), and dried in air. Yield: 0.07 g (0.02 mmol, 57 %). This material exhibited the same analytical results as the one obtained by the solvothermal method.

Synthesis of $[Fe_3Zn_6(OMe_2bta)_{12}Cl_6]\cdot DMF$ (5): solvothermal method. A mixture of $Fe(ClO_4)_2\cdot 6H_2O$ (0.05 g, 0.20 mmol), anhydrous $ZnCl_2$ (0.05 g, 0.36 mmol) and OMe_2btaH

(0.13 g, 0.72 mmol) was dissolved in 4 mL of DMF and the solution was placed in a glass tube (10 mL). The tube was sealed and heated at 120 °C for 20 h, then cooled to room temperature. The resulting red block-shaped crystals of **5** were collected by filtration, washed with DMF (3 × 1 mL). Yield: 0.07 g (0.02 mmol, 38 %).

Vapor diffusion method. A mixture of $Fe(ClO_4)_2 \cdot 6H_2O$ (0.05 g, 0.20 mmol), anhydrous $ZnCl_2$ (0.05 g, 0.36 mmol) and OMe_2btaH (0.13 g, 0.72 mmol) was placed in a small vial (5 mL) and dissolved in 3 mL of DMF. The vial was then placed in a larger vial (30 mL) containing 6 mL of DMF and 182 µL of 2,6-lutidine. The larger vial was sealed and left undisturbed for 10 days. The resulting red block-shaped crystals of **5** were collected by filtration, washed with DMF (3 × 1 mL), and dried in air. Yield: 0.08 g (0.03 mmol, 44 %). The material obtained by the vapour diffusion method showed the same analytical results as the one obtained by the solvothermal method.

Table 3.6 Elemental analyses[a] of all the compounds described in this chapter.

Compound	C (%)	H (%)	N (%)
1	37.74 (37.31)	3.92 (4.17)	20.85 (20.30)
2	40.30 (40.34)	3.82 (3.74)	21.16 (21.02)
3	47.86 (48.09)	4.22 (4.26)	18.77 (18.69)
4	39.26 (39.47)	3.39 (3.44)	17.06 (17.20)
5	39.68 (39.85)	3.42 (3.47)	17.19 (17.36)

[a] Calculated values are given within parentheses.

Table 3.7 List of infrared frequencies of all the compounds presented in this chapter.

Compound	Infrared frequencies (KBr, cm^{-1})
1	3408 (br), 3080 (br), 2498 (br), 2345 (br), 1623 (m), 1579 (m), 1487 (vs), 1449 (sh), 1270 (vs), 1195 (s), 1002 (s), 925 (w), 809 (w), 785 (s), 746 (vs), 687 (m), 641 (m), 558 (m), 438 (w)
2	3212 (br), 3083 (w), 2970 (s), 2874 (s), 2494 (br), 2318 (br), 1947 (w), 1614(w), 1577 (m), 1500 (vs), 1479(sh), 1267 (vs), 1200 (s), 1181(sh), 1153 (w), 1024 (s), 1001 (sh), 874 (s), 808 (m), 785 (s), 745 (vs), 692 (m), 640 (m), 556 (m), 431 (w)
3	3425 (br), 3065 (m), 2966 (m), 2927 (m), 2921 (m), 2855 (m), 2365 (br), 1679 (m), 1569 (vs), 1471 (w), 1457 (s), 1427 (sh), 1374 (s), 1331 (w), 1287 (m),

	1256 (w), 1195 (vs), 1165 (s), 1082 (w), 1050 (w), 1012 (sh), 998 (s), 931 (w), 849 (vs), 825 (sh), 721 (w), 689 (s), 617 (m), 570 (w), 494 (s), 463 (m), 439 (sh)
4	3471 (br), 3087 (w), 3004 (w), 2939 (m), 2834 (w), 1729 (w), 1628 (w), 1679 (m), 1581 (w), 1497 (vs), 14562 (m), 1441 (m), 1332 (s), 1296 (m), 1223 (vs), 1188 (sh), 1166 (vs), 1013 (s), 888 (s), 832 (s), 798 (sh), 738 (w), 728 (w), 601 (w), 501 (m)
5	3431 (br), 3088 (w), 3005 (w), 2940 (m), 2834 (w), 1729 (w), 1627 (w), 1676 (m), 1581 (w), 1496 (vs), 1462 (m), 1442 (m), 1331 (s), 1296 (m), 1223 (vs), 1188 (sh), 1166 (vs), 1013 (s), 888 (s), 833 (s), 798 (sh), 737 (w), 728 (w), 601 (w), 501 (m)

3.3.3 Structure Determination

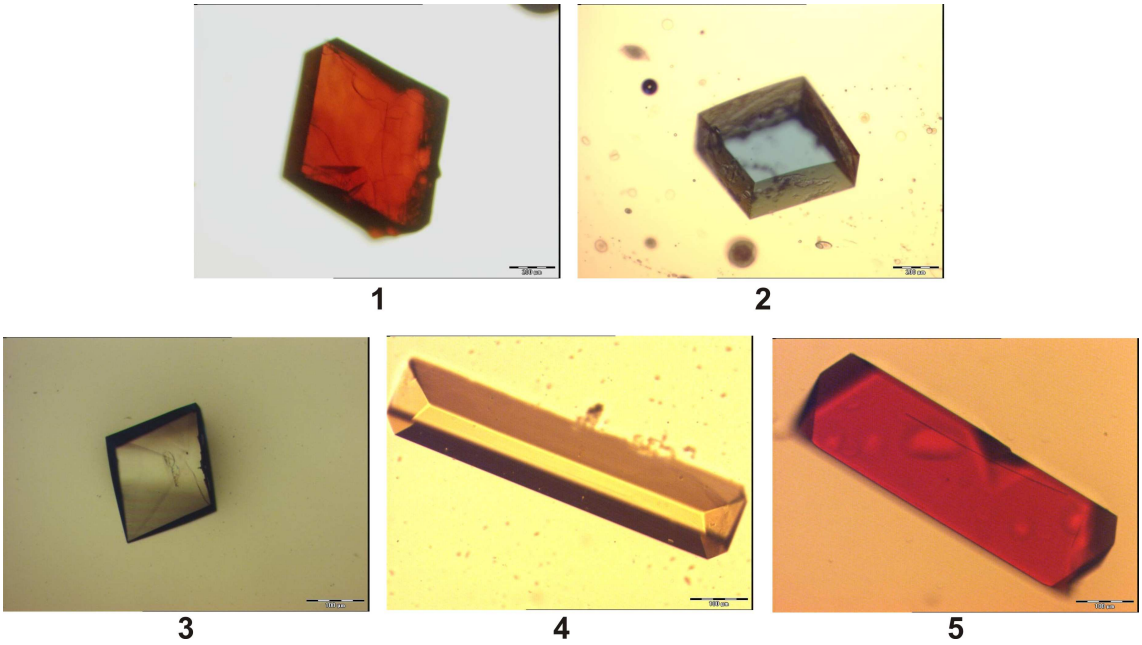

Figure 3.29 Optical micrographs of the single crystals of **1**-**5**.

Single crystals suitable for X-ray crystallographic analysis were selected following examination under microscope (Figure 3.29).

Table 3.8 Single crystal X-ray data and refinement summary for **1-5**.

Compound	**1**	**2**	**3**
Formula	$C_{144}H_{174}Co_9N_{42}O_{36}$	$C_{94}H_{104}N_{42}Ni_9O_{28}$	$C_{117}H_{135}N_{39}O_{15}Zn_9$
Formula mass	3599.58	2798.33	2916.08
T/K	193(2)	193(2)	193(2)
λ/Å	0.71073	0.71073	0.71073
Crystal dimensions/mm	0.38×0.58×0.62	0.38×0.54×0.54	0.31×0.31×0.38
Crystal system	Hexagonal	Hexagonal	Triclinic
Space group	$R\bar{3}c$	$R\bar{3}$	$P\bar{1}$
a/Å	27.398(4)	22.553(3)	14.4593(3)
b/Å	27.398(4)	22.553(3)	18.509(4)
c/Å	37.107(7)	22.578(5)	28.740(6)
α/°			97.34(3)
β/°			97.54(3)
γ/°			112.90(3)
V/Å^3	24122(7)	9946(3)	6888(2)
Z	6	3	2
D_c/g cm^{-3}	1.487	1.257	1.406
M/mm^{-1}	0.991	1.317	1.609
F(000)	11178	3834	3000
θ Range/°	2.04-25.90	2.08–25.87	2.07–26.02
Measured reflections	61510	26018	54595
Independent reflections	5209	4266	25147
Data/restraints/ parameters	5209/0/349	4266/0/231	25147/52/1571
R_1 (I >2σ(I))[a]	0.0488	0.0988	0.0595
wR_2 (all data)[b]	0.1372	0.3176	0.1695
Goodness-of-fit on F^2	1.045	1.194	0.871
$\Delta\rho_{max,\ min}$/e Å^{-3}	1.28 / –1.10	2.36 / –0.77	1.58 / –0.76

Table 3.8 (continued)

Compound	**4**	**5**
Formula	$C_{96}H_{96}Cl_6N_{36}O_{24}Zn_9$	$C_{96}H_{96}Cl_6Fe_3N_{36}O_{24}Zn_6$
Formula mass	2939.12	2910.72
T/K	223(2)	223(2)
λ/Å	0.71073	0.71073
Crystal dimensions/mm	0.19×0.31×0.42	0.08×0.15×0.46
Crystal system	Monoclinic	Monoclinic
Space group	$P2_1/n$	$P2_1/n$
a/Å	21.848(4)	19.847(4)
b/Å	15.490(3)	15.759(3)
c/Å	22.499(5)	28.428(6)
α/°	90.00	90.00
β/°	99.02(3)	110.43(3)
γ/°	90.00	90.00
V/Å^3	7520(3)	8332(3)
Z	2	2
D_c/g cm^{-3}	1.298	1.160
M/mm^{-1}	1.581	1.257
F(000)	2976	2952
θ Range/°	2.26-25.93	1.69-24.02
Measured reflections	58162	45149
Independent reflections	14496	13026
Data/restraints/ parameters	14496/0/784	13026/0/774
R_1 (I >2σ(I))[a]	0.0645	0.0901
wR_2 (all data)[b]	0.2319	0.2949
Goodness-of-fit on F^2	1.056	1.059
$\Delta\rho_{max, min}$/e Å^{-3}	1.678, -0.428	2.362, -0.693

[a] $R_1 = \sum||F_o| - |F_c||/ \sum|F_o|$. [b] $wR_2 = \{\sum [w(F_o^2 - F_c^2)^2]/ \sum[w(F_o^2)^2]\}^{1/2}$.

Since the as-synthesized crystals of each compound "age" on standing at room temperature for few hours, they were covered with polybutene oil after being removed from the mother liquor for X-ray diffraction studies. Intensity data of all the compounds were collected on a STOE IPDS diffractometer employing monochromated Mo-K_α radiation (λ = 0.71073 Å). Initial structures were solved by direct methods and refined by full-matrix least-squares techniques based on F^2 using the SHELXL-97 program.[187] Hydrogen atoms were placed at calculated positions and refined using a riding model. All non-hydrogen atoms were refined anisotropically. Details of data collection and refinement of the compounds are summarized in Table 3.8.

3.4 Summary

The work presented in this chapter illustrates that the use of benzotriazolate type of ligands represents a successful synthetic strategy for the preparation of polynuclear transition metal coordination compounds. Five homo- and heterononanuclear Co(II), Ni(II), Zn, and Fe(II)-Zn compounds (**1**-**5**) containing μ_3-benzotriazolate ligands have been synthesized, and their structural, magnetic, electrochemical, UV-Vis, and Mössbauer properties have been described. The existence of a η^1:η^1:η^1:μ_3 coordination mode of benzotriazolates in Co(II) coordination chemistry has been established through the synthesis and characterization of $[Co_9(bta)_{12}(MeOH)_{18}][(NO_3)_6]\cdot 9C_6H_6$ (**1**). The successful design, synthesis and characterization of the first heterononanuclear Fe^{II} SCO compound $[Fe_3Zn_6Cl_6(OMe_2bta)_{12}]$ (**5a**) based on a 1,2,3-triazolate ligand, are demonstrated. The syntheses, structures and spectroscopic properties of its solvated form (**5**) and homonuclear analogues (**4** and **4a**) are also described. Magnetochemical analysis shows net antiferromagnetic intramolecular coupling in $[Co_9(bta)_{12}(MeOH)_{18}][(NO_3)_6]\cdot 9C_6H_6$ (**1**), whereas both ferro- and antiferromagnetic coupling is observed in $[Ni_9(bta)_{12}(NO_3)_6(MeOH)_6]\cdot 4THF$ (**2**). Mössbauer spectroscopic investigations on **5a** reveal a HS→LS transition for only the central Fe(1) ion upon cooling, while the HS states of the two adjacent octahedrally coordinated Fe(2) ions remain unchanged upon variation of temperature. This unique SCO behaviour is rare, and has been previouly reported only for a trinuclear Fe^{II} compound.[195d-e] The different SCO behaviour of the Fe ions in compound **5** can be rationalized in terms of different strengths of the local ligand-fields exerted by each set of N-donor atoms comprising the ligand cage of the

Fe centres. Whereas the central Fe(1) ion is coordinated exclusively via the more nucleophilic N^1 donor atoms of the benzotriazolate ligands, the coordination environment of the two adjacent Fe(2) ions is formed exclusively by a set of six N^2 donor atoms stemming from the coordinated benzotriazolate ligands. The lower nucleophilicity of the N^2 triazolate donor atoms thus finds its expression in the fact that these Fe(2) centres retain their HS state under all experimental conditions.

Comparative Mössbauer studies on solvated **5** (which does not display SCO behaviour), and desolvated (**5a**) materials suggest that the present Fe^{II} SCO system is very sensitive to the presence of lattice solvent molecules, which is a well-established phenomenon shown by many other SCO systems.[191d,191g,191i,191p,195m] Electrochemical investigations on **5** show a reversible oxidation of the Fe^{II} ions, occuring at a potential significantly higher than that of ferrocene. Both, X-ray diffraction studies (223 K) and UV-Vis analyses (298 K) of **5** indicate the presence of both HS and LS Fe^{II} ions at the respective measurement temperatures. Unfortunately, the complicated time-dependent release of solvent DMF molecules results in "aging" of the crystals of **5**, preventing from performing any further time- and temperature-dependent studies to correlate the magnetic and SCO behaviour of **5** and **5a** at various conditions. Nevertheless, the previous experience (*cf.* Chapter 2)[10c] on 1,2,3-triazole-based heteropentanuclear compounds indicate that the present SCO system (**5a**) might represent one member of a family of compounds having composition $[M_3Zn_6X_6L_{12}]$, which can be prepared by the variation of 3d transition metal (M^{II} = Co, Ni, or Cu) ions, 1,2,3-triazolate ligands or monodentately coordinated halogenides (X = Cl, Br, or I). Notably, the heterononanuclear Co^{II} compound isostructural with **5** might show interesting SCO behaviour, comparable with **5a**, since SCO in Co^{II} compounds is well-documented, although less commonly observed than for Fe^{II} compounds.[201]

Chapter 4

Two- and Three-Dimensional Coordination Polymers Containing Benzobistriazolate Ligands and Zinc Ions

4.1 Introduction

Research activity on metal-coordination polymers has undergone a renaissance in recent years.[202] Typically, organic linkers are used in conjunction with metal ions having preferential coordination numbers and geometries, which provide a degree of control over the final structure. Porous coordination polymers, which are now frequently referred to as metal-organic frameworks (MOFs), contain well-defined pores and cavities, similar to zeolites, rendering them interesting candidates that possess exciting physical properties, such as optical,[37] magnetic,[11b,23c-e,38] and electronic properties,[39] as well as various potential applications such as catalysis,[40,69] ion exchange,[41] gas storage,[42] separation,[43] sensing,[44] polymerization,[45] and drug delivery.[46] While many MOFs so far have been synthesized using 3d transition metal ions and multidentate arylcarboxylate[22] ligands, there are very few examples on MOFs that contain exclusively N-donor ligands such as 4,4'-bipyridines,[30] pyrazolates,[52,53,203] 1,2,4-triazolates,[204] or tetrazolates.[96h,205] Though there are few reports of coordination polymers containing benzotriazolate based ligands,[10e,11b] the area of MOF type of compounds using benzobistriazolate as linkers as yet remained largely unexplored. In this chapter, a novel cubic MOF, "**MFU-4**", (MFU being the acronym for *M*etal-organic *F*ramework *U*lm University) $[Zn_5Cl_4(BBTA)_3]\cdot 3DMF$ (**1**) (H_2-BBTA = 1H,5H-benzo(1,2-d:4,5-d')bistriazole; DMF = *N*,*N*'-dimethylformamide), constructed from $\{Zn_5Cl_4\}^{6+}$ secondary building units (SBUs) interconnected with BBTA linkers, is presented. The incentive of using BBTA type of linkers came from the previous work on T_d symmetrical homo- and heteropentanuclear metal compounds of the type $[MZn_4Cl_4L_6]$[10c] (M^{II} = Zn, Fe, Co, Ni, or Cu; L = 1,2,3-benzotriazolate ligand) (*cf.* Chapter 2) which indicated that similar structural building units might be employed for the construction of periodic cubic frameworks (Figure 4.1).

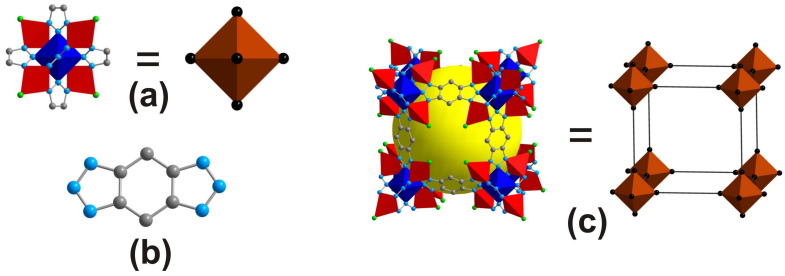

Figure 4.1 Construction principle of cubic **MFU-4** type frameworks (c) comprising T_d symmetrical $\{Zn_5Cl_4\}^{6+}$ coordination units (a), linked by linear benzobistriazolate linkers (b). (octahedrally coordinated Zn, blue octahedra; tetrahedrally coordinated Zn, red tetrahedra; N, light blue; C, grey; Cl, green). The light yellow sphere represents a larger cavity inside **MFU-4** framework.

Initial molecular mechanics investigations suggested that there should be exactly one way of assembling $\{Zn_5Cl_4\}^{6+}$ SBUs and $\{BBTA\}^{2-}$ dianions into a cubic lattice, assuming that all N-donor atoms of the BBTA ligands are coordinated with metal centers. Indeed, this working model proved to be correct leading to the directed solvothermal synthesis of **1** (**MFU-4**). However, in the course of comparative investigations on suitable preparation conditions, it was discovered that the yield of this compound is delicately dependent on the solvent used in synthesis. Thus, employing *N*,*N*'-dimethylacetamide (DMA) as solvent instead of *N*,*N*'-dimethylformamide (DMF), **2** (molecular formula: $[ZnCl(BBTA)_{0.5}(DMA)]$) crystallizes from the reaction mixture, which constitutes a densely packed 2D layered coordination polymer, in contrast to the porous cubic framework of **1**. The main difference between both structures is the coordination mode of the BBTA ligands: in contrast to **1**, only two (N^1 and N^3) of the triazolate N-donor atoms are coordinated to zinc ions in **2**. To the best of knowledge, **2** is the first example of a 2D coordination polymer containing BBTA ligand.

More recently, microwave-assisted synthesis of MOFs has attracted much attention. This technique often leads to a rapid and efficient synthesis of porous materials within a few minutes,[32] instead of days of typical solvothermal routes, and, moreover, it offers phase selectivity[33] and facile control over crystal morphology[34]. This method has been successfully applied for the rapid synthesis of several well-known porous MOFs such as **MOF-5**, **MIL-77** (MIL is the acronym for *M*atérial *I*nstitut *L*avoisier), **MIL-100**, or **MIL-101**.[35] Encouraged by these facts, an efficient microwave synthesis, which leads to **1** at very short reaction times (typically 10 min) with acceptable yields, has been established.

In this chapter, the syntheses, structural characterizations, as well as thermal, fluorescent, and sorption properties of the above mentioned novel coordination polymers are presented.

4.2 Results and Discussion

4.2.1 Syntheses

Amide solvents (such as DMF and DMA) slowly generate the base (dimethylamine) in the reaction medium under solvothermal conditions. The *in-siu* gentrated base can abstract the acidic protons from H_2-BBTA ligand. Though the role of the reactive amide solvents is similar for the synthesis of both compounds (Scheme 4.1) described in this chapter, two different coordination polymers using DMF (**1**) and DMA (**2**), have been obtained. Both compounds can be obtained starting from a variety of reaction mixtures with different ratios of $ZnCl_2$:H_2-BBTA (2:1, 3:1 and 4:1). However, **2** can be obtained in pure phase at 120 °C under solvothermal conditions while the solvothermal synthesis of **1** requires higher temperature (140 °C). To reduce the synthesis time from several days to only a few minutes, a microwave synthesis has been developed for **1**. Both compounds are stable in air, insoluble in water and in common organic solvents.

Compound **1**:

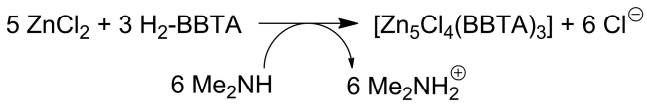

Compound **2**:

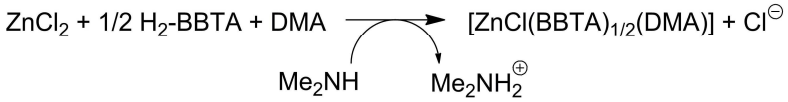

Scheme 4.1 Chemical equations for the preparation of **1** and **2**.

4.2.2 Characterization

Scanning electron microscopy. SEM images show mostly cubic microcrystals with truncated corners, along with very few octahedral microcrystals having formed during the synthesis of **1** by the solvothermal method (Figure 4.2a). Crystals of similar shape, with a lower fraction of octahedral microcrystals, however, were obtained from microwave synthesis of **1** (Figure 4.2b).

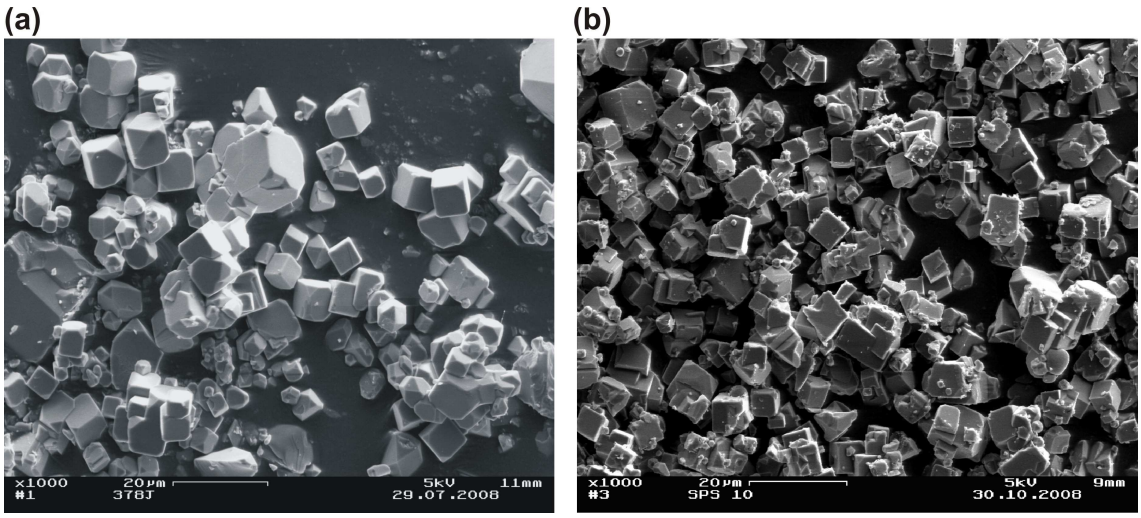

Figure 4.2 SEM images of as-synthesized **1** by (a) solvothermal method and (b) microwave irradiation method.

EDX analysis. An EDX measurement (Figure 4.3) performed on as-synthesized **1** by the solvothermal method shows that the relative ratio of Zn:Cl is 1:1.32, which closely matches the theoretical ratio (1:1.25).

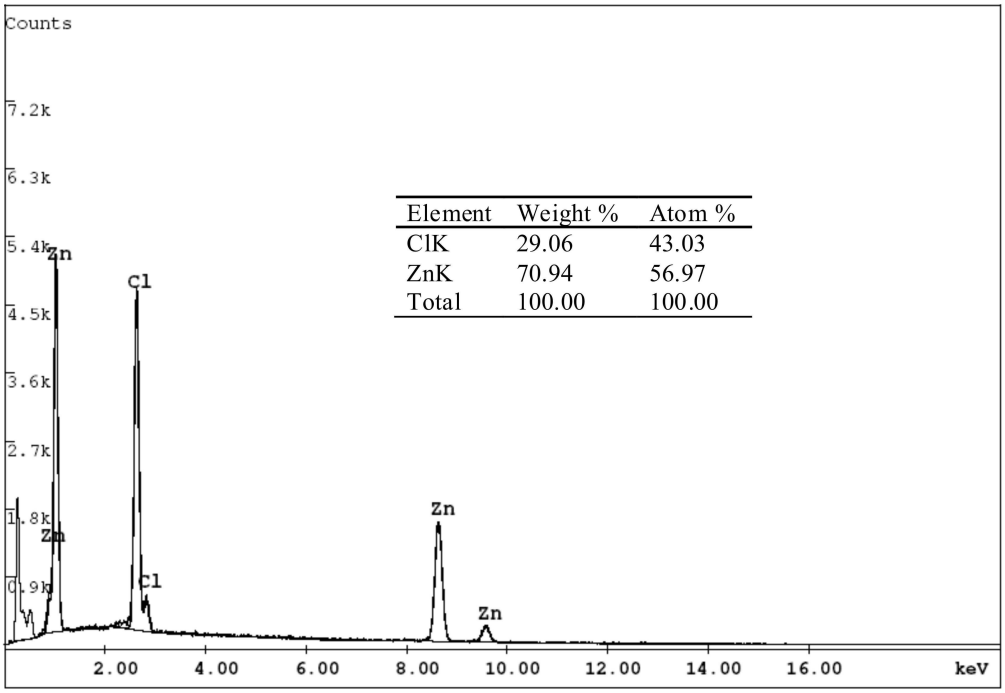

Figure 4.3 EDX spectrum of **1**.

X-ray powder diffraction. Phase purity of **1** and **2** were examined using XRPD patterns recorded from **1** and **2** at ambient conditions. Though it was impossible to get specimens of **1** containing ‘only cubic’ and ‘only octahedral’ crystal species, the simulated XRPD pattern

obtained from single crystal X-ray diffraction data performed on an octahedral single crystal of **1** matches quite well with the experimental XRPD patterns (Figure 4.4) of specimens of **1** from both batch 1 (containing ~ 95 % cubic crystals) and batch 2 (containing ~ 1:1 ratio of cubic and octahedral crystals), confirming that both cubic and octahedral crystals are identical phases with different habitus. The experimental XRPD patterns of **2** are also consistent with the simulated ones as gleaned from the single-crystal X-ray diffraction data (Figure 4.5).

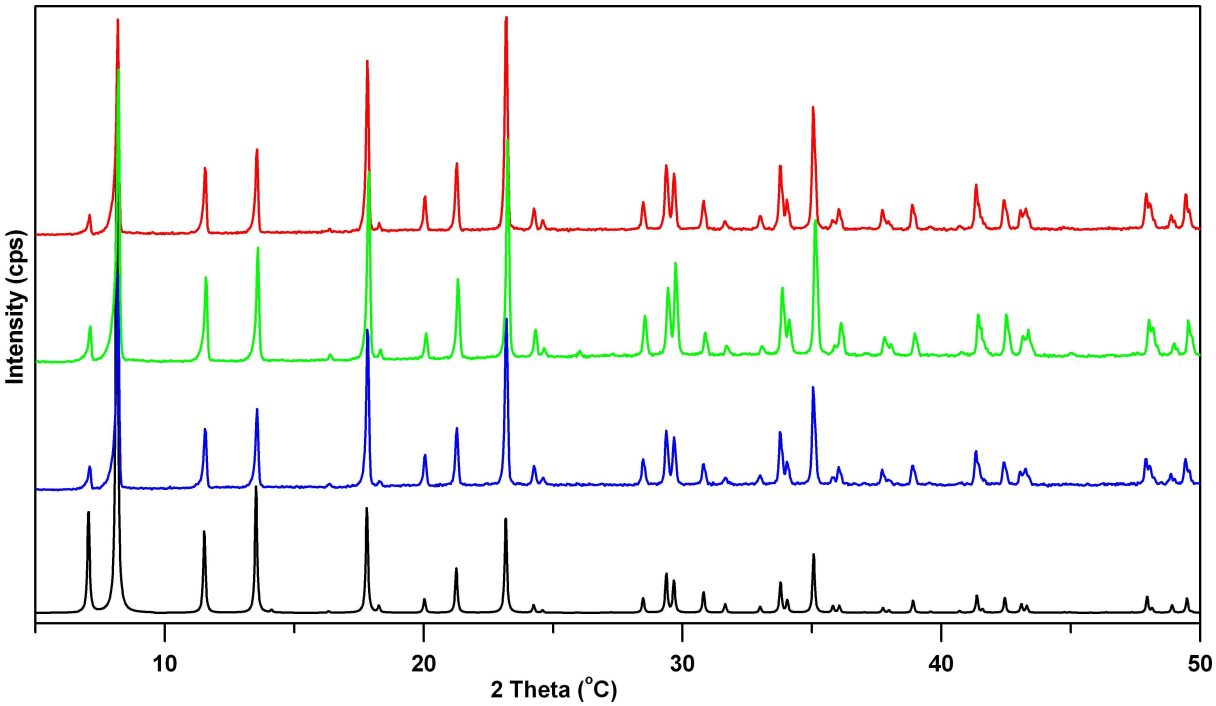

Figure 4.4 Theoretical XRPD pattern (black) and experimental XRPD patterns of **1** synthesized by solvothermal method (batch 1, blue; batch 2, green) and microwave assisted method (red).

Variable temperature X-ray powder diffraction (VTXRPD) studies (Figure 4.6) show that **1** is stable up to 350 ºC and crystallinity is retained upon the loss of occluded DMF molecules. In the temperature range 350–400 ºC, ZnO appears as new crystal phase which predominates above 450 ºC, when the framework has completely decomposed.

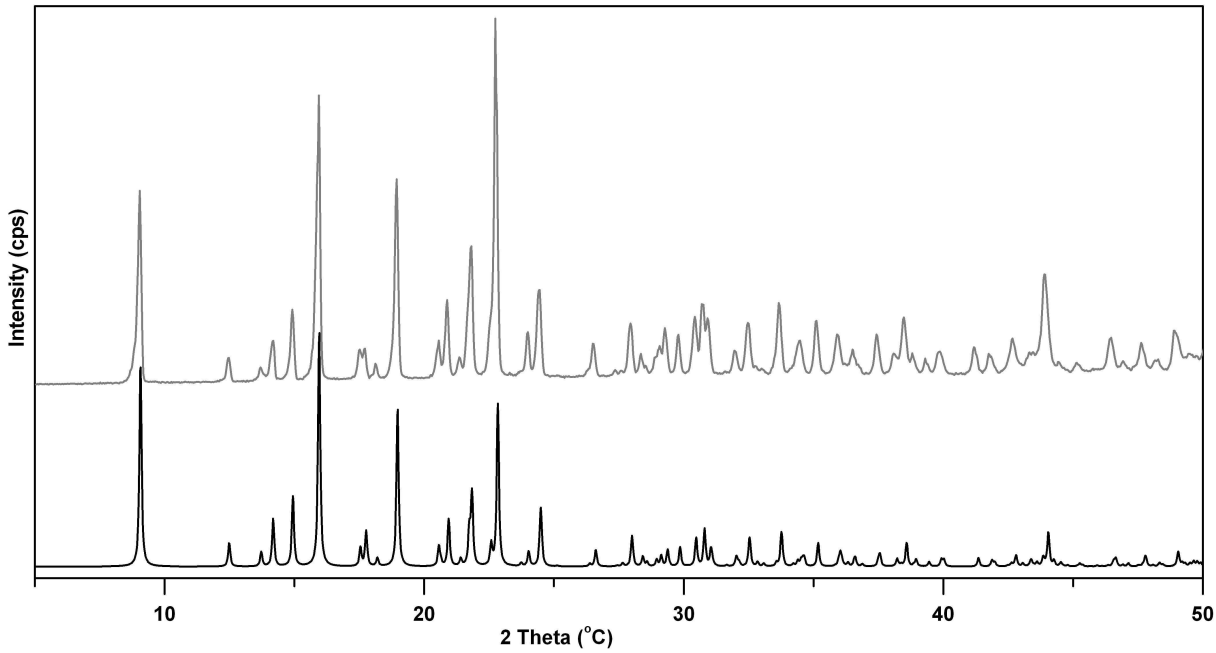

Figure 4.5 Theoretical (black) and experimental (grey) XRPD patterns of **2**.

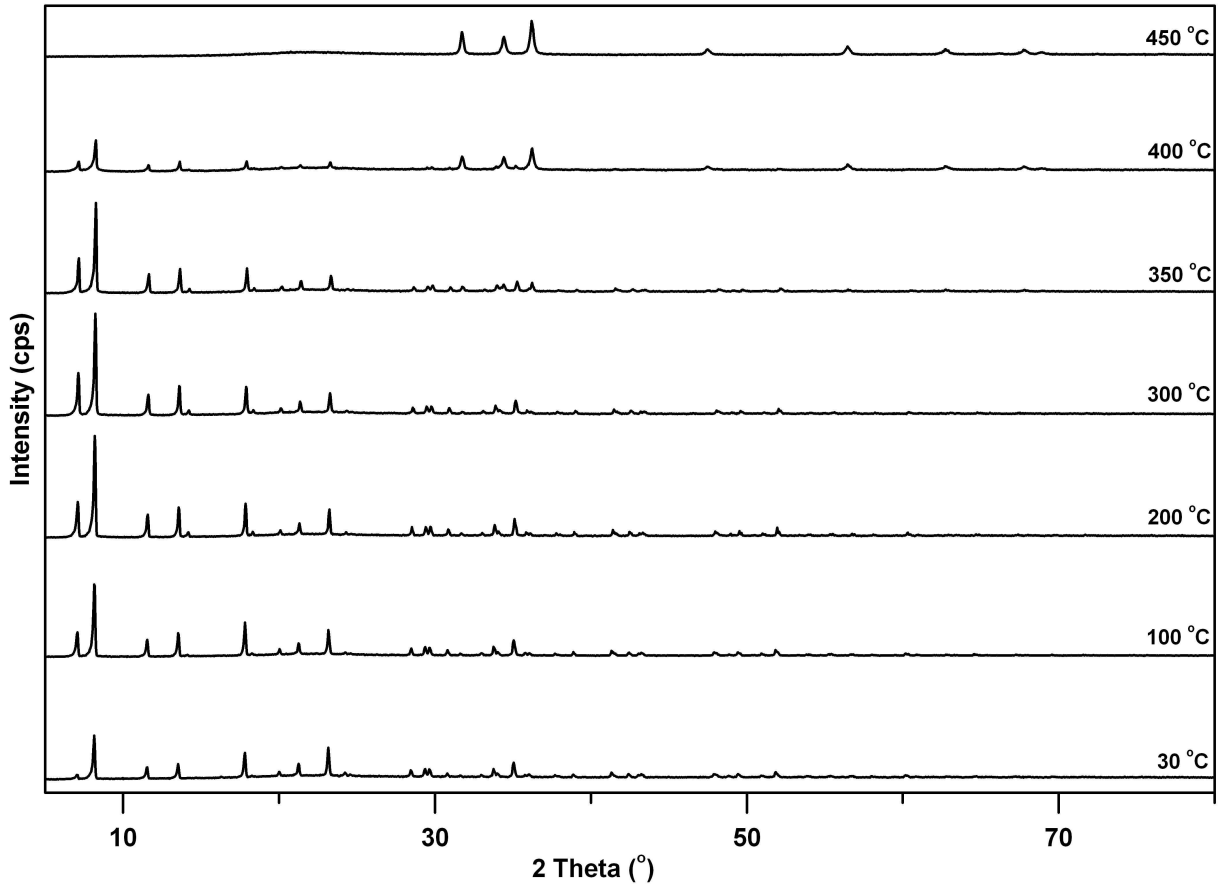

Figure 4.6 VTXRPD plots of **1** in the range 30-600 °C.

From the variable temperature XRPD patterns (Figure 4.7), it becomes obvious that **2** is stable only up to 200 ºC. After that, the compound starts to decompose giving rise to an

amorphous phase which persists until 350 ºC. Above 350 ºC, first signs of formation of crystalline ZnO appear, and above 450 ºC, the amorphous phase has completely disappeared, leading exclusively to crystalline ZnO.

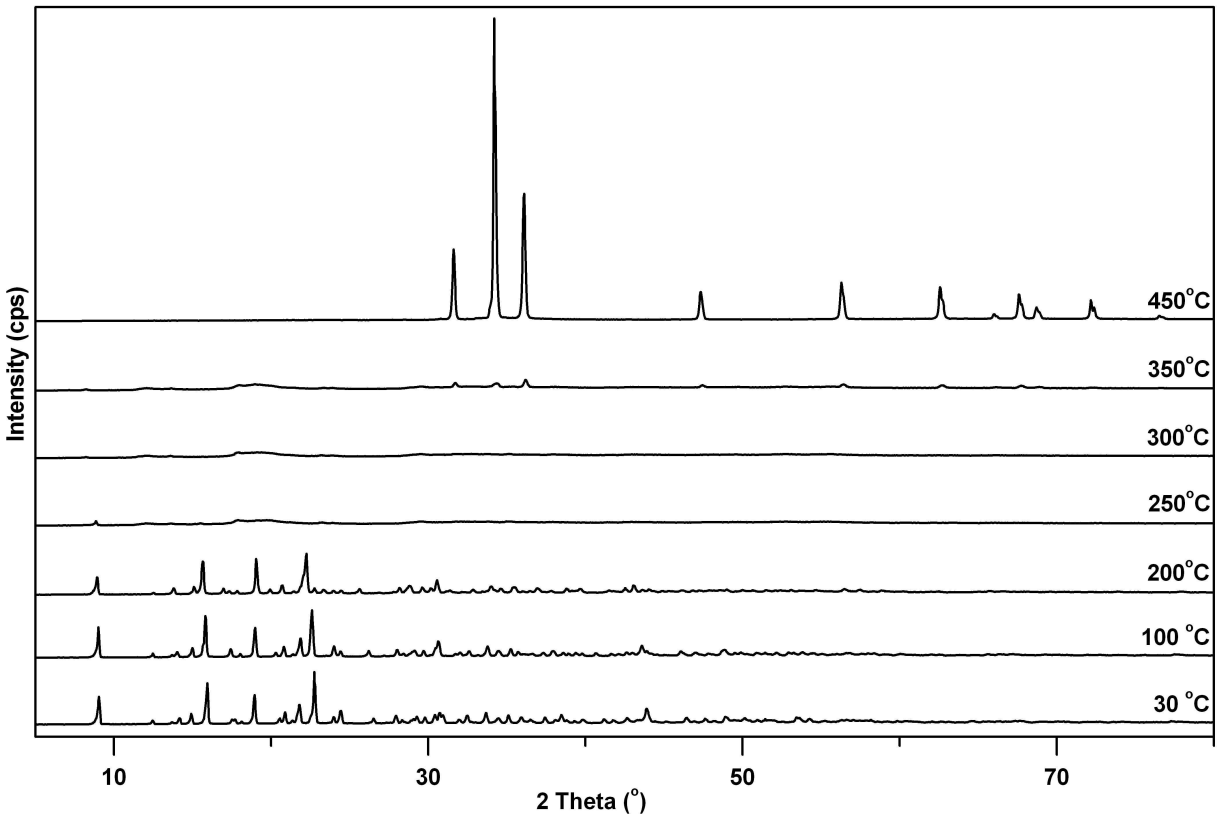

Figure 4.7 VTXRPD plots of **2** in the range 30-500 °C.

Thermogravimetric analysis. In order to examine the thermal stability of the compounds, thermogravimetric analyses (TGA) were performed on polycrystalline samples of **1** and **2** in a nitrogen atmosphere.

In the TG curve of **1** (Figure 4.8) synthesized both by solvothermal and microwave assisted method, the first weight loss step (17.8 % for solvothermal method, 20.5 % for microwave irradiation method) in the range 120-300 ºC is attributed to the removal of three DMF molecules per formula unit (calc. 18.8 %), which is consistent with the results from elemental analysis. No further weight loss is observed until 400 ºC, when the framework starts to decompose leading to ZnO. The guest DMF molecules can be removed from the larger cavities of **1** by heating at 250 ºC under vacuum for 24 h. The fully desolvated (activated) sample shows no significant weight loss until 400 ºC (Figure 4.8), suggesting complete removal of occluded DMF molecules.

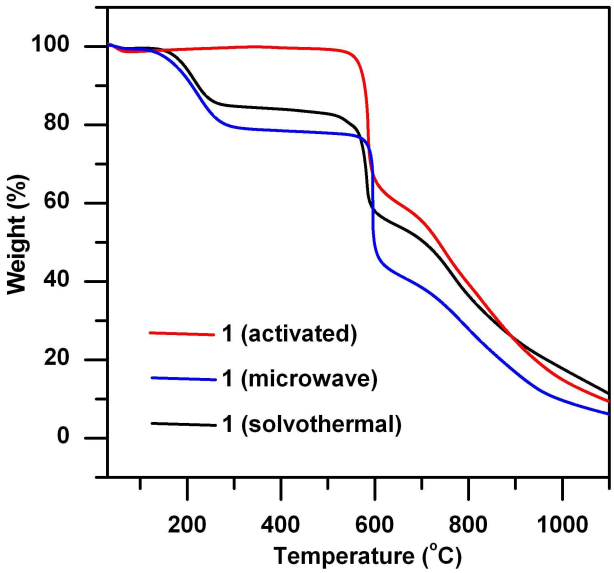

Figure 4.8 TG analyses under N_2 atmosphere of as-synthesized (solvothermal method, black; microwave irradiation method, blue) and activated (red) **1**.

In the TG curve of **2** (Figure 4.9), three weight loss steps are observed. The first weight loss of 31.6 % in the range 150–300 ºC is attributed to the loss of one coordinated DMA molecule per formula unit (cald. 32.6 %). The second weight loss of 28.8 % in the range of 400–650ºC is due to the removal of 0.5 molecule of coordinated BBTA ligand per formula unit (cald. 29.6 %), suggesting that **2** starts to decompose in this temperature region. The third weight loss step is also due to the decomposition of the compound leading to formation of ZnO.

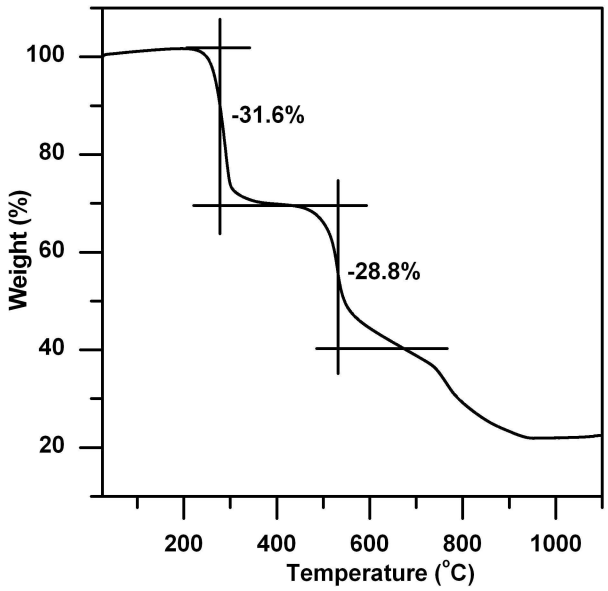

Figure 4.9 TG analysis of **2** under N_2 atmosphere.

TG-MS analysis. TG-MS analysis was carried out in order to identify the occluded solvent molecules present inside the larger cavities of **MFU-4**. The existence of volatile DMF as well as its thermal decomposition products (dimethylamine and formaldehyde), liberated by heating **1**, have been confirmed by TG-MS analysis (Figure 4.10). The m/z = 73 profile shows a signal at 226 °C and 244 °C, which can be assigned to the presence of DMF. Both m/z = 44 and m/z = 30 profiles exhibit signal at 234 °C due to the presence of dimethylamine and formaldehyde, respectively.

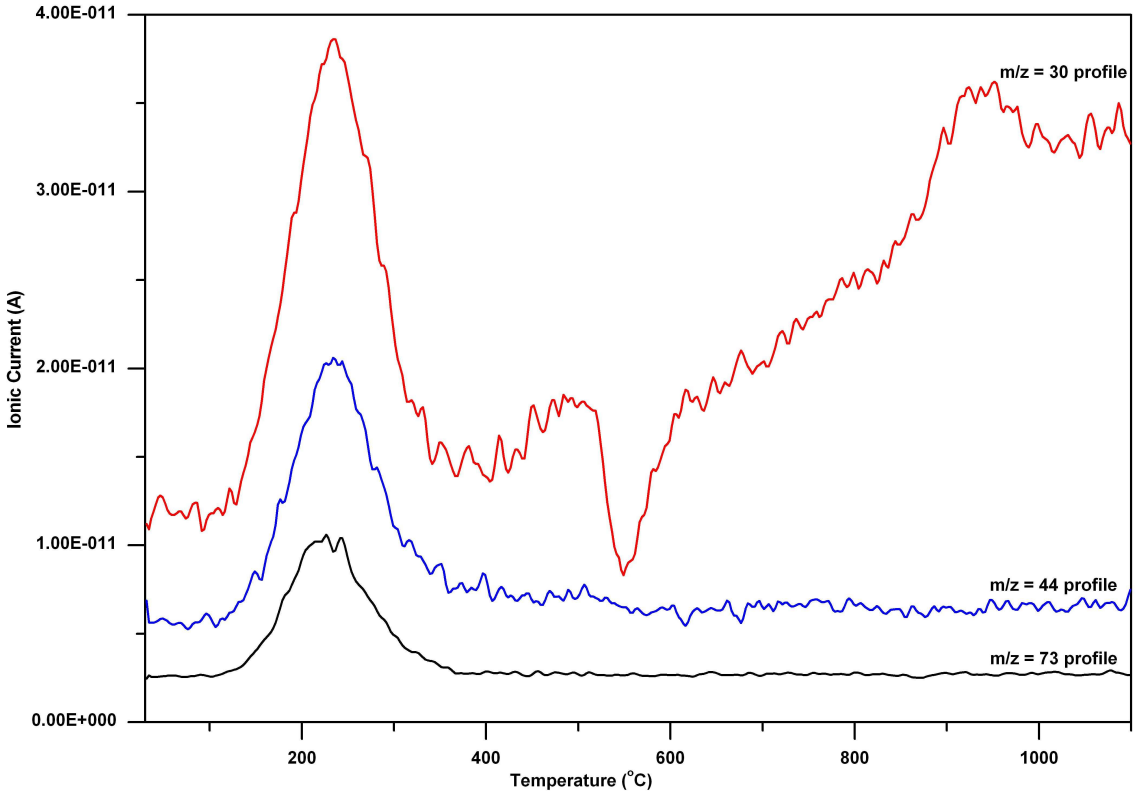

Figure 4.10 Ion-chromatograms of gases released by heating **1** under Ar atmosphere (m/z = 73 profile, black; m/z = 44 profile, blue; m/z = 30 profile, red).

Infrared spectroscopy. In the FT-IR spectrum of **1** (Figure 4.11), the strong absorption band at 1680 cm^{-1} is due to the C=O stretching frequency of non-coordinated DMF molecules. The guest DMF molecules can be removed from the larger cavities of **1** by heating at 250 °C under vacuum for 24 h. The complete removal of DMF molecules is confirmed by the absence of this strong band at 1680 cm^{-1} in the FT-IR spectrum of the fully desolvated (activated) sample of **1** (Figure 4.11). The IR spectra of **1** synthesized both by solvothermal and microwave assisted method are similar (Figure 4.11), as expected.

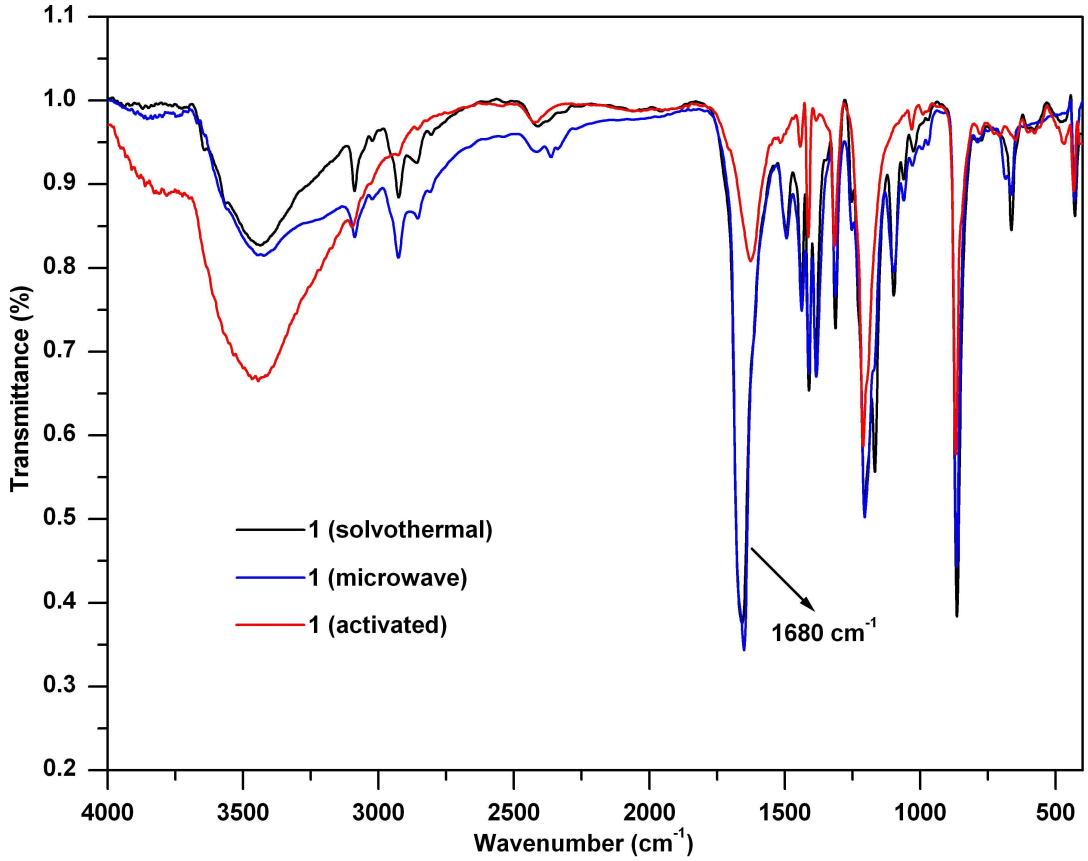

Figure 4.11 FT-IR spectra of as-synthesized (solvothermal method, black; microwave irradiation method, blue) and activated (red) **1**.

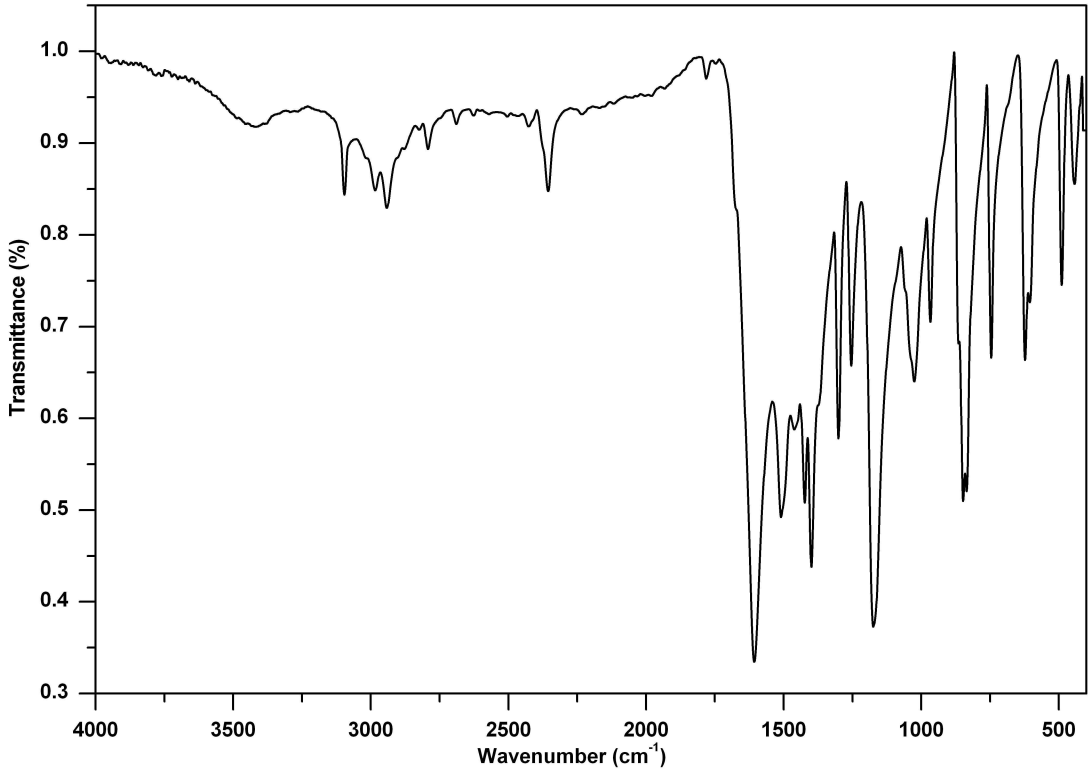

Figure 4.12 FT-IR spectrum of **2**.

UV-Vis spectroscopy. The solid-state UV-Vis spectra of free H_2-BBTA ligand displays two weak abosrption peaks at 255 and 295 nm in the UV region, as depicted in Figure 4.13. The coordinated BBTA ligand in both **1** and **2**, also exhibit weak absorption peaks at the same positions. In addition, both **1** and free H_2-BBTA show one broad absorption band at 410 and 370 nm, respectively. Compound **2**, on the other hand, shows two additional weak, sharp absorption peaks at 370 and 380 nm.

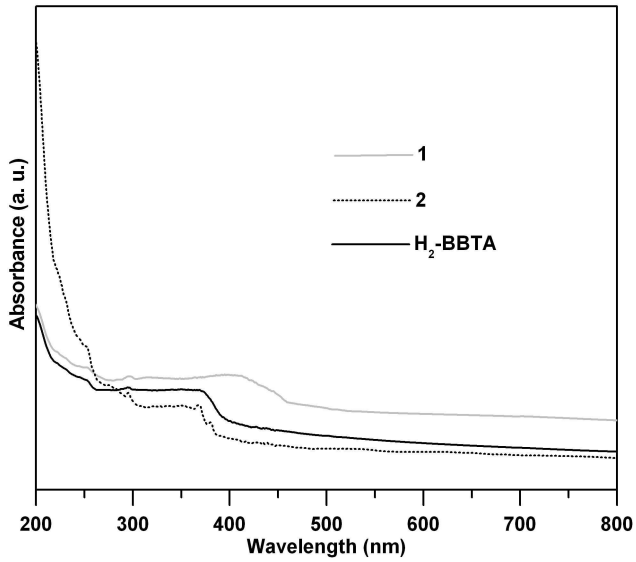

Figure 4.13 Soild-state UV-Vis spectra of **1**, **2**, and free H_2-BBTA ligand.

Luminescence spectroscopy. Inspired by the strong fluorescence emissions of previously reported coordination polymers[166] and metal-organic frameworks[10e] containing zinc ions and benzotriazolate ligands, the luminescent properties of **1** and **2** were investigated. As shown in Figure 4.14, free H_2-BBTA exhibits a broad fluorescence emission band centered at ~550 nm upon excitation at a wavelength of 300 nm. Because the emission band of **1** is similar to that of the free H_2-BBTA ligand, it should be assigned to the intraligand π-π* transition of the BBTA ligand. A broad band of this kind is also observed in the fluorescence emission spectrum of **2**, however with a significant blue-shift. In addition, **2** shows some sharp emission bands at 390, 400, 420, and 445 nm which may be assigned to charge transfer between the deprotonated BBTA ligand and the zinc ions.

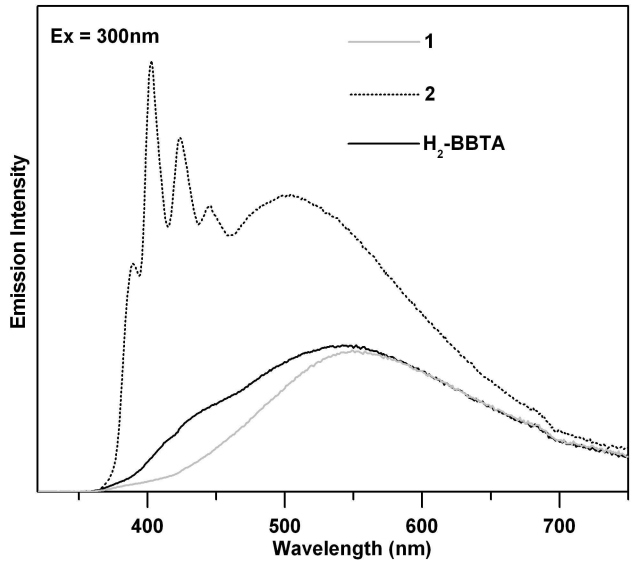

Figure 4.14 Soild-state photoluminescence spectra of **1**, **2**, and free H_2-BBTA ligand.

4.2.3 Rietveld Refinement

Initial TG analysis of **1** shows that the occluded guest DMF molecules can be removed at a temperature above 350 °C. Therefore, the X-ray powder diffraction data collected at this temperature were used for a Rietveld structure refinement. The intention of this process was to check the thermal stability of the framework and to elucidate whether or not the occluded solvent molecules can be cleanly removed from the compound, without significant loss of crystallinity. In fact, it was possible to determine the crystal structure of the compound only from this data set, whereas any efforts of solving the crystal structure from VTXRPD data collected from a sample held at a temperature in the range from 30 to 300 °C were unsuccessful. In these cases, large discrepancies between experimental and calculated intensities with high, unacceptable R-values were observed. Moreover, the unit cell volume of **1** at 350 °C was slightly smaller than the corresponding unit cell volume from samples kept at lower temperature (Table 4.1), suggesting that a slight shrinkage of the structure has taken place after removal of DMF molecules. The mechanism by which DMF molecules can be liberated from the cavities of **1** remains enigmatic however, since the very small pore aperture of the A-cells interconnecting the solvent-filled larger B-cells restricts the diffusion of DMF molecules across the crystal lattice at ambient conditions (Figure 4.16, see later). The final Rietveld plot is presented in Figure 4.15 whereas the details of the refinement process are described in Experimental Section of this chapter. Selected bond lengths of **1** obtained from the refinement process are presented in Table 4.2.

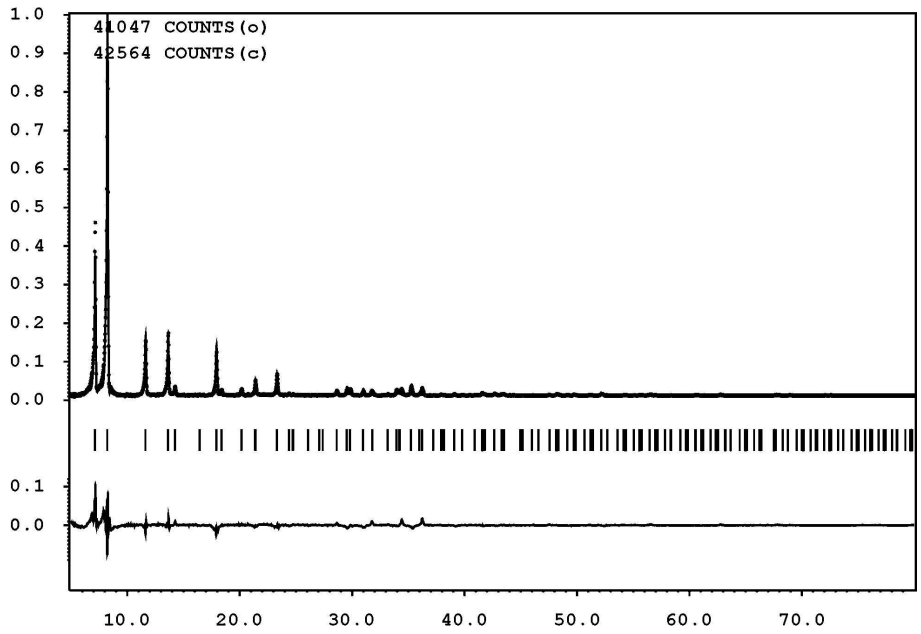

Figure 4.15 Rietveld refinement plots for heat-treated **1**. Dotted and solid lines represent observed and calculated patterns, respectively with peak markers and the difference plot shown at the bottom. XRPD data were collected at 350 °C with a total heating period of 8 h.

Table 4.1 Change of lattice parameters of **1** obtained from VTXRPD data.

Measurement Temperature (°C)	a = b= c (Å)	V (Å^3)	M_{20}	F_{20}
30	21.739(1)	10273(2)	92.68	128.58
100	21.7295(8)	10260(1)	53.51	79.67
200	21.689(2)	10203(3)	58.84	79.31
300	21.644(4)	10139(6)	23.44	33.58
350	21.6265(9)	10114.9(4)	19.52	33.60

Figure 4.2 Selected bond lengths (Å) of **1** obtained from Rietveld refinement using X-ray diffraction data from powders sampled at 350 °C.

Zn(2)–Cl(1)	2.320(8)	Zn(1)–N (2)	2.29(2)	N(1)–C(2)	1.45(2)
Zn(2)–N(1)	1.90(1)	N(1)–N(2)	1.292(8)	C(1)–C(2)	1.39(2)

4.2.4 Structure Description

The single crystal X-ray diffraction study reveals that **1** exhibits a cubic six-connected net (Figure 4.16) which may be conceptually derived in two stages: first, the nodes (vertices) of

the net are replaced by cationic pentanuclear $\{Zn_5Cl_4\}^{6+}$ coordination units; second, the links (edges) of the net are replaced by finite rods ('struts') of $\{BBTA\}^{2-}$ dianions.

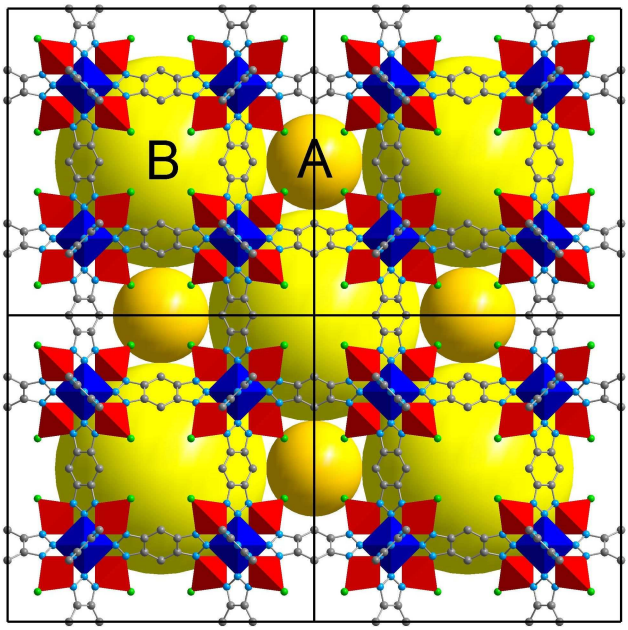

Figure 4.16 Ball-and-stick representation of the **MFU-4** framework along the crystallographic *a*-direction (octahedrally coordinated Zn, blue octahedra; tetrahedrally coordinated Zn, red tetrahedra; N, light blue; C, grey; Cl, green). All hydrogen atoms are removed for clarity. The larger, light yellow spheres represent the cavities of B-cells whereas the smaller, dark yellow spheres represent the cavities of A-cells.

In the pentanuclear coordination units, six BBTA ligands are monodentately coordinated to the central octahedrally coordinated Zn ion. The six BBTA ligands span a Cartesian coordinate system with the Cartesian axes running through the metal ion at the origin and the N^2 atoms of the coordinated ligands. The BBTA ligands are twisted around their coordinative bond to the central metal ion such that the nitrogen atoms are placed on the edges of an imaginary tetrahedron. At the corners of this tetrahedron are placed four additional Zn ions which are coordinated to three N donor atoms of the BBTA ligands and a chloride anion creating a distorted tetrahedral coordination environment. Each BBTA ligand shows a $\eta^1{:}\eta^1{:}\eta^1{:}\eta^1{:}\eta^1{:}\eta^1{:}\mu_6$ coordination motif similar to the coordination mode of discrete low-molecular Zn coordination compounds described in Chapter 2. Furthermore, each Zn_5 unit is connected to six BBTA ligands by 18 Zn–N bonds, with each ligand coordinating one central and two peripheral Zn atoms. In **1**, the octahedrally coordinated Zn atom shows a Zn-N distance of 2.212(7) Å, and the tetrahedrally coordinated Zn atom shows a Zn-N distance of

2.046(6) Å (Table 4.3). These values are in good agreement to other Zn triazolate compounds (1.98–2.05 Å for tetrahedral coordination, 2.14–2.22 Å for octahedral coordination).[166,206]

Table 4.3 Principal bond lengths (Å) of **1** obtained from single crystal X-ray data.

Zn(1)-N(1)#1	2.046(6)	Zn(2)-N(2)	2.212(7)	N(2)-N(1)#1	1.312(7)
Zn(1)-N(1)	2.046(6)	Zn(2)-N(2)#4	2.212(7)	C(1)-N(1)#1	1.372(8)
Zn(1)-N(1)#2	2.046(6)	Zn(2)-N(2)#4	2.212(7)	C(1)-C(1)#1	1.390(12)
Zn(1)-Cl(1)	2.106(5)	Zn(2)-N(2)#4	2.212(7)	C(1)-C(2)	1.422(8)
Zn(2)-N(2)#3	2.212(7)	N(1)-N(2)	1.312(7)	C(2)-C(1)#5	1.422(8)
Zn(2)-N(2)#3	2.212(7)	N(1)-C(1)#1	1.372(8)		

Symmetry operators used to create equivalent atoms are #1: –z+1/2, x, -y+1/2; #2: y, -z+1/2, -x+1/2; #3: y, z, x; #4: -y+1/2, z, -x+1/2; #5: -x+1, y, z.

An estimation with the program PLATON/SQUEEZE[167] using the powder data of **1** kept at 350 °C reveals that the total potentially accessible void volume is 5372 $Å^3$ which is 53.1 % of the unit cell volume. By analogy to **MOF-5**,[17] the framework of **1** has two different types of cavities (the smaller and the larger ones are referred to as A and B cells, respectively)[207] arranged in an alternating fashion (Figure 4.17). A-cells are represented by the cubic arrangement of chloride ligands having a minimum non-bonding distance of 4.257(4) Å to each other. The centre of the A-cells has a distance of 3.68 Å to each Cl atom. The aperture joining the two structurally different cavities is built up by 4 Cl atoms at a distance from 3.01 Å from its geometric centre. Taking the van der Waals radii of Cl atoms (1.75 Å) into account, imaginary spheres with a diameter of 3.87 Å could fit into the A-cells (which roughly corresponds to the van der Waals diameter of Ar atoms), and the aperture would admit the passage of an imaginary sphere with a diameter of 2.52 Å. Each of the larger B-cells, on the other hand, is surrounded by twelve phenyl rings, and an imaginary sphere with a diameter of 11.94 Å would fit into it, taking the van der Waals radii of C atoms into account. Due to their very large volume, the B-cells are filled with 6 DMF guest molecules each. These occluded solvent molecules are highly disordered; thus it was impossible to refine their locations from the electron density distribution obtained from X-ray diffraction data. For consideration of the smeared electron density associated with the occluded DMF molecules, it was necessary to assign accordingly, partially occupied split positions for a total of three DMF molecules per asymmetric unit. The high mobility of the solvent within the B-cells is indicated by the fact that even reduction of the crystallographic symmetry did not serve to localize the $HC(O)N(CH_3)_2$ atomic sites.

Owing to the construction principle of **MFU-4** (**1**), DMF molecules moving from one B-cell into another must pass through an A-cell. The small pore diameter of A-cells as well as the small aperture connecting the two types of cells severely restricts the transport of DMF molecules at ambient conditions. According to TG analysis, however, the occluded DMF molecules can be removed completely upon heat treatment (above 250 °C) of **1** under high vacuum. This could, at least partially, be due to decomposition of DMF molecules at this temperature producing smaller molecular fragments which could pass through the A-cells. In fact, the existence of volatile DMF as well as its decomposition products, liberated by heating **1**, has been confirmed by TG-MS analysis (Figure 4.11).

Compound **2** exhibits a 2D layered framework (Figure 4.17) crystallizing in a monoclinic crystal system, within space group $P2_1/c$. The 2D layers extend into the *yz*-plane of the crystallographic lattice while they are stacked along crystallographic *a*-direction. Each Zn center is placed in a distorted tetrahedral coordination environment (Figure 4.18a) consisting of one chloride ion, the O-donor atom stemming from a monodentately coordinated DMA molecule, and two N atoms from two different BBTA ligands with two different Zn-N distances: 1.992(6) and 1.995(5) Å (Table 4.4). These values are in good agreement with other Zn triazolate complexes having tetrahedral zinc centers. The two BBTA ligands are inclined with respect to each other. Each ligand exhibits a $\mu_{1,3}$-bridging coordination mode which was previously documented for other compounds containing Zn ions and benzotriazolate anions.[166]

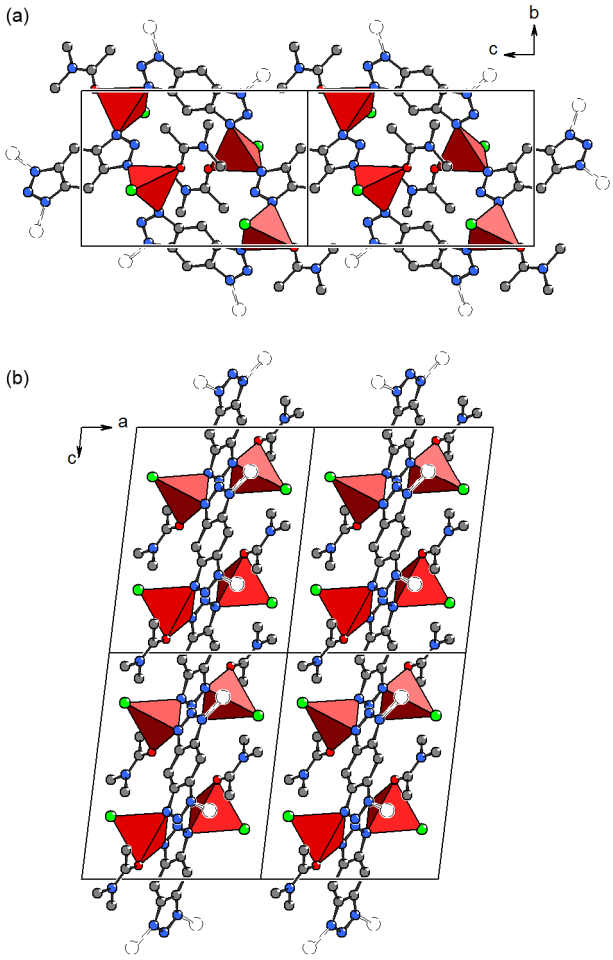

Figure 4.17 Crystal packing diagrams of **2**. (a) Ball-and-stick representation of a single 2D coordination polymer layer. (b) Same representation showing the stacking of adjacent 2D layers of **2** along the crystallographic a-direction. (Zn, red tetrahedra; N, light blue; C, grey; Cl, green). Zinc atoms located outside of the unit cell boundaries are displayed as broken spheres. Hydrogen atoms are omitted for clarity.

Table 4.4 Principal bond lengths (Å) of **2** obtained from single crystal X-ray data.

Zn(1)-O(1)	1.961(5)	N(3)-N(2)#2	1.320(7)	C(3)-C(2)#4	1.377(9)
Zn(1)-N(3)	1.992(6)	N(3)-C(1)	1.388(8)	C(4)-N(4)	1.299(9)
Zn(1)-N(1)	1.995(5)	O(1)-C(4)	1.265(9)	C(4)-C(6)	1.498(11)
Zn(1)-Cl(2)	2.207(3)	C(1)-C(3)	1.392(9)	N(4)-C(7)	1.456(11)
N(1)-N(2)	1.330(8)	C(1)-C(2)#2	1.393(9)	N(4)-C(5)	1.459(11)
N(1)-C(2)	1.390(8)	C(2)-C(3)#3	1.377(9)		
N(2)-N(3)#1	1.320(7)	C(2)-C(1)#1	1.393(9)		

Symmetry operators used to create equivalent atoms are #1: -x+1, y-1/2, -z+1/2; #2: -x+1, y+1/2, -z+1/2; #3: x, -y+1/2, z+1/2; #4: x, -y+1/2, z-1/2.

4.2.5 Sorption Properties

Nitrogen, hydrogen and water adsorption studies were performed on **1**. The nitrogen adsorption measurement revealed that the compound adsorbs almost no nitrogen at -196 ºC and pressure up to 1 bar. Therefore, the specific surface area and pore volume could not be determined from the nitrogen adsorption experiment, as it is routinely done for the characterization of porous materials. However, a surface area calculated from a Monte Carlo integration technique, where the probe molecule is "rolled" over the framework inner surface as described by T. Düren *et al.*[208] predicts an accessible surface area as high as 1611 $m^2 g^{-1}$ indicating that **MFU-4** should possess a porous framework.

This permanent porosity could be proven using hydrogen adsorption revealing a remarkable accessible inner pore volume. The hydrogen adsorption isotherm follows type-I behavior and the maximum uptake achieved at -196 ºC and 1 bar is 1.62 wt. % (Figure 4.18). The selective adsorption of hydrogen over nitrogen at -196 ºC is rare and has been previously demonstrated only for few MOFs with short linkers.[93o,104,209] The "sieving effect" in these compounds can be attributed to the small aperture of the pores.

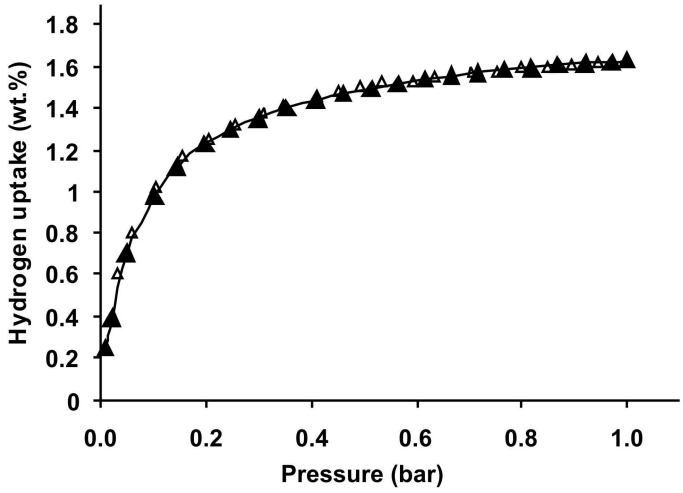

Figure 4.18 Hydrogen adsorption (solid symbols) and desorption (empty symbols) isotherms measured for **MFU-4** at -196 ºC up to 1 bar.

The permanent porosity of **1** has also been confirmed by water adsorption measurements at 25 ºC. The kinetic diameter of water (0.265 nm) is even smaller than that of hydrogen (0.289 nm) which leads to the assumption that water should also be adsorbed on **MFU-4**.

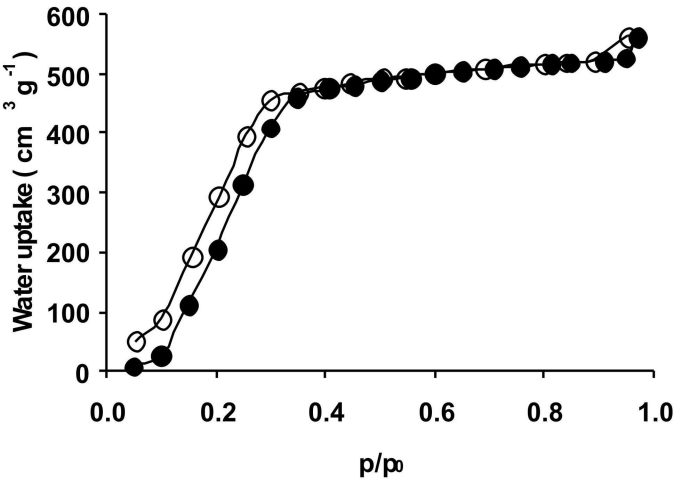

Figure 4.19 Water adsorption (solid symbols) and desorption (empty symbols) isotherm measured for **1** at 25 ºC.

As depicted in Figure 4.19, the water adsorption shows a steep uptake in the region from p/p_0 = 0.1 up to 0.35, following saturation. The pore volume estimated from the water adsorption isotherm at p/p_0 = 0.9 is 0.42 cm^3 g^{-1}. It should be noted that the estimation of micropore volume using a water vapor adsorption isotherm often yields slightly different (usually underestimated) values as compared to adsorption data using other probe molecules (such as nitrogen or argon). In case of water, the hydrophobic-hydrophilic properties of the surface govern the adsorption process and the adsorptive itself strongly interacts via hydrogen bonds leading to adsorption phenomena different from nitrogen adsorption experiments.[210]

The water adsorption measurement was repeated two times on the same sample. Between the measurements the sample was evacuated at 250 ºC for 24 hours. The exactly reproducible nature of the isotherm points at the high stability of the framework against moisture. The combination of molecular sieving characteristics and moisture stability suggests the potential application of **MFU-4** in gas separation processes where hydrogen molecules (or similarly: helium atoms) have to be separated from mixture of gases (e.g. CO_2, CO, O_2 or N_2).

4.3 Experimental Section

4.3.1 Materials and General Methods

The H_2-BBTA ligand was synthesized as described previously.[211] All other starting materials were of reagent grade and used as received from the commercial supplier. Fourier transform infrared (FT-IR) spectra were recorded from KBr pellets in the range 4000–400 cm^{-1} on a

Bruker IFS FT-IR spectrometer. The following indications are used to characterize absorption bands: very strong (vs), strong (s), medium (m), weak (w), shoulder (sh), and broad (br). Elemental analyses (C, H, N) were carried out on a Perkin-Elmer 2400 Elemental Analyzer. Thermogravimetric analyses (TGA) were performed with a TGA/SDTA851 Mettler Toledo analyzer in a temperature range of 25–1100 °C in flowing nitrogen at a heating rate of 10 °C min^{-1}. TG-MS analysis was carried out using a STA 409 PC/PG-Luxx (Netzsch) simultaneous thermal analyzer coupled with a QMS 403C-Aeolos Mass Spectrometer in a temperature range of 30–1100 °C under Ar atmosphere with a heating rate 5 °C min^{-1}. Ambient temperature X-ray powder diffraction (XRPD) patterns were measured using a Philips X'Pert PRO powder diffractometer operated at 40 kV, 40 mA for Cu target (λ = 1.5406 Å) with a scan speed of 30 s $step^{-1}$ and a step size of 0.008°. Temperature-dependent X-ray powder diffraction measurements were performed in air with the same diffractometer equipped with an Anton Paar HTK 1200N reaction chamber. The heating rate between two temperatures was 5 °C min^{-1} and once the corresponding temperature was reached, the sample was held at this temperature for 1 h before measuring the pattern. The simulated powder patterns were calculated using data from single crystal X-ray diffraction. Energy dispersive X-ray analysis (EDX) was performed on an EDAX (Phönix) X-ray detection system with 30 mm^2 SUTW window. SEM images were recorded using a Zeiss DSM 962 scanning electron microscope. The solid-state fluorescence emission spectra were collected on a SPEX Fluorolog II spectrofluorometer (Spex Industries, Edison, NJ) in the range of 320-750 nm at room temperature using an excitation wavelength of 300 nm. Powder samples were enclosed between two microscope slides having a thickness of 0.2 mm each. The area occupied by the samples was *ca.* 5 mm × 5 mm. Solid state UV-Vis spectra were recorded on an Analytik Jena Specord 50 UV-Vis spectrometer in the range of 200–800 nm with a lamp change at 450 nm. The powder samples were applied as suspensions in Nujol, mounted between two quartz plates. The nitrogen and hydrogen sorption isotherms at -196 °C up to 1 bar were measured using a Quantachrome Autosorb-1C apparatus. High purity gases were used for the adsorption experiments (nitrogen 99.999 %, hydrogen 99.999 %). Water adsorption isotherms were measured with a Quantachrome Hydrosorb 1000 apparatus. Prior to the measurements, the samples were evacuated at 250 °C for 24 h. The amount of activated sample used for the adsorption measurements was 150 mg.

Safety Note! Benzobistriazolate compounds are potentially explosive, and caution should be exercised when dealing with such derivatives. However, the small quantities used in this study were not found to present a hazard.

4.3.2 Syntheses

Synthesis of $Zn_5Cl_4(BBTA)_3]\cdot 3DMF$ (1): solvothermal method. A mixture of anhydrous $ZnCl_2$ (0.14 g, 1.00 mmol) and H_2-BBTA (0.04 g, 0.25 mmol) was dissolved in 4 mL of DMF and the solution was placed in a glass tube (10 mL). The tube was sealed and heated at 140 ºC for 3 days, then cooled to room temperature. The supernatant was removed and the remaining yellow microcrystalline solid was washed with DMF (3 × 1 mL) and dried in air to yield 0.06 g (0.05 mmol, 27 %, batch 1) of **1** as mostly cubic microcrystals along with very few octahedral microcrystals. Larger single crystals of X-ray quality were grown under slightly different reaction conditions (batch 2). A solution of anhydrous $ZnCl_2$ (0.05 g, 0.37 mmol) and H_2-BBTA (0.02 g, 0.12 mmol) in 2 mL of DMF was placed in a 10 mL glass tube, the tube was sealed and heated at 140 °C for 3 days, and then the mixture was cooled to room temperature to produce a mixture of X-ray quality, yellow octahedral crystals and smaller, yellow cubic microcrystals. A single crystal X-ray diffraction study was performed by selecting an octahedral crystal of dimensions 0.08×0.06×0.06 mm^3 from this mixture. The yield was 0.03 g (0.03 mmol, 35%, batch 2). Crystals precipitated in both batches showed the same analytical results. Anal. Calcd for $C_{27}H_{27}Cl_4N_{21}O_3Zn_5$: C, 27.89; H, 2.34; N, 25.30. Found: C, 27.97; H, 2.82; N, 25.80 %. IR (KBr, cm^{-1}): 3438 (br), 3080 (w), 2918 (w), 2848 (w), 2392 (br), 1652 (vs), 1487 (w), 1434 (w), 1408 (m), 1381 (m), 1310 (m), 1237 (w), 1200 (s), 1163 (sh), 1092 (m), 1056 (w), 862 (s), 659 (m), 569 (w), 469 (w), 425 (m).

Microwave irradiation method. A mixture of $ZnCl_2$ (0.07 g, 0.51 mmol) and H_2-BBTA (0.02 g, 0.12 mmol) in DMF (1 mL) was placed in a Pyrex sample tube (10 mL). The tube was sealed and placed in a microwave synthesizer (CEM, Discover S). The resulting mixture was heated to 155 °C at 300 W, kept under these conditions for 10 min and then cooled to room temperature. A yellow, cubic microcrystalline material (0.03 g, 22 %) was obtained by centrifugation, washing with DMF (3 × 1 mL) and drying in air at ambient conditions. This material exhibited the same analytical results as the one obtained by the solvothermal method.

Synthesis of $[ZnCl(BBTA)_{0.5}(DMA)]$ (2). A mixture of anhydrous $ZnCl_2$ (0.05 g, 0.37 mmol) and H_2-BBTA (0.02 g, 0.12 mmol) was dissolved in 4 mL of DMA and the solution was placed in a glass tube (10 mL). The tube was sealed and heated at 120 °C for 3 days, then cooled to room temperature. The resulting colorless, block-shaped crystals were collected by filtration, washed with DMA (3 × 1 mL) and dried in air to yield 0.03 g of **2** (0.03 mmol, 35

%). Anal. Calcd for $C_7H_{10}ClN_4OZn$: C, 31.48; H, 3.77; N, 20.98. Found: C, 31.62; H, 3.84; N, 21.08 %. IR (KBr, cm^{-1}): 3409 (br), 3096 (w), 2972 (w), 2934 (w), 2783 (w), 2349 (w), 1606 (s), 1498 (w), 1421 (w), 1397 (m), 1298 (m), 1252 (w), 1168 (s), 1021 (m), 963 (w), 846 (s), 834 (sh), 744 (m), 620 (m), 602 (sh), 487 (m), 439 (w).

4.3.3 Structure Determination

From single crystal X-ray data. Single crystals suitable for X-ray crystallographic analysis were selected following examination under a microscope (Figure 4.20).

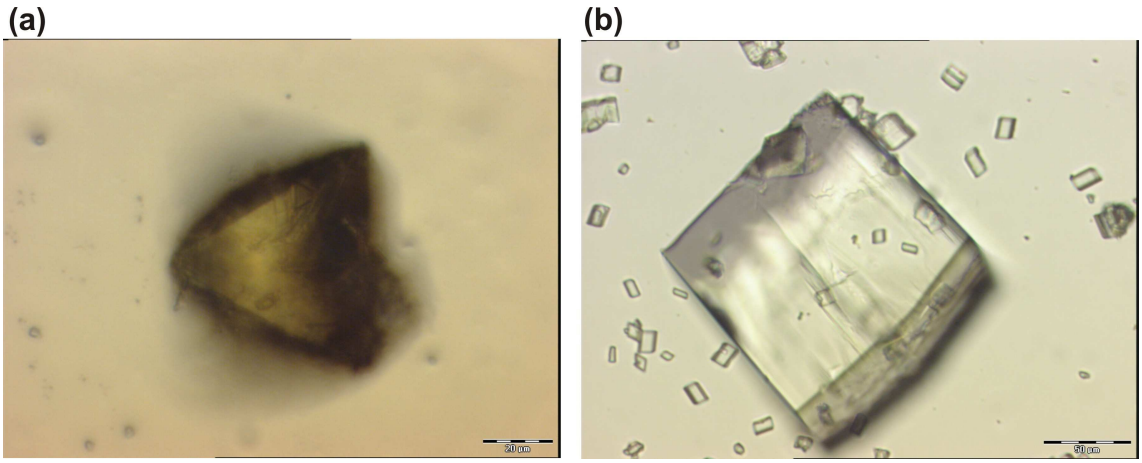

Figure 4.20 Optical micrographs of the single crystals of compound **1** (a) and **2** (b).

Intensity data of **1** were collected on a diffractometer equipped with a STOE imaging plate detector system IPDS 2T, using MoK_α radiation with graphite monochromatization (λ = 0.71073 Å) at T = 103 K. Initial structures were solved by direct methods and refined by full-matrix least-squares techniques based on F^2 using SHELXS-97 and SHELXL-97 software.[187] Single crystal X-ray diffraction studies of **2** were performed on a STOE IPDS diffractometer employing monochromated MoK_α radiation (λ = 0.71073). Initial structures were solved by direct methods and refined by full-matrix least-squares techniques based on F^2 using the SHELXL-97 program.[187] Hydrogen atoms were placed at calculated positions and refined using a riding model. All non-hydrogen atoms were refined anisotropically. Details of single crystal X-ray data collection and refinement of **1** and **2** are summarised in Table 4.5.

Table 4.5 Single crystal X-ray data and structure refinement parameters for **1** and **2.**

Compound	**1**	**2**
Formula	$C_{27}H_{27}Cl_4N_{21}O_3Zn_5$	$C_7H_{10}ClN_4OZn$
Formula mass	1162.35	267.01
T/K	103(2)	293(2)
λ/Å	0.71073	0.71073
Crystal dimensions/mm	0.08×0.06×0.06	0.15×0.23×0.23
Crystal system	Cubic	Monoclinic
Space group	$Fm\bar{3}m$	$P2_1/c$
a/Å	21.697(3)	9.812(2)
b/Å		8.6012(17)
c/Å		12.571(3)
β/°		96.91(3)
V/Å^3	10214(2)	1053.3(4)
Z	8	4
D_c/g cm^{-3}	1.482	2.071
μ/mm^{-1}	2.573	2.558
F(000)	4624	636
θ Range/°	4.60-26.77	2.88-25.95
Measured reflections	16467	11882
Independent reflections/Rint	542/0.1181	1920/0.1948
Data/restraints/parameters	542/0/48	1920/0/127
R_1 (I >2σ(I))[a]	0.0678	0.0576
wR_2 (all data)[b]	0.1514	0.1600
Goodness-of-fit on F^2	1.199	0.884
$\Delta\rho_{max, min}$/e Å^{-3}	0.977, -0.725	0.919, –0.760

[a] $R_1 = \sum||F_o| - |F_c||/ \sum|F_o|$. [b] $wR_2 = \{\sum [w(F_o^2 - F_c^2)^2]/ \sum[w(F_o^2)^2]\}^{1/2}$.

From powder diffraction data. Lattice parameters of **1** at different temperatures were determined using the PROSZKI package.[212] Structure determination, independent from single crystal X-ray diffraction studies, was performed using the EXPO2004 package,[213] which combines a full pattern decomposition program (EXTRA) and a direct method program (SIR97) optimized for powder diffraction data. During pattern decomposition, the lattice parameters were not refined. The whole crystal model, *i.e.* the zinc, chlorine, nitrogen and

carbon atoms, was found using the direct method. The Rietveld refinement was carried out using the Jana2000 program.[214] Weak geometric restraints on bond distances were used during the refinement process. The preferred orientation was chosen along the [111] direction and it was refined applying the March-Dollase formula. Details of crystal data and structure refinement parameters of **1** obtained from Rietveld refinement are summarised in Table 4.6.

Table 4.6 Crystal data and structure refinement parameters of **1** obtained from Rietveld refinement using powder data at 350 °C.

Formula	$C_{18}Cl_4N_{18}Zn_5$
Formula mass/g mol^{-1}	937.03
Calculated density/g cm^{-3}	1.2303
Crystal system	Cubic
Space group	$Fm\bar{3}m$, No. 225
a/Å	21.6265(9)
V/Å^3	10114.9(4)
Z	8
T/K	623(2)
Figures of merit	M_{21}= 19.52; F_{21}= 33.60
2θ Range/$^\circ$	5-80
Number of observations	3748
R_p	9.03
R_{wp}	13.67
R_{obs}	10.62
R_{wobs}	8.81

4.4 Summary

An unprecedented cubic framework (**1**, **MFU-4**), constructed from $\{BBTA\}^{2-}$ dianions and $\{Zn_5Cl_4\}^{6+}$ coordination units, have been successfully prepared and fully characterized. Compared to the solvothermal synthesis, the preparation of **1** by microwave irradiation method leads to a large reduction in reaction time. A different coordination mode of the benzobistriazolate ligands has been established by the synthesis and characterization of coordination polymer **2**, which demonstrates that the particular choice of solvent plays a crucial role in the synthesis of crystalline phases of coordination polymers of similar

composition, especially MOFs. Thermogravimetric analysis indicates that **MFU-4** possesses a slightly higher thermal stability (350 °C) than **MOF-5**. Strong luminescence exhibited by these novel coordination polymers suggests that they might be excellent candidates for photoactive material.

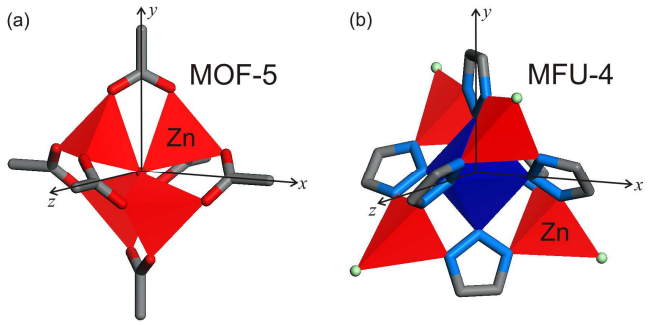

Figure 4.21 Structural differences between coordination units in (a) **MOF-5**, and (b) **MFU-4** (octahedrally coordinated Zn, blue octahedron; tetrahedrally coordinated Zn, red tetrahedra; N, light blue; C, grey; Cl, green).

The crystal lattice of **MFU-4** resembles **MOF-5** in terms of structural parameters as both are cubic, and both possess two different types of cavities. However, the coordination unit of **MFU-4** framework differs from **MOF-5** (Figure 4.21) with regard to the fact that **MFU-4** contains zinc ions within different coordination environments (one octahedral and four tetrahedral metal centers) while **MOF-5** has only tetrahedral zinc centers. As evidenced by the previous work on low-molecular homo- and heteropentanuclear coordination compounds bearing structurally similar $\{MZn_4Cl_4\}^{6+}$ cores (M^{II} = Zn, Fe, Co, Ni, or Cu) (*cf.* Chapter 2),[10c] replacement of the octahedrally coordinated zinc centers in **MFU-4** by redox-active 3d or 4d transition metal ions should be feasible without affecting the framework structure, a non-trivial task which has remained elusive for **MOF-5** type compounds so far.[215] Such heterometallic **MFU-4** type frameworks could be useful in catalytic redox reactions provided that a facile synthesis for an extended benzobistriazolate ligand could be developed which allows for free diffusion of molecules in the voids of the constituting framework lattice.

Chapter 5

Conclusions and Outlook

The work presented in this dissertation clearly indicates that benzotriazole and its derivatives are important precursors for the synthesis of polynuclear metal coordination compounds and coordination polymers. The synthetic strategies described in earlier literature mostly used metal(II) β-diketonates as starting materials for the preparation of polynuclear compounds based on benzotriazolate ligands. The synthetic strategy of employing metal(II) β-diketonates as starting materials is based on the proton transfer between metal(II) β-diketonates and benzotriazole ligand, and subsequent partial replacement of the β-diketonato ligands by the deprotonated benzotriazole ligands. The synthetic approaches for the preparation of homo- and heteropolynulear coordination compounds described in this thesis are completely different from those reported previously. As demonstrated in Chapter 2 and 3, homo- and heteropolynulear metal coordination compounds have been successfully synthesized using metal(II) halides as well as nitrates and acetates as synthetic precursors. For the preparation of homo- and heteropentanuclear coordination compounds of general formula $[MZn_4Cl_4(Me_2bta)_6]\cdot 2DMF$ (M^{II} = Zn^{II}, Fe^{II}, Co^{II}, Ni^{II}, or Cu^{II}; Me_2btaH = 5,6-dimethyl-1,2,3-benzotriazolate ligand) presented in Chapter 2, the appropriate metal precursors and benzotriazolate ligands have been dissolved at the theoretical stoichiometric ratio in polar solvent such as DMF. Subsequently, the vapour of a weakly coordinating auxiliary base such as 2,6-lutidine was allowed to diffuse into the reaction medium, which abstracts the acidic –NH protons from benzotriazole ligands. Thus, the deprotonated benzotriazolate ligands can use all three nitrogen donor atoms to coordinate with metal centers in a bridging $\eta^1{:}\eta^1{:}\eta^1{:}\mu_3$ binding mode. Furthermore, a facile and rapid synthetic route, naming “direct addition of lutidine” which is much faster than the time-consuming “vapour diffusion of lutidine” approach, has been successfully developed to prepare compounds of general formula $[MZn_4Cl_4(Me_2bta)_6]$. In this way, gram-scale quantities of compounds having the general formula $[MZn_4Cl_4(Me_2bta)_6]\cdot 2C_6H_5Br$ (C_6H_5Br = bromobenzene) can be produced via the direct addition of lutidine into a methanol solution containing stoichiometric required amounts of the metal salts and ligands, followed by recrystallisation of the resulting solid from bromobenzene. The three homononanuclear Ni(II), Co(II), and Zn(II) compounds described in Chapter 3 have been prepared by an additional approach using an excess of ligand, which acts

as auxiliary base leading to the deprotonation of the other benzotriazolate ligands. This strategy enabled the preparation of three novel compounds, namely $[Co_9(bta)_{12}(MeOH)_{18}][(NO_3)_6]\cdot 9C_6H_6$ (C_6H_6 = benzene), $[Ni_9(bta)_{12}(NO_3)_6(MeOH)_6]\cdot 4THF$ (THF = tetrahydrofuran), and $[Zn_9(Me_2bta)_{12}(CH_3COO)_6]\cdot 3DMF$ (DMF = *N*,*N*'-dimethylformamide). The other two nonanuclear compounds described in Chapter 3 have the molecular formulae $[Zn_9(OMe_2bta)_{12}Cl_6]\cdot DMF$ (OMe_2btaH = 5,6-dimethoxy-1,2,3-benzotriazole) and $[Fe_3Zn_6(OMe_2bta)_{12}Cl_6]\cdot DMF$. The latter two compounds have been synthesized using the "vapor diffusion of lutidine" strategy previously employed to prepare the homo- and heteropentanuclear compounds of the type $[MZn_4Cl_4L_6]\cdot 2DMF$ (M^{II} = Zn^{II}, Fe^{II}, Co^{II}, Ni^{II}, or Cu^{II}; L = 1,2,3-benzotriazolate ligand) as described in Chapter 2. Three of the compounds {$[Zn_5Cl_4(Me_2bta)_6]\cdot 2DMF$, $[Zn_9(OMe_2bta)_{12}Cl_6]\cdot DMF$, and $[Fe_3Zn_6(OMe_2bta)_{12}Cl_6]\cdot DMF$} have been synthesized by the solvothermal procedure, in addition to the vapour diffusion method. In the solvothermal approach, thermal decomposition of an amide solvent such as DMF liberates a base (dimethylamine in the case of DMF) in the reaction medium. This *in-situ* generated base abstracts the acidic protons from the 1,2,3-benzotriazole ligands. However, the solvothermal route was unsuccessful for the synthesis of all the other compounds described in Chapter 2 and 3.

The graph theory reveals further features of the pentanuclear benzotriazolate complexes. The Kuratowski-type of homo- and heteropentanuclear coordination units $[M^{II}Zn_4Cl_4(Me_2bta)_6]$ (M^{II} = Zn^{II}, Fe^{II}, Co^{II}, Ni^{II}, or Cu^{II}) described in Chapter 2 represent the rare class of minimum nonplanar building units bearing T_d point group symmetry and $K_{3,3}$ topology, from which a large number of cubic porous frameworks, having the topology of **MFU-4** type of frameworks (*cf.* Chapter 4), can be constructed. The fundamental study on the versatile, easily accessible molecular complexes would offer possibilities for rational systematic design of the corresponding frameworks and optimization of their functional properties. Single crystal X-ray data reveal that the open-shell metal ions in all heteropentanuclear complexes are in high-spin state without undergoing any Jahn-Teller distortion, which has been further verified by electronic spectroscopy and magnetic measurements. Thermogravimetric analyses on all of these discrete molecular complexes reveal high thermal stability up to 400 °C. TOF-MS analyses, and comparative solution and solid-state UV-Vis spectroscopy confirm that all these pentanuclear coordination units maintain their structural integrity in solution. The exceptionally high thermal and solvolytic stability along with the availability of redox-active, open-shell metal ions as well as coordinatively unsaturated Zn sites would enable such compounds to perform homogenous redox and Lewis-acid catalyzed reactions, which would

subsequently provide insights into the mechanistic aspects for the proposed catalytic properties of structurally related **MFU-4** type of frameworks. Moreover, such compounds might display interesting combinations of useful properties such as luminescence or reversible electron transfer.

The successful synthesis and characterization of the nonanuclear cobalt compound $[Co_9(bta)_{12}(MeOH)_{18}][(NO_3)_6]\cdot 9C_6H_6$ (C_6H_6 = benzene) described in Chapter 3 demonstrates the existence of a $\eta^1{:}\eta^1{:}\eta^1{:}\mu_3$ coordination mode of benzotriazolate ligands in Co(II) coordination chemistry. Magnetochemical analysis show net antiferromagnetic intramolecular coupling in the Co(II)-based compound $[Co_9(bta)_{12}(MeOH)_{18}][(NO_3)_6]\cdot 9C_6H_6$, whereas both ferro- and antiferromagnetic coupling is observed in Ni(II)-based compound $[Ni_9(bta)_{12}(NO_3)_6(MeOH)_6]\cdot 4THF$.

Mössbauer spectroscopic investigations on the heterononanuclear compound $Fe_3Zn_6Cl_6(OMe_2bta)_{12}]$ presented in Chaper 3 reveal a HS→LS (HS: high-spin, LS: low-spin) transition for only the central Fe(II) ion upon cooling, while the HS states of the two adjacent octahedrally coordinated Fe(II) ions remain unchanged upon variation of temperature. This unique spin-crossover (SCO) behaviour is rare, and has been previously reported only for a trinuclear Fe^{II} compound.[195d-e] Comparative Mössbauer studies on the solvated form of this compound (which does not display SCO behaviour), and desolvated materials suggest that the present Fe^{II} SCO system is very sensitive to the presence of lattice solvent molecules, which is a well-established phenomenon shown by many other SCO systems.[191d,191g,191i,191p,195m] Electrochemical investigations on this compound show a reversible oxidation of the Fe^{II} ions, occuring at a potential significantly higher than that of ferrocene. Both, X-ray diffraction studies (223 K) and UV-Vis analyses (298 K) of this compound indicate the presence of both HS and LS Fe^{II} ions at the respective measurement temperatures. Unfortunately, the complicated time-dependent release of solvent DMF molecules results in “aging” of the crystals of this compound, preventing from performing any further time- and temperature-dependent studies to correlate the magnetic and SCO behaviour of solvated and desolvated forms of this material at various conditions. Nevertheless, the previous experiments (*cf.* Chapter 2)[10c] on 1,2,3-triazole-based heteropentanuclear compounds indicate that the present SCO system might represent one member of a family of compounds having composition $[M_3Zn_6X_6L_{12}]$, which can be prepared by the variation of 3d transition metal (M^{II} = Co, Ni, or Cu) ions, 1,2,3-triazolate ligands or monodentately coordinated halogenides (X = Cl, Br, or I). Notably, the heterononanuclear Co^{II} compound isostructural with this heterononanuclear Fe^{II} compound might show interesting SCO behaviour, comparable with the Fe^{II} compound, since

SCO in Co^{II} compounds is well-documented, although less commonly observed than for Fe^{II} compounds.[201]

The multidentate nature of the binding mode, and especially the $\eta^1:\eta^1:\eta^1:\mu_3$-coordination of benzotriazolate ligands provoked the employment of the ligand benzobistriazole (H_2-BBTA) for the design of a porous 3D cubic coordination framework. The deprotonated form of H_2-BBTA ligand has the ability to coordinate to metal centers in a bridging $\eta^1:\eta^1:\eta^1:\eta^1:\eta^1:\eta^1:\mu_6$ mode, and thus can act as linear "spacers" between discrete metal-organic coordination units used as "nodes" to form 3D cubic framework. Thus, assuming the tetrahedral symmetrical $\{Zn_5Cl_4\}^{6+}$ coordination units (*cf.* Chapter 2) at the vertices, and the $\{BBTA\}^{2-}$ dianions at the edges of a cubic lattice, molecular mechanics simulations clearly indicated that there should be exactly one way of assembling $\{Zn_5Cl_4\}^{6+}$ SBUs and $\{BBTA\}^{2-}$ dianions into a periodic cubic framework. In reality, this working model proved to be correct leading to the directed solvothermal synthesis of a 3D cubic porous framework $[Zn_5Cl_4(BBTA)_3]\cdot 3DMF$ (**MFU-4**). However, in the course of comparative investigations on suitable preparation conditions, it was discovered that the successful formation of this compound is delicately dependent on the solvent used in synthesis. Thus, employing *N*,*N*'-dimethylacetamide (DMA) as solvent instead of *N*,*N*'-dimethylformamide (DMF), another compound possessing molecular formula $[ZnCl(BBTA)_{0.5}(DMA)]$ crystallizes from the reaction mixture, which constitutes a densely packed 2D layered coordination polymer, in contrast to the porous cubic framework of **MFU-4**. The main difference between both structures is the coordination mode of the BBTA ligands: in contrast to **MFU-4**, only two (N^1 and N^3) of the triazolate N-donor atoms are coordinated to zinc ions in the 2D layered coordination polymer.

Thus, a different coordination mode of the benzobistriazolate ligands has been established through the synthesis and characterization of the 2D coordination polymer. Though the role of amide solvents remains the same (*i.e.*, liberation of dimethylamine *in-situ* due to their decomposition under solvothermal conditions), the achievement of two different coordination polymers using two different amide solvents demonstrates that the particular choice of solvent plays a crucial role in the synthesis of crystalline phases of metal-organic frameworks having similar composition. Both of the above mentioned coordination polymers exhibit strong luminescence emission properties, which suggest that they might be excellent candidates for photoactive materials. For the rapid synthesis of **MFU-4**, a microwave irradiation method, which takes only a few minutes (typically 10 minutes) compared to several hours or even days required for conventional solvothermal synthesis, has been successfully developed. Thermogravimetric analysis indicates that **MFU-4** possesses a slightly higher thermal stability

(350 °C) than the protypical **MOF-5**. As evidenced by the previous work on low-molecular homo- and heteropentanuclear coordination compounds bearing structurally similar $\{MZn_4Cl_4\}^{6+}$ cores (M^{II} = Zn, Fe, Co, Ni, or Cu) (*cf.* Chapter 2), replacement of the octahedrally coordinated zinc centers in **MFU-4** by redox-active 3d or 4d transition metal ions should be feasible without affecting the framework structure, a non-trivial task which has remained elusive for **MOF-5** type compounds so far. Such heterometallic **MFU-4** type frameworks could be useful in catalytic redox reactions provided that a facile synthesis for an extended benzobistriazolate ligand could be developed which allows for free diffusion of molecules in the voids of the constituting framework lattice. Moreover, the tetrahedral Zn centers in **MFU-4** are strongly Lewis acidic sites, thus might be useful in catalytic reactions, which are normally promoted by Lewis acids. The high inner surface area enables **MFU-4** to achieve high capacity (1.62 wt. %) for hydrogen adsorption. Due to the presence of small apertures inside **MFU-4** framework, it exhibits a highly selective adsorption for hydrogen vs. nitrogen at -196 °C. The framework is stable against moisture and has a specific pore volume of 0.42 $cm^3\ g^{-1}$ estimated from the water adsorption isotherm. The "molecular sieving" characteristics suggests that **MFU-4** can be used in gas separation processes where hydrogen molecules (or similarly: helium atoms) have to be separated from mixture of gases (e.g. CO_2, CO, O_2 or N_2).

Kapitel 5

Zusammenfassung und Ausblick

Die in dieser Dissertation dargestellten Arbeiten zeigen deutlich, dass Benzotriazol und seine Derivate wichtige Liganden für die Synthese von mehrkernigen Metallkomplexen und Koordinationspolymeren sind. Synthese-Strategien aus früheren Arbeiten verwendeten überwiegend Metall(II)-β-Diketonate als Edukte für die Herstellung von mehrkernigen Verbindungen auf Basis von Benzotriazolat-Liganden. Bei der Verwendung von Metall(II)-β-Diketonaten als Ausgangsmaterialien wird der Protonentransfers zwischen den Metall(II)-β-Diketonaten und den Benzotriazolat-Liganden ausgenutzt, wodurch die Benzotriazolat-Liganden deprotoniert werden und einen Teil der vorhandenen β-Diketonato-Liganden ersetzen. Die in dieser Arbeit aufgezeigten synthetischen Ansätze für die Herstellung von homo- und heteropolynuklearen Komplexverbindungen weichen vollständig von der zuvor erläuterten Synthesestrategie ab. Wie in Kapitel 2 und 3 gezeigt wurde, konnten homo- und heteropolynukleare Metallkoordinationsverbindungen erfolgreich mit Metall(II)-Halogeniden sowie mit Nitraten und Acetaten als synthetische Ausgangsstoffe synthetisiert werden. Für die in Kapitel 2 beschriebene neuartige Synthese von homo- und heteropentanuklearen Komplexverbindungen der allgemeinen Formel $[MZn_4Cl_4(Me_2bta)_6]\cdot 2DMF$ (M^{II} = Zn^{II}, Fe^{II}, Co^{II}, Ni^{II}, oder Cu^{II}; Me_2btaH = 5,6-Dimethyl-1,2,3-Benzotriazolat-Liganden) wurden zunächst die geeigneten Metallsalze und Benzotriazolat-Liganden im theoretischen stöchiometrischen Verhältnis in einem polaren Lösungsmittel wie DMF gelöst. Durch anschließende Dampfdiffusion einer schwach koordinierenden Hilfsbase wie etwa 2,6-Lutidin in die Reaktionslösung werden die aciden Protonen am Stickstoffatom der Benotriazolat-Liganden entfernt. Dadurch stehen alle drei Stickstoffatome der Benzotriazolat-Liganden zur Koordination mit den Metallkernen zur Verfügung (verbrückende $\eta^1{:}\eta^1{:}\eta^1{:}\mu_3$-Koordination). Ein einfacherer und schnellerer synthetischer Ansatz um Verbindungen mit der allgemeinen Formel $[MZn_4Cl_4(Me_2bta)_6]$ herzustellen wurde durch die „direkte Zugabe von Lutidin“ erfolgreich entwickelt, der sich durch deutlich kürzere Reaktionszeiten als der zeitaufwändige Ansatz der „Dampfdiffusion von Lutidin“ auszeichnet. Verbindungen der allgemeinen Formel $[MZn_4Cl_4(Me_2bta)_6]\cdot 2C_6H_5Br$ (C_6H_5Br = Brombenzol) können auf diese Weise im Grammmaßstab erhalten werden, wenn Lutidin zu einer stöchiometrischer Mengen an Metallsalzen und Liganden in methanolischer Lösung gegeben wird und man den erhaltenen

Niederschlag aus Brombenzol umkristallisiert. Ein weiterer Ansatz beruht auf der Verwendung eines Überschusses des Liganden, der als Hilfsbase zur Deprotonierung der übrigen Benzotriazolat-Liganden dient. Auf diese Weise sind die in Kapitel 3 beschriebenen homononanuklearen Ni(II)-, Co(II)- und Zn(II)-Verbindungen $[Co_9(bta)_{12}(MeOH)_{18}][(NO_3)_6]\cdot 9C_6H_6$ (C_6H_6 = Benzol), $[Ni_9(bta)_{12}(NO_3)_6(MeOH)_6]\cdot 4THF$ (THF = Tetrahydrofuran), und $[Zn_9(Me_2bta)_{12}(CH_3COO)_6]\cdot 3DMF$ (DMF = *N*,*N*'-Dimethylformamid) zugänglich. Die beiden anderen neunkernigen Verbindungen der molekularen Formel $[Zn_9(OMe_2bta)_{12}Cl_6]\cdot DMF$ (OMe_2btaH = 5,6-Dimethoxy-1,2,3-Benzotriazol) und $[Fe_3Zn_6(OMe_2bta)_{12}Cl_6]\cdot DMF$, die in Kapitel 3 beschrieben sind, wurden durch die Methode der „Dampfdiffusion von Lutidin“ synthetisiert. Die Herstellung erfolgte analog zu der in Kapitel 2 vorgestellten Synthese der homo- und heteropentanuklearen Verbindungen des Typs $[MZn_4Cl_4L_6]\cdot 2DMF$ (M^{II} = Zn^{II}, Fe^{II}, Co^{II}, Ni^{II}, oder Cu^{II}; L = 1,2,3-Benzotriazolat-Ligand). Drei der oben beschriebenen nonanuklearen Verbindungen, nämlich $[Zn_5Cl_4(Me_2bta)_6]\cdot 2DMF$, $[Zn_9(OMe_2bta)_{12}Cl_6]\cdot DMF$ und $[Fe_3Zn_6(OMe_2bta)_{12}Cl_6]\cdot DMF$, konnten nicht nur durch Dampfdiffusion, sondern auch durch solvothermalen Synthesebedingungen erhalten werden. Bei dem solvothermalen Ansatz wird die Hilfsbase *in-situ* durch thermische Zersetzung von Lösungsmitteln mit Amidgruppen freigesetzt etwa Dimethylamin im Falle des Lösungsmittels DMF. Diese *in-situ* geschaffene Base spaltet die aciden Protonen der 1,2,3-Benzotriazol-Liganden ab. Allerdings blieb der solvothermale Ansatz für die Synthese aller übrigen in Kapitel 2 und 3 beschrieben Verbindungen bisher erfolglos.

Durch die Graphentheorie werden weitere strukturelle Eigenschaften der pentanuclearen Benzotriazolat-Koordinationsverbindungen offenbart. Die in Kapitel 2 beschriebenen homo- und heteropentanuklearen Koordinationseinheiten $[M^{II}Zn_4Cl_4(Me_2bta)_6]$ (M^{II} = Zn^{II}, Fe^{II}, Co^{II}, Ni^{II}, oder Cu^{II}), stellen eine neue Familie von Komplexverbindungen des „Kuratowski-Typs“ dar, die sich strukturell durch T_d-Punktgruppensymmetrie und den minimalen nicht-planaren $K_{3,3}$-Graphen auszeichnen. Basierend auf diesen Sekundärbausteinen lassen sich neuartige mikroporöse Gerüstverbindung ableiten, die eine **MFU-4**-artige Gerüststruktur aufweisen (*vgl.* Kapitel 4). Grundlagenstudien zu den präparativ leicht zugänglichen molekularen Komplexverbindungen des Kuratowski-Typs würden die Möglichkeit einer rationalen und systematischen Planung der resultierenden Gerüstverbindungen ermöglichen, sowie die Vorhersage und Optimierung ihrer funktionellen Eigenschaften. Durch Einkristallröntgenstrukturanalysen kann gezeigt werden, dass sich die offenschaligen Metallionen in allen heteropentanuklearen Komplexen im High-Spin-Zustand befinden, wobei

keine Jahn-Teller-Verzerrung auftritt. Dieser Sachverhalt wurde darüber hinaus durch Elektronenspektroskopie und magnetische Messungen weiter bestätigt. Thermogravimetrische Untersuchungen zeigen, dass die niedermolekularen Komplexverbindungen eine hohe thermische Stabilität von bis zu 400 C aufweisen. TOF-MS-Untersuchungen an Lösungen der Komplexe zeigen dass die fünfkernigen Koordinationseinheiten ihre strukturelle Integrität in Lösung beibehalten, was auch durch den Vergleich der UV-Vis Spektren der Komplexe in Lösung und im Festkörper weiter bestätigt wird. Die außergewöhnlich hohe thermische und solvolytische Stabilität zusammen mit der Verfügbarkeit von redoxaktiven, offenschaligen Metallionen sowie koordinativ ungesättigten Zn-Metallzentren sollte dazu führen, dass diese Verbindungen als homogene Katalysatoren in Redoxreaktionen und Lewis-Säure-katalysierten Reaktionen eingesetzt werden könnten. Dadurch könnten in Folge auch weitere Einblicke in die mechanistischen Vorgänge bei den postulierten katalytischen Reaktionen in **MFU-4**-artigen Gerüstverbindungen gewonnen werden. Darüber hinaus könnten nützlichen Eigenschaften in derartige Verbindungen auf interessante Weise kombiniert werden, wie etwa Lumineszenz oder reversibler Elektronentransfer.

Die in Kapitel 3 beschriebene erfolgreiche Synthese und Charakterisierung der neunkernigen Kobalt-Verbindung $[Co_9(bta)_{12}(MeOH)_{18}][(NO_3)_6]\cdot 9C_6H_6$ (C_6H_6 = Benzol) zeigt dass eine $\eta^1{:}\eta^1{:}\eta^1{:}\mu_3$-Koordination der Benzotriazolat-Liganden auch bei Co(II)-Koordintationsverbindungen möglich ist. Magnetochemische Untersuchungen belegen eine antiferromagnetische intramolekulare Kopplung von Co(II)-Zentren in $[Co_9(bta)_{12}(MeOH)_{18}][(NO_3)_6]\cdot 9C_6H_6$, während bei der strukturanalogen Ni(II)-Verbindung $[Ni_9(bta)_{12}(NO_3)_6(MeOH)_6]\cdot 4THF$ sowohl ferro- als auch antiferromagnetische Kopplungen beobachtet wurden.

Durch Mössbauer-Spektroskopie an der in Kapitel 3 vorgestellten heterononanuklearen Verbindung $[Fe_3Zn_6Cl_6(OMe_2bta)_{12}]$ wurde gezeigt, dass beim Abkühlen auf tiefe Temperaturen nur für das mittlere Fe(II)-Ion ein Übergang von der High-Spin zur Low-Spin Konfiguration (HS→LS) auftritt, während sich die Spinzustände der zwei unmittelbar benachbarten oktaedrisch koordinierten Fe(II)-Ionen nicht ändern. Dieses einzigartige SCO-Verhalten (SCO: Spin-Crossover) ist selten und wurde in der Literatur bislang nur für eine dreikernige Fe^{II}-Verbindung beschrieben.[195d-e] Vergleichende Studien durch Mössbauer-Spetroskopie an der solvatisierten Verbindung (die kein SCO-Verhalten aufweist) und Pulvern einer lösungsmittelfreien Probezeigen, dass das vorliegende Fe^{II}-SCO-System sehr empfindlich auf das Vorhandensein von Gitter-Lösungsmittelmolekülen reagiert. Dieses gut untersuchte Phänomen tritt auch bei vielen anderen SCO-Systemen auf.[191d,191g,191i,191p,195m] Die

elektrochemischen Untersuchungen zu dieser Verbindung zeigen eine reversible Oxidation der Fe^{II}-Ionen, die bei einem deutlich höheren Potential als für Ferrocen auftritt. Sowohl die Röntgenbeugungsstudien (223 K) als auch die UV-Vis-Untersuchungen (298 K) dieser Verbindung weisen auf das gleichzeitige Auftreten einer HS als auch einer LS-Konfiguration der Fe^{II}-Ionen bei den jeweiligen Messtemperaturen hin. Leider führt die komplizierte zeitabhängige Freisetzung von DMF-Molekülen zu einer schlecht kontrollierbaren „Alterung" der Kristalle dieser Verbindung. Daher konnten keine weiteren zeit- und temperaturabhängigen Untersuchungen zum magnetischen und SCO-Verhalten der solvatisierten sowie lösungsmittelfreien Probe durchgeführt werden. Allerdings weisen die vorangegangen Untersuchungen (*vgl.* Kapitel 2)[10c] an heteropentanuklearen Verbindungen auf Basis von 1,2,3-Benzotriazolat darauf hin, dass das spezielle, hier vorliegende SCO-System lediglich ein Beispiel aus einer ganzen Serie neuartiger Verbindungen der Zusammensetzung $[M_3Zn_6X_6L_{12}]$ sein könnte. Diese weiteren Derivate könnten etwa durch Variation des 3d-Übergangsmetalls (M^{II} = Co^{II}, Ni^{II} oder Cu^{II}), der 1,2,3-Triazolat-Liganden sowie des einzähnig koordinierten Halogenidions (X = Cl, Br oder I) hergestellt werden. Bemerkenswerterweise ist die neunkernige Co^{II}-Verbindung isostrukturell zur neunkernigen Fe^{II}-Verbindung. Da SCO-Phänomene von Co^{II}-Verbindungen in der Literatur gut dokumentiert sind, wenngleich auch weniger häufig ist als für Fe^{II}-Verbindungen, wäre daher für die isostrukturelle neunkernige Co^{II}-Verbindung ebenfalls ein interessantes SCO-Verhalten zu erwarten, das mit dem der Fe^{II}-Verbindung vergleichbar sein könnte.[201]

Die verbrückende, mehrzähnige Koordination von Benzotriazolat-Liganden, und insbesondere die Geometrie des Komplexes bei der $\eta^1{:}\eta^1{:}\eta^1{:}\mu_3$-Koordination war der Anlass für die Verwendung des Liganden Benzobistriazol (H_2-BBTA) zum Aufbau einer mikroporösen dreidimensionalen Gerüststruktur. Die deprotonierte Form des H_2-BBTA-Liganden ist in der Lage im $\eta^1{:}\eta^1{:}\eta^1{:}\eta^1{:}\eta^1{:}\mu_6$-Koordinationsmodus an sechs Metallzentren zu koordinieren. Der verbrückende Ligand dient hierbei als linearer „Stützpfeiler" zwischen den einzelnen, diskreten metallorganischen Komplexeinheiten, die als Knotenpunkte der dreidimensionalen Gerüststruktur fungieren. Nimmt man nun an, dass sich die $\{Zn_5Cl_4\}^{6+}$-Koordinationseinheiten (*vgl.* Kapitel 2) an den Knotenpunkten und die $\{BBTA\}^{2-}$-Dianionen auf den Kanten eines kubischen Gitters befinden, dann weisen Molekularmechanik-Simulationen eindeutig darauf hin, dass es nur genau ein Möglichkeit gibt mit den beiden Sekundärbausteine $\{Zn_5Cl_4\}^{6+}$ und $\{BBTA\}^{2-}$ ein periodisches kubisches Netzwerk aufzubauen. Diese Arbeitshypothese erwies sich als korrekt, da die Solvothermasynthese zielgerichtet zu der mikroporösen dreidimensionalen Gerüstverbindung

$[Zn_5Cl_4(BBTA)_3]\cdot 3DMF$ (**MFU-4**) führte. In Vergleichsstudien zu den geeigneten Synthesebedingungen stellte sich heraus, dass die erfolgreiche Bildung dieser Verbindung sehr stark vom in der Synthese eingesetzten Lösungsmittel abhängt. Wenn als Lösungsmittel *N,N'*-Dimethylacetamid (DMA) anstelle von *N,N'*-Dimethylformamid (DMF) verwendet wird, so wird eine andere kristalline Verbindung der Formel $[ZnCl(BBTA)_{0.5}(DMA)]$ erhalten. Diese weitere Verbindung ist ein Koordinationspolymer das aus dicht gepackten zweidimensionalen Schichten aufgebaut ist, im Gegensatz zu der mikroporösen kubischen Gerüststruktur von **MFU-4**. Der wesentliche Unterschied zwischen den beiden Strukturen liegt in der Koordination des BBTA-Liganden: Im Vergleich zu **MFU-4** koordinieren nur zwei der drei Stickstoffatome der Triazolatgruppe (N^1 and N^3) an die Zink-Ionen in der zweidimensionalen Schichtstruktur.

Auch wenn die Rolle des Amidlösungsmittel in beiden Festkörpersynthesen die gleiche ist, *d.h.,* dass eine Freisetzung von Dimethylamin aufgrund der thermischen Zersetzung des Lösungsmittels erfolgt, zeigt die erfolgreiche Synthese zweier verschiedener Koordinationspolymere unter den vergleichbaren Synthesebedingungen, dass die jeweilige Wahl des Lösungsmittels eine entscheidende Rolle bei der Synthese kristalliner Phasen von Metall-Organischen Gerüstverbindungen spielt. Beide der oben erwähnten Koordinationspolymere weisen photolumineszente Eigenschaften auf, was für eine Verwendung als photoaktive Materialien spräche. Um die Synthese von **MFU-4** zu beschleunigen, wurde eine Mikrowellensynthese entwickelt, bei der die Verbindung in wenigen Minuten erhalten wird, im Vergleich zu mehreren Stunden oder Tagen, die für die konventionelle solvothermale Synthese erforderlich sind. Thermogravimetrische Untersuchungen weisen darauf hin, dass **MFU-4** eine höhere Temperaturbeständigkeit (350 C) aufweist als das bekannte **MOF-5**. Wie frühere Arbeiten an niedermolekularen homo- und heteropentanuklearen Komplexverbindungen mit strukturell ähnlichen $\{MZn_4Cl_4\}^{6+}$-Koordinationseinheiten (M^{II} = Zn, Fe, Co, Ni, oder Cu) zeigen (*vgl.* Kapitel 2), sollte eine isotype Substitution der oktaedrisch koordinierten Zink-Zentren in **MFU-4** durch redoxaktive 3d- oder 4d-Übergangsmetallionen möglich sein. Dies ist eine nicht-triviale Aufgabe, die bisher für **MOF-5**-analoge Verbindungen noch nicht umgesetzt werden konnte. Derartige heterometallische **MFU-4**-Gerüststrukturen könnten bei der Verwendung in katalytischen Redoxreaktionen vorteilhaft sein, unter der Voraussetzung dass ein einfacher synthetischer Zugang zu verlängerten Bistriazol-Liganden entwickelt wird, wodurch die freie Diffusion von Molekülen in den Hohlräumen der **MFU-4**-analogen Gittergerüststruktur ermöglicht werden sollte. Darüber hinaus haben die vierfach koordinierten Zn-Zentren in **MFU-4** stark Lewis-

sauren Charakter und könnten somit auch für all jene katalytischen Reaktionen vorteilhaft sein, die normalerweise ebenso von Lewis-Säuren beschleunigt werden. Durch die hohe innere Oberfläche hat **MFU-4** eine gute Kapazität (1,62 Massenanteile) für die Wasserstoffadsorption. Aufgrund der vorhandenen engen Porendimensionen ist die Verbindung selektiv bezüglich der Aufnahme von Gasen: bei -196 C wird ausschließlich Wasserstoff adsorbiert, während keinerlei Stickstoffaufnahme festzustellen ist. Die Gerüststruktur ist hydrolysestabil und hat, ein anhand der Wasserdampfadsorptionsisotherme abgeschätztes spezifisches Porenvolumen von 0,42 cm^3 g^{-1}. Die „Molekularsieb"-Eigenschaften weisen darauf hin, dass **MFU-4** zur Trennung von Gasen eingesetzt werden könnte, etwa zur Abtrennung von Wasserstoffmolekülen (oder ähnlich: Helium-Atomen) von anderen Gassorten (z. B. CO_2, CO, O_2 oder N_2).

References

1. W. Giger, C. Schaffner, H.-P. E. Kohler, *Environ. Sci. Technol.*, **2006**, *40*, 7186.
2. (a) I. Dugdale, J. B. Cotton, *Corros. Sci.*, **1963**, *3*, 69. (b) J. B. Cotton, I. R. Scholes, *Br. Corr. J.*, **1967**, *2*, 1. (c) R. Walker, *Anticorrosion*, **1970**, *17*, 9. (d) G. W. Poling, *Corros. Sci.*, **1970**, *10*, 359. (e) N. Morito, W. Suetaka, *J. Jpn. Inst. Met.*, **1971**, *35*, 1165.
3. (a) F. Mansfield, T. Smith, *Corrosion (Houston)*, **1973**, *29*, 105. (b) S. M. Mayanna, T. H. V. Setty, *Corros. Sci.*, **1975**, *15*, 625.
4. (a) R. Walker, *Metal Finish.*, 1973, 63. (b) R. Walker, *Corrosion (Houston, TX, U. S.)*, **1973**, *29*, 290. (c) I. C. G. Ogle, G. W. Poling, *Can. Metall. Q.*, **1975**, *14*, 37.
5. (a) R. F. Robert, *J. Electron Spectrosc. Relat. Phenom.*, **1974**, *4*, 273. (b) D. Chadwick, T. Hashemi, *J. Electr. Spectrosc. Relat. Phenom.*, **1977**, *10*, 79.
6. (a) L. D. Brown, J. A. lbers, A. R. Siedle, *Inorg. Chem.*, **1978**, *17*, 3026. (b) S. Zanias, C. P. Raptopoulou, A. Terzis, T. F. Zafiropoulos, *Inorg. Chem. Commun.*, **1999**, *2*, 48.
7. A. L. Spek, A. R. Siedle, J. Reedijk, *Inorg. Chim. Acta*, **1985**, *100*, L15.
8. H. M. J. Hendriks, P. J. M. W. L. Birker, G. C. Verschoor, J. Reedijk, *Dalton Trans.*, **1982**, 623.
9. J. H. Marshall, *Inorg. Chem.*, **1978**, *17*, 3711.
10. (a) X. L. Wang, C. Qin, S.-X. Wu, K.-Z. Shao, Y. Q. Lan, S. Wang, D. S. Zhu, Z.-M. Su, E.-B. Wang, *Angew. Chem., Int. Ed.*, **2009**, *48*, 5291. (b) S. Biswas, M. Tonigold, M. Speldrich, P. Kögerler, D. Volkmer, *Eur. J. Inorg. Chem.*, **2009**, 3094. (c) S. Biswas, M. Tonigold, D. Volkmer, *Z. Anorg. Allg. Chem.*, **2008**, *634*, 2532. (d) S. Biswas, M. Grzywa, H. P. Nayek, S. Dehnen, I. Senkovska, S. Kaskel, D. Volkmer, *Dalton Trans.*, **2009**, 6487. (e) Y.-Y. Qin, J. Zhang, Z.-J. Li, L. Zhang, X.-Y. Cao, Y.-G. Yao, *Chem. Commun.* **2008**, 2532. (f) C. Gkioni, V. Psycharis, C. P. Raptopoulou, *Polyhedron*, **2009**, *28*, 3425.
11. (a) Y.-L. Bai, J. Tao, R. B. Huang, L. S. Zheng, *Angew. Chem., Int. Ed.*, **2008**, *47*, 5344. (b) X.-M. Zhang, Z.-M. Hao, W.-X. Zhang, X.-M. Chen, *Angew. Chem., Int. Ed.*, **2007**, *46*, 3456.
12. (a) E. G. Bakalbassis, E. Diamantopoulou, S. P. Perlepes, C. P. Raptopoulou, V. Tangoulis, A. Terzis, T. F. Zafiropoulos, *J. Chem. Soc., Chem. Commun.*, **1995**, 1347. (b) V. Tangoulis, C. P. Raptopoulou, A. Terzis, E. G. Bakalbassis, E. Diamantopoulou, S. P. Perlepes, *Inorg. Chem.*, **1998**, *37*, 3142. (c) V. Tangoulis, C. P. Raptopoulou, A. Terzis, E. G. Bakalbassis, E. Diamantopoulou, S. P. Perlepes, *Mol. Cryst. Liq. Cryst.*, **1999**, *335*,

463.

13. (a) M. Murrie, D. Collison, C. D. Garner, M. Helliwell, P. A. Tasker, S. S. Turner, *Polyhedron*, **1998**, *17*, 3031. (b) J. Handley, D. Collison, C. D. Garner, M. Helliwell, R. Docherty, J. R. Lawson, P. A. Tasker, *Angew. Chem., Int. Ed.*, **1993**, *32*, 1036. (c) W. Jinling, Y. Ming, Y. Yun, Z. Shuming, M. Fangming, *Chin. Sci. Bull.*, **2002**, *47*, 890.
14. J. Reedijk, G. Roelofsen, A. R. Siedle, A. L. Spek, *Inorg. Chem.*, **1979**, *18*, 1947.
15. (a) D. Collison, E. J. L. McInnes, E. K. Brechin, *Eur. J. Inorg. Chem.*, **2006**, 2725. (b) J. Tabernor, L. F. Jones, S. L. Heath, C. Muryn, G. Aromí, J.Ribas, E. K. Brechin, D. Collison, *Dalton Trans.*, **2004**, 975. (c) R. H. Laye, Q. Wei, P. V. Mason, M. Shanmugam, S. J. Teat, E. K. Brechin, D. Collison, E. J. L. McInnes, *J. Am. Chem. Soc*., **2006**, *128*, 9020. (d) L. F. Jones, E. K. Brechin, D. Collison, A. Harrison, S. J. Teat, W. Wernsdorfer, *Chem. Commun.*, **2002**, 2974. (e) L. F. Jones, G. Rajaraman, J. Brockman, M. Murugesu, J. Raftery, S. J. Teat, W. Wernsdorfer, G. Christou, E. K. Brechin, D. Collison, *Chem.– Eur. J.*, **2004**, *10*, 5180. (f) L. F. Jones, E. K. Brechin, D. Collison, J. Raftery, S. J. Teat, *Inorg. Chem.*, **2003**, *42*, 6971. (g) L. F. Jones, J. Raftery, S. J. Teat, D. Collison, E. K. Brechin, *Polyhedron*, **2005**, *24*, 2443. (h) R. Shaw, R. H. Laye, L. F. Jones, D. M. Low, C. Talbot-Eeckelaers, Q. Wei, C. J. Milios, S. Teat, M. Helliwell, J. Raftery, M. Evangelisti, M. Affronte, D. Collison, E. K. Brechin, E. J. L. McInnes, *Inorg. Chem.*, **2007**, *46*, 4968. (i) D. M. Low, L. F. Jones, A. Bell, E. K. Brechin, T. Mallah, E. Rivière, S. J. Teat, E. J. L. McInnes *Angew. Chem., Int. Ed.*, **2003**, *42*, 3781.
16. (a) V. L. Himes, A. D. Mighell, A. R. Siedle, *J. Am. Chem. Soc*., **1981**, *103*, 211. (b) G. F. Kokoszka, J. Baranowski, C. Goldstein, J. Orsini, A. D. Mighell, V. L. Himes, A. R. Siedle, *J. Am. Chem. Soc*., **1983**, *105*, 5627. (c) Y.-X. Yuan, P.-J. Wei, W. Qin, Y. Zhang, J.-L. Yao, R.-A. Gu, *Eur. J. Inorg. Chem.*, **2007**, 4980.
17. H. Li, M. Eddaoudi, M. O'Keeffe, O. M. Yaghi, *Nature*, **1999**, *402*, 276.
18. R. L. Griffith, *J. Chem. Phys.*, **1943**, *11*, 499.
19. J. C. Bailar Jr., *Preparative Inorganic Reactions*, Interscience Publishers/JohnWiley & Sons, New York, **1964**, vol. 1, pp. 1-25.
20. R. Robson, *J. Chem. Soc., Dalton Trans.*, **2000**, 3735.
21. (a) B. Moulton, M. J. Zaworotko, *Chem. Rev.*, **2001**, *101*, 1629. (b) S. Subramanian, M. J. Zaworotko, *Angew. Chem., Int. Ed.*, **1995**, *34*, 2127. (c) T. L. Hennigar, D. C. MacQuarrie, P. Losier, R. D. Rogers, M. J. Zaworotko, *Angew. Chem., Int. Ed.*, **1997**, *36*, 972. (d) K. Biradha, C. Seward, M. J. Zaworotko, *Angew. Chem., Int. Ed.*, **1999**, *38*, 492.
22. (a) O. M. Yaghi, G. Li, H. Li, *Nature*, **1995**, *378*, 703. (b) O. M. Yaghi, H. Li, C. Davis,

D. Richardson, T. L. Groy, *Acc. Chem. Res.*, **1998**, *31*, 474. (c) M. Eddaoudi, D. B. Moler, H. Li, B. L. Chen, T. M. Reineke, M. O'Keeffe, O. M. Yaghi, *Acc. Chem. Res.*, **2001**, *34*, 319. (d) N. L. Rosi, M. Eddaoudi, J. Kim, M. O'Keeffe, O. M. Yaghi, *CrystEngComm*, **2002**, *4*, 401. (e) O. M. Yaghi, M. O'Keeffe, N. W. Ockwig, H. K. Chae, M. Eddaoudi, J. Kim, *Nature*, **2003**, *423*, 705. (f) J. L. C. Rowsell, O. M. Yaghi, *Microporous Mesoporous Mater.*, **2004**, *73*, 3. (g) N. W. Ockwig, O. Delgado-Friedrichs, M. O'Keeffe, O. M. Yaghi, *Acc. Chem. Res.*, **2005**, *38*, 176.

23. (a) S. S. Y. Chui, S. M. F. Lo, J. P. H. Charmant, A. G. Orpen, I. D. Williams, *Science*, **1999**, *283*, 1148. (b) J. S. Seo, D. Whang, H. Lee, S. I. Jun, J. Oh, Y. J. Jeon, K. Kim, *Nature*, **2000**, *404*, 982. (c) C. Janiak, *J. Chem. Soc., Dalton Trans.*, **2003**, 2781. (d) S. L. James, *Chem. Soc. Rev.*, **2003**, *32*, 276. (e) S. Kitagawa, R. Kitaura, S. Noro, *Angew. Chem., Int. Ed.*, **2004**, *43*, 2334. (f) C. N. R. Rao, S. Natarajan, R. Vaidhyanathan, *Angew. Chem., Int. Ed.*, **2004**, *43*, 1466.
24. G. S. Papaefstathiou, L. R. MacGillivray, *Angew. Chem., Int. Ed.*, **2002**, *41*, 2070.
25. (a) A. F. Wells, *Three-Dimensional Nets and Polyhedra*, Wiley, New York, **1977**. (b) A. F. Wells, *Further Studies of Three-dimensional Nets*, ACA Monograph, Washington, DC, **1979**. (c) A. F. Wells, *Structural Inorganic Chemistry*, 5th edn., Clarendon Press, Oxford, **1984**.
26. Z. Wang, PhD Thesis, University of South Florida, **2006**.
27. (a) B. Moulton, J. Lu, A. Mondal, M. J. Zaworotko, *Chem. Commun.*, **2001**, 863. (b) S. A. Bourne, J. J. Lu, A. Mondal, B. Moulton, M. J. Zaworotko, *Angew. Chem., Int. Ed.*, **2001**, *40*, 2111. (c) J. J. Lu, A. Mondal, B. Moulton, M. J. Zaworotko, *Angew. Chem., Int. Ed.*, **2001**, *40*, 2113. (d) Z. Wang, V. Ch. Kravtsov, M. J. Zaworotko, *Angew. Chem., Int. Ed.* **2005**, *44*, 2877.
28. (a) D. J. Tranchemontagne, J. L. Mendoza-Cortés, M. O'Keeffe, O. M. Yaghi, *Chem. Soc. Rev.*, **2009**, *38*, 1257. (b) J. Kim, B. Chen, T. M. Reineke, Hailian Li, Mohamed Eddaoudi, D. B. Moler, M. O'Keeffe, O. M. Yaghi, *J. Am. Chem. Soc.*, **2001**, *123*, 8239.
29. Ch. Baerlocher, L. B. McCusker, D. H. Olson, *Atlas of Zeolite Framework Types*, 6th rev. edn., Elsevier, Amsterdam, The Nederlands, **2007**. See also http://www.iza-structure.org/databases/.
30. (a) A. J. Blake, N. R. Champness, P. Hubbertstey, W. Li, M. A. Withersby, M. Schröder, *Coord. Chem. Rev.*, **1999**, *183*, 117. (b) B. Moulton, M. J. Zaworotko, *Chem. Rev.*, **2001**, *101*, 1629. (c) O. R. Evans, W. Lin, *Acc. Chem. Res.*, **2002**, *35*, 511. (d) K. Biradha, Y. H. Hongo, M. Fujita, *Angew.Chem., Int. Ed.*, **2000**, *39*, 3843. (e) C. J. Kepert, M. J.

Rosseinsky, *Chem. Commun.*, **1999**, 375. (f) L. Carlucci, G. Ciani, P. Macchi, D. M. Proserpio, *Chem. Commun.*, **1998**, 1837. (g) L. Carlucci, G. Ciani, D. M. Proserpio, S. Rizzato, *J. Chem. Soc., Dalton Trans.*, **2000**, 3821. (h) L. Carlucci, G. Ciani, D. M. Proserpio, S. Rizzato, *Chem. Commun.*, **2001**, 1198.

31. H. Li, M. Eddaoudi, T. L. Groy, O. M. Yaghi, *J. Am. Chem. Soc.*, **1998**, *120*, 8571.
32. S. H. Jhung, J. W. Yoon, J.-S. Hwang, A. K. Cheetham, J.-S. Chang, *Chem. Mater.*, **2005**, *17*, 4455.
33. S. H. Jhung, J.-S. Chang, J.-S. Hwang, S.-E. Park, *Microporous Mesoporous Mater.*, **2003**, *64*, 33.
34. Y. K. Hwang, J.-S. Chang, S.-E. Park, D. S. Kim, U. K. Kwon, S. H. Jhung, J.-S. Hwang, M. S. Park, *Angew. Chem., Int. Ed.*, **2005**, *45*, 556.
35. J. Y. Choi, J. Kim, S. H. Jhung, H.-K. Kim, J.-S. Chang, H. K. Chae, *Bull. Korean Chem. Soc.*, **2006**, *27*, 1523.
36. (a) M. L. Tong, X. M. Chen, S. R. Batten, *J. Am. Chem. Soc.*, **2003**, *125*, 16170. (b) J. F. Ma, J. Yang, G. L. Zheng, L. Li, J. F. Liu, *Inorg. Chem.*, **2003**, *42*, 7531. (c) X. M. Zhang, R. Q. Fang, H. S. Wu, *J. Am. Chem. Soc.*, **2005**, *127*, 7670. (d) D. Li, T. Wu, X. P. Zhou, R. Zhou, X. C. Huang, *Angew. Chem., Int. Ed.*, **2005**, *44*, 4175. (e) K. T. Youm, M. G. Kim, J. Ko, M. J. Jun, *Angew. Chem., Int. Ed.*, **2006**, *45*, 4003. (f) R. J. Hill, D. L. Long, N. R. Champness, P. Hubberstey, M. Schröder, *Acc. Chem. Res.*, **2005**, *38*, 337.
37. (a) M. D. Allendorf, C. A. Bauer, R. K. Bhakta, R. J. T. Houk, *Chem. Soc. Rev.*, **2009**, *38*, 1330. (b) F. Serpaggi, G. Férey, E. Antic-Fidancev, *J. Solid State Chem.*, **1999**, *148*, 347. (c) F. Millange, C. Serre, J. Marrot, N. Gardant, F. Pellé and G. Férey, *J. Mater. Chem.*, **2004**, *14*, 642. (d) O. R. Evans, W. Lin, *Acc. Chem. Res.*, **2002**, *35*, 511. (e) E. Y. Lee, S. Y. Jang, M. P. Suh, *J. Am. Chem. Soc.*, **2005**, *127*, 6374. (f) B. D. Chandler, D. T. Cramb, G. K. H. Shimizu, *J. Am. Chem. Soc.*, **2006**, *128*, 10403. (g) W. J. Rieter, K. M. L. Taylor, H. An, W. Lin, W. Lin, *J. Am. Chem. Soc.*, **2006**, *128*, 9024. (h) J.-R. Li, Y. Tao, Q. Yu, X.-H. Bu, *Chem. Commun.*, **2007**, 1527. (i) Y. Liu, G. Li, X. Li, Y. Cui, *Angew. Chem., Int. Ed.*, **2007**, *46*, 6301. (j) Y.-Q. Sun, J. Zhang, Y.-M. Chen, G.-Y. Yang, *Angew. Chem., Int. Ed.*, **2005**, *44*, 5814. (k) B. Zhao, X.-Y. Chen, P. Cheng, D.-Z. Liao, S.-P. Yan, Z.-H. Jiang, *J. Am. Chem. Soc.*, **2004**, *126*, 15394.
38. (a) M. Kurmoo, *Chem. Soc. Rev.*, **2009**, *38*, 1353. (b) G. Férey, *Nat. Mater.*, **2003**, *2*, 136. (c) D. Maspoch, D. Ruiz-Molina, J. Veciana, *J. Mater. Chem.*, **2004**, *14*, 2713. (d) G. J. Halder, C. J. Kepert, B. Moubaraki, K. S. Murray, J. D. Cashion, *Science*, **2002**, *298*, 1762. (e) P. D. C. Dietzel, Y. Morita, R. Blom, H. Fjellvaag, *Angew. Chem., Int. Ed.*,

2005, *44*, 6354. (f) W. Ouellette, M. H. Yu, C. J. O'Connor, D. Hagrman, J. Zubieta, *Angew. Chem., Int. Ed.*, **2006**, *45*, 3497. (g) C. Yu, S. Ma, M. J. Pechan, H.-C. Zhou, *J. Appl. Phys.*, **2007**, *101*, 09E108/101–09E108/103. (h) Z. Wang, Y. Zhang, T. Liu, M. Kurmoo, S. Gao, *Adv. Funct. Mater.*, **2007**, *17*, 1523. (i) B. Moulton, M. J. Zaworotko, *Curr. Opin. Solid State Mater. Sci.*, **2002**, *6*, 117. (j) S. R. Batten, K. S. Murray, *Coord. Chem. Rev.*, **2003**, *246*, 103.

39. (a) T. Okubo, R. Kawajiri, T. Mitani, T. Shimoda, *J. Am. Chem. Soc.*, **2005**, *127*, 17598. (b) Q. Ye, Y.-M. Song, G.-X. Wang, K. Chen, D.-W. Fu, P. W. H. Chan, J.-S. Zhu, S. D. Huang, R.-G. Xiong, *J. Am. Chem. Soc.*, **2006**, *128*, 6554. (c) Z. Xu, *Coord. Chem. Rev.*, **2006**, *250*, 2745. (d) M. Alvaro, E. Carbonell, B. Ferrer, F. X. Llabrés i Xamena, H. Garcia, *Chem.–Eur. J.*, **2007**, *13*, 5106. (e) A. Kuc, A. Enyashin, G. Seifert, *J. Phys. Chem. B*, **2007**, *111*, 8179.

40. (a) J.-Y. Lee, O. K. Farha, J. Roberts, K. A. Scheidt, S.-B. T. Nguyen, J. T. Hupp, *Chem. Soc. Rev.*, **2009**, *38*, 1450. (b) A. U. Czaja, N. Trukhan, U. Müller, *Chem. Soc. Rev.*, **2009**, *38*, 1284. (c) L. Ma, C. Abney, W. Lin, *Chem. Soc. Rev.*, **2009**, *38*, 1248. (d) N. Guillou, Q. Gao, P. M. Forster, J. S. Chang, M. Noguès, S.-E. Park, G. Férey, A. K. Cheetham, *Angew. Chem. Int. Ed.*, **2001**, *40*, 2831. (e) J. S. Seo, D. Whang, H. Lee, S. I. Jun, J. Oh, Y. J. Jeon, K. Kim, *Nature*, **2000**, *404*, 982. (f) A. Corma, *J. Catal.*, **2003**, *216*, 298. (g) W. Lin, *J. Solid State Chem.*, **2005**, *178*, 2486. (h) R.-Q. Zou, H. Sakurai, S. Han, R.-Q. Zhong and Q. Xu, *J. Am. Chem. Soc.*, **2007**, *129*, 8402. (j) F. X. Llabrés i Xamena, O. Casanova, R. Galiasso Tailleur, H. Garcia, A. Corma, *J. Catal.*, **2008**, *255*, 220. (j) U. Müller, M. M. Schubert, O. M. Yaghi, *Handbook of Heterogeneous Catalysis*, Wiley-VCH, Weinheim, 2nd edn., **2008**, vol. 1, pp. 247–262.

41. (a) T. Y. Shvareva, S. Skanthakumar, L. Soderholm, A. Clearfield, T. E. Albrecht-Schmitt, *Chem. Mater.*, **2007**, *19*, 132. (b) D. F. Sava, V. C. Kravtsov, F. Nouar, L. Wojtas, J. F. Eubank, M. Eddaoudi, *J. Am. Chem. Soc.*, **2008**, *130*, 3768. (c) Y. Liu, G. Li, X. Li and Y. Cui, *Angew. Chem., Int. Ed.*, **2007**, *46*, 6301. (d) B. F. Hoskins, R. Robson, *J. Am. Chem. Soc.*, **1990**, *112*, 1546. (e) G. B. Gardner, D. Venkataraman, J. S. Moore, S. Lee, *Nature*, **1995**, *374*, 792. (e) E. Lee, J. Kim, J. Heo, D. Whang, K. Kim, *Angew. Chem., Int. Ed.*, **2001**, *40*, 399.

42. (a) P. M. Forster, J. Eckert, J. S. Chang, S.-E. Park, G. Férey, A. K. Cheetham, *J. Am. Chem. Soc.*, 2003, 125, 1309. (b) N. L. Rosi, J. Eckert, M. Eddaoudi, D. T. Vodak, J. Kim, M. O'Keeffe, O. M. Yaghi, *Science*, **2003**, *300*, 1127. (c) G. Férey, M. Latroche, C. Serre, F. Millange, T. Loiseau, A. Percheron-Guégan, *Chem. Commun.*, **2003**, 2976. (d) M. D.

Ward, *Science*, **2003**, *300*, 1104. (e) J. L. C. Rowsell, O. M. Yaghi, *Angew. Chem., Int. Ed.*, **2005**, *44*, 4670. (f) X. Lin, J. Jia, P. Hubberstey, M. Schröder and N. R. Champness, *CrystEngComm*, **2007**, *9*, 438. (g) D. J. Collins, H.-C. Zhou, *J. Mater. Chem.*, **2007**, *17*, 3154. (h) R. E. Morris, P. S. Wheatley, *Angew. Chem., Int. Ed.*, **2008**, *47*, 4966. (i) S. Q. Ma, D. Sun, J. M. Simmons, C. D. Collier, D. Yuan, H.-C. Zhou, *J. Am. Chem. Soc.*, **2008**, *130*, 1012. (j) M. Dincă, J. R. Long, *Angew. Chem., Int. Ed.*, **2008**, *47*,6766.

43. (a) J.-R. Li, O. K. Farha, R. J. Kuppler, H.-C. Zhou, *Chem. Soc. Rev.*, **2009**, *38*, 1477. (b) F. Schüth, K. S. W. Sing, *Handbook of Porous Solids*, Wiley-VCH, Weinheim, **2002**. (c) M. J. Rosseinsky, *Microporous Mesoporous Mater.*, **2004**, *73*, 15. (d) R. Q. Snurr, J. T. Hupp, S. T. Nguyen, *AIChE J.*, **2004**, *50*, 1090. (e) O. M. Yaghi, G. Li, H. Li, *Nature*, **1995**, *378*, 703. (f) Q. M. Wang, D. Shen, M. Bulow, M. L. Lau, S. Deng, F. R. Fitch, N. O. Lemcoff, J. Semanscin, *Microporous Mesoporous Mater.*, **2002**, *55*, 217. (g) R. Custelcean, B. A. Moyer, *Eur. J. Inorg. Chem.*, **2007**, 1321.
44. (a) B. Zhao, X.-Y. Chen, P. Cheng, D.-Z. Liao, S.-P. Yan, Z.-H. Jiang, *J. Am. Chem. Soc.*, **2004**, *126*, 15394. (b) B. Chen, Y. Yang, F. Zapata, G. Lin, G. Qian, E. B. Lobkovsky, *Adv. Mater.*, **2007**, *19*, 1693. (c) B. Chen, L. Wang, F. Zapata, G. Qian, E. B. Lobkovsky, *J. Am. Chem. Soc.*, **2008**, *130*, 6718. (d) B. V. Harbuzaru, A. Corma, F. Rey, P. Atienzar, J. L. Jorda, H. Garcia, D. Ananias, L. D. Carlos, J. Rocha, *Angew. Chem., Int. Ed.*, **2008**, *47*, 1080.
45. (a) T. Uemura, N. Yanai, S. Kitagawa, *Chem. Soc. Rev.*, **2009**, *38*, 1228. (b) T. Uemura, R. Kitaura, Y. Ohta, M. Nagaoka, S. Kitagawa, *Angew. Chem., Int. Ed.*, **2006**, *45*, 4112. (c) C. J. Chuck, M. G. Davidson, M. D. Jones, G. Kociok-Köhn, M. D. Lunn, S. Wu, *Inorg. Chem.*, **2006**, *45*, 6595. (d) T. Uemura, D. Hiramatsu, Y. Kubota, M. Takata, S. Kitagawa, *Angew. Chem., Int. Ed.*, **2007**, *46*, 4987.
46. (a) P. Horcajada, C. Serre, M. Vallet-Regí, M. Sebban, F. Taulelle, G. Férey, *Angew. Chem., Int. Ed.*, **2006**, *45*, 5974. (b) M. Vallet-Regí, F. Balas, D. Arcos, *Angew. Chem., Int. Ed.*, **2007**, *46*, 7548. (c) P. Horcajada, C. Serre, G. Maurin, N. A. Ramsahye, F. Balas, M. Vallet-Regí, M. Sebban, F. Taulelle, G. Férey, *J. Am. Chem. Soc.*, **2008**, *130*, 6774.
47. *Chem. Soc. Rev.*, **2009**, *38*, 1201-1508.
48. M. Fujita, Y. J. Kwon, S. Washizu, K. Ogura, *J. Am. Chem. Soc.*, **1994**, *116*, 1151.
49. O. Ohmori, M. Fujita, *Chem. Commun.*, **2004**, 1586.
50. S. Hasegawa, S. Horike, R. Matsuda, S. Furukawa, K. Mochizuki, Y. Kinoshita, S. Kitagawa, *J. Am. Chem. Soc.*, **2007**, *129*, 2607.
51. C. D. Wu, A. Hu, L. Zhang, W. Lin, *J. Am. Chem. Soc.*, **2005**, *127*, 8940.

52. Y. Lu, M. Tonigold, B. Bredenkötter, D. Volkmer, J. Hitzbleck, G. Langstein, *Z. Anorg. Allg. Chem.*, **2008**, *634*, 2411.
53. M. Tonigold, Y. Lu, B. Bredenkötter, B. Rieger, S. Bahnmüller, J. Hitzbleck, G. Langstein, D. Volkmer, *Angew. Chem., Int. Ed.*, **2009**, *48*, 7546.
54. Y. K. Hwang, D.-Y. Hong, J.-S. Chang, S. H. Jhung, Y.-K. Seo, J. Kim, A. Vimont, M. Daturi, C. Serre, G. Férey, *Angew. Chem., Int. Ed.*, **2008**, *47*, 4144.
55. N. V. Maksimchuk, M. N. Timofeeva, M. S. Melgunov, A. N. Shmakov, Y. A. Chesalov, D. N. Dybtsev, V. P. Fedin, O. A. Kholdeeva, *J. Catal.*, **2008**, *257*, 315.
56. F. X. Llabrés i Xamena, O. Casanova, R. Galiasso Tailleur, H. Garcia, A. Corma, *J. Catal.*, **2008**, *255*, 220.
57. D. Jiang, T. Mallat, F. Krumeich, A. Baiker, *J. Catal.*, **2008**, *257*, 390.
58. M. J. Ingleson, J. P. Barrio, J. Bacsa, C. Dickinson, H. Park, M. J. Rosseinsky, *Chem. Commun.*, **2008**, 1287.
59. A. Pramanik, S. Abbina, G. Das, *Polyhedron*, **2007**, *26*, 5225.
60. B. Xiao, H. Hou, Y. Fan, *J. Organomet. Chem.*, **2007**, *692*, 2014.
61. L. Alaerts, E. Séguin, H. Poelman, F. Thibault-Starzyk, P. A. Jacobs, D. E. De Vos, *Chem.–Eur. J.*, **2006**, *12*, 7353.
62. S. De Rosa, G. Giordano, T. Granato, A. Katovic, A. Siciliano, F. Tripicchio, *J. Agric. Food Chem.*, **2005**, *53*, 8306.
63. K. Schlichte, T. Kratzke, S. Kaskel, *Microporous Mesoporous Mater.*, **2004**, *73*, 81.
64. F. Gándara, B. Gomez-Lor, E. Gutiérrez-Puebla, M. Iglesias, M. A. Monge, D. M. Proserpio, N. Snejko, *Chem. Mater.*, **2008**, *20*, 72.
65. B. Gomez-Lor, E. Gutierrez-Puebla, M. Iglesias, M. A. Monge, C. Ruiz-Valero, N. Snejko, *Inorg. Chem.*, **2002**, *41*, 2429.
66. M. H. Alkordi, Y. Liu, R. W. Larsen, J. F. Eubank, M. Eddaoudi, *J. Am. Chem. Soc.*, **2008**, *130*, 12639.
67. F. Gándara, A. García-Cortés, C. Cascales, B. Gomez-Lor, E. Gutiérrez-Puebla, M. Iglesias, A. Monge, N. Snejko, *Inorg. Chem.*, **2007**, *46*, 3475.
68. K. S. Suslick, P. Bhyrappa, J. H. Chou, M. E. Kosal, S. Nakagaki, D. W. Smithenry, S. R. Wilson, *Acc. Chem. Res.*, **2005**, *38*, 283.
69. S. Horike, M. Dincă, K. Tamaki, J. R. Long, *J. Am. Chem. Soc.*, **2008**, *130*, 5854.
70. R.-Q. Zou, H. Sakurai, Q. Xu, *Angew. Chem., Int. Ed.*, **2006**, *45*, 2542.
71. F. X. Llabrés i Xamena, A. Abad, A. Corma, H. Garcia, *J. Catal.*, **2007**, *250*, 294.
72. J. W. Han, C. L. Hill, *J. Am. Chem. Soc.*, **2007**, *129*, 15094.

73. S. H. Cho, B. Ma, S. T. Nguyen, J. T. Hupp, T. E. Albrecht-Schmitt, *Chem. Commun.*, **2006**, 2563.
74. A. M. Shultz, O. K. Farha, J. T. Hupp, S. T. Nguyen, *J. Am. Chem. Soc.*, **2009**, *131*, 4204.
75. J. S. Seo, D. Whang, H. Lee, S. I. Jun, J. Oh, Y. J. Jeon, K. Kim, *Nature*, **2000**, *404*, 982.
76. U. Ravon, M. E. Domine, C. Gaudillere, A. Desmartin-Chomel, D. Farrusseng, *New J. Chem.*, **2008**, *32*, 937.
77. M. J. Ingleson, J. P. Barrio, J.-B. Guilbaud, Y. Z. Khimyak, M. J. Rosseinsky, *Chem. Commun.*, **2008**, 2680.
78. (a) O. R. Evans, H. L. Ngo, W. Lin, *J. Am. Chem. Soc.*, **2001**, *123*, 10395. (b) A.G. Hu, H. L. Ngo, W. Lin, *J. Am. Chem. Soc.*, **2003**, *125*, 11490.
79. (a) U. Müller, L. Lobree, M. Hesse, O. M. Yaghi, M. Eddaoudi, *Patent*, WO 03/101975, **2003**. (b) S. Hermes, M.-K. Schröter, R. Schmid, L. Khodeir, M. Muhler, A. Tissler, R. W. Fischer, R. A. Fischer, *Angew. Chem.*, **2005**, *117*, 6394. (c) U. Müller, O. Metelkina, H. Junicke, T. Butz, O. M. Yaghi, *Patent*, US 2004/081611, **2004**.
80. (a) L. Ma, C. Abney, W. Lin, *Chem. Soc. Rev.*, **2009**, *38*, 1248. (b) L. X. Dai, *Angew. Chem., Int. Ed.*, **2004**, *43*, 5726. (c) C. Li, *Catal. Rev. Sci. Eng.*, **2004**, *46*, 419. (d) K. Ding, *Pure Appl. Chem.*, **2006**, *78*, 293. (e) M. Heitbaum, F. Glorius, I. Escher, *Angew. Chem., Int. Ed.*, **2006**, *45*, 4732. (f) B. Kesanli, W. Lin, *Coord. Chem. Rev.*, **2003**, *246*, 305. (g) W. Lin, *J. Solid State Chem.*, **2005**, *178*, 2486.
81. D. N. Dybtsev, A. L. Nuzhdin, H. Chun, K. P. Bryliakov, E. P. Talsi, V. P. Fedin, K. Kim, *Angew. Chem., Int. Ed.*, **2006**, *45*, 916.
82. K. Tanaka, S. Oda, M. Shiro, *Chem. Commun.*, **2008**, 820.
83. C. Wu, W. Lin, *Angew. Chem., Int. Ed.*, **2007**, *46*, 1075.
84. (a) A. Corma, *Chem. Rev.* **1997**, *97*, 2373. (b) A. K. Cheetham, G. Férey, T. Loiseau, *Angew. Chem. Int. Ed.*, **1999**, *38*, 3268.
85. (a) H. C. Foley, *J. Microporous Mater.*, **1995**, *4*, 407. (b) T. Kyotani, *Carbon*, **2000**, *38*, 269.
86. Pores are classified, depending on their width, as micropores (<2 nm), mesopores (2-50 nm), and macropores (>50 nm); see: IUPAC Manual of Symbols and Terminology, Appendix 2, Pt. 1, Colloid and Surface Chemistry. *Pure Appl. Chem.*, **1972**, *31*, 578.
87. (a) S. Brunauer, L. S. Deming, W. E. Deming, E. Teller, *J. Am. Chem. Soc.*, **1940**, *62*, 1723. (b) S. J. Gregg, K. S. W. Sing, *Adsorption, Surface Area, and Porosity*, Academic Press, London, 2nd edn., **1984**.
88. (a) O. M. Yaghi, M. O'Keeffe, M. Kanatzidis, *J. Solid State Chem.*, **2000**, *152*, 1. (b) O.

M. Yaghi, M. O'Keeffe, *J. Solid State Chem.*, **2005**, *178*, v. (c) L. J. Barbour, *Chem. Commun.*, **2006**, 1163.

89. G. B. Gardner, D. Venkataraman, J. S. Moore, S. Lee, *Nature*, **1995**, *374*, 792.
90. M. Kondo, T. Yoshitomi, K. Seki, H. Matsuzaka, S. Kitagawa, *Angew. Chem., Int. Ed.*, **1997**, *36*, 1725.
91. (a) H. K. Chae, D. Y. Siberio-Perez, J. Kim, Y.-B. Go, M. Eddaoudi, A. J. Matzger, M. O'Keeffe, O. M. Yaghi, *Nature*, **2004**, *427*, 523. (b) G. Férey, C. Mellot-Draznieks, C. Serre, F. Millange, J. Dutour, S. Surblé, I. Margiolaki, *Science*, **2005**, *309*, 2040.
92. A. W. Chester, P. Clement, S. Han, *Patent*, US 6136291, **2000**.
93. (a) M. Kondo, T. Okubo, A. Asami, S. Noro, T. Yoshimoti, S. Kitagawa, T. Ishii, H. Matsukawa, K. Seki, *Angew. Chem., Int. Ed.*, **1999**, *38*, 140. (b) M. Kondo, M. Shimamura, S.-I. Noro, S. Minakoshi, A. Asami, K. Seki, S. Kitagawa, *Chem. Mater.*, **2000**, *12*, 1288. (c) S. Noro, S. Kitagawa, M. Kondo, K. Seki, *Angew. Chem., Int. Ed.*, **2000**, *39*, 2082. (d) R. Kitaura, K. Seki, G. Akiyama, S. Kitagawa, *Angew. Chem., Int. Ed.*, **2003**, *42*, 428. (e) K. Seki, *Chem. Commun.*, **2001**, 1496. (f) K. Seki, S. Takamizawa, W. Mori, *Chem. Lett.*, **2001**, 332. (g) K. Seki, S. Takamizawa, W. Mori, *Chem. Lett.*, **2001**, 122. (h) K. Seki, W. Mori, *J. Phys. Chem. B*, **2002**, *106*, 1380. (i) K. Seki, *Phys. Chem. Chem. Phys.*, **2002**, *4*, 1968. (j) S. Takamizawa, W. Mori, M. Furihata, S. Takeda, K. Yamaguchi, *Inorg. Chim. Acta*, **1998**, *283*, 268. (k) S. Takamizawa, E. Nakata, T. Sato, T. Akatsuka, *Inorg. Chem.*, **2005**, *44*, 1362. (l) M. Eddaoudi, J. Kim, N. Rosi, D. Vodak, J. Wachter, M. O'Keeffe, O. M. Yaghi, *Science*, **2002**, *295*, 469. (m) T. Düren, L. Sarkisov, O. M. Yaghi, R. Q. Snurr, *Langmuir*, **2004**, *20*, 2683. (n) X. Lin, A. J. Blake, C. Wilson, X. Z. Sun, N. R. Champness, M. W. George, P. Hubberstey, R. Mokaya, M. Schröder, *J. Am. Chem. Soc.*, **2006**, *128*, 10745. (o) D.-N. Dybtsev, H. Chun, S. Y. Yoon, D. Kim, K. Kim, *J. Am. Chem. Soc.*, **2004**, *126*, 32. (p) R. Kitaura, R. Matsuda, Y. Kubota, S. Kitagawa, M. Takata, T. C. Kobayashi, M. Suzuki, *J. Phys. Chem. B*, **2005**, *109*, 23378. (q) S. Bourrelly, P. L. Llewellyn, C. Serre, F. Millange, T. Loiseau, G. Férey, *J. Am. Chem. Soc.*, **2005**, *127*, 13519. (r) T. Loiseau, L. Lecroq, C. Volkringer, J. Marrot, G. Férey, M. Haouas, F. Taulelle, S. Bourrelly, P. L. Llewellyn, M. Latroche, *J. Am. Chem. Soc.*, **2006**, *128*, 10223. (s) H. R. Moon, N. Kobayashi, M. P. Suh, *Inorg. Chem.*, **2006**, *45*, 8672. (t) A. C. Sudik, A. R. Millward, N. W. Ockwig, A. P. Côté, J. Kim, O. M. Yaghi, *J. Am. Chem. Soc.*, **2005**, *127*, 7110. (u) D. N. Dybtsev, H. Chun, K. Kim, *Angew. Chem., Int. Ed.*, **2004**, *43*, 5033.
94. (a) T. M. Reineke, M. Eddaoudi, M. O'Keeffe, O. M. Yaghi, *Angew. Chem., Int. Ed.*,

1999, *38*, 2590. (b) M. Eddaoudi, H. Li, O. M. Yaghi, *J. Am. Chem. Soc.*, **2000**, *122*, 1391. (c) A. R. Millward, O. M. Yaghi, *J. Am. Chem. Soc.*, **2005**, *127*, 17998. (d) A. J. Fletcher, E. J. Cussen, T. J. Prior, C. K. Kepert, M. J. Rosseinsky, K. M. Thomas, *J. Am. Chem. Soc.*, **2001**, *123*, 10001. (e) A. J. Fletcher, E. J. Cussen, D. Bradshaw, M. J. Rosseinsky, K. M. Thomas, *J. Am. Chem. Soc.*, **2004**, *126*, 9750. (f) D. Li, K. Kaneko, *J. Phys. Chem. B*, **2000**, *104*, 8940. (g) D. Li, K. Kaneko, *Chem. Phys. Lett.*, **2001**, *335*, 50. (h) S. Takamizawa, E. Nakata, H. Yokoyama, K. Mochizuki, Mori, W. *Angew. Chem., Int. Ed.*, **2003**, *42*, 4331. (i) L. Pan, K. M. Adams, H. E. Hernandez, X. Wang, C. Zheng, Y. Hattori, K. Kaneko, *J. Am. Chem. Soc.*, **2003**, *125*, 3062. (j) C. D. Wu, W. Lin, *Angew. Chem., Int. Ed.*, **2005**, *44*, 1958. (k) J. Chen, M. Ohba, D. Zhao, W. Kaneko, S. Kitagawa, *Cryst. Growth Des.*, **2006**, *6*, 664. (l) J. A. R. Navarro, E. Barea, J. M. Salas, N. Masciocchi, S. Galli, A. Sironi, C. O. Ania, J. B. Parra, *Inorg. Chem.*, **2006**, *45*, 2397. (m) X. Guo, G. Zhu, Z. Li, F. Sun, Z. Yang, S. Qiu, *Chem. Commun.*, **2006**, 3172. (n) C. D. Wu, W. Lin, *Dalton Trans.*, **2006**, 4563. (o) R. Matsuda, R. Kitaura, S. Kitagawa, Y. Kubota, R. V. Belosludov, T. C. Kobayashi, H. Sakamoto, T. Chiba, M. Takata, Y. Kawazoe, Y. Mita, *Nature*, **2005**, *436*, 238. (p) S. Ma, H.-C. Zhou, *J. Am. Chem. Soc.*, **2006**, *128*, 11734.

95. (a) L. J. Murray, M. Dincă, J. R. Long, *Chem. Soc. Rev.*, **2009**, *38*, 1294. (b) L. Pan, M. B. Sander, X. Huang, J. Li, M. R. Smith Jr., E. W. Bittner, B. C. Bockrath, J. K. Johnson, *J. Am. Chem. Soc.*, **2004**, *126*, 1308. (c) J. C. Rowsell, A. R. Millward, K. S. Park, O. M. Yaghi, *J. Am. Chem. Soc.*, **2004**, *126*, 5666. (d) E. Y. Lee, M. P. Suh, *Angew. Chem., Int. Ed.*, **2004**, *43*, 2798. (e) H. T. Xu, Y. D. Li, *J. Mol. Struct.*, **2004**, *693*, 11. (f) X. Zhao, B. Xiao, A. J. Fletcher, K. M. Thomas, D. Bradshaw, M. J. Rosseinsky, *Science*, **2004**, *306*, 1012. (g) B. Kesanli, Y. Cui, M. R. Smith, E. W. Bittner, B. C. Bockrath, W. Lin, *Angew. Chem., Int. Ed.*, **2005**, *44*, 72. (h) B. Panella, M. Hirscher, *Adv. Mater.*, **2005**, *17*, 538. (i) T. Sato, W. Mori, C. N. Kato, E. Yanaoka, T. Kuribayashi, R. Ohtera, Y. Shiraishi, *J. Catal.*, **2005**, *232*, 186. (j) Y. Kubota, M. Takata, R. Matsuda, R. Kitaura, S. Kitagawa, K. Kato, M. Sakata, T. Kobayashi, *Angew. Chem., Int. Ed.*, **2005**, *44*, 920. (k) H. Chun, D. N. Dybtsev, H. Kim, K. Kim, *Chem.–Eur. J.*, **2005**, *11*, 3521. (l) M. Dincă, J. R. Long, *J. Am. Chem. Soc.*, **2005**, *127*, 9376. (m) S. Takamizawa, E.-I. Nakata, *CrystEngComm*, **2005**, *7*, 476. (n) B. Chen, N. W. Ockwig, A. R. Millward, D. S. Contreras, O. M. Yaghi, *Angew. Chem., Int. Ed.*, **2005**, *44*, 4745. (o) J. Y. Lee, J. Li, J. Jagiello, *J. Solid State Chem.*, **2005**, *178*, 2527. (p) S. H. Jhung, J. H. Lee, J. S. Chang, *Bull. Korean Chem. Soc.*, **2005**, *26*, 880. (q) S. H. Jhung, J. W. Yoon, H. K. Kim, J. S.

Chang, *Bull. Korean Chem. Soc.*, **2005**, *26*, 1075. (r) T. Yildirim, M. R. Hartman, *Phys. Rev. Lett.*, **2005**, *95*, 215504. (s) J. Y. Lee, L. Pan, S. P. Kelly, J. Jagiello, T. J. Emge, J. Li, *Adv. Mater.*, **2005**, *17*, 2703. (t) J. Perles, M. Iglesias, M.-A. M. Luengo, M. A. Monge, C. R. Valero, N. Snejko, *Chem. Mater.*, **2005**, *17*, 5837. (u) D. Sun, Y. Ke, T. M. Mattox, B. A. Ooro, H.-C. Zhou, *Chem. Commun.*, **2005**, 5447. (v) A. Dailly, J. J. Vajo, C. C. Ahn, *J. Phys. Chem. B*, **2006**, *110*, 1099. (w) J. L. C. Rowsell, O. M. Yaghi, *J. Am. Chem. Soc.*, **2006**, *128*, 1304. (x) C. Prestipino, L. Regli, J. G. Vitillo, F. Bonino, A. Damin, C. Lamberti, A. Zecchina, P. L. Solari, K. O. Kongshaug, S. Bordiga, *Chem. Mater.*, **2006**, *18*, 1337. (y) K. O. Kongshaug, H. Fjellvåg, *Inorg. Chem.*, **2006**, *45*, 2424. (z) P. D. C. Dietzel, B. Panella, M. Hirscher, R. Blom, H. Fjellvåg, *Chem. Commun.*, **2006**, 959.

96. (a) A. G. Wong-Foy, A. J. Matzger, O. M. Yaghi, *J. Am. Chem. Soc.*, **2006**, *128*, 3494. (b) D. Sun, S. Ma, Y. Ke, D. J. Collins, H.-C. Zhou, *J. Am. Chem. Soc.*, **2006**, *128*, 3896. (c) B. Panella, M. Hirscher, H. Pütter, U. Müller, *Adv. Funct. Mater.*, **2006**, *16*, 520. (d) S. V. Kolotilov, A. V. Shvets, V. N. Solomakha, *Theoretical and Experimental Chemistry*, **2006**, *42*, 43. (e) Q. R. Fang, G. S. Zhu, M. Xue, Q. L. Zhang, J. Y. Sun, X. D. Guo, S. L. Qiu, S. T. Xu, P. Wang, D. J. Wang, Y. Wei, *Chem.–Eur. J.*, **2006**, *12*, 3754. (f) M. Kramer, U. Schwarz, S. Kaskel, *J. Mater. Chem.*, **2006**, *16*, 2245. (g) P. Krawiec, M. Kramer, M. Sabo, R. Kunschke, H. Fröde, S. Kaskel, *Adv. Eng. Mater.*, **2006**, *8*, 293. (h) M. Dincă, A. F. Yu, J. R. Long, *J. Am. Chem. Soc.*, **2006**, *128*, 8904. (i) B. Chen, S. Ma, F. Zapata, E. B. Lobkovsky, J. Yang, *Inorg. Chem.*, **2006**, *45*, 5718. (j) E. Poirier, R. Chahine, P. Bénard, L. Lafi, G. Dorval-Douville, P. A. Chandonia, *Langmuir*, **2006**, *22*, 8784. (k) Y. Li, R. T. Yang, *J. Am. Chem. Soc.*, **2006**, *128*, 726. (l) Y. W. Li, R. T. Yang, *J. Am. Chem. Soc.*, **2006**, *128*, 8136. (m) U. Müller, M. Schubert, F. Teich, H. Pütter, K. Schierle-Arndt, J. Pastré, *J. Mater. Chem.*, **2006**, *16*, 626. (n) X. Lin, J. Jia, X. Zhao, K. M. Thomas, A. J. Blake, G. S. Walker, N. R. Champness, P. Hubberstey, M. Schröder, *Angew. Chem., Int. Ed.*, **2006**, *45*, 7358. (o) J. Jia, X. Lin, A. J. Blake, N. R. Champness, P. Hubberstey, L. Shao, G. Walker, C. Wilson, M. Schröder, *Inorg. Chem.*, **2006**, *45*, 8838. (p) J.A. Rood, B. C. Noll, K. W. Henderson, *Inorg. Chem.*, **2006**, *45*, 5521.
97. (a) P. M. Grant, *Nature*, **2003**, *424*, 129. (b) R. Coontz, B. Hanson, *Science*, **2004**, *305*, 957, and other articles in this issue.
98. J.-R. Li, R. J. Kuppler, H.-C. Zhou, *Chem. Soc. Rev.*, **2009**, *38*, 1477.
99. (a) D. Bradshaw, J. B. Claridge, E. J. Cussen, T. J. Prior, M. J. Rosseinsky, *Acc. Chem. Res.*, **2005**, *38*, 273. (b) S. Kitagawa, M. Kondo, *Bull. Chem. Soc. Jpn.*, **1998**, *71*, 1739.

(c) S. Kitagawa, K. Uemura, *Chem. Soc. Rev.*, **2005**, *34*, 109. (d) A. J. Fletcher, K. M. Thomas, M. J. Rosseinsky, *J. Solid State Chem.*, **2005**, *178*, 2491.

100. D. G. Samsonenko, H. Kim, Y. Sun, G.-H. Kim, H.-S. Lee, K. Kim, *Chem.–Asian J.*, **2007**, *2*, 484.
101. L. Pan, D. H. Olson, L. R. Ciemnolonski, R. Heddy, J. Li, *Angew. Chem., Int. Ed.*, **2006**, *45*, 616.
102. S. Surblé, F. Millange, C. Serre, T. Düren, M. Latroche, S. Bourrelly, P. L. Llewellyn, G. Férey, *J. Am. Chem. Soc.*, **2006**, *128*, 14889.
103. L. Pan, B. Parker, X. Y. Huang, D. H. Olson, J. Lee, J. Li, *J. Am. Chem. Soc.*, **2006**, *128*, 4180.
104. S. Q. Ma, X. S.Wang, C. D. Collier, E. S. Manis, H.-C. Zhou, *Inorg. Chem.*, **2007**, *46*, 8499.
105. Y. Zou, S. Hong, M. Park, H. Chun, M. S. Lah, *Chem. Commun.*, **2007**, 5182.
106. C.-J. Li, Z.-J. Lin, M.-X. Peng, J.-D. Leng, M.-M. Yang, M.-L. Tong, *Chem. Commun.*, 2008, 6348.
107. J. Y. Lee, D. H. Olson, L. Pan, T. J. Emge, J. Li, *Adv. Funct. Mater.*, **2007**, 17, 1255.
108. Y. Li, R. T. Yang, *Langmuir*, **2007**, *23*, 12937.
109. S. M. Humphrey, J.-S. Chang, S. H. Jhung, J. W. Yoon, P. T. Wood, *Angew. Chem., Int. Ed.*, **2007**, *46*, 272.
110. J. W. Yoon, S. H. Jhung, Y. K. Hwang, S. M. Humphrey, P. T. Wood, J.-S. Chang, *Adv. Mater.*, **2007**, *19*, 1830.
111. J.-R. Li, Y. Tao, Q. Yu, X.-H. Bu, H. Sakamoto, S. Kitagawa, *Chem.–Eur. J.*, **2008**, *14*, 2771.
112. J. A. R. Navarro, E. Barea, A. Rodríguez-Diéguez, J. M. Salas, C. O. Ania, J. B. Parra, N. Masciocchi, S. Galli, A. Sironi, *J. Am. Chem. Soc.*, **2008**, *130*, 3978.
113. R. Banerjee, A. Phan, B. Wang, C. Knobler, H. Furukawa, M. O'Keeffe, O. M. Yaghi, *Science*, **2008**, *319*, 939.
114. B. Wang, A. P. Côté, H. Furukawa, M. O'Keeffe, O. M. Yaghi, *Nature*, **2008**, 453, 207.
115. B. L. Chen, Y. Y. Ji, M. Xue, F. R. Fronczek, E. J. Hurtado, J. U. Mondal, C. D. Liang, S. Dai, *Inorg. Chem.*, **2008**, *47*, 5543.
116. M. Xue, S. Q. Ma, Z. Jin, R. M. Schaffino, G. S. Zhu, E. B. Lobkovsky, S. L. Qiu, B. L. Chen, *Inorg. Chem.*, **2008**, *47*, 6825.
117. S. Q. Ma, X. S. Wang, D. Q. Yuan, H.-C. Zhou, *Angew. Chem., Int. Ed.*, **2008**, *47*, 4130.

118. Y.-S. Bae, O. K. Farha, A. M. Spokoyny, C. A. Mirkin, J. T. Hupp, R. Q. Snurr, *Chem. Commun.*, **2008**, 4135.
119. K. Li, D. H. Olson, J. Y. Lee, W. Bi, K. Wu, T. Yuen, Q. Xu, J. Li, *Adv. Funct. Mater.*, **2008**, *18*, 2205.
120. Y.-S. Bae, K. L. Mulfort, H. Frost, P. Ryan, S. Punnathanam, L. J. Broadbelt, J. T. Hupp, R. Q. Snurr, *Langmuir*, **2008**, *24*, 8592.
121. R. Kitaura, K. Fujimoto, S. Noro, M. Kondo, S. Kitagawa, *Angew. Chem., Int. Ed.*, **2002**, *41*, 133.
122. T. K. Maji, K. Uemura, H. C. Chang, R. Matsuda, S. Kitagawa, *Angew. Chem., Int. Ed.*, **2004**, *43*, 3269.
123. T. K. Maji, G. Mostafa, R. Matsuda, S. Kitagawa, *J. Am. Chem. Soc.*, **2005**, *127*, 17152.
124. P. L. Llewellyn, S. Bourrelly, C. Serre, Y. Filinchuk, G. Férey, *Angew. Chem., Int. Ed.*, **2006**, *45*, 7751.
125. B. L. Chen, S. Q. Ma, E. J. Hurtado, E. B. Lobkovsky, H.-C. Zhou, *Inorg. Chem.*, **2007**, *46*, 8490.
126. S. Q. Ma, X. S. Wang, E. S. Manis, C. D. Collier, H.-C. Zhou, *Inorg. Chem.*, **2007**, *46*, 3432.
127. H. Hayashi, A. P. Côté, H. Furukawa, M. O'Keeffe, O. M. Yaghi, *Nat. Mater.*, **2007**, 6, 501.
128. T. K. Maji, R. Matsuda, S. Kitagawa, *Nat. Mater.*, **2007**, *6*, 142.
129. S. K. Ghosh, J. P. Zhang, S. Kitagawa, *Angew. Chem., Int. Ed.*, **2007**, *46*, 7965.
130. B. L. Chen, S. Q. Ma, E. J. Hurtado, E. B. Lobkovsky, C. D. Liang, H. G. Zhu, S. Dai, *Inorg. Chem.*, **2007**, *46*, 8705.
131. B. L. Chen, S. Q. Ma, F. Zapata, F. R. Fronczek, E. B. Lobkovsky, H.-C. Zhou, *Inorg. Chem.*, **2007**, *46*, 1233.
132. D. Tanaka, K. Nakagawa, M. Higuchi, S. Horike, Y. Kubota, L. C. Kobayashi, M. Takata, S. Kitagawa, *Angew. Chem., Int. Ed.*, **2008**, *47*, 3914.
133. Y. E. Cheon, M. P. Suh, *Chem.–Eur. J.*, **2008**, *14*, 3961.
134. J. P. Zhang, X. M. Chen, *J. Am. Chem. Soc.*, **2008**, *130*, 6010.
135. S. K. Ghosh, S. Bureekaew, S. Kitagawa, *Angew. Chem., Int. Ed.*, **2008**, *47*, 3403.
136. P. K. Thallapally, J. Tian, M. R. Kishan, C. A. Fernandez, S. J. Dalgarno, P. B. McGrail, J. E. Warren, J. L. Atwood, *J. Am. Chem. Soc.*, **2008**, *130*, 16842.
137. S. Uchida, R. Kawamoto, H. Tagami, Y. Nakagawa, N. Mizuno, *J. Am. Chem. Soc.*, **2008**, *130*, 12370.

138. S. Q. Ma, D. Sun, X. S. Wang, H.-C. Zhou, *Angew. Chem., Int. Ed.*, **2007**, *46*, 2458.
139. V. Krungleviciute, K. Lask, A. D. Migone, J. Y. Lee, J. Li, *AIChE J.*, **2008**, *54*, 918.
140. M. Hartmann, S. Kunz, D. Himsl, O. Tangermann, *Langmuir*, **2008**, *24*, 8634.
141. L. Alaerts, C. E. A. Kirshhock, M. Maes, M. A. van der Veen, V. Finsy, A. Depla, J. A. Martens, G. V. Baron, P. A. Jacobs, J. F. M. Denayer, D. E. De Vos, *Angew. Chem., Int. Ed.*, **2007**, *46*, 4293.
142. L. Alaerts, M. Maes, L. Giebeler, P. A. Jacobs, J. A. Martens, J. F. M. Denayer, C. E. A. Kirschhock, D. E. De Vos, *J. Am. Chem. Soc.*, **2008**, *130*, 14170.
143. V. Finsy, H. Verelst, L. Alaerts, D. E. De Vos, P. A. Jacobs, G. V. Baron, J. F. M. Denayer, *J. Am. Chem. Soc.*, **2008**, *130*, 7110.
144. P. S. Bárcia, F. Zapata, J. A. C. Silva, A. E. Rodrigues, B. Chen, *J. Phys. Chem. B*, **2007**, *111*, 6101.
145. S. Kulprathipanja, R. W. Neuzil, *US Patent*, 4 445 444, **1984**, UOP.
146. L. Bastin, P. S. Barcia, E. J. Hurtado, J. A. C. Silva, A. E. Rodrigues, B. Chen, *J. Phys. Chem. C*, **2008**, *112*, 1575.
147. J. J. M. Beenakker, V. D. Borman, S. Y. Krylov, *Chem. Phys. Lett.*, **1995**, *232*, 379.
148. B. Chen, X. Zhao, A. Putkham, K. Hong, E. B. Lobkovsky, E. J. Hurtado, A. J. Fletcher, K. M. Thomas, *J. Am. Chem. Soc.*, **2008**, *130*, 6411.
149. D. Noguchi, H. Tanaka, A. Kondo, H. Kajiro, H. Noguchi, T. Ohba, H. Kanoh, K. Kaneko, *J. Am. Chem. Soc.*, **2008**, *130*, 6367.
150. H. Guo, G. Zhu, I. J. Hewitt, S. Qiu, *J. Am. Chem. Soc.*, **2009**, *131*, 1646.
151. J. Won, J. S. Seo, J. H. Kim, H. S. Kim, Y. S. Kang, S.-J. Kim, Y. Kim, J. Jegal, *Adv. Mater.*, **2005**, *17*, 80.
152. A. Car, C. Stropnik, K.-V. Peinemann, *Desalination*, **2006**, *200*, 424.
153. E. V. Perez, K. J. Balkus, Jr, J. P. Ferraris, I. H. Musselman, *J. Membr. Sci.*, **2009**, *328*, 165.
154. (a) B. J. Hathaway, *Comprehensive Coordination Chemistry*, vol. 2 (ed.: G. Wilkinson), Pergamon, Oxford, **1987**. (b) R. D. Cannon, R. P. White, *Prog. Inorg. Chem.*, **1988**, *36*, 195.
155. (a) C. Serre, F. Millange, S. Surblé, G. Férey, *Angew. Chem., Int. Ed.*, **2004**, *43*, 6286. (b) G. Férey, C. Serre, C. Mellot-Draznieks, F. Millange, S. Surblé, J. Dutour, I. Margiolaki, *Angew. Chem., Int. Ed.*, **2004**, *43*, 6296. (c) C. Mellot-Draznieks, C. Serre, S. Surblé, N. Audebrand, G. Férey, *J. Am. Chem. Soc.*, **2005**, *127*, 16273. (d) G. Férey, C. Mellot-Draznieks, C. Serre, F. Millange, J. Dutour, S. Surblé, I. Margiolaki, *Science*,

2005, *309*, 2040. (e) S. Surblé, C. Serre, C. Mellot-Draznieks, F. Millange, G. Férey, *Chem. Commun.*, **2006**, 284. (f) S. Surblé, F. Millange, C. Serre, T. Düren, M. Latroche, S. Bourrelly, P. L. Llewellyn, G. Férey, *J. Am. Chem. Soc.*, **2006**, *128*, 14889. (g) P. Horcajada, S. Surblé, C. Serre, D.-Y. Hong, Y.-K. Seo, J.-S. Chang, J.-M. Grenèche, I. Margiolaki, G. Férey, *Chem. Commun.*, **2007**, 2820.

156. (a) H. Kyoama, Y. Saito, *Bull. Chem. Soc. Jpn.*, **1954**, *27*, 112. (b) R. M. Gordon, H. B. Silver, *Can. J. Chem.*, **1983**, *61*, 1218. (c) W. Clegg, D. R. Harbron, C. D. Homan, P. A. Hunt, I. R. Little, B. P. Straughan, *Inorg. Chim. Acta.*, **1991**, *186*, 51. (d) D. B. D. Amico, F. Cadderazzo, L. Labella, F. Marchetti, G. Pampaloni, *Inorg. Chem. Commun.*, **2002**, *5*, 733. (e) C. S. McCowan, T. L. Groy, M. T. Caudle, *Inorg. Chem.*, **2002**, *41*, 1120. (f) H. Hou, L. Li, G. Li, Y. Fan, Y. Zhu, *Inorg. Chem.*, **2003**, *42*, 3501. (g) A. Karmakar, J. B. Baruah, *Polyhedron*, **2008**, *27*, 3409.
157. (a) L. Pauling, J. Sherman, *Proc. Nat. Acad. Sci., Wash.*, **1934**, *20*, 340. (b) A. Tulinsky, C. R. Worthington, E. Pignataro, *Acta Cryst.*, **1959**, *12*, 623. (c) A. Tulinsky, C. R. Worthington, *Acta Cryst.*, **1959**, *12*, 626. (d) A. Tulinsky, *Acta Cryst.*, **1959**, *12*, 634.
158. M. K. Ehlert, S. J. Rettig, A. Storr, R. C. Thompson, J. Trotter, *Acta Cryst.*, **1994**, *C50*, 1023.
159. *Acid Catalysis in Modern Organic Syntheses*, vol. 1 (eds.: H. Yamamoto, K. Ishihara), Wiley-VCH, Weinheim, **2008**, pp. 151-174.
160. H. B. Linden, *Eur. J. Mass Spectrom.*, **2004**, *10*, 459.
161. J. Rubim, I. G. R. Gutz, O. Sala, W. J. Orville-Thomas, *J. Mol. Struct.*, **1983**, *100*, 571.
162. K. Nakamoto, Infrared and Raman Spectra of Inorganic and Coordination Compounds, Wiley Interscience, New York, 2nd edn., **1970**, pp. 249.
163. Y. C. Chien, H. P. Wang, K. S. Lin, Y.-J. Huang, Y.-W. Yang, *Chemosphere*, **2000**, *40*, 383.
164. A. Gilbert, J. Baggott, *Essentials of Molecular Photochemistry*, CRC Press, Boca Raton, Florida, **1991**, pp. 87–89.
165. (a) A. B. P. Lever, *Inorganic Electronic Spectroscopy*, Elsevier Publishing Company, Amsterdam, **1968**, ch. 9, pp. 317–349. (b) The *Dq* and *B* values were estimated by using the transition energy ratio diagrams on pp. 393–400 of the same book as in ref. 165a.
166. (a) R.-F. Hu, J. Zhang, Y. Kang, Y.-G. Yao, *Inorg. Chem. Commun.*, **2005**, *8*, 828. (b) J. Lu, K. Zhao, Q.-R. Fang, J.-Q. Xu, J.-H. Yu, X. Zhang, H.-Y. Bie, T.-G. Wang, *Cryst. Growth Des.*, **2005**, *5*, 1091.
167. A. L. Spek, *J. Appl. Cryst.*, **2003**, *36*, 7.

168. H. Schilder, H. Lueken, *J. Magn. Magn. Mater.*, **2004**, *281*, 17.

169. C. Görller-Walrand, K. Binnemans, Handbook on the Physics and Chemistry of Rare Earths, (Eds.: K. A. Gschneidner Jr., L. Eyring), Elsevier, Amsterdam, **1996**, vol. 23, ch. 155, pp. 121.

170. F. E. Mabbs, D. J. Machin, *Magnetism and Transition Metal Complexes*, Chapman and Hall, London, **1973**.

171. H. Lueken, *Magnetochemie*, Teubner, Stuttgart, **1999**.

172. (a) F. Harary, *Chemical Applications of Graph Theory* (ed.: A. T. Balaban), Academic Press, London, **1976**, ch. 2. (b) A. T. Balaban, *ibid.*, ch. 3. (c) C. Mislow, *Bull. Soc. Chim. Belg.*, **1977**, *86*, 595. (d) D. M. Walba, *Tetrahedron*, **1985**, *41*, 3161. (e) J. Simon, *Graph Theory and Topology in Chemistry* (eds.: R. B. King, D. H. Rouvray), Elsevier, Amsterdam, **1987**, pp. 43. (f) C. O. Dietrich-Buchecker, J.-P. Sauvage, *Bioinorganic Chemistry Frontiers*, vol. 2 (ed.: H. Dugas), Springer-Verlag, Berlin, **1991**, pp. 195-248. (g) C. Liang, K. Mislow, *J. Math. Chem.*, **1994**, *15*, 245. (h) D. K. Mitchell, J.-C. Chambron, *J. Chem. Educ.*, **1995**, *72*, 1059. (i) H. Dodziuk, *Modern Conformational Analysis*, Series: Methods in Stereochemical Analysis (ed.: A. P. Marchand), Wiley-VCH, Weinheim, **1995**.

173. C. Kuratowski, *Fund. Math.*, **1930**, *15*, 271.

174. (a) H. E. Simmons III, PhD Thesis, Harvard University, **1980**. (b) J. E. Maggio, *Tetrahedron Lett.*, **1981**, *22*, 287. (c) J. K. Kouba, *J. Am. Chem. Soc.*, **1981**, *103*, 1579. (d) S. A. Benner, J. E. Maggio, H. E. Simmons III, *J. Am. Chem. Soc.*, **1981**, *103*, 1581. (e) L. A. Paquette, M. Vazeux, *Tetrahedron Lett.*, **1981**, *22*, 291.

175. (a) D. Kuck, A. Schuster, *Angew. Chem., Int. Ed.*, **1988**, *27*, 1192. (b) D. Kuck, B. Paisdor, D. Gestmann, *Angew. Chem., Int. Ed.*, **1994**, *33*, 1251. (c) D. Kuck, A. Schuster, D. Gestmann, *J. Chem. Soc., Chem. Commun.*, **1994**, 609. (d) D. Kuck, A. Schuster, *J. Chem. Soc., Perkin Trans 1*, **1995**, 721. (e) D. Kuck, *Synlett*, **1996**, 949. (f) D. Gestmann, H. Pritzkow, D. Kuck, *Liebigs Ann.*, **1996**, 1349. (g) D. Kuck, *Liebigs Ann./Recueil*, **1997**, 1043. (h) D. Kuck, R. A. Krause, D. Gestmann, F. Posteher, A. Schuster, *Tetrahedron*, **1998**, *54*, 5247. (i) D. Kuck, *The Centropolyindanes and Related Centro-Fused Polycyclic Organic Compounds.* In *Carbon Rich Compounds I, Topics in Current Chemistry* (ed.: A. de Meijere), Springer, Heidelberg, **1998**, vol. 196, pp. 168-208. (j) D. Kuck, *Benzoannelated Fenestranes*. In *Advances in Theoretically Interesting Molecules* (ed.: R. P. Thummel,), JAI Press, Greenwich, London, **1998**. (k) M. Harig, D. Kuck, *Eur. J. Org. Chem.*, **2006**, 1647. (l) D. Kuck, *Molecules with Nonstandard*

Topological Properties: Centrohexaindane, Kuratowski's Cyclophane and Other Graph-theoretically Nonplanar Molecules. In *Strained Hydrocarbons. Beyond the Van't Hoff and LeBel Hypothesis* (ed.: H. Dodziuk), Wiley-VCH, Weinheim, **2009**, ch. 9, pp. 425-447.

176. (a) M. Hisatome, N. Watanabe, T. Sakamoto, K. Yamakawa, *J. Organomet. Chem.*, **1977**, *125*, 79. (b) M. Hisatome, Y. Kawaziri, K. Yamakawa, *Tetrahedron Lett.*, **1979**, 1777. (c) M. Hisatome, Y. Kawaziri, K. Yamakawa, *Tetrahedron Lett.*, **1982**, 1713.
177. (a) A. J. Burn, G. W. Smith, *J. Chem. Soc., Chem. Commun.*, **1965**, 394. (b) C. D. Scattergood, P. G. Bonney, J. M. Slater, C. D. Garner, W. Clegg, *J. Chem. Soc., Chem. Commun.*, **1987**, 1749. (c) A. Müller, E. Krickemeyer, A. Hildebrand, H. Bögge, K. Schneider, M. Lemke, *Chem. Soc., Chem. Commun.*, **1991**, 1685. (d) S. Bernès, F. Sécheresse, Y. Jeannin, *Inorg. Chim. Acta*, **1992**, *191*, 11. (e) Y. Jeannin, F. Sécheresse, S. Bernès, F. Robert, *Inorg. Chim. Acta*, **1992**, *198-200*, 493.
178. (a) C. D. Scattergood, P. G. Bonney, J. M. Slater, C. D. Garner, W. Clegg, *J. Chem. Soc., Chem. Commun.*, **1987**, 1749. (b) A. Müller, E. Krickemeyer, A. Hildebrand, H. Bögge, K. Schneider, M. Lemke, *J. Chem. Soc., Chem. Commun.*, **1991**, 1685. (c) S. Bernès, F. Sécheresse, Y. Jeannin, *Inorg. Chim. Acta*, **1992**, *191*, 11. (d) Y. Jeannin, F. Sécheresse, S. Bernès, F. Robert, *Inorg. Chim. Acta*, **1992**, *198-200*, 493.
179. C.-T. Chen, P. Gantzel, J. S. Siegel, K. K. Baldrigde, R. B. English, D. M. Ho, *Angew. Chem., Int. Ed.*, **1988**, *34*, 2657.
180. D. M. Walba, R. M. Richards, R. C. Haltiwanger, *J. Am. Chem. Soc.*, **1982**, *104*, 3219.
181. T. Otsubo, F. Ogura, S. Misumi, *Tetrahedron Lett.*, **1983**, *24*, 4851.
182. (a) I. I. Creaser, J. M. Harrowfield, A. J. Herlt, A. M. Sargeson, J. Springborg, R. J. Geue, M. R. Snow, *J. Am. Chem. Soc.*, **1977**, *99*, 3181. (b) I. I. Creaser, R. J. Geue, G. M. Harrowfield, A. J. Herlt, A. M. Sargeson, M. R. Snow, J. Springborg, *J. Am. Chem. Soc.*, **1982**, *104*, 6016.
183. J. E. P. Dahl, J. M. Moldowan, T. M. Peakman, J. C. Clardy, E. Lobkovsky, M. M. Olmstead, P. W. May, T. J. Davis, J. W. Steeds, K. E. Peters, A. Pepper, A. Ekuan, R. M. K. Carlson, *Angew. Chem., Int. Ed.*, **2003**, *42*, 2040.
184. (a) E. H. Braye, L. F. Dahl, W. Hübel, D. L. Wampler, *J. Am. Chem. Soc.*, **1962**, *84*, 4633. (b) P. F. Jackson, B. F. G. Johnson, J. Lewis, J. N. Nicholls, *J. Chem. Soc., Chem. Commun.*, **1980**, 564. (c) J. Lewis, B. F. G. Johnson, *Pure Appl. Chem.*, **1982**, *54*, 97.
185. (a) M. Momenteau, J. Mispelter, B. Loock, E. Bisagni, *J. Chem. Soc., Perkin Trans 1*, **1983**, 189. (b) Y. Okuno, K. Uoto, Y. Sasaki, O. Yonemitsu, T. Tomohiro, *J. Chem.*

Soc., Chem. Commun., **1987**, 874. (c) F. Barigelletti, L. D. Cola, V. Balzani, P. Belser, A. V. Zelewsky, F. Vögtle, F. Ebmeyer, S. Grammenudi, *J. Am. Chem. Soc.*, **1989**, *111*, 4662. (d) J. J. Bour, W. V. D. Berg, P. P. J. Schlebos, R. P. F. Kanters, M. F. J. Schoondergang, W. P. Bosman, J. M. M. Smits, P. T. Beurskens, J. J. Steggerda, P. V. D. Sluis, *Inorg. Chem.*, **1990**, *29*, 2971. (e) K. Hegetschweiler, H. Schmalle, H. M. Streit, W. Schneider, *Inorg. Chem.*, **1990**, *29*, 3625.

186. W. W. Wendlandt, H. G. Hecht, *Reflectance Spectroscopy*, Interscience Publishers/ JohnWiley & Sons, New York, **1966**.
187. G. M. Sheldrick, SHELXL-97, *Program for X-ray Crystal Structure Refinement*, University of Göttingen, Göttingen, Germany, **1997**.
188. J. S. Miller, A. J. Epstein, *Angew. Chem., Int. Ed.*, **1994**, *33*, 385.
189. P. Rey, D. Luneau, A. Cogne, *Magnetic Molecular Materials*, (Eds: D. Gatteschi, O. Kahn, J. S. Miller, F. Palacio), Kluwer, Dodrecht, The Netherlands, **1991**.
190. G. J. T. Cooper, G. N. Newton, P. Kögerler, D.-L. Long, L. Engelhardt, M. Luban, L. Cronin, *Angew. Chem., Int. Ed.*, **2007**, *46*, 1340.
191. (a) E. König, *Coord. Chem. Rev.*, **1968**, *3*, 471. (b) L. Sacconi, *Pure Appl. Chem.*, **1971**, *27*, 161. (c) H. A. Goodwin, *Coord. Chem. Rev.*, **1976**, *18*, 293. (d) P. Gütlich, *Struct. Bonding*, **1981**, *44*, 82. (e) E. König, G. Ritter, S. K. Kulshrestha, *Chem. Rev.*, **1985**, *85*, 219. (f) E. König, *Prog. Inorg. Chem.*, **1987**, *35*, 527. (g) H. Toftlund, *Coord. Chem. Rev.*, **1989**, *94*, 67. (h) E. König, *Struct. Bonding*, **1991**, *76*, 51. (i) P. Gütlich, A. Hauser, H. Spiering, *Angew. Chem., Int. Ed.*, **1994**, *33*, 2024. (j) A. Hauser, J. Jeftić, H. Romstedt, R. Hinek, H. Spiering, *Coord. Chem. Rev.*, **1999**, *190-192*, 471. (k) J. A. Real, *Transition Metals in Supramolecular Chemistry*, ed. J. P. Sauvage, John Wiley & Sons Ltd., **1999**. (l) P. Gütlich, Y. Garcia, H. A. Goodwin, *Chem. Soc. Rev.*, **2000**, *29*, 419. (m) J. A. Real, A. B. Gaspar, V. Niel, M. C. Muñoz, *Coord. Chem. Rev.*, **2003**, *236*, 121. (n) *Spin Crossover in Transition Metal Compounds I–III, Topics in Current Chemistry*, ed. P. Gütlich, H. A. Goodwin, Springer, Heidelberg, **2004**, vol. *233–235*. (o) A. B. Gaspar, V. Ksenofontov, M. Seredyuk, P. Gütlich, *Coord. Chem. Rev.*, **2005**, *249*, 2661. (p) J. A. Real, A. B. Gaspar, M. C. Muñoz, *Dalton Trans.*, **2005**, 2062.
192. (a) J. Kröber, E. Codjovi, O. Kahn, F. Grolière, C. Jay, *J. Am. Chem. Soc.*, **1993**, *115*, 9810. (b) O. Kahn, C. Jay, J. Kröber, R. Claude, F. Grolière, *Eur. Pat.*, 0666561, **1995**. (c) O. Kahn, C. J. Martinez, *Science*, **1998**, *279*, 44. (d) A. Bousseksou, C. Vieu, J.-F. Létard, P. Demont, J.-P. Tuchagues, L. Malaquin, J. Menegotto, L. Salmon, *Int. Pat.*, 019695, **2003**. (e) A. Bousseksou, G. Molnár, P. Demont, J. Menegotto, *J. Mater. Chem.*,

2003, *13*, 2069. (f) J.-F. Létard, P. Guionneau, L. Goux-Capes, *Top. Curr. Chem.*, **2004**, *235*, 221. (g) J.-F. Létard, O. Nguyen, N. Daro, *Fr. Pat.*, 0512476, **2005**. (h) S. Bonhommeau, T. Guillon, L. M. L. Daku, P. Demont, J. S. Costa, J.-F. Létard, G. Molnár, A. Bousseksou, *Angew. Chem., Int. Ed.*, **2006**, *45*, 1625. (i) J.-F. Létard, N. Daro, S. Auffret, *Fr. Pat.*, 0704174, **2007**. (j) J.-F. Létard, O. Nguyen, N. Daro, *Eur. Pat.*, 065996, **2007**. (k) J.-F. Létard, O. Nguyen, N. Daro, *US Pat.*, 0311401, **2008**.

193. E. Diamantopoulou, T. F. Zafiropoulos, S. P. Perlepes, *Polyhedron*, **1994**, *13*, 1593.

194. G. V. Seguel, B. L. Rivas, C. Novas, *J. Chil. Chem. Soc.*, **2005**, *50*, 401.

195. (a) E. König, K. J. Watson, *Chem. Phys. Lett.*, **1970**, *6*, 457. (b) B. A. Katz, C. E. Strouse, *J. Am. Chem. Soc.*, **1979**, *101*, 6214. (c) M. Mikami, M. Konno, Y. Saito, *Acta Cryst.*, **1980**, *B36*, 275. (d) G. Vos, R. A. le Fêbre, R. A. G. de Graaff, J. G. Haasnoot, J. Reedijk, *J. Am. Chem. Soc.*, **1983**, *105*, 1682. (e) G. Vos, R. A. G. de Graaff, J. G. Haasnoot, A. M. van der Kraan, P. de Vaal, J. Reedijk, *Inorg. Chem.*, **1984**, *23*, 2905. (f) L. Weil, G. Kiel, C. P. Köhler, H. Spiering, P. Gütlich, *Inorg. Chem*, **1986**, *25*, 1565. (g) L. Wiehl, *Acta Cryst.*, **1993**, *B49*, 289. (h) M. Thomann, O. Kahn, J. Guilhem, F. Varret, *Inorg. Chem.*, **1994**, *33*, 6029. (i) J. Jung, F. Bruchhaüser, R. Feile, H. Spiering, P. Gütlich, *Z. Phys. B*, **1996**, *100*, 517. (j) J. J. A. Kolnaar, G. van Dijk, H. Kooijman, A. L. Spek, V. G. Ksenofontov, P. Gütlich, J. G. Haasnoot, J. Reedijk, **1997**, *36*, 2433. (k) J. J. A. Kolnaar, M. I. de Heer, H. Kooijman, A. L. Spek, G. Schmitt, V. Ksenofontov, P. Gütlich, J. G. Haasnoot, J. Reedijk, *Eur. J. Inorg. Chem.*, **1999**, 881. (l) Y. Garcia, P. Guionneau, G. Bravic, D. Chasseau, J. A. K. Howard, O. Kahn, V. Ksenofontov, S. Reiman, P. Gütlich, *Eur. J. Inorg. Chem.*, **2000**, 1531. (m) P. Gütlich, H. A. Goodwin, *Top. Curr. Chem.*, **2004**, *233*, 1. (n) P. Guionneau, M. Marchivie, G. Bravic, J.-F. Létard, D. Chasseau, *Top. Curr. Chem.*, **2004**, *234*, 97. (o) J. Kusz, P. Gütlich, H. Spiering, *Top. Curr. Chem.*, **2004**, *234*, 129. (p) K. Nakano, N. Suemura, S. Kawata, A. Fuyuhiro, T. Yagi, S. Nasu, S. Morimoto, S. Kaizaki, *Dalton Trans.*, **2004**, 982. (q) B. A. Leita, B. Moubaraki, K. S. Murray, J. P. Smith, J. D. Cashion, *Chem. Commun.*, **2004**, 156. (r) K. Nakano, S. Kawata, K. Yoneda, A. Fuyuhoro, T. Yagi, S. Nasu, S. Morimoto, S. Kaizaki, *Chem. Commun.*, **2004**, 2892. (s) M. H. Klingele, B. Moubaraki, J. D. Cashion, K. S. Murray, S. Brooker, *Chem. Commun.*, **2005**, 987. (t) K. Yoneda, K. Adachi, S. Hayami, Y. Maeda, M. Katada, A. Fuyuhiro, S. Kawata, S. Kaizaki, *Chem. Commun.*, **2006**, 45. (u) J. A. Kitchen, A. Noble, C. D. Brandt, B. Moubaraki, K. S. Murray, S. Brooker, *Inorg. Chem.*, **2008**, *47*, 9450.

196. (a) B. N. Figgs, M. A. Hitchman, *Ligand-Field Theory and its Applications*, Wiley-VCH,

New York, **2000**. (b) C. J. Ballhausen, *Introduction to Ligand Field Theory*, McGraw-Hill, New York, **1962**.

197. O. Kahn, *Molecular Magnetism*, VCH Publishers, New York, **1993**.
198. B. G. Wybourne, *Spectroscopic Properties of Rare Earths*, Wiley, New York, London, Sydney, **1965**.
199. G. J. T. Cooper, G. N. Newton, D.-L. Long, P. Kögerler, M. H. Rosnes, M. Keller, L. Cronin, *Inorg. Chem.*, **2009**, *48*, 1097.
200. A. Boido, R. Budries, C. C. Boido, P. Ioan, E. Terranova, A. Chiarini, F. Sparatore, *Chem. Biodiversity*, **2005**, *2*, 1290.
201. H. A. Goodwin, *Top. Curr. Chem.*, **2004**, *234*, 23.
202. (a) G. Férey, *Chem. Soc. Rev.*, **2008**, *37*, 191. (b) A. J. Blake, N. R. Champness, P. Hubberstey, W. S. Li, M. A. Withersby, M. Schröder, *Coord. Chem. Rev.*, **1999**, *183*, 117.
203. (a) H. J. Choi, M. Dincă, J. R. Long, *J. Am. Chem. Soc.*, **2008**, *130*, 7848. (b) L. Hou, Y.-Y. Lin, X.-M. Chen, *Inorg. Chem.*, **2008**, *47*, 1346.
204. (a) A. B. Lysenko, E. V. Govor, H. Krautscheid, K. V. Domasevitch, *Dalton Trans.*, **2006**, 3772. (b) G. Yang, R. G. Raptis, *Chem. Commun.*, **2004**, 2058. (c) C. Yang, X. Wang, M. A. Omary, *J. Am. Chem. Soc.*, **2007**, *129*, 15454. (d) C.-Y. Su, A. M. Goforth, M. D. Smith, P. J. Pellechia, H.-C. zur Loye, *J. Am. Chem. Soc.*, **2004**, *126*, 3576. (e) W. Ouellette, M. H. Yu, C. J. O'Connor, D. Hagrman, J. Zubieta, *Angew. Chem., Int. Ed.*, **2006**, *45*, 3497.
205. (a) M. Dincă, A. Dailly, Y. Liu, C. M. Brown, D. A. Neumann, J. R. Long, *J. Am. Chem. Soc.*, **2006**, *128*, 16876. (b) M. Dincă, W. S. Han, Y. Liu, A. Dailly, C. M. Brown, J. R. Long, *Angew. Chem., Int. Ed.*, **2007**, *46*, 1419.
206. (a) I. Sotofte, K. Nielsen, *Acta Chem. Scand. A*, **1981**, *35*, 739. (b) W. S. Sheldrick, P. Bell, *Z. Naturforsch., B: Chem. Sci.*, **1986**, *41*, 1117. (c) X. Meng, Y. Song, H. Hou, Y. Fan, G. Li, Y. Zhu, *Inorg. Chem.*, **2003**, *42*, 1306. (d) F. Jian, H. Xiao, P. Sun, *Acta Crystallogr., Sect. E: Struct. Rep. Online*, **2004**, *60*, m38. (e) Z. An, H. Sun, R.-S. Wang, *Acta Crystallogr., Sect. E: Struct. Rep. Online*, **2005**, *61*, m-2157.
207. S. Amirjalayer, M. Tafipolsky, R. Schmid, *Angew. Chem., Int. Ed.*, **2007**, *46*, 463.
208. T. Düren, F. Millange, G. Férey, K. S. Walton, R. Q. Snurr, *J. Phys. Chem. C*, **2007**, *111*, 15350.
209. (a) J. Luo, H. Xu, Y. Liu, Y. Zhao,L. L. Daemen, C. Brown, T. V. Timofeeva, S. Ma, H.-C. Zhou, *J. Am. Chem. Soc.*, **2008**, *130*, 9627. (b) S. Ma, X.-S. Wang, D. Yuan, H.-

C. Zhou, *Angew. Chem.*, **2008**, *120*, 4198.

210. P. Küsgens, M. Rose, I. Senkovska, H. Fröde, A. Henschel, S. Siegle, S. Kaskel, *Microporous Mesoporous Mater.*, **2009**, *120*, 325.
211. (a) H. Hart, D. Ok, *J. Org. Chem.*, **1986**, *51*, 979. (b) M. D. Coburn, J. K. Berlin, *Synthesis*, **1974**, 869. (c) J. H. Boyer, R. S. Buriks, *Organic Syntheses*, Wiley, New York, **1973**, collect. vol. 5, pp. 1067.
212. W. Łasocha, K. Lewinski, *J. Appl. Cryst.*, **1994**, *27*, 437.
213. A. Altomare, M. C. Burla, M. Camalli, B. Carrozzini, L. Cascarano, C. Giacovazzo, A. Guagliardi, A. G. G. Moliterni, G. Polidori, R. Rizzi, *J. Appl. Crystallogr.*, **1999**, *32*, 339.
214. V. Petricek, M. Dusek, L. Palatinus, Jana2000, *The crystallographic computing system*, Institute of Physics, Praha, Czech Republic, **2000**.
215. Y. Wang, B. Bredenkötter, B. Rieger, D. Volkmer, *Dalton Trans.*, **2007**, 689.

List of Abbreviations

General Abbreviations

Abbreviation	Complete form	Chemical formula
Ph	phenyl	-C_6H_5
Me	methyl	-CH_3
MeOH	methanol	CH_4O
EtOH	ethanol	C_2H_6O
THF	tetrahydrofuran	C_4H_8O
DCM	dichloromethane	CH_2Cl_2
Me_2CO	acetone	C_3H_6O
MeCN	acetonitrile	C_2H_3N
DMF	*N, N'*-dimethylformamide	C_3H_7NO
DMA	*N, N'*-dimethylacetamide	C_4H_9NO
DMSO	dimethyl sulfoxide	C_2H_6OS
NMP	1-methyl-2-pyrrolidone	C_5H_9NO
taH	1,2,3-triazole	$C_2H_3N_3$
btaH	1,2,3-benzotriazole	$C_6H_5N_3$
MebtaH	5-methyl-1,2,3-benzotriazole	$C_7H_7N_3$
Me_2btaH	5,6-dimethyl-1,2,3-benzotriazole	$C_8H_9N_3$
OMe_2btaH	5,6-dimethoxy-1,2,3-benzotriazole	$C_8H_9N_3O_2$
bta-CH_2OH	benzotriazole-1-methanol	$C_7H_7N_3O$
H_2-BBTA	benzobistriazole	$C_6H_4N_6$
tmbma	tris(N-methylbenzimidazole-2-ylmethyl)amine	$C_{27}H_{27}N_7$
acacH	acetylacetone	$C_5H_8O_2$
bzacH	benzoylacetone	$C_{10}H_{10}O_2$
tropH	tropolone	C_7H_6O
ttaH	thenyltrifluoroacetone	$C_8H_5F_3O_2S$
tfpbdH	4,4,4-trifluoro-1-phenyl-1,3-butanedione	$C_{10}H_7F_3O_2$
Ph/Me-pdH	1-phenyl-1,3-butanedione	$C_{10}H_{10}O_2$
Ph/Ph-pdH	1,3-diphenyl-1,3-propanedione	$C_{15}H_{12}O_2$
C_4H_3S/CF_3-pdH	4,4,4-trifluoro-1-(2-thienyl-1,3-butanedione)	$C_8H_5F_3O_2S$
dbmH	dibenzoylmethane	$C_{15}H_{12}O_2$

General Abbreviations (continued)

Abbreviation	Complete form	Chemical formula
HMTA	hexamethylenetetramine	$C_6H_{12}N_4$
bpy	4,4’-bipyridine	$C_{10}H_8N_2$
btapa	1,3,5-benzenetricarboxylic acid tris[N-(4- pyridyl) amide]	$C_{24}H_{18}N_6O_3$
H_2-bpb	1,4-bis(4’-pyrazolyl)benzene	$C_{12}H_{10}N_4$
H_2-bdpb	1,4-bis[(3,5-dimethyl)-pyrazol-4-yl]benzene	$C_{16}H_{18}N_4$
H_2-bdc	1,4-benzenedicarboxylic acid	$C_8H_6O_4$
H-pymo	2-pyrimidine-2-ol	$C_4H_4N_2O$
H-Phim	2-phenylimidazole	$C_9H_8N_2$
D-asp	D-aspartate	$C_4H_7NO_4$
bpe	*trans*-1,2-bis(4-pyridyl)ethylene	$C_{12}H_{10}N_2$
py	pyridyl	C_5H_5N
H_2-sal	salen or 2,2’-ethylenebis(nitrilomethylidene)diphenol	$C_{16}H_{16}N_2O_2$
pbbm	1,1’-(1,5-pentanediyl)bis(1*H*-benzimidazole)	$C_{19}H_{20}N_4$
ac	acetyl	C_2H_3O
H_3-btc	benzene-1,3,5-tricarboxylic acid	$C_9H_6O_6$
H_2-hfipbb	4,4’-(hexafluoroisopropylidene)bis(benzoic acid)	$C_{17}H_{10}F_6O_4$
H_3-imdc	4,5-imidazole dicarboxylic acid	$C_5H_4N_2O_4$
H_2-nds	1,5-naphthalenedisulfonic acid	$C_{10}H_8O_6S_2$
H_6-tcpp	tetra-(*p*-carboxyphenyl)porphyrin	$C_{46}H_{30}N_4O_8$
H_3-btt	1,3,5-benzenetris(tetrazol-5-yl)	$C_9H_6N_{12}$
H_2-bpdc	4,4’-biphenyldicarboxylic acid	$C_{14}H_{10}O_4$
$py_2(PhF_5)_2Por$	5,15-dipyridyl-10,20-bis(pentafluorophenyl) porphyrin	$C_{42}H_{18}F_{10}N_6$
H_4-tcpb	1,2,4,5-tetrakis(4-carboxyphenyl)benzene	$C_{34}H_{22}O_8$
H_2-ndc	2,6-naphthalenedicarboxylic acid	$C_{12}H_8O_4$
bdc-NH_2	2-aminobenzene-1,4-dicarboxylate	$C_8H_5NO_4$
H_2-pda	1, 4-phenylendiacetic acid	$C_{10}H_{10}O_4$
H_2-pzdc	pyrazine-2,3-dicarboxylic acid	$C_6H_4N_2O_4$
pyz	pyrazine	$C_4H_4N_2$
H_4-ntc	naphthalene-1,4,5,8-tetracarboxylic acid	$C_{14}H_8O_8$
H_2-tbip	5-tert-butylisophthalic acid	$C_{12}H_{14}O_4$

General Abbreviations (continued)

Abbreviation	Complete form	Chemical formula
H_2-bdt	1,4-benzeneditetrazole	$C_8H_6N_8$
H_4-bptc	4,4’-bipyridine-2,6,2’,6’-tetracarboxylic acid	$C_{14}H_8N_2O_8$
H_2-adc	9,10-anthracenedicarboxylic acid	$C_{16}H_{10}O_4$
H-apt	4-aminophenyltetrazole	$C_7H_6N_5$
H_3-pyta	2,4,6-pyridinetricarboxylic acid	$C_8H_5NO_6$
dabco	1,4-diazabicyclo[2.2.2]octane	$C_6H_{12}N_2$
H_3-btb	1,3,5-benzenetribenzoic acid	$C_{21}H_{18}O_6$
H_2-pdc	pyridine-2,4-dicarboxylic acid	$C_7H_5NO_4$
H_2-dtp	2,3-pyrazineditetrazole	$C_6H_4N_{10}$
H-fpymo	5-fluoropyrimidine-2-ol	$C_4H_3N_2OF$
H-im	imidazole	$C_3H_4N_2$
H-nim	2-nitroimidazole	$C_3H_3N_3O_2$
H-cbim	5-chlorobenzimidazole	$C_7H_5N_2Cl$
H_2-gla	glutaric acid	$C_5H_8O_4$
H_2-cnc	4-carboxycinnamic acid	$C_{10}H_8O_4$
dpt	3,6-di-4-pyridyl-1,2,4,5-tetrazine	$C_{12}H_8N_6$
H_3-tatab	4,4’,4’’-S-triazine-2,4,6-triyltribentoic acid	$C_{24}H_{12}N_3O_6$
H_2-cdc	1,12-dicarba-*closo*-dode-caborane-1,12-dicarboxylic acid	$C_4H_{12}O_4B_{10}$
dpni	*N*,*N’*-di-(4-pyridyl)-1,4,5,8-naphthalene tetracarboxydiimide	$C_{24}H_{12}N_4O_4$
H_3-dhbc	2,5-dihydroxybenzoic acid	$C_7H_6O_4$
H_2-dpyg	1,2-di(4-pyridyl)glycol	$C_{12}H_{12}N_2O_2$
H_2-pydc	pyridine-2,3-dicarboxylic acid	$C_7H_5NO_4$
bpp	1,3-bis(4-pyridyl)propane	$C_{13}H_{14}N_2$
H-pur	purine	$C_5H_4N_4$
H_3-tci	tris(2-carboxyethyl)isocyanuric acid	$C_{12}H_{15}N_3O_9$
H_2-fma	fumaric acid	$C_4H_4O_4$
H_2-bpndc	benzophenone-4,4’-dicarboxylic acid	$C_{15}H_{10}O_5$
H_4-cyclam	1,4,8,11-tetraazacyclotetradecane	$C_{10}H_{24}N_4$
H_4-mtb	methanetetrabenzoic acid	$C_{29}H_{20}O_8$
H-etz	3,5-diethyl-1,2,4-triazole	$C_6H_{11}N_3$

General Abbreviations (continued)

Abbreviation	Complete form	Chemical formula
H_4-tcom	tetrakis[4-(carboxyphenyl)oxamethyl]methane	$C_{32}H_{28}O_{12}$
H_2-bbdc	5-*tert*-butyl-1,3-benzenedicarboxylic acid	$C_{12}H_{14}O_4$
H_2-pyen	5-methyl-4-oxo-1,4-dihydropyridine-3-carbaldehyde	$C_{16}H_{18}N_4O_2$
XRPD	X-ray powder diffraction	
TGA	thermogravimetric analysis	
TG-MS	thermogravimmetry – mass spectroscopy	
TOF-MS	Time of Flight – Mass Spectroscopy	
LIFDI	Liquid Injection Field Desorption Ionization	
EDX	energy dispersive X-ray	
FT-IR	fourier transform – infrared	
UV-VIS	ultraviolet-visible	
NMR	nuclear magnetic resonance	
ICP-AES	inductively coupled plasma – atomic emission spectroscopy	
DRS	diffuse reflectance spectrum	
MOF	metal-organic framework	
MFU	Metal-organic Framework Ulm University	
MIL	Matérial Institute Lavoisier	
POST	Pohang University of Science and Technology	
MAMS	mesh-adjustable molecular sieve	
VLPP	vertex-linked polygons or polyhedra	
SBU	secondary building unit	
RT	room temperature	
2D	two-dimensional	
3D	three-dimensional	
SCO	spin-crossover	
HS	high-spin	
LS	low-spin	

IR Abbreviations

Abbreviation	Complete form
br	broad
w	weak
m	medium
s	strong
vs	very strong
sh	shoulder

NMR Abbreviations

Abbreviation	Complete form
δ	chemical shift
ppm	parts per million
s	singlet
dd	doublet of doublet

Acknowledgements

The research presented in this dissertation would not have been possible without the generous help and support of many people. In this section, I would like to thank and acknowledge all of them.

Firstly, I would like to thank my advisor Prof. Dr. Dirk Volkmer for his intellectual and professional guidance, for the opportunity to work in an exciting research group, and especially for allowing me a large degree of independence and creative freedom to explore a wide range of synthetic aspirations.

I am grateful to Prof. Dr. Nicola Hüsing, who commented on my research and reviewed the thesis.

I would like to thank the following persons for collecting single crystal X-ray data: Mr. Bernhard Müller (Institute of Inorganic Chemistry I, Ulm University), Dr. Hari P. Nayek (Philipps-Universität Marburg), and Prof. Dr. Mathias Weil (Vienna University of Technology).

I would like to express my sincere gratitude to Mrs. Elvira Kaltenecker-Zeisberger of our research group for helping me with infrared spectroscopy, thermogravimetic analysis, and Raman spectroscopy.

I am thankful to Ms. Daniela Mannes (Institute of Inorganic Chemistry I, Ulm University) for aid with TGA/IR analysis.

I am grateful to Mr. Samuel Blessing (Institute of Inorganic Chemistry I, Ulm University) for collecting X-ray powder diffraction data.

I would like to thank Dr. Peter Reuter of our research group for help with the scanning electron microscopy, AAS, and EDX analysis.

I would like to express my hearty gratitude to Dr. Carlheinz Röcker (Institute of Biophysics, Ulm University) for help with the solid-state fluorescence studies, and Ms. Ilona Stengel (Institute of Organic Chemistry II, Ulm University) for aid with the fluorescence studies in solution.

I would like to thank Dr. Irena Senkovska (Dresden University of Technology) for help with the gas sorption studies, and TG-MS analysis.

Acknowledgements

I am grateful to Dr. Manfred Speldrich (RWTH Aachen University) for performing the magnetic studies.

I would like to thank Dr. Herald Kelm (Technische Universität Kaiserslautern) for recording the Mösbauer data.

I am thankful to Mr. Egmont Pascher (Mikroanalytisches Labor Pascher) for aid with the ICP-AES analysis.

I would like to express my sincere gratitude to Prof. Dr. Stefanie Dehnen (Philipps-Universität Marburg), Prof. Dr. Paul Kögerler (RWTH Aachen University), Prof. Dr. Stefan Kaskel (Dresden University of Technology), and Prof. Dr. Hans.-Jörg. Krüger (Technische Universität Kaiserslautern) for their nice collaboration with our research group, and especially for the correction of my research manuscripts.

I am thankful to my practical students: Mr. Sebastian Berth and Ms. Felicia Seichter for the preparation of many of my compounds.

I would like to thank the following excellent services of Ulm University: NMR spectroscopy, mass spectroscopy (Dr. Markus Wunderlin), and elemental analysis.

I am grateful to all the members of our research group, especially to Dr. Maciej Grzywa for Rietveld refinement, Mr. Markus Tonigold for solving most of the single crystal X-ray structures, Dr. Jian-Hua Bu and Dr. Björn Bredenkötter for the synthesis of organic ligands, Mrs. Petra Murszat and Mr. Siegfried Graßhoff for ordering chemicals and other materials.

I wish to thank my friends from Ulm and rest of the world for their suggestions and cooperations.

I would like to thank my family members for constant long-distance support, personal inspiration, and so much more that I can not explain here.

Curriculum Vitae

Name	Mr. Shyam Biswas
Date of Birth	18th June, 1983
Place of Birth	North 24 Parganas, West Bengal, India
Sex	Male
Marital Status	Single
Nationality	Indian

Education

PhD in Chemistry	(2006-2010) Institute of Inorganic Chemistry II, Materials and Catalysis, Ulm University, Germany
Thesis Supervisor	Prof. Dr. Dirk Volkmer
Thesis Title	Design, Synthesis, and Characterization of Coordination Compounds and Coordination Polymers Based on 1,2,3-Triazolate Ligands
Master of Science	(2004-2006) Department of Chemistry, Indian Institute of Technology Kanpur, India
Thesis Supervisor	Prof. Dr. Jitendra K. Bera
Thesis Title	Electrochemical Studies of Ru_2^{4+} Paddlewheel Complexes Involving Naphthyridine Based Ligands
Bachelor of Science	(2001-2004) Chemistry (Honors), University of Calcutta, Kolkata, India

Publications

1. Homo- and Heteropentanuclear Coordination Compounds with T_d symmetry - the Solid State Structures of $[MZn_4(L)_4(L')_6]$ (M = Co^{II} or Zn; L = chloride or acac; L' =

1,2,3-benzotriazolate)

S. Biswas, M. Tonigold, D. Volkmer, *Z. Anorg. Allg. Chem.*, **2008**, *634*, 2532.

2. Nonanuclear Coordination Compounds Featuring $\{M_9L_{12}\}^{6+}$ Cores (M = Ni^{II}, Co^{II} or Zn^{II}; L = 1,2,3-Benzotriazolate)

   S. Biswas, M. Tonigold, M. Speldrich, P. Kögerler, D. Volkmer, *Eur. J. Inorg. Chem.*, **2009**, 3094.

3. A Cubic Coordination Framework Constructed from Benzobistriazolate Ligands and Zinc Ions Having Selective Gas Sorption Properties

   S. Biswas, M. Grzywa, H. P. Nayek, S. Dehnen, I. Senkovska, S. Kaskel, D. Volkmer, *Dalton Trans*., **2009**, 6487. Selected as Hot article by the referees and the editorial board. Also highlighted on the front page of the same issue of Dalton Transactions.

4. Syntheses and Magnetostructural Investigations on Kuratowski-type Homo- and Heteropentanuclear Coordination Compounds $[MZn_4Cl_4(L)_6]$ (M^{II} = Zn, Fe, Co, Ni, or Cu; L = 5,6-dimethyl-1,2,3-benzotriazolate) Represented by the Nonplanar $K_{3,3}$ Graph

   S. Biswas, M. Tonigold, M. Speldrich, P. Kögerler, M. Weil, D. Volkmer, *Inorg. Chem.*, **2010**, *49*, 7424.

5. Thermal spin-crossover in the $[M_3Zn_6Cl_6L_{12}]$ (M = Zn, Fe^{II}; L = 5,6-dimethoxy-1,2,3-benzotriazolate) system: structural, electrochemical, Mössbauer, and UV-Vis spectroscopic studies

   S. Biswas, M. Tonigold, H. Kelm, H.-J. Krüger, D. Volkmer, *Dalton Trans*., **2010**, 9851.

6. Two different 3D coordination frameworks based on benzobisimidazole linker generated under similar conditions: synthesis, structures and thermal properties

   S. Biswas, Y.-Y. Liu, M. Tonigold, M. Weil, D. Volkmer, manuscript in preparation.

Conferences, Meetings, and Workshops Attended

1. "1st International Conference on Metal-Organic Frameworks and Open Framework Compounds"

   October 8-10, 2008, Augsburg, Germany.

2. Topical workshop: "MOF Modelling for PhD students" in the DFG Priority Program

"Porous Metal-Organic Frameworks" (SPP 1362)
February 24-25, 2009, Dresden, Germany.

3. 21. Deutsche Zeolith-Tagung: "Poröse, nanostrukturierte Funktionsmaterialien-Synthese, Charakterisierung, Eigenschaften und Anwendungen"
   March 4-6, 2009, Kiel, Germany. Participated with poster.
4. Autumn School: "Application of Neutrons and Synchrotron Radiation in Engineering Materials Science"
   31 Aug. - 4 Sept., 2009, Lauenburg near Hamburg, Germany.
5. Kickoff Meeting of the DFG Priority Program "Porous Metal-Organic Frameworks" (SPP 1362)
   October 1-2, 2009, Dresden, Germany. Participated with poster.
6. Annual Meeting of the "MACADEMIA" (*M*etal-organic frameworks *A*s *C*atalysts and *A*dsorbents: *D*iscovery and *E*ngineering of *M*aterials for *I*ndustrial *A*pplications Project
   June 20-23, 2010, Château Liblice, Czech Republic.

Disclaimer

Most of the figures, schemes, tables and texts used in Chapters 2-5 have been taken (as such or after modification) from my own publications listed in the **Publications** section (pages 186-187). Most figures, tables and texts of Chapter 1 have been taken (as such or after modification) from various references listed in the **References** section (pages 158-178). The details of the sources of the figures, schemes, tables and texts for each chapter are shown in the following tables.

Chapter 2

Texts:

Section No.	Section Title	Page No.(s)	Publication No.(s)
2.1	Introduction	36-39	4
2.2.1	Syntheses	40-41	1, 4
2.2.2	Characterization		
	X-ray powder diffraction	41-44	4
	EDX Analysis	45-48	1, 4
	ICP-AES analysis	48-49	4
	TOF-MS analysis	49-51	4
	Thermogravimetric analysis	51-53	1, 4
	Infrared spectroscopy	53-55	1, 4
	UV-Vis spectroscopy	55-59	4
2.2.3	Structure Description	60-65	1, 4
2.2.4	Magnetic Properties	65-70	4
2.2.5	Graph Theoretical Representation	70-72	4
2.3.1	Materials and General Methods	72-73	1, 4
2.3.2	Syntheses	73-75	1, 4
2.3.3	Structure Determination	77-79	1, 4
2.4	Summary	80	1, 4

Figures:

Figure No.(s)	Page No.(s)	Publication No.(s)

2.1	38	4
2.2	39	4
2.3	40	1
2.6, 2.8, 2.9, 2.10	42-44	4
2.12-2.18	45-48	4
2.19-2.20	50-51	4
2.21-2.23	52-53	4
2.25-2.26	54-55	4
2.27-2.30	56, 58-59	4
2.32	61	1, 4
2.33	62	4
2.34	65	1, 4
2.35-2.38	67-69	4
2.39	70	4
2.40	72	4
2.41	77	4

Tables:

Table No.(s)	Page No.(s)	Publication No.(s)
2.3	49	4
2.4	63-64	1
2.5	64	4
2.6	69	4
2.7	75	4
2.8	75-77	4
2.9	78-79	1, 4

Scheme:

Scheme No.	Page No.	Publication No.(s)
2.1	41	1, 4

Disclaimer

Chapter 3

Texts:

Section No.	Section Title	Page No.(s)	Publication No.(s)
3.1	Introduction	81-84	2, 5
3.2.1	Syntheses	84-86	2, 5
3.2.2	Characterization		
	X-ray powder diffraction	86-88	2, 5
	EDX Analysis	88-89	5
	ICP-AES analysis	89	5
	Infrared spectroscopy	90-92	2, 5
	Thermogravimetric analysis	92-95	2, 5
	TG-IR analysis	95-97	5
	UV-Vis spectroscopy	97-99	2, 5
	Electrochemistry	99-100	5
3.2.3	Structure Description	100-108	2, 5
3.2.4	Magnetic Properties	109-111	2
3.2.5	Mössbauer Spectroscopy	111-113	5
3.3.1	Materials and General Methods	113-114	2, 5
3.3.2	Syntheses	114-116	2, 5
3.3.3	Structure Determination	117-120	2, 5
3.4	Summary	120-121	2, 5

Figures:

Figure No.(s)	Page No.(s)	Publication No.(s)
3.1	81	2
3.2	84	5
3.3, 3.5-3.7	86-88	2, 5
3.8	89	5
3.9-3.13	90-92	2, 5
3.14-3.18	93-95	2, 5

3.19-3.20	96	5
3.21-3.23	97-99	2, 5
3.24	100	5
3.25	102-103	2, 5
3.26	107-108	2, 5
3.27	110	2
3.28	112	5
3.29	117	2, 5

Tables:

Table No.(s)	Page No.(s)	Publication No.(s)
3.4-3.5	105	5
3.8	118-119	2, 5

Scheme:

Scheme No.	Page No.	Publication No.
3.1	85	5

Chapter 4

Texts:

Section No.	Section Title	Page No.(s)	Publication No.
4.1	Introduction	122-123	3
4.2.1	Syntheses	124	3
4.2.2	Characterization		
	Scanning electron microscopy	124-125	3
	EDX analysis	125	3
	X-ray powder diffraction	125-128	3
	Thermogravimetric analysis	128-129	3
	TG-MS analysis	130	3
	UV-Vis spectroscopy	132	3

	Luminescence spectroscopy	132-133	3
4.2.3	Rietveld Refinement	133-134	3
4.2.4	Structure Description	134-138	3
4.2.5	Sorption Properties	139-140	3
4.3.1	Materials and General Methods	140-141	3
4.3.2	Syntheses	142-143	3
4.3.3	Structure Determination	143-145	3
4.4	Summary	145-146	3

Figures:

Figure No.(s)	Page No.(s)	Publication No.
4.1	123	3
4.2	125	3
4.4-4.7	126-128	3
4.8-4.9	129	3
4.10	130	3
4.11-4.12	131	3
4.13	132	3
4.14	133	3
4.15	134	3
4.16	135	3
4.17	138	3
4.18	139	3
4.19	140	3
4.21	146	3

Tables:

Table No.(s)	Page No.	Publication No.
4.1-4.2	134	3
4.3	136	3
4.4	138	3

4.5	144	3
4.6	145	3

Chapter 5

Texts:

Section Title	Page No.(s)	Publication No.(s)
Conclusions and Outlook	147-151	1-5

Chapter 1

Texts:

Section No.	Section Title	Page No.(s)	Reference No.(s)
1.2.1	Synthesis and Applications	1-2	1
1.2.2	Role as Corrosion Inhibitors	2	2-5
1.2.3	Coordination Modes	2-4	6-16
1.2.4	Penta- and Nonanuclear Compounds	5-10	9-13, 16
1.3.1	History and Scope	11-12	26
1.3.2	Design Principles	12-17	22c, 26, 28
1.3.3	Synthesis	17-19	22b,f
1.3.4	Role as Functional Materials		
	Catalytic properties	19-24	40, 69
	Gas adsorption properties	24-34	26, 43

Figures:

Figure No.(s)	Page No.(s)	Reference No.(s)
1.4	3	6a, 6b
1.5	4	7
1.6	4	8
1.7	6	9, 13
1.8	8	9-13, 16
1.9	9	12c

1.10	10	13a
1.11	11	17
1.12	12	26
1.13	13	26
1.14-1.16	13-15	26
1.17	16	22c
1.18	20	40a
1.19	23	75
1.20	25	26

Tables:

Table No.	Page No.(s)	Reference No.
1.2	20-22	40a
1.3	26-29	43a
1.4	30-32	43a
1.5	33	43a